

U.S. weighs a crackdown on
risky pathogen studies p. 242

Timing of eating affects how
calories are burned pp. 251 & 276

On the edge of ultraefficient
networks p. 270

Science

\$15
21 OCTOBER 2022
science.org

 AAAS

COLOR PATTERNING

A ground plan for butterfly wings
pp. 249 & 304

BII | Prize for
Science | Innovation

Bringing research to life—and science to market

Behind every life-changing solution is an entrepreneurial scientist—a creative mind who proved an idea in the lab and dared to carry it out in the world.

To encourage more scientists to translate their research, BioInnovation Institute (BII) and *Science* present a new annual award.

Our three winners will have their essays published in *Science* magazine and will be invited into BII's entrepreneurial ecosystem. In addition, the Grand Prize winner will receive a prize of USD 25,000, and each runner-up will receive USD 10,000 at a grand award ceremony in Copenhagen, Denmark.

The call for applications has just opened.
Apply before November 1, 2022.
www.bii.dk/scienceprize

See film from the
grand award
ceremony 2022



Benedetto Marelli, Grand Prize Winner 2022

Presented by BII & *Science*

BII BioInnovation
Institute

Science

Apply before November 1, 2022
www.bii.dk/scienceprize





Better, quicker, smarter: The Zhejiang Lab is helping to make intelligent computing a reality.

10 fundamental scientific questions on intelligent computing

*Intelligent computing is a general framework and paradigm covering new theoretical methods, architecture systems, and technical capabilities that support the digital revolution in the emerging era of the Intelligent Internet of Everything. Its advent raises a myriad of issues from the basic (privacy rights) to the esoteric (human vs. machine). The Zhejiang Lab and Science have jointly solicited fundamental scientific questions with great significance for the future of intelligent computing. The following 10 questions, found to be most profound and challenging, were put forward by a panel of experts from around the world.**

How do we define intelligence and establish the evaluation and standardization framework for intelligent computing?

Broadly speaking, intelligence is the ability to analyze and appropriately respond to input (data). Many say that a truly intelligent system should be able to adapt to its environment—to learn, to reason, and to evolve. Yet how can we know whether that is the case for any given system?

The traditional evaluation of whether a system is intelligent is the Turing Test—can a human distinguish whether the system is a human or computer? Other, weaker, metrics exist such as asking whether the system performs its designated tasks accurately, or whether it can generalize beyond the

data it has been trained on. The rules for evaluation should be dependent on broader social contexts that allow for fairness and transparency.

Whether a standard framework for intelligent computing can be established is still an open question, as there is no universally agreed-upon metric upon which to conduct the debate. The rules pertinent to one system may run afoul of rules established for another, and the sands upon which that system is built may shift.

Is there a unified theory for analog computing?

Analog computing uses hardware to simulate algorithms, measuring continuous signals such as voltage or light intensity. It offers the advantages of low energy consumption and high computing efficiency in solving specific problems. But it fell out of favor many years ago with the advent of digital computing (which counts instead of measures), in part because at that time it was difficult to scale up and to verify analog systems.

Yet because of its ability to mimic components of biological networks such as synapses and neurons, analog computing has seen a resurgence. Different algorithms and platforms have evolved, all trying to establish more efficient ways to measure in the analog domain.

At present, though, it is an unrefined practice, using many kinds of physical carriers and calculation methods for simulation and calculation. It

awaits a unified theoretical model to help promote its standardization and large-scale application.

Where will the major innovations in computing come from, and will quantum computing approach the computational power of the human brain?

Joint design and coevolution of hardware and software will likely be a driving force behind major computing advances. Innovation is coming from all levels: We're seeing breakthroughs in emerging devices with unique properties almost every year. These drive—and are driven by—how they are organized into circuits and hierarchical systems, then into the algorithms and applications in which they are deployed.

Some new devices may not be useful for conventional computing, but might make neural networks efficient, while newer computing models may need unconventional hardware support. For example, new architecture will be needed to emulate the behavior of astrocytes (star-shaped glial cells in the central nervous system), which have been found to play an important role in cognition and differ in significant ways from neurons.

Quantum computers are operated differently from general purpose computers. It is still early in their development—currently they are mostly used for massive number-crunching activities such as encryption. Whether they will someday be able to simulate the cognitive-computing and even emotive ability of the human brain is a matter of active research.

What new devices will be built (transistors, chip design, and hardware paradigms: photonics, spintronics, biomolecules, carbon nanotubes)?

These and other devices already exist, or are actively being researched, at the nanometer scale, and further scaling is likely. The key is to make them better and make better use of them.

For example, there are many devices that are essential resistors, which can be programmed into levels, and those levels are memorized and transferred. A variety of technologies—electronic, photonic, etc.—can exhibit very similar behavior. These may be made to act very much like synapses in the brain in that the signal can be transferred, amplified, or reduced, and the excitations are integrated to build up synaptical waves that will be the basis of universal devices.

An issue is how to combine multiple physical dimensions, such as wavelength and polarization modes, to develop the corresponding optoelectronic interconnection devices. Power, performance, area, and cost need to be addressed to scale the technologies and allow them to evolve.

How could intelligent computing enable intelligent machines?

The term “machine” is an essential concept for “computing.” A machine—intelligent or otherwise—primarily has three components: a sensor that gathers external excitations (data), a memory that stores the information collected by the sensor, and a logic unit that collects data from the memory and performs inferences upon it, taking actions or sending signals.

An intelligent machine will perform intelligent computing. The question then becomes whether we can create an intelligent computing paradigm.

How can we understand the storage and retrieval of memory based on the digital twin brain?

The spatiotemporal dynamics of memory storage and retrieval suggests that it is highly controllable, giving hope that faulty memory can be repaired. Yet the synergistic and dynamic nature of brain networks hinders the exploration of the complex properties of memory.

Researchers have already created digital twins of different organs, including the brain, modeling and simulating their multiscale structure and function for research into pathologies such as Alzheimer's disease and epilepsy. While these simulations are arguably much less complex than human memory, they do demonstrate a proof-of-concept. Digital twins of the brain and its parts should allow researchers to break through the spatiotemporal scale and accuracy limitations of existing research into memory, its pathology, and its modulation.

Memory comprises the connections between the senses, emotions, concepts, and motor movements. As such, even if we succeed in replicating the entire brain, we cannot ignore those connections.

What is the most efficient path to converge silicon-based and carbon-based learning?

Silicon-based computing is gradually reaching its physical limits. Meanwhile, the human brain—the highest known form of carbon-based computing—lacks the speed, accuracy, and reliability of silicon. Carbon- and silicon-based computing platforms differ from each other in myriad ways. The former relies on a sparse but highly connected network of neurons, which is slow in terms of signal processing but very good at certain applications. Silicon platforms, on the other hand, rely on a highly integrated two-dimensional layout that boasts much faster transfer speeds.

Researchers are investigating at least two pathways to converge these systems: One is to build a mathematical model of the neural network

based on current silicon-based architecture. Another is to build deep neural networks with layers upon layers of network connections.

In their current incarnations, simple interconnects don't do computing. Perhaps one path to convergence would include building components that act more like neuronal synapses, integrating information and participating in the computational processes, rather than just acting as a relay.

How to build interpretable and efficient AI algorithms?

Efficient artificial intelligence (AI) algorithms with interpretability have long been pursued. Can new mathematical methodologies such as tensor networks, combined with the effective integration of expert knowledge, logical reasoning, and autonomous learning, bridge the divide between interpretability and efficiency in AI technology? Will that integration break the existing status of deep learning as "black box algorithm" and establish a new generation of interpretable systems that can be applied to different fields and different scenarios (voice, image, video, digital twin, metaverse, etc.)?

Can strong intelligent computing with features of self-learning, evolvability, and self-reflection be realized?

The goal of intelligent computing is to solve large-scale complex problems efficiently and autonomously in the human-machine-object space. The approaches of *weak intelligent computing (weak AI)* can obtain good results for such problems to a certain extent, but essentially, they rely heavily on the customized input of human a priori knowledge such as artificially preset physical symbol systems, neural network models, and behavioral rule sets.

Strong intelligent computing (strong AI) can change dynamically depending on the input and the environment. In different contexts, self-learning ability allows the system to avoid repeating the output of previous internal states; evolvability allows the system to adaptively improve its architectural pattern; self-reflection enables the system to expand the generalizability of the model based on the experience of solving historical

tasks. Therefore, one of the fundamental scientific challenges for future intelligent computing is to study the computing theory of higher-order complexity and to explore the automatic construction paradigm for solving major scientific problems, as well as letting the computer independently perform task comprehension and decomposition, optimized dynamic path construction, and kernel development model and evolution.

How can we use real-world data to discover and generalize knowledge?

There is a significant argument in the computing field as to whether machine learning can truly generalize, or whether it simply reiterates what is already known in a more efficient manner. Being able to identify objects or labels in a test set, it could be argued, is nothing more than saying that this object shares sufficient characteristics with those that were used to define it in the first place.

Therefore, intelligent computing needs to complete the calculation tasks originally performed by human predefined logic in an active, heuristic, and open intelligent form, and the effectiveness of these calculations need to be verified in the real world. Knowledge discovery is the premise of knowledge-driven applications, which makes it a significant indicator of how strong AI is. Knowledge discovery of real-world data is a major scientific problem to be solved by intelligent computing. The ability to be active and heuristic in open-world computing is an important milestone for intelligent computing to reach if it is to perceive anomalies, discover rules, summarize knowledge, and solve the limitations of logic program execution through finite-state machines.

Sponsored by



之江实验室
ZHEJIANG LAB

*The above is a compilation of contributions from (in alphabetical order):

Yiran Chen (Duke University)
Dawei Feng (China Computer Federation)
Ajay Jacob (University of Southern California)
Tianzi Jiang (Chinese Academy of Sciences)
Shangzhong Jin (Zhejiang Lab)
Chao Li (Zhejiang Lab)
Deyi Li (Chinese Association for Artificial Intelligence)
Wei Liu (Beijing University of Posts and Telecommunications)
Lei Meng (Shandong University)
Jiong Qiu (Zhejiang Zhelien Technology Co.)

Qinru Qiu (Syracuse University)
Shiju Ran (Capital Normal University)
Hongcai Shang (Beijing University of Chinese Medicine)
Yiyu Shi (University of Notre Dame)
Tuo Shi (Zhejiang Lab)
Gang Su (University of Chinese Academy of Sciences)
Huaimin Wang (China Computer Federation)
Tao Wang (China Computer Federation)
Zhiwei Wang (AGI-Lab Shanghai)
Chuyu Xiong (Chengdu Cyberkey Technology Co.)

Kele Xu (China Computer Federation)
Junchi Yan (Shanghai Jiao Tong University)
F. Richard Yu (Carleton University)
Zhifeng Zhao (Zhejiang Lab)
Ji Zhang (Zhejiang Lab)
Yu Zhang (Zhejiang Lab)
Tianshu Zhou (Zhejiang Lab)
Shiqiang Zhu (Zhejiang Lab)



Reproducibility

Sustainability

CST scientists have always been dedicated to helping researchers find answers and identify solutions. As scientists, we've always been passionate about sustainability, too. And now more than ever, sustainable solutions are needed. CST has committed to achieving net-zero emissions by 2029. And we've joined 1% for the Planet as its first life sciences industry member. Doing good science is important. So is just doing good.

www.cellsignal.com



© 2022 Cell Signaling Technology, Inc. All rights reserved. | For Research Use Only. Not For Use In Diagnostic Procedures. | 22-BCH-89002-AUG22



Antibodies for
Research



Immunoassay
Kits



Customs &
Services



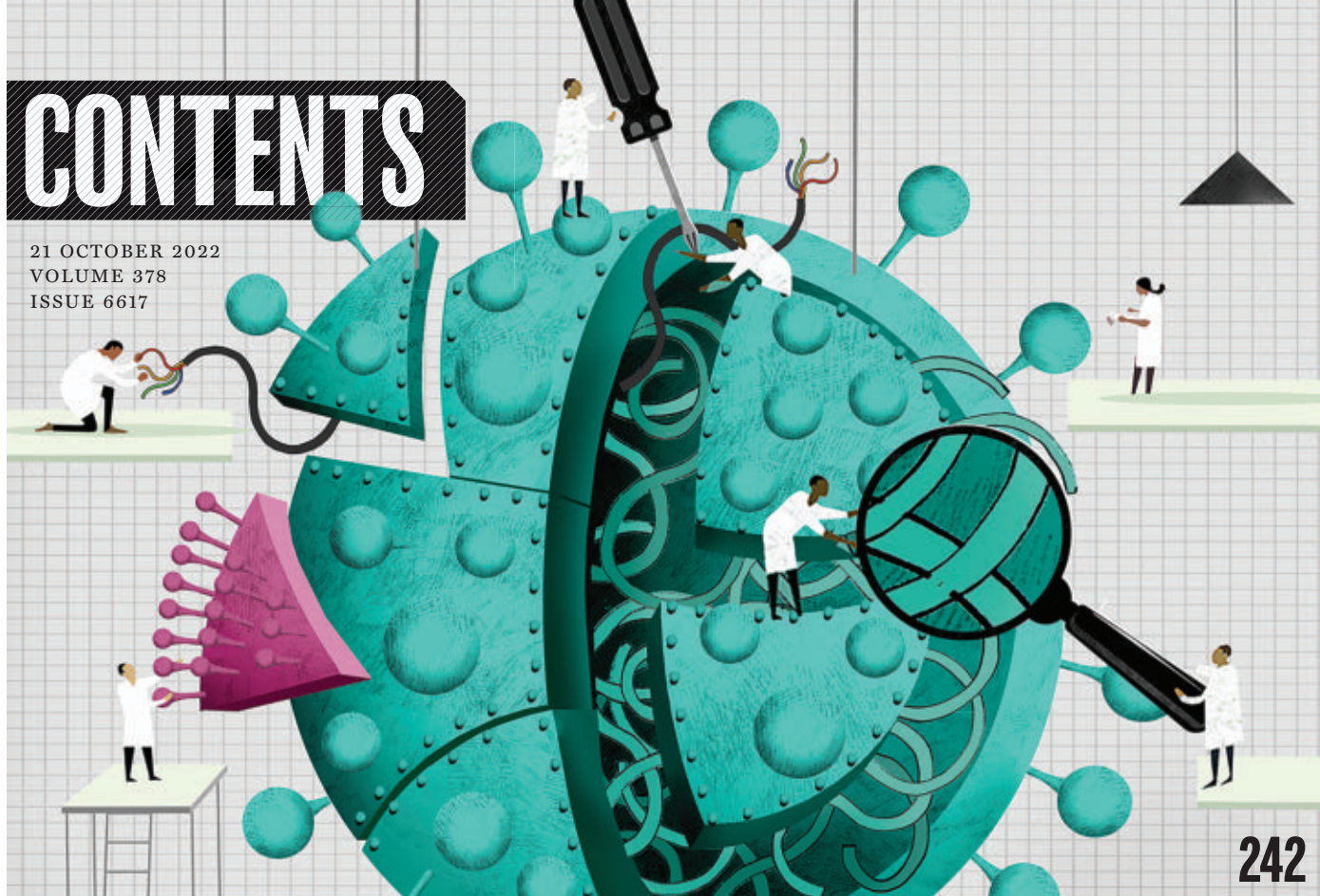
Application
Workflow
Solutions



Industry-leading
Validation
Process

CONTENTS

21 OCTOBER 2022
VOLUME 378
ISSUE 6617



242

NEWS

IN BRIEF

232 News at a glance

IN DEPTH

234 Heart risks fuel debate over COVID-19 boosters

With benefits unclear, some scientists question new round of shots for young people
By J. Couzin-Frankel

235 Brazil's election is a cliffhanger for scientists

Second Bolsonaro term could be "final nail" for science and environment
By S. Moutinho

237 How the Black Death left its mark on immune system genes

Study of DNA from medieval victims and survivors finds gene that helped protect people from deadly pathogen
By A. Gibbons

238 Has a new dawn arrived for space-based solar power?

Better technology and falling launch costs revive interest in a science-fiction technology
By D. Clerly

240 'Recoded' bacteria shrug off viral attacks

Modified cells don't allow invaders to replicate and don't share DNA
By M. Leslie
RESEARCH ARTICLE BY J. F. ZÜRCHER ET AL.
10.1126/SCIENCE.ADD8943

FEATURES

242 Making trouble

The United States is moving to tighten oversight of studies that could make viruses more dangerous. But how far should it go?
By J. Kaiser

INSIGHTS

POLICY FORUM

246 Science, misinformation, and the role of education

"Competent outsiders" must be able to evaluate the credibility of science-based arguments
By J. Osborne and D. Pimentel

PERSPECTIVES

249 How butterfly wings got their pattern

Gene regulatory elements play a crucial role in the pattern formation of butterfly wings
By M. Espeland and L. Podsiadlowski
REPORT p. 304

250 An ultraminiaturized spectrometer

Scaling down spectrometers could allow their application in consumer devices
By J. Quereda and A. Castellanos-Gomez
REPORT p. 296

251 The timing of eating controls energy use

Synchronizing food intake with the body clock boosts thermogenesis and limits obesity
By D. Lagarde and L. Kazak
RESEARCH ARTICLE p. 276

252 Sex matters in liver fat regulation

Growth hormone orchestrates a complex, sex-dependent balancing act
By D. J. Waxman and R. D. Kineman
REPORT p. 290

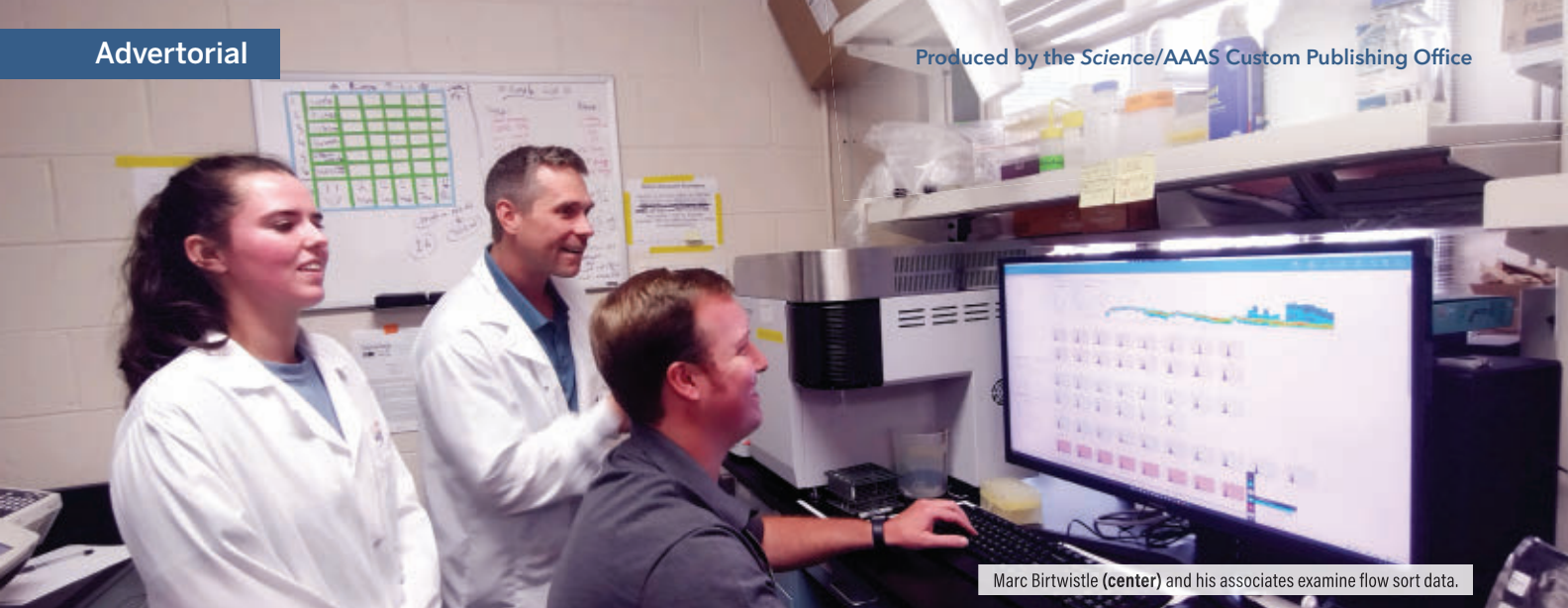
BOOKS ET AL.

254 Babbling bats and raucous reefs

Bioacoustics can aid in understanding and conserving species and ecosystems
By B. Gottesman

255 A neurosurgeon's climate fight

Cutting greenhouse emissions will require less brain and more (collective) brawn
By A. R. Aron



Marc Birtwistle (center) and his associates examine flow sort data.

Full spectrum flow cytometry for anticancer drug combinations: A Q&A with Marc Birtwistle, professor of chemical and biomolecular engineering at Clemson University

Combining two or more therapeutic agents has become a cornerstone of cancer therapy. However, predicting the concerted action of multiple drugs in tumors remains challenging due to the complexity and heterogeneity of the tumor microenvironment, the unknown interacting landscape of driver mutations, and anticancer drug resistance.

Marc Birtwistle, professor of chemical and biomolecular engineering at Clemson University, told *Science* how full spectrum flow cytometry on their Cytek® Northern Lights™ system helps his team understand the behavior of cancer cells and how they respond to combination therapy.

Science: What is the mission of your team? And how does the full spectrum flow cytometer support your research?

Marc Birtwistle (MB): We build mathematical models to understand what is happening inside cancer cells and how they might respond to drug combinations. But, despite much knowledge about cancer biology, it's still hard to predict the effect of drug combinations on cancer cells.

One knowledge gap for models is how important cancer genes and mutations interact with one another to control drug response, and it's currently hard to explore such questions experimentally due to, among other factors, limits on multiplexing. We devised this idea called MuSIC (multiplexing using spectral imaging and combinatorics). It turns out that if you have fluorophore combinations that are physically close enough such that one fluorophore can "talk" to another through FRET (Förster resonance energy transfer), and you measure that fluorescence not by a single data point but by looking at an entire emission spectrum, you'd be able to infer not only how much of each fluorophore is there, but also how much of their combinations is there. The Cytek® Northern Lights™ full spectrum flow cytometer is the perfect tool to verify and implement experimentally the theory we started developing.

Science: What are the advantages of using Northern Lights™ over other flow cytometry options?

MB: Available reagents can often be used with much more confidence because fluorophores with overlapping emission can usually be unmixed effectively with the Northern Lights™. If you're getting into higher-dimensional or high-parameter analysis

on the single-cell level, the spectral detection capabilities of the Cytek instrument make that much more possible in a pretty straightforward way. This flow cytometer is easy to use, and if you have a little experience with regular flow cytometry, there is almost no learning curve. The instrument is also relatively affordable on the spectrum of all flow cytometers. It's very robust with little if any downtime.

Science: How will flow cytometry change over the next 5-10 years? And what impact will that have on your research?

MB: People want to sort the different cell types that are in a tumor to analyze, culture, and study them, and high-dimensional analysis greatly facilitates that. Right now, the main option to get high-dimensional flow data is mass cytometry, and those instruments are more expensive, harder to use, and destroy cells during measurements. This Cytek instrument will get more and more market share because if people can have a flow cytometer at the same price as other ones but be able to easily measure 30 or 40 parameters, why wouldn't they do that? Cytek is coming out with a flow-sorting option with which you could sort rare cell populations from high-dimensional analysis, and I think that'll be game-changing in biomedical science. Imagine being able to test hypotheses about which rare cancer cells are resistant to drugs and follow up after sorting to see the time scales on which that resistance develops or fades. Besides that, there is room to increase analysis speed, sensitivity, spectral resolution, and number of excitation lasers to further push multiplexing.

Reimagining cell analysis to fuel scientific discovery

Cytek Biosciences is a leading single-cell analysis solutions company that delivers high-resolution, high-content, high-sensitivity cell analysis by utilizing the full spectrum of fluorescence signatures from multiple lasers to differentiate fluorescent tags on single cells.

www.cytekbio.com

Sponsored by



LETTERS

256 Regulatory insight from low-income countries

By J. K. Mukonzo et al.

256 The challenge of open access incentives

By M. Lerdau

257 Preserving credibility of open access journals

By B. Zhong and X. Liu

RESEARCH

IN BRIEF

259 From *Science* and other journals

RESEARCH ARTICLES

262 Cell biology

Mammalian oocytes store mRNAs in a mitochondria-associated membraneless compartment S. Cheng et al.

RESEARCH ARTICLE SUMMARY; FOR FULL TEXT: DOI.ORG/10.1126/SCIENCE.ABQ4835

263 Structural biology

Structure of the hepatitis C virus E1E2 glycoprotein complex A. Torrents de la Peña et al.

270 Computer networks

Delocalized photonic deep learning on the internet's edge A. Sludds et al.

PODCAST

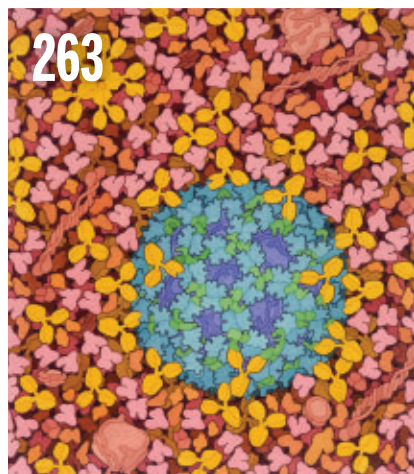


Illustration of hepatitis C virus (blue) in serum with antibodies (yellow) binding to multiple epitopes on the E1E2 surface glycoprotein



The world's largest marine protected area, in Hawaii, protects commercially important tuna species, providing spillover benefits for the longline fishing industry in nearby waters.

276 Metabolism

Time-restricted feeding mitigates obesity through adipocyte thermogenesis C. Hepler et al.

PERSPECTIVE p. 251

284 Cystic fibrosisMolecular structures reveal synergistic rescue of $\Delta 508$ CFTR by Trikafta modulators K. Fiedorczuk and J. Chen

REPORTS

290 Evolutionary biology

An evolutionary trade-off between host immunity and metabolism drives fatty liver in male mice J. Nikkanen et al.

PERSPECTIVE p. 252

296 Optics

Miniaturized spectrometers with a tunable van der Waals junction H. H. Yoon et al.

PERSPECTIVE p. 250

300 Wildlife disease

Disease outbreaks select for mate choice and coat color in wolves S. Cubaynes et al.

304 Evolution

Deep cis-regulatory homology of the butterfly wing pattern ground plan A. Mazo-Vargas et al.

PERSPECTIVE p. 249

308 Membranes

Highly flexible and superhydrophobic MOF nanosheet membrane for ultrafast alcohol-water separation L.-H. Xu et al.

313 Marine conservation

Spillover benefits from the world's largest fully protected MPA S. Medoff et al.

317 Cell biology

MTCH2 is a mitochondrial outer membrane protein insertase A. Guna et al.

DEPARTMENTS

230 Editorial

Antarctic marine life under pressure By B. Meyer and S. Kawaguchi

231 Editorial

Remember, do no harm? By H. H. Thorp

326 Working Life

Lost in a sea of faces By D. S. Ling

ON THE COVER

Butterfly wing patterns are mosaics of colored scales, as shown in this high-magnification image of a painted lady (*Vanessa cardui*) wing. A shared set of deeply conserved gene regulatory sequences are shown to control color pattern formation across species, suggesting that an ancient genetic architecture underlies wing pattern development. See pages 249 and 304.

Photo: Anyi Mazo-Vargas

Science Careers323

SCIENCE (ISSN 0036-8075) is published weekly on Friday, except last week in December, by the American Association for the Advancement of Science, 1200 New York Avenue, NW, Washington, DC 20005. Periodicals mail postage (publication No. 484460) paid at Washington, DC, and additional mailing offices. Copyright © 2022 by the American Association for the Advancement of Science. The title SCIENCE is a registered trademark of the AAAS. Domestic individual membership, including subscription (12 months): \$165 (\$74 allocated to subscription). Domestic institutional subscription (51 issues): \$2212; Foreign postage extra: Air assist delivery: \$98. First class, airmail, student, and emeritus rates on request. Canadian rates with GST available upon request. GST #125488122. Publications Mail Agreement Number 1069624. Printed in the U.S.A.

Change of address: Allow 4 weeks, giving old and new addresses and 8-digit account number. **Postmaster:** Send change of address to AAAS, P.O. Box 96178, Washington, DC 20090-6178. **Single-copy sales:** \$15 each plus shipping and handling available from backissues.science.org; bulk rate on request. **Authorization to reproduce** material for internal or personal use under circumstances not falling within the fair use provisions of the Copyright Act can be obtained through the Copyright Clearance Center (CCC), www.copyright.com. The identification code for Science is 0036-8075. Science is indexed in the Reader's Guide to Periodical Literature and in several specialized indexes.

Antarctic marine life under pressure

Bettina Meyer

is a professor in the department of Polar Biological Oceanography at the Alfred Wegener Institute Helmholtz Centre for Polar and Marine Research, Bremerhaven, Germany. bettina.meyer@awi.de

So Kawaguchi

is a principal research scientist at the Australian Antarctic Division in the Department of Climate Change, Energy, the Environment and Water, Tasmania, Australia. so.kawaguchi@aad.gov.au

Next week, the Convention on the Conservation of Antarctic Marine Living Resources (CCAMLR) convenes in Hobart, Tasmania, to examine the state of marine life in the Southern Ocean. As part of the Antarctic Treaty System, this convention entered into force in 1982, and its focus on the region's environmental integrity has never been more important, given the increasing effects of climate change and commercial fishing. An important focus over the past 40 years has been Antarctic krill, *Euphausia superba* (hereafter krill), a keystone species that helps to hold this marine ecosystem together. Climate and fishing stresses should prompt the CCAMLR to address whether management of krill fishing is at a level that protects the Southern Ocean from losing its overall balance of marine life and the oceanic processes that regulate global climate.

The Antarctic krill is a pelagic crustacean, endemic in the Southern Ocean. It serves as a direct energy link between the ocean's primary producers (phytoplankton) and higher trophic levels such as fish, seabirds, penguins, seals, and whales. Krill comprise 300 to 500 million tonnes of biomass, the largest population of a multicellular wild animal species on Earth. Consequently, this species plays a critical role in marine biogeochemical cycles that affect climate and ocean productivity.

Unfortunately, krill have declined in parts of the Atlantic sector of the Southern Ocean since the 1920s. This region, where nearly 70% of krill are located, is also home to the largest krill predator colonies and the largest krill fishing industry in the Southern Ocean. Since 2010, the annual krill catch in the southwest Atlantic sector has been increasing steadily. Recently, the time required to reach the krill catch limit in the Antarctic Peninsula has become shorter each year. As a result, krill fishing pressure around the South Orkney Islands has increased. In both of these subareas of the Southern Ocean, krill catches are now more concentrated in space and time than ever before.

The demand for krill will likely grow, driven by at least two industries: the increasing production of fish through aquaculture, resulting in higher demand for fishmeal, and the increasing demand for high-value pharma- and nutraceutical products from krill oil and krill meal. Fishing vessels equipped with new and efficient krill-fishing technology are supporting these

demands. At the same time, other pressures challenge the krill population, including the recovery of baleen whales that rely on krill as their main food source. Also, a warming ocean around the Antarctic Peninsula could reduce krill growth and reproduction rates, which would result in a smaller krill biomass. This could in turn affect the survival of predators, including penguins, seals, and whales.

Fisheries in the southwest Atlantic are managed by the CCAMLR. The organization strives to employ an ecosystem-based approach to ensure not only the sustainability of the krill population itself, but also the absence of any long-term adverse effects on krill-dependent predators, by regulating fisheries. The real question is whether the catch limit is set and distributed at the right scale in time and space, currently and

into the future. The answer requires more research to better understand krill biology and krill interaction with its predators. Also unclear is how these interactions are affected by climate change. Resolving these unknowns will be fundamental to improving management if the krill fishery is to expand sustainably while conserving the ecosystem. In this context, a krill expert group was initiated under the umbrella of the Scientific Committee on Antarctic Research (SCAR) to support providing biological information critical

for CCAMLR's krill management efforts.

The most pressing questions include determining the proportion of female and juvenile krill that are captured by commercial fishing and its effect on the krill population. Research can only answer these questions if there is cooperation with the fishing industry itself. In contrast to research vessels, the new generation of krill fishing vessels operate almost year-round. A collaboration would allow regular scientific krill sampling during data-poor austral autumn and winter to fill knowledge gaps.

It is time for international efforts, from federal funding agencies to nongovernmental organizations and industry, to support this research direction. At the same time, CCAMLR must forge a new krill management strategy that focuses on a spatial and seasonal allocation of catch limits at the Antarctic Peninsula, ensuring the balance of the Southern Ocean ecosystem.

—Bettina Meyer and So Kawaguchi

“...the region's environmental integrity has never been more important...”

Remember, do no harm?

When the advocacy group America's Frontline Doctors appeared on the steps of the United States Supreme Court in 2020, falsely stating that hydroxychloroquine was a cure for COVID-19, their pronouncement was virally shared by right-wing media and soundly debunked by medical academicians. A year later, one of these frontliners, Joseph Ladapo, became the surgeon general of Florida and a faculty member at the University of Florida College of Medicine. He has continued to spread dangerous misinformation about COVID-19 while his academic colleagues are shamefully silent.

Many assumed that Ladapo's faculty appointment was the result of political pressure by the university's administration as it aimed to please Florida Governor Ron DeSantis. It was unsurprising that anti-vax DeSantis wanted a surgeon general with anti-science views. But it was shocking that the medical school accepted Ladapo as a colleague. Even more shocking was a statement from the university president in the *Tampa Bay Times* confirming that Ladapo was voted into his position by the faculty and approved through the usual procedures. Even Ladapo's former supervisor at the University of California, Los Angeles, considered his approach to COVID-19 so dangerous as to violate the Hippocratic oath to do no harm, and declined to endorse him as the state surgeon general.

In his own defense, Ladapo told *Politico* that he was disappointed with the criticism because good science requires respect for all perspectives. "It's OK to disagree, and I've had no problem with disagreement," he said, "but what has been really disappointing is how disagreement has become a ticket or a passport to activate personal attacks." No one would disagree that personal attacks are out of bounds, but his depiction of science is off the mark. Unequal perspectives do not deserve equal time, and challenging scientific consensus requires evidence that has been subjected to peer review and published with all the data disclosed so that the scientific community can replicate the findings. Ladapo recently has been circulating an unattributed study apparently showing that the risk of heart complications from mRNA vaccines to COVID-19 makes them harmful for males under 40. To be taken seriously, such a major challenge to

scientific consensus requires rigorous review and wide evaluation of the underlying data. Nothing like that happened. "Ladapo's dissemination of flawed data that purports a risk of cardiac death among men age 18 to 39 after mRNA vaccines was baseless, reckless, and irresponsible," said cardiologist Eric Topol. "The risk of myocarditis in this demographic is real and notable, but all studies with close follow-up have indicated it is typically mild and fully resolves in nearly all affected."

Ladapo has tried to initiate a scientific "debate" on Twitter about the study, saying "I love the discussion that we've stimulated." This move is from page 1 of the anti-science playbook. A credentialed scientist from outside

the field questions scientific consensus in a public manner that undermines trust in science. Many have played this role during the pandemic, but the pattern reaches back decades to scientists who have, for political purposes, challenged consensus on tobacco, ozone, strategic defense, and climate change.

This raises the question of what responsibility the scientific community has to condemn its members when they enable the spread of misinformation. The situation at the University of Florida creates an opportunity to wrestle with this issue. Ladapo has confirmed his doubters' fears and has betrayed the responsibilities afforded by academic freedom and tenure. So far, the university doesn't seem to

want to wrestle with the situation. When I asked for a comment, the university health system did not specifically address the Ladapo affair but said in a statement that they continued to support recommendations from the Centers for Disease Control and Prevention on vaccination and that "peer-reviewed publications and data analyses are the gold standard in ensuring accurate conclusions are drawn from the research questions scientists are asking." That's far from an adequate response.

It's easy to blame the politicians, right-wing cable TV hosts, and podcast hucksters for spreading misinformation. But is it defensible to blame these folks without also acknowledging that unchallenged members of the scientific community are making it possible for them to sow this doubt? Until the scientific community deals with misinformation from within, it cannot expect to deal with it from without.

—H. Holden Thorp



H. Holden Thorp
Editor-in-Chief,
Science journals.
hthorp@aaas.org;
@hholdenthorp

"...unchallenged members of the scientific community are making it possible...to sow...doubt..."

NEWS

IN BRIEF

Edited by
Jeffrey Brainard

A gash (center, left) in the dish of the famed Arecibo Observatory radio telescope, caused by an equipment collapse, has left it unusable since 2020.

ASTRONOMY

U.S. wants to use Arecibo site for science education

The Arecibo Observatory in Puerto Rico, for decades home to the world's largest radio telescope, will be a leading research center no more. The U.S. National Science Foundation (NSF) last week invited proposals to transform the facility, which was badly damaged when a radio receiver crashed down on its iconic 305-meter dish in 2020, into a center for science education and outreach. Before the collapse,

Arecibo actively supported science education, welcoming nearly 100,000 visitors a year. Some astronomers have urged NSF to build a new large telescope at the site. But the NSF announcement suggests it has no such plans. Researchers also worry the new center's budget—\$5 million over 5 years—won't be enough to maintain several smaller instruments still operating at the observatory or support its existing technical staff.

Trump pressure on CDC detailed

PUBLIC HEALTH | The administration of former President Donald Trump repeatedly pressured senior staff at the U.S. Centers for Disease Control and Prevention (CDC) to edit or suppress reports offering grim news about COVID-19, a U.S. House of Representatives select subcommittee reported this week. During 5 months in 2020, political appointees took the unusual step of targeting 18 reports written for CDC's flagship *Morbidity and Mortality Weekly Report (MMWR)* that they perceived as undermining Trump's rosier view of the pandemic, the report says. CDC staff members pushed back, and just five reports were altered or delayed. A political appointee demanded that *MMWR* be shut down if he could not read draft reports, which CDC by policy had not shared with outsiders. "This would be a red line, I think, for all of us," Henry Walke, a CDC incident manager for

coronavirus response, told the subcommittee. Some findings from the Democrat-led panel were previously reported by news organizations, but its 91-page report offers new details from interviews with 19 current and former senior officials, including Robert Redfield, CDC's director under Trump. Former Trump administration officials cited in the report have dismissed it as partisan.

Journals call for climate justice

HEALTH POLICY | Ahead of a major climate policy conference in Egypt in November, 259 health journals are asking wealthy nations to step up support for lower income nations, such as those in Africa, disproportionately affected by climate change. "It is highly unjust that the most impacted nations have contributed the least to global cumulative emissions," says the editorial, written by editors of journals based in Africa and published

this week by all the participating journals. It highlights how climate change is linked to drought, famine, flooding, and the resulting harm to the health and wealth of African nations. The editorial calls for changes in financing to low-income countries to help them adapt to the effects of climate change, such as by providing them grants instead of loans. Signers include the BMJ, Lancet, and JAMA families of journals and *The New England Journal of Medicine*.

Mask wearing improved behavior

COVID-19 | People in China who wear masks to protect against COVID-19 behave more ethically in public than those who don't, researchers found. The result challenges a hypothesis that masks encourage deviant behavior by increasing anonymity. The researchers did 10 different studies involving more than 68,000 participants.

Some tallied antisocial behavior of masked and unmasked people in public, such as pedestrians who ran red lights and bicyclists parking in no-parking zones. Another study measured whether participants lied about solving an unsolvable puzzle. In all these cases, masked people obeyed rules and acted ethically more often than unmasked ones, the researchers report this week in the *Proceedings of the National Academy of Sciences*.

Sharing antibiotics is no Rx

PUBLIC HEALTH | Thérèse Coffey, the United Kingdom's secretary for health, drew criticism last week after she reportedly said at an official meeting that she had shared leftover antibiotics with others, which is illegal in that country. Health researchers worry excessive prescribing and use of antibiotics will foster drug-resistant microbes. Coffey's comment came during a discussion of the pressure on physicians to handle caseloads. The government is considering allowing pharmacies to provide patients antibiotics without a doctor's prescription.

Warming cancels crab harvest

FISHERIES SCIENCE | In a first, the state of Alaska last week canceled the \$250 million Bering Sea snow crab season because of a population crash that scientists blame largely on a marine heat wave. The population of the crab, *Chionoecetes opilio*, plummeted from an estimated 11.7 billion in 2018 to about 2 billion this year. Temperatures on the Bering's bottom, where the crabs dwell, reached 3.5°C in 2018, up from 1.5°C in 2017, and stayed high for at least 2 years. Adjusting to the warmer waters would have stressed and

potentially starved them, the National Oceanic and Atmospheric Administration said. After temperatures returned to normal starting in 2020, however, the crabs didn't reappear. That indicates they did not temporarily move away in search of cooler water.

Blended viral strain draws fire

COVID-19 | Twitter exploded with outrage this week about a study in which scientists engineered the spike protein of Omicron—the fast-spreading but relatively mild variant of SARS-CoV-2 that's now pervasive—into a deadlier strain of the coronavirus found in Washington state early in the pandemic. The objective was to learn whether the protein alone explains Omicron's lower pathogenicity. The hybrid virus killed 80% of infected mice, according to a preprint posted on 14 October by Boston University (BU) researchers. Critics worried it could escape the lab. They also argued that the work, partially funded by the National Institutes of Health (NIH), qualifies as “gain-of-function” (GOF) research that makes risky pathogens more dangerous and should have gone through a high-level federal review (see p. 242). BU officials said the study, conducted under the second highest level of biosafety precautions, BSL-3, was not GOF research because it resulted in a virus less deadly to mice than the original Washington strain, which killed 100% of the animals. They also said it was not subject to GOF review because NIH funds were only used for developing tools used in the experiment. Several non-BU virologists pointed out the mice were engineered to be extremely sensitive to SARS-CoV-2, which only kills about 1% of people.

Ukrainian science hangs on

As a new wave of Russian missiles began to rain down on Ukraine on 10 October, killing and wounding civilians, science was hit as well. One rocket blew out windows at the science ministry and the Taras Shevchenko National University of Kyiv. Also damaged was the headquarters of the National Academy of Sciences of Ukraine. Its president, Anatoly Zagorodny, 71, added repairing the premises to a to-do list that includes maintaining a pulse in 160 science institutes and paying salaries to some 27,000 staff as the war drains Ukraine's budget. *Science* interviewed Zagorodny, a theoretical physicist, at the academy's headquarters a few days before 10 October. A longer version of this interview is at <https://scim.ag/3QsZagorodny>.

Q: Many Ukrainian scientists have fled. How will you entice them to come home after the war?

A: It really will be a big challenge. Many Ukrainian students are studying elsewhere in Europe. We need to ensure that international cooperation doesn't contribute to the brain drain.

Q: How are those who stayed being helped?

A: The Austrian Academy of Sciences, ALLEA [All European Academies], PAN [the Polish Academy of Sciences], and others have announced, or are going to announce, special calls for support. And we are in conversation with PAN and the U.S. National Academy of Sciences on their new program [to invite proposals from teams of Polish scientists and colleagues in Ukraine]. We also appealed to leading manufacturers for scientific equipment. As of today, four companies—Agilent, Bruker, Carl Zeiss, and Analytik Jena—have nobly decided to donate urgently needed instruments totaling more than \$4 million. We're deeply grateful.

Q: As Russia attacks civilian targets, you could face a long winter.

A: We will recommend to institutes how to save equipment [for example, sample freezers and mass spectrometers that maintain a vacuum] and infrastructure if they lose electricity and heating. It's terrorism, pure and simple. But Ukrainian people are united. I don't know anyone who doesn't believe we will be victorious.



Alaska's snow crab harvest, canceled this year by the state, totaled more than 16.6 million kilograms in 2020.



A teen receives a dose of the new Omicron-specific COVID-19 booster in a Pennsylvania pharmacy last month. Data on boosters' benefits for young people are lacking.

COVID-19

Heart risks fuel debate over COVID-19 boosters

With benefits unclear, some scientists question new round of shots for young people

By Jennifer Couzin-Frankel

Florida Surgeon General Joseph Ladapo ignited a furor this month when, based on a state analysis purporting to show COVID-19 vaccines were linked to cardiac deaths in young men, he advised men ages 18 to 39 to steer clear of the shots. Scientists slammed his warning and decried the eight-page analysis, which was anonymous and not peer reviewed, for its lack of transparency and flawed statistics.

Still, COVID-19 vaccines do have a rare but worrisome cardiac side effect. Myocarditis, an inflammation of the heart muscle that can cause chest pain and shortness of breath, has disproportionately struck older boys and young men who received the shots. Only one out of several thousand in those age groups is affected, and most quickly feel better. The number of deaths tentatively linked to vaccine myocarditis around the world has been tiny. But several new studies suggest the heart muscle can take months to heal, and some scientists worry about what this means for patients long term. The U.S. Food and Drug Administration (FDA) has ordered vaccinemakers Pfizer and Moderna to conduct a raft of studies to assess these risks.

As they parse emerging data and fret over knowledge gaps, scientists and doctors are divided over whether such concerns should influence vaccine recommendations, especially

now that a new COVID-19 wave is looming and revamped boosters are hitting the scene. Nearly all urge vaccinating young people with the first two vaccine doses, but the case for boosters is more complicated. A key problem is that their benefits are unknown for the age group at highest risk of myocarditis, who are at lower risk of severe COVID-19 and other complications than older adults.

"I'm a vaccine advocate, and I would still vaccinate children," says Jane Newburger, a pediatric cardiologist at Boston Children's Hospital who has cared for and studied post-vaccine myocarditis patients. But Michael Portman, a pediatric cardiologist at Seattle Children's Hospital who's also studying patients, says he would hesitate to recommend boosters to healthy teens. "I don't want to cause panic," Portman says—but he craves more clarity on the risk-benefit ratio.

Earlier this month, a team from Kaiser Permanente Northern California and the U.S. Centers for Disease Control and Prevention (CDC) reported the risk of myocarditis or pericarditis—inflammation of the tissue surrounding the heart—was about one in 6700 in 12- to 15-year-old boys following the second vaccine dose, and about one in 16,000 following the first booster. In 16- and 17-year-olds, it was about one in 8000 after the second dose and one in 6000 after the first booster. Men ages 18 to 30 have a somewhat elevated risk as well.

Many scientists suspect vaccine-driven myocarditis is somehow triggered by an immune reaction following the COVID-19 shot. A study from Germany published last month in *The New England Journal of Medicine* suggested it may be driven by an inflammatory response associated with SARS-CoV-2's spike protein, which the messenger RNA (mRNA) vaccines coax the body to produce. The group reported finding certain antibodies in both vaccine-induced myocarditis patients and patients with severe COVID-19, which itself can cause myocarditis. The same antibodies, which interfere with normal inflammation control, also turned up in children who developed a rare, dangerous condition called multisystem inflammatory syndrome (MIS-C) after a bout of COVID-19. "I think it's really another mechanism," says Karin Klingel, a cardiac pathologist at the University of Tübingen who helped lead the work. But whether the antibodies are directly causing myocarditis remains unclear.

Most postvaccine myocarditis patients are briefly hospitalized and their symptoms quickly abate. Newburger's hospital has tracked 22 patients who developed the condition, and she is largely reassured by their healing. Portman agrees: "Many of these kids are asymptomatic after they leave the hospital."

But what he sees in the youngsters during follow-up appointments nags at him:

Although their heart rhythm is normal and they usually feel fine, MRI scans of their heart often show something called late gadolinium enhancement (LGE), which signifies injury to the muscle. In June, Portman and his colleagues reported in *The Journal of Pediatrics* that 11 of 16 patients had LGE about 4 months after their bout of myocarditis, although the area affected in the heart had shrunk since they were hospitalized. This month, a CDC team reported that among 151 patients who had follow-up cardiac MRIs after at least 3 months, 54% had abnormalities, mostly LGE or inflammation.

How much to worry about lingering scarring in vaccinated patients is a question mark. Right now, this “doesn’t seem to correlate to adverse clinical outcomes,” says Peter Liu, chief scientific officer of the University of Ottawa Heart Institute. Nonetheless, “We’re tracking these” patients over time, Liu says, in a registry study of about 200 affected people across Canada so far. “We need longer term data to reassure us and the public,” agrees Hunter Wilson, a pediatric cardiologist at Children’s Healthcare of Atlanta who supports boosters for young people. (He recently led a study comparing outcomes from myocarditis induced by vaccines, by COVID-19 itself, and by MIS-C, which is available as a preprint and is under journal review.)

FDA is requiring six myocarditis studies each from Pfizer and Moderna, the makers of the two mRNA vaccines. Newburger, who’s also keen for longer term data, co-leads one of them in conjunction with the Pediatric Heart Network; the study, which Portman is involved in as well, aims to start recruiting up to 500 patients later this fall. The various studies will assess not only full-blown myocarditis, but also a shadow version called subclinical myocarditis, in which individuals remain symptom-free.

Subclinical myocarditis may be more common than thought. Christian Müller, director of the Cardiovascular Research Institute at University Hospital Basel, recently collected blood samples from almost 800 hospital workers 3 days after they got a COVID-19 booster. None met the criteria for myocarditis but 40 had high levels of troponin, a molecule that can indicate damage to the heart muscle. Chronic heart problems and other preexisting conditions might be to blame in 18 cases, but for the other 22 cases—2.8% of participants, women and men—Müller believes the vaccine caused troponin levels to rise. The findings, which he presented at a meeting in August, align

with those of a recently published study from Thailand.

The good news: In both studies, troponin levels quickly fell to normal. And a brief troponin spike without symptoms doesn’t concern Müller: “If we’re healthy and we lose 1000, 2000 [heart muscle cells], that is irrelevant,” he says. What worries him is a potential cumulative effect of annual boosters. “I’m highly concerned if we consider this a recurrent phenomenon.”

The big question is whether any risk, however minimal, to the heart is outweighed by the benefits of a booster. Young people are rarely hospitalized for COVID-19, but the virus is not risk-free for them either. Last year, a study of nearly 1600 college athletes prior to vaccination found 2.3% had either clinical or subclinical myocarditis after a bout of COVID-19. Other serious effects of infection include MIS-C and Long Covid. Studies in adults suggest vaccination reduces the risk of Long Covid by anywhere from 15% to 80%. “Because of that, I really think vaccination is worth it,” Liu says.

Müller does not: He’s glad his teenage daughters received their initial vaccine series but has no plans get them a booster. Paul Offit, an infectious disease specialist at the Children’s Hospital of Philadelphia, thinks that if the goal is to stave off severe illness, there’s little evidence healthy people under age 65 need a booster dose—and certainly not adolescents.

Countries are divided as well: In Switzerland, Germany, and Denmark, the new bivalent boosters are recommended mainly for older adults and vulnerable younger ones. In the United States, in contrast, CDC now recommends that everyone age 5 and up, regardless of health history, get boosted.

Complicating the risk-benefit analysis are the pandemic’s ever-changing currents. Omicron, now the dominant variant, “seems a whole lot milder” than its predecessors, Newburger says. CDC reports that as of August, at least 86% of children in the United States have been infected by SARS-CoV-2, which may reduce their risk of future infections. At the same time, “We’re seeing so much less vaccine myocarditis now” than last year, Newburger says. She doesn’t know why, but the trend might alleviate concerns about the side effect. “Everything is a moving target.”

The uncertainty is frustrating—but that’s the story of the pandemic, says Walid Gellad, a physician who studies drug safety at the University of Pittsburgh: “Everything that we need to know we end up learning after we needed to know it.” ■

“Everything that we need to know we end up learning after we needed to know it.”

Walid Gellad,
University of Pittsburgh

RESEARCH POLICY

Brazil’s election is a cliffhanger for scientists

Second Bolsonaro term could be “final nail” for science and environment

By **Sofia Moutinho**

Brazil’s presidential race is much closer than the polls predicted—and scientists are fretting. Many fear that another term for President Jair Bolsonaro, the right-wing former army captain who frequently attacked science, would bring irreversible damage to science, education, the environment—and even to Brazilian democracy itself. Bolsonaro has cast doubts on the Brazilian voting system and signaled he will not recognize the results if he loses.

His rival, leftist former President Luiz Inácio “Lula” da Silva, comes with his own baggage: He was convicted on corruption charges in 2018 and spent 18 months in prison before his sentence was annulled. But he has promised to invest more in science and to chart a greener course than during his first presidency, from 2003 to 2011.

In September, polling data suggested Lula had a comfortable lead and might even win an absolute majority in the first round on 2 October. But he only received 48% of the vote, whereas Bolsonaro did better than expected with 43%, necessitating a 30 October runoff. “I’m worried,” says Luiz Davidovich, a professor and physicist at the Federal University of Rio de Janeiro’s main campus and former president of the Brazilian Academy of Sciences. “What is at stake now is democracy itself, the freedom of thinking, and the survival of science in Brazil.”

Bolsonaro’s government made deep cuts in science and education budgets. He also ridiculed evidence-based COVID-19 measures such as vaccination and social distancing while promoting unproven treatments such as hydroxychloroquine. Last year, a parliamentary inquiry recommended Bolsonaro be charged with crimes against humanity for his administration’s

botched response to the pandemic, which killed more than 600,000 Brazilians.

Bolsonaro's administration promoted development in the Amazon and often turned a blind eye to illegal deforestation, resulting in the loss of 31,000 square kilometers of vegetation, an area the size of Belgium, during his 4 years in power. (According to the independent research group MapBiomas, only 2.4% of satellite-based deforestation alerts issued by federal environmental agencies between 2019 and 2021 resulted in follow-up inspections or enforcement.) The government created new rules that weakened environmental inspections, and in March, Bolsonaro proposed a new law allowing mining concessions inside Indigenous reserves. The bill, which critics say violates Indigenous sovereignty rights guaranteed under Brazil's constitution, was fast-tracked and is now under consideration in Congress.

The government has also weakened federal agencies and institutions in charge of monitoring and acting on deforestation, such as the Brazilian Institute of Environment and Renewable Natural Resources and the National Space Agency (*Science*, 27 May, p. 910). Even a new government would "have a hard time to stop the destruction and rebuild the institutions," says Mercedes Bustamante, an ecologist at the Federal University of Brasília and a member of the Intergovernmental Panel on Climate Change.

During Lula's presidency a decade ago, science funding grew, especially during his first term. Lula also presided over a booming economy that lifted millions out of poverty, but his administration was tainted by accusations of corruption, culminating in the impeachment of his successor Dilma Rousseff in 2016 and Lula's arrest and conviction for corruption and money laundering in 2018. His 12-year sentence was annulled in 2020 because the judge who convicted him was deemed partial, but Lula was never officially absolved. He proclaims his innocence and argues his prosecution was politically motivated.

Regardless of his past, many scientists and environmental advocates believe he is the better alternative. Whereas Bolsonaro's election platform is vague on science, calling for more private funding for technological innovation in companies, Lula's platform describes science as "stra-

tegical and central to transforming Brazil into a truly sovereign and developed country." The former union leader often boasts about opening more public universities than any other president and promises new investments to foster scientific and technological development. His campaign has pledged to follow a "zero deforestation" policy, combat illegal land use, and restore degraded areas. His platform says Brazil will honor its commitment to reduce

ing the pledge to make Brazil a leader in the fight against climate change.

Davidovich has some faith that Lula will honor his promises. In June, he and colleagues at the Brazilian Academy of Sciences prepared a report containing science, education, and environmental policy advice for the next government. Lula sent a representative to discuss his plans with the group—the only candidate to do so. "This is a very positive sign," Davidovich says. "It shows they are open for dialogue and interested in science and innovation."

Repairing Brazil's image abroad would be one of Lula's most important challenges, says physicist and ecologist Paulo Artaxo at the University of São Paulo's main campus. "Brazil will have to go back to be an important player in the international scenario, not only in climate and environmental issues, but as a leader in Latin America," he says.

But a Lula government would be severely constrained. The Brazilian Congress has already approved the budget for 2023, which contains major cuts for science and education that the Brazilian Society for the Advancement of Science, in an open letter last month, called a "suicidal strategy" for science. As a last-minute act, Bolsonaro also approved by decree a cut of 1.2 billion reais (\$225 million) to the National Fund for Scientific and Technological Development. The cut could hamper operations at Sirius, a recently completed accelerator that will generate intense radiation for biology and materials studies.

The composition of the new Congress elected on 2 October would also hamper a Lula government. No party won an absolute majority, but Bolsonaro's Liberal Party has the largest number of seats in both houses of parliament, tipping Congress further to the right. If Lula becomes president, his Worker's Party would have to

form difficult alliances with center-right parties to govern.

That's still much better than another term for the sitting president, Bustamante says. "This election is not about what a new government can build; it is about what is left for us to protect," she says. "Four more years of Bolsonaro would be to put a final nail in the coffin for science and the environment in Brazil." ■

Sofia Moutinho is a science journalist in Rio de Janeiro.



Luiz Inacio "Lula" da Silva (left) and Jair Bolsonaro (right) face off in a 28 August election debate. Bolsonaro has signaled he may not accept defeat.

carbon emissions under the 2015 Paris agreement. (Bolsonaro's government has been criticized for its permissive approach to calculating those carbon emissions.)

Lula didn't always prioritize the environment. Marina da Silva, his former environment minister, left his government in 2008 because she opposed Lula's development plans, including the construction of the Belo Monte hydropower dam, a massive project in Para state. But Lula recently won back her support by adopting several points of da Silva's environmental agenda, includ-



Scientists studying the Black Death pulled DNA from bones buried in London's East Smithfield Cemetery.

HUMAN EVOLUTION

How the Black Death left its mark on immune system genes

Study of DNA from medieval victims and survivors finds gene that helped protect people from deadly pathogen

By Ann Gibbons

On a drizzly April morning in 2006, a geneticist had the sobering task of helping sort 50 boxes of bones in the Museum of London's basement into two stacks. One contained the remains of people who died 700 years ago during the Black Death. In the other were bones from survivors of the plague who had been buried a year or more later in the same medieval cemetery near the Tower of London.

As Jennifer Klunk, then a graduate student at McMaster University, examined the remains, she wondered what made the two groups different. "Why did some people die during the Black Death and others didn't?" Klunk, now at Daicel Arbor Biosciences, remembers thinking.

Other scholars have been pondering that mystery for centuries. But now, by analyzing DNA from those old bones and others from London and Denmark, Klunk and her colleagues have found an answer: The survivors were much more likely to carry gene variants that boosted their immune response to *Yersinia pestis*, the flea-borne bacterium that causes the plague. One variant alone appears to have increased the chance of surviving the plague by 40%, they reported in *Nature* this week. "We were blown away. ... It's not a small effect," says Hendrik Poinar,

an evolutionary geneticist at McMaster and co-lead author of the study (and Klunk's Ph.D. adviser).

The findings also indicate the Black Death caused a dramatic jump in the proportion of people carrying the protective variant; it is the strongest surge of natural selection on the human genome documented so far. But the improved immunity came at a cost: Today, the variant is also associated with higher risk of autoimmune diseases.

"This is a truly impressive paper," says population geneticist David Enard at the University of Arizona, who is not part of the study. "The implications of the potential speed and power of natural selection in immune genes are wild."

The Black Death is the deadliest pandemic recorded in human history. In the mid-14th century, it killed 30% to 50% of all people living in Europe, the Middle East, and Africa. Researchers have long thought the catastrophe must have left a mark on the genome of survivors, giving future generations some immunity against resurgences of the plague. But identifying that mark has proved difficult, in part because genes involved in immunity rapidly change in frequency as new pathogens arrive. It is "not feasible" to detect the plague's genomic signature in living humans, says molecular anthropologist Anne Stone of Arizona State University, Tempe, who is not part of the study.

Over the past decade, new techniques for analyzing ancient DNA made it possible to search for the legacies of pathogens in the genomes of people who died long ago. But researchers studying the plague struggled to find enough well-dated samples from victims and survivors to reveal real differences in the frequency of immune genes.

Poinar found an answer to that problem in the East Smithfield Cemetery in London, on land that King Edward III bought for a plague pit. Its thousands of burials represent a well-dated time capsule. Plague victims who died in 1348 and 1349, when the disease first ravaged the city, are buried in mass graves at the bottom; survivors who died in 1350 or later are above them. The team extracted bone samples from 318 skeletons from this cemetery and two others in London, as well as from 198 remains found at five sites in Denmark. This gave them well-dated samples from some 500 people who lived during a 100-year window before, during, and after the plague.

After Klunk extracted and sequenced DNA from the bones, a team co-led by human geneticists Luis Barreiro and Tauras Vilgalys of the University of Chicago used the highest quality DNA from 206 individuals to examine 356 genes associated with immune responses. The team identified an astonishing 245 gene variants that rose or fell in frequency before and after the Black Death in people in London, four of which were also found in samples from Denmark.

Changes in the code for one gene stood out: *ERAP2*, which encodes a protein called endoplasmic reticulum aminopeptidase 2. Previous work had shown *ERAP2* helps immune cells recognize and fight threatening viruses. The team confirmed it also can suppress *Y. pestis* bacteria by measuring how the genes of cultured human immune cells responded to the pathogen.

The researchers found two variants, or alleles, of *ERAP2* in their samples. They differ by just one letter in the genetic code. But that difference—which determines whether the gene produces a full-size or truncated protein—had a big impact on immunity. People who inherited two copies of the allele for the full protein were twice as likely to have survived the plague as those who inherited the variant making the truncated version.

An analysis of 143 samples from London also indicated that, before the Black Death, 40% of Londoners carried one or two copies of the protective variant. But only 35% of plague victims carried it. And after the plague, the share of Londoners carrying the protective variant rose to more than 50%

within just a few generations. In Denmark, where the sample size was smaller, the proportion of people carrying the protective variant rose from 45% before the Black Death to 70% after.

Although the 10-percentage-point increase seen in London might not seem like a lot, researchers have never before documented such a rapid surge in a human genetic variant, Barreiro says. “Given the fairly large size of the population [of London] at the time, a 10% change in allele frequency in only three or four generations is highly unusual,” he says. It is among the fastest examples of natural selection ever detected in humans, says population geneticist Monty Slatkin of the University of California, Berkeley, who is not part of the study.

Today, the protective variant is still found in about 45% of British people in the 1000 Genomes database, a catalog of genetic variation. That is surprisingly high, because the protective variant has a downside. Earlier work has shown it comes with a higher risk of developing autoimmune disorders, such as Crohn disease and rheumatoid arthritis. “Once the pandemic is gone, this cost becomes apparent,” Enard says. The variant’s high proportion suggests natural selection continued to favor it until recently, presumably because the plague remained endemic in Europe and Asia into the 19th century.

Researchers are now checking to see whether the protective variant and three other potential plague-resistance variants identified by the *Nature* study are present and show frequency shifts in other ancient populations, especially in Africa. One recent study from Norway, which analyzed DNA from 54 people who lived before, during, and after the Black Death in Trondheim, found no big swings in the four genes, says Tom Gilbert, an evolutionary biologist at the University of Copenhagen who co-led the work. But Gilbert and population geneticist Ziyue Gao of the University of Pennsylvania say that if researchers can confirm such gene surges in more populations, that could help rule out the possibility that the new findings were skewed, for example by the way researchers commonly reconstruct degraded DNA sequences.

Still, Gilbert expects the results to hold up. And they have led him to wonder whether genetic shifts—and not better pest control or improved cleanliness—explain why *Y. pestis* is less dangerous today than it was in the 14th century. “We have assumed that the plague went away because we’ve become cleverer at cleaning our houses and keeping rats out,” Gilbert says. “But wouldn’t it be awesome if it went away because we became immune, not just because we have better hygiene?” ■

ENERGY TECHNOLOGY

Has a new dawn arrived for space-based solar power?

Better technology and falling launch costs revive interest in a science-fiction technology

By Daniel Clery

Late last month in Munich, engineers at the European aerospace firm Airbus showed off what might be the future of clean energy. They collected sunlight with solar panels, transformed it into microwaves, and beamed the energy across an aircraft hangar, where it was turned back to electricity that, among other things, lit up a model of a city. The demo delivered just 2 kilowatts over 36 meters, but it raised a serious question: Is it time to resurrect a scheme long derided as science fiction and launch giant satellites to collect solar energy in space? In a high orbit, liberated from clouds and nighttime, they could generate power 24 hours a day and beam it down to Earth.

“It’s not new science, it’s an engineering problem,” says Airbus engineer Jean-Dominique Coste. “But it’s never been done at [large] scale.”

The urgent need for green energy, cheaper access to space, and improvements in technology could finally change that, proponents of space solar power believe. “Once someone makes the commercial investment, it will bloom. It could be a trillion-dollar industry,” says former NASA researcher John Mankins, who evaluated space solar power for the agency a decade ago.

Major investments are likely far in the future, and myriad questions remain including whether beaming gigawatts of power down to the planet can be done efficiently—and without frying birds, if not people. But the idea is moving from concept papers to an increasing number of tests on the ground and in space. The European Space Agency (ESA)—which sponsored the Munich demo—will next month propose to its member states a program of ground experiments to assess the viability of the scheme. The U.K. government this year offered up to £6 million in grants to test technologies. Chinese, Japa-

nese, South Korean, and U.S. agencies all have small efforts underway. “The tone and tenor of the whole conversation has changed,” says NASA policy analyst Nikolai Joseph, author of an assessment NASA plans to release in the coming weeks. What once seemed impossible, space policy analyst Karen Jones of Aerospace Corporation says, may now be a matter of “pulling it all together and making it work.”

NASA first investigated the concept of space solar power during the mid-1970s fuel crisis. But a proposed space demonstration mission—with ’70s technology lofted in the

Space Shuttle and assembled by astronauts—would have cost about \$1 trillion. The idea was shelved and, according to Mankins, remains a taboo subject for many at the agency.

Today, both space and solar power technology have changed beyond recognition. The efficiency of photovoltaic (PV) solar cells has increased 25% over the past decade, Jones says, while costs have plummeted.

Microwave transmitters and receivers are a well-developed technology in the telecoms industry. Robots being developed to repair and refuel satellites in orbit could be turned to building giant solar arrays.

But the biggest boost for the idea has come from falling launch costs. A solar power satellite big enough to replace a typical nuclear or coal-powered station will need to be kilometers across, demanding hundreds of launches. “It would require a large-scale construction site in orbit,” says ESA space scientist Sanjay Vijendran.

Private space company SpaceX has made the notion seem less outlandish. A SpaceX Falcon 9 rocket lofts cargo at about \$2600 per kilogram—less than 5% of what it cost on the Space Shuttle—and the company promises rates of just \$10 per kilogram on its gigantic Starship, due for its first launch this year (*Science*, 12 August, p. 702). “It’s changing the equation,” Jones says. “Economics is everything.”

“Once someone makes the ... investment, it will bloom. It could be a trillion-dollar industry.”

John Mankins, space solar power consultant

Similarly, mass production is reducing the cost of space hardware. Satellites are typically one-offs built with expensive space-rated components. NASA's Perseverance rover on Mars, for example, cost \$2 million per kilogram. In contrast, SpaceX can churn out its Starlink communication satellites for less than \$1000 per kilogram. That approach could work for giant space structures made of huge numbers of identical low-cost components, Mankins, now with the consultancy Artemis Innovation Management Solutions, has long argued. Combine low-cost launches and this "hypermodularity," he says, and "suddenly the economics of space solar power become obvious."

Better engineering could make those economics more favorable. Coste says Airbus's demo in Munich was 5% efficient overall, comparing the input of solar energy with the output of electricity. Ground-based solar arrays do better, but only when the Sun shines. If space solar can achieve 20% efficiency, recent studies say it could compete with existing energy sources on price.

Lower weight components will also improve the cost calculus. "Sandwich panels," pizza box-size devices with PV cells on one side, electronics in the middle, and a microwave transmitter on the other, could help. Put thousands of these together like a tiled floor and they form the basis of a space solar satellite without a lot of heavy cabling to shift power around. Researchers have been testing prototypes on the ground for years, but in 2020 a team at the U.S. Naval Research Laboratory (NRL) got its aboard the Air Force's X-37B experimental space plane.

"It's still in orbit, producing data the whole time," says project leader Paul Jaffe of NRL. The panel is 8% efficient at converting solar power into microwaves but does not send them to Earth. Next year, however, the Air Force plans to test a sandwich panel that will beam its energy down. And a team at the California Institute of Technology will launch its prototype panel in December with SpaceX.

The drawback of sandwich panels is that the microwave side must always face toward Earth so, as the satellite orbits, the PV side sometimes turns away from the Sun. To maintain 24-hour power, a satellite will need mirrors to keep that side illuminated, with the added benefit that the mirrors can also concentrate light onto the PV. A 2012 NASA study by Mankins put forward a design in which a bowl-shaped

tronicly steering the beam toward Earth whatever the satellite's orientation. This design, Cash says, delivers the most power for its mass, making it "the most competitive economically."

If a space-based power station ever does fly, the power it generates will need to get to the ground efficiently and safely. In a recent ground-based test, Jaffe's team at NRL beamed 1.6 kilowatts over 1 kilo-

meter, and teams in Japan, China, and South Korea have similar efforts. But current transmitters and receivers lose half their input power. For space solar, power beaming needs 75% efficiency, Vijendran says, "ideally 90%."

The safety of beaming gigawatts through the atmosphere also needs testing. Most designs aim to produce a beam kilometers wide so that any spacecraft, plane, person, or bird that strays into it only receives a tiny—hopefully harmless—portion of the 2-gigawatt transmission. Receiving antennas are cheap to build but they "need a lot of real estate," Jones says, although she says you could grow crops under them or site them offshore.

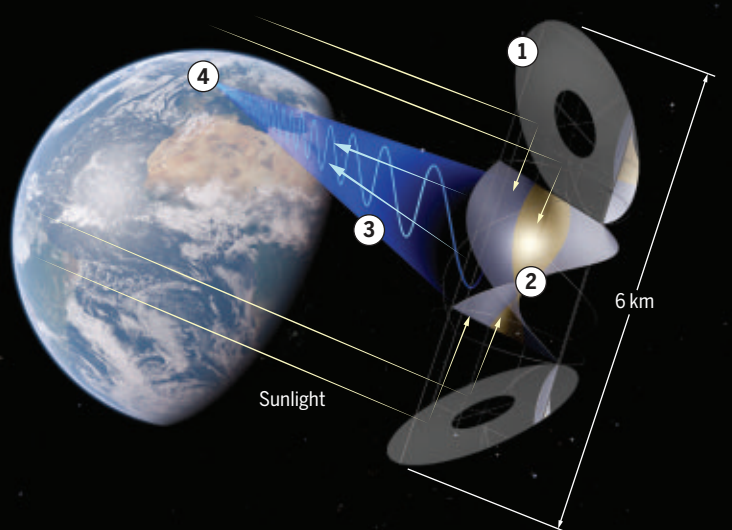
For now, Europe is where public agencies are taking space solar power most seriously. "There's a commitment there that you don't see in the U.S.," Jones says. Last year, ESA commissioned two cost/benefit studies of space solar. Vijendran says they concluded it could conceivably match ground-based renewables on cost. But even at a higher price,

comparable to nuclear power, its around-the-clock availability—unlike conventional solar or wind—would make it competitive.

In November, ESA will ask member states to fund an assessment of whether the technical hurdles can be overcome. If the news is good, the agency will lay out plans for a full effort in 2025. Armed with €15 billion to €20 billion, ESA could put a megawatt-scale demonstration facility in orbit by 2030 and scale up to gigawatts—the equivalent of a conventional power station—by 2040, Vijendran says. "It's like a moonshot." ■

Here comes the Sun

The plummeting cost of space launches and electronics may make space solar power viable. All designs need photovoltaic (PV) cells, sometimes fed by mirrors, and microwave transmitters to beam down energy, and all will be kilometers wide, requiring assembly in orbit. Below is a design concept from the International Electric Company.



1 Catching light

Lightweight mirrors, on either end, deflect sunlight toward the central solar array. Satellite rotates to keep them pointing sunward.

2 Making power

PV cells convert light to electricity, which is used to generate microwaves.

3 Beam it down

Phased array of transmitters focuses gigawatt-power beam anywhere on Earth in line of sight.

4 Receiving station

Kilometers-wide array of antennas, on land or offshore, converts microwaves to electricity for the power grid.

structure with thousands of individually steerable thin-film mirrors directs light onto the PV array.

Ian Cash of the United Kingdom's International Electric Company has developed a different approach. His proposed satellite uses large, fixed mirrors angled to deflect light onto a PV and microwave array while the whole structure rotates to keep the mirrors pointing sunward (see graphic, above). Power from the PV cells is converted to microwaves and fed to 1 billion small perpendicular antennas, which together act as a "phased array," elec-

MICROBIOLOGY

'Recoded' bacteria shrug off viral attacks

Modified cells don't allow invaders to replicate and don't share DNA

By **Mitch Leslie**

Call it a genetic firewall. By partially rewriting the genetic code in bacteria, two groups of researchers have found they can thwart invading viruses, which must hijack the microbes' genetic machinery to replicate. The strategy, described this week in *Science* and in a preprint posted in July, could shield drug-producing bacteria from viral attacks and keep potentially dangerous genes from escaping from genetically modified organisms.

"These are important steps forward," says synthetic biologist Ned Budisa of the University of Manitoba, who wasn't connected to the research. "Both works have great technological promise."

Nearly every living thing relies on the same genetic code. Various sequences of three DNA nucleotides, called codons, tell a cell which amino acid to install where in a protein. So-called transfer RNAs, or tRNAs, read the codons and act on their instructions. Each type of tRNA carries a specific amino acid that it adds to a growing protein strand only when it recognizes the correct codon. Cells also carry three kinds of stop codons that tell them when to stop making a protein.

Because organisms share this genetic programming language, they can gain new abilities by acquiring genes from other organisms. The common language also allows researchers to insert human genes into bacteria, coaxing the cells to manufacture drugs such as insulin. But a universal genetic code leaves cells vulnerable to interlopers such as viruses and plasmids, DNA snippets that reproduce inside bacteria and can ferry genes among them.

For years, researchers have tried to block this traffic. In 2013, synthetic biologist George Church of Harvard Medical School and colleagues genetically tweaked the bacterium *Escherichia coli*, replacing one of its stop codons with another version. The team modified the bacterium's tRNAs so that when it reads the original stop codon—say, in the genome of an invading virus—it installs an inappropriate amino acid that

impairs the viral protein. The modified microbe could safely synthesize its own proteins but was resistant to several kinds of viruses and plasmids.

Last year, synthetic biologist Jason Chin of the University of Cambridge and his team went a step further. They swapped out the same stop codon in *E. coli*, but they added another layer of protection. They replaced two of the codons for the amino acid serine in the microbe's genome with two different serine codons. They then deleted the tRNAs that would recognize the original serine codons. This modified bacterial strain, dubbed Syn61Δ3, could not read two serine

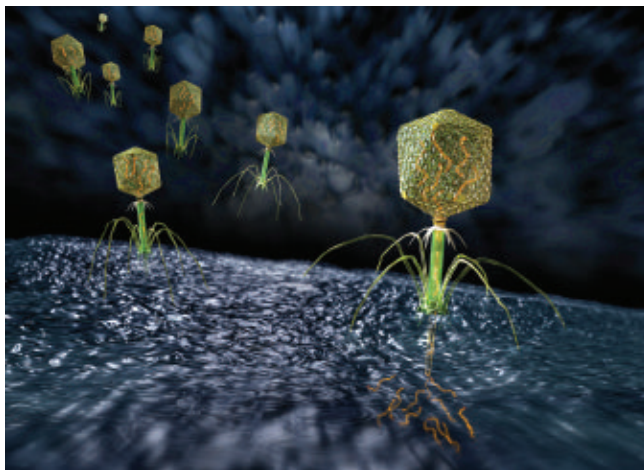
genetic code, they could not share the plasmid with other bacteria. "We have created a form of life that doesn't read the canonical genetic code and that writes its genetic information in a form that can't be read" by other organisms, Chin says.

Church's and Nyerges's team followed a similar strategy. The researchers endowed Syn61Δ3 with modified tRNAs that misread two of the serine codons carried by invading viruses, inserting leucine instead of serine. Compared with the original Syn61Δ3, the altered microbes became more resistant to the 12 viruses that scientists had plucked from environmental samples, the team revealed in July. The paper "shows a way to make any organism resistant to all viruses—and with one step," Church says. (The team also made sure the microbes require an amino acid that doesn't occur in nature, ensuring they can't survive if they escape.)

Such recoding might help prevent viral outbreaks in factories that use bacteria to churn out drugs or other products. And by recoding genetically modified organisms, researchers might prevent other organisms from acquiring their DNA. The bacteria could also help biologists study the evolution of the genetic code itself, says synthetic biologist Chang Liu of the University of California, Irvine. Now, researchers

can "ask why the genetic code is the way it is." Church says viruses are unlikely to evolve strategies for getting around this defense because it involves more than 200,000 changes to the microbes' genome. And synthetic biologist Drew Endy of Stanford University says the researchers deserve credit for the rigor with which they tested the viral resistance of the bacteria. "One of the most beautiful things they've done here is they've gone out into the wild" to find viruses, he says.

Still, he and others aren't so sure the bugs are genetically locked off from other living things. "We still need to be very careful," Budisa says. "I can't put my hand in a fire and say, 'This is a perfect firewall.'" Endy agrees. "It's an arms race between human ingenuity and natural biodiversity," he says, "and we don't know how long the race is yet to run." ■



Bacteria with a revised genetic code resist attacks from invaders, such as viruses known as bacteriophages (green).

codons found in invaders, helping it shrug off bacteria-infecting viruses.

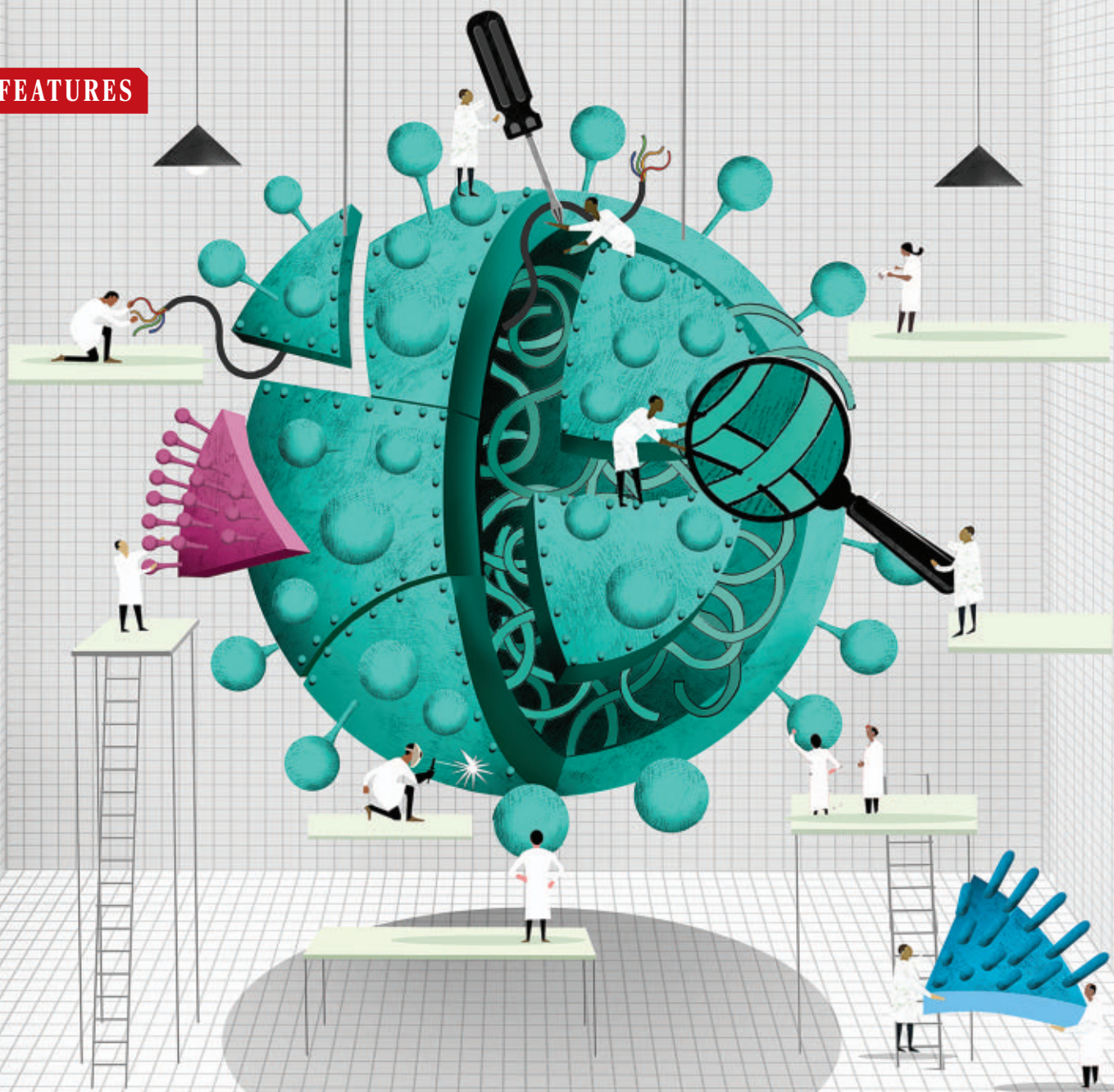
Still, Syn61Δ3 isn't invincible. A team led by Church and his postdoc Akos Nyerges showed it was susceptible to 12 types of viruses isolated from various sources, including pig manure and a chicken shed. So Chin and colleagues have added new protections. They devised tRNAs that actively ruin viral proteins by delivering the wrong amino acids—including proline and alanine—in response to outsiders' serine codons.

The group tested its improved Syn61Δ3 by exposing it to a pair of viruses fished out of the River Cam in Cambridge. Both killed the original Syn61Δ3 but spared upgraded versions, the scientists report this week in *Science*. They also showed that although the improved Syn61Δ3 cells could exchange a plasmid engineered to use their modified

Subscribe to **News from Science** for unlimited access to authoritative, up-to-the-minute news on research and science policy.



bit.ly/NewsFromScience



MAKING TROUBLE

The United States is moving to tighten oversight of studies that could make viruses more dangerous. But how far should it go? **By Jocelyn Kaiser**

In a U.S. government lab in Bethesda, Maryland, virologists plan to equip the strain of the monkeypox virus that spread globally this year, causing mostly rash and flulike symptoms, with genes from a second monkeypox strain that causes more serious illness. Then they'll see whether any of the changes make the virus more

lethal to mice. The researchers hope that unraveling how specific genes make monkeypox more deadly will lead to better drugs and vaccines.

Some scientists are alarmed by the planned experiments, which were first reported by *Science* (16 September, p. 1252). If a more potent version of the outbreak strain accidentally escaped the high-containment, high-security

lab at the National Institute of Allergy and Infectious Diseases (NIAID), it could spark an "epidemic with substantially more lethality," fears epidemiologist Thomas Inglesby, director of the Center for Health Security at the Johns Hopkins University Bloomberg School of Public Health. That's why he and others argue the experiments should undergo a special review required for especially risky U.S.-

funded studies that might create a pathogen that could launch a catastrophic pandemic.

But it's not clear that the rules apply to the proposed study. In a 2018, a safety panel determined it was exempt from review. Monkeypox did not meet the definition of a "potential pandemic pathogen" (PPP), the panel decided, because it didn't spread easily. Now, with monkeypox widespread, the National Institutes of Health (NIH) is planning to reexamine the work, but it still might not qualify as "enhancing" a PPP, the agency says. That's because the study will swap natural mutations, not create new ones, so it is not expected to create a monkeypox strain more virulent than the two already known.

The monkeypox controversy marks just the latest flare-up in a decade-old debate over exactly when a study that alters a pathogen is too risky for the U.S. government to fund—and who should have the power to decide. That wrangling became especially ferocious over the past 2 years, as the COVID-19 pandemic spawned allegations, so far unproven, that SARS-CoV-2 escaped from a laboratory in China. Now, in the pandemic's wake, the U.S. government appears poised to make sizable changes to how it manages so-called gain-of-function (GOF) studies that tweak pathogens in ways that could make them spread faster or more dangerous to people.

Last month, an expert panel convened by NIH and its parent agency, the Department of Health and Human Services (HHS), released a draft report that recommends the GOF rules be broadened to include pathogens and experiments that are exempt from the current scheme. If the recommendation is adopted—which could come next year—the monkeypox study could come under tighter scrutiny. And other researchers working with viruses such as Ebola, seasonal flu strains, measles, and even common cold viruses could face new oversight and restrictions.

Some scientists are watching nervously, worried that an expanded definition could worsen what they already see as a murky, problematic oversight system. The existing rules, they say, have caused confusion and delays that have deterred scientists from pursuing studies critical to understanding emerging pathogens and finding ways to fight them. If not implemented carefully, the proposed changes could "greatly impede research into evolving or emerging viruses," worries virologist Linda Saif of Ohio State University, Wooster. She and others say expanding the regulations could add costly red tape, potentially driving research overseas or into the private sector, where U.S. regulations don't apply or are looser.

Others say the proposed changes don't go far enough. They'd like to see the U.S. government create an entirely new independent

body to oversee risky research, and for the public to get far more information about proposed experiments that could have fearsome consequences. Some have even called for curbing the now common practice of collecting viruses from wild animals and studying them in the lab, saying it only increases the risks that the viruses—or modified versions—will jump to humans.

"We really should be asking important questions about whether that work should continue," Inglesby says. And virologist James LeDuc, who retired last year as director of the University of Texas Medical Branch's Galveston National Laboratory, says, "It's one thing to recognize that these viruses exist in nature.

"There are significant potential risks to both under- and overregulation."

Jesse Bloom.
Fred Hutchinson Cancer Center

It's another to modify them so that you can study them if in fact they could become human pathogens."

All sides agree on one thing: The proposed rules represent a potential pivot point in the debate over the funding of high-risk GOF studies by the U.S. government, which is one of the world's largest supporters of virology research. "There are significant potential risks to both under- and overregulation in this field," says virologist Jesse Bloom of the Fred Hutchinson Cancer Center, who like LeDuc is part of a group of scientists pushing for the changes. "The goal," he adds, "needs to be to find the right balance."

THE CONTROVERSY over studies that enhance or alter pathogens ignited a decade ago, but such work goes back more than a century. To make vaccines, for example, virologists have long passaged, or repeatedly transferred, a virus between dishes of animal cells or whole animals, so that it loses its ability to harm people but grows better—a gain of function. Since the late 1990s, genetic engineering techniques have made these studies much more efficient by allowing virologists to assemble new viral strains from genomic sequences and to add specific mutations.

In 2011, two such NIH-funded experiments with H5N1 avian influenza set off alarm bells worldwide. Virologists Yoshihiro Kawaoka at the University of Wisconsin, Madison, and

the University of Tokyo and Ronald Fouchier at Erasmus University Medical Center were interested in identifying mutations that could enable the virus, which normally infects birds, to also spread easily among mammals, including humans. Small but frightening outbreaks had shown H5N1 could spread from birds to people, killing 60% of those infected. By introducing mutations and passaging, Kawaoka and Fouchier managed to tweak the virus so it could spread between laboratory ferrets, a stand-in for humans.

Controversy erupted after Fouchier discussed the work at a scientific meeting prior to publication. Soon, worries that the information could land in the wrong hands or that the tweaked virus could escape the lab prompted journal editors and government officials to call for a review by an HHS panel called the National Science Advisory Board for Biosecurity (NSABB). HHS established NSABB after the 2001 anthrax attacks in the United States to consider so-called dual use research that could be used for both good and ill. During the review, flu researchers worldwide voluntarily halted their GOF experiments. Ultimately, NSABB concluded the scientific benefits of the studies outweighed the risks; the H5N1 papers were published and the work resumed.

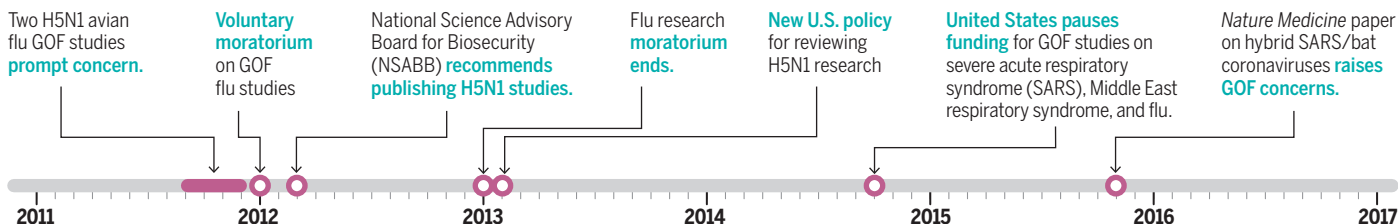
Then in mid-2014, several accidents at U.S. labs working with pathogens, along with worries about some new GOF papers, prompted the White House to impose a second "pause" on U.S.-funded GOF research. It halted certain studies with influenza and the coronaviruses that cause Middle East respiratory syndrome (MERS) and severe acute respiratory syndrome (SARS), SARS-CoV-2 cousins that have caused small though deadly outbreaks. NIH ultimately identified 29 potential GOF projects in its funding portfolio. After reviews, the agency allowed 18 to resume because it determined they didn't meet the risky GOF definition or were urgent to protect public health. Some, for example, adapted MERS to infect mice, a step that can help researchers develop treatments. The remaining 11 studies had GOF components that were removed or put on hold.

DURING THE SECOND PAUSE, U.S. officials promised to come up with a more comprehensive approach to identifying and potentially blocking risky studies before they began. Advocates of tighter rules also pushed for less-risky approaches for studying altered viruses, such as using weakened virus strains, computer models, or "pseudoviruses" that can't replicate.

Many virologists, however, argued that only studies with live virus can accurately show the effect of a mutation. "There's only so much you can learn [from alternative tech-

An unfolding debate

Researchers have long conducted gain-of-function (GOF) research that gives viruses and other pathogens new capabilities. But a decade ago, studies that enabled H5N1 avian flu to more easily spread among mammals kicked off a debate that continues today over how tightly the United States should regulate such research.



niques,” says University of Michigan, Ann Arbor, virologist Michael Imperiale, who supported the H5N1 GOF studies. “Sometimes using intact virus is the best approach.”

In 2017, the debate culminated with the release of the current HHS policy, dubbed Potential Pandemic Pathogens Care and Oversight (P3CO). It requires that an HHS panel review any NIH-funded study “reasonably anticipated” to create or use an enhanced version of an already highly virulent, highly transmissible pathogen that might cause a pandemic. But it exempts natural, unmodified viruses and GOF work done to develop vaccines or as part of surveillance efforts, such as tweaking a circulating flu virus to assess the risks of a newly observed variant.

The HHS committee charged with implementing the policy, which operates behind closed doors, has since reviewed only three projects, and approved all. Two were continuations of Kawaoka’s and Fouchier’s H5N1 work. (Both grants are now expired.) The third involved work with H7N9 avian influenza, but the investigator later agreed to use a nonpathogenic flu strain.

Other concerning studies have been given a pass, critics say. As an example, they point to work led by coronavirus expert Ralph Baric of the University of North Carolina, Chapel Hill. In the 2000s, his team became interested in determining whether bat coronaviruses had the potential to infect humans. (COVID-19 has since shown the answer is emphatically yes.) But the researchers often could not grow the viruses in the laboratory or enable them to infect mice. So they created hybrid, or chimeric, viruses, grafting the gene encoding the surface protein, or “spike,” that the wild bat virus uses to enter a host cell into a SARS strain that infects mice.

NIH let this work continue during the 2014 pause. The researchers had no intention of making the mouse-adapted SARS virus more risky to people, Baric has said. But something unexpected happened when his lab added spike from a bat coronavirus called SHC014: The chimeric virus sickened mice carrying a human lung cell receptor. Baric’s team reported in 2015 in *Nature Medicine*. The hybrid virus could not be stopped

by existing SARS antibodies or vaccines. In essence, critics of the work assert, it created a potential pandemic pathogen.

A review panel might “deem similar studies building chimeric viruses based on circulating [bat coronavirus] strains too risky to pursue,” Baric acknowledged. Yet he has also called these chimeric viruses “absolutely essential” to efforts to test antiviral drugs and vaccines against coronaviruses, and many virologists agree. They also argue that Baric’s work and related experiments provided an early warning that, if heeded, might have helped the world prepare for the COVID-19 pandemic.

**“I worry that people will ...
[fear] ... accidentally
tripping a wire.”**

Gigi Kwik Gronvall,
Johns Hopkins University

THE PANDEMIC HAS SUPERCHARGED the GOF debate, in large part because of unproven but high-profile allegations—including from former President Donald Trump—that SARS-CoV-2 emerged from a laboratory in Wuhan, China. One prominent advocate of the lab-leak theory, Senator Rand Paul (R-KY), a senior member of the Senate’s health panel, has sparred with NIAID Director Anthony Fauci over experiments in virologist Shi Zhengli’s lab at the Wuhan Institute of Virology (WIV). With money from an NIH grant to a U.S. nonprofit organization, the EcoHealth Alliance, Shi had created chimeras by adding spike proteins from wild bat coronaviruses to a SARS-related bat strain called WIV1. The WIV researchers used methods developed by Baric, who has collaborated with Shi.

Last year, documents obtained by the Intercept showed that—like Baric’s work during the 2014 pause—NIH had exempted the EcoHealth grant from the P3CO policy. (The agency later explained that the bat corona-

viruses were not known to infect humans.) But NIH also said that if Shi’s lab observed a 10-fold increase in a chimeric virus’ growth compared with WIV1, it wanted to be informed, because the experiments could then require a P3CO review.

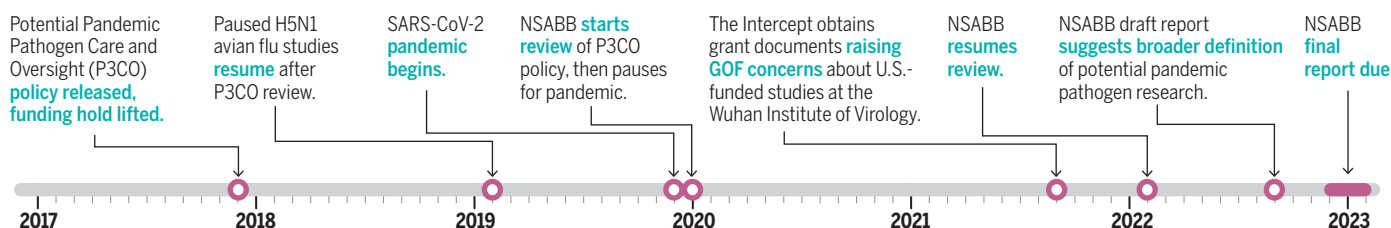
The documents show WIV did observe increased growth in the lungs of infected mice and more weight loss and death in some animals. NIH has said EcoHealth failed to report these “unexpected” results promptly as required, but EcoHealth disputes this. Paul and some proponents of the lab-leak theory have gone further, alleging that NIH actively conspired with EcoHealth to hide the risks of the study.

As often is the case in GOF debates, there is no scientific consensus on whether the WIV experiments—or the results—crossed a red line. Paul and some scientists have fiercely argued that they were unacceptably risky. Others forcefully disagree. NIH officials, meanwhile, have emphasized that the hybrid viruses created by Shi’s lab were genetically too distant from SARS-CoV-2 to have generated the pandemic.

EVEN AS NIH officials have defended their assessment of the EcoHealth grant, they have conceded the pandemic made it clear that the GOF rules needed a fresh look. In February, NIH asked NSABB to broaden an existing review of the P3CO policy, launched in January 2020 to examine ways to increase transparency in the review board’s membership and deliberations. Now, NSABB had bigger issues to weigh: Some White House officials even wanted the panel to consider whether the United States should simply ban funding for some kinds of GOF studies.

In September, an NSABB working group released a draft report that does not go that far. It does recommend that GOF work done for vaccine development and pathogen surveillance no longer be automatically exempt from P3CO review. It also recommends that the definition of a pathogen that triggers a review be significantly expanded to include two new categories not explicitly covered by the current rules.

One category would sweep in “potentially



highly transmissible pathogens having low or moderate virulence or case-fatality rates.” That definition would cover SARS-CoV-2, which studies suggest kills about 1% of infected people. It also could include tuberculosis bacteria, measles, seasonal flu, and the noroviruses that cause stomach bugs, Saif and others suggest.

The second category would include pathogens that are “less transmissible” but have “higher virulence or case-fatality rates.” That definition could include rabies, the Nipah virus spread by fruit bats, and Ebola, which is deadly but isn’t easily transmitted because it’s spread through blood or other body fluids.

Even with the new rules, determining whether a pathogen or experiment fits into a reviewable category will remain a judgment call. Predicting whether a virus can become “highly transmissible,” for example, can be difficult. So can defining “low or moderate” virulence, acknowledges working group co-chair Syra Madad, an epidemiologist at New York University, speaking in a personal capacity. Policymakers should provide illustrative examples, her panel said. Its final recommendations are due out in December or January 2023.

Some researchers worry this subjectivity will deter researchers from pursuing valuable pathogen science, for fear they’ll get entangled in red tape. “When things are unpredictable, I worry that people will avoid going close to the line for fear of accidentally tripping a wire,” says Gigi Kwik Gronvall, a biosecurity specialist at Johns Hopkins.

Other scientists, however, say even an expanded policy could be too lax. Shi’s WIV1 chimeric virus experiments, for example, still might not qualify for review because the starting viruses weren’t known to cause human disease. And the NIAID monkeypox studies may not qualify because they aren’t creating new genes. Still, the gene swapping is “like changing the machinery of a clock where you have a lot of different pieces that work together. We don’t know exactly how it is going to work,” says monkeypox virologist Gustavo Palacios of the Icahn School of Medicine at Mount Sinai.

To close some gaps, a group of GOF crit-

ics organized by Inglesby has urged NSABB to expand the review requirements to include GOF studies of any pathogen, however harmless, that could be manipulated to become a PPP. And others have urged that the reviews be conducted by a new, independent agency rather than HHS, which they argue has been reluctant to aggressively regulate studies it funds through NIH.

Currently, NIH is funding at least 11 grants that likely should have gone through P3CO review but did not, estimates molecular biologist Richard Ebright of Rutgers University, Piscataway, a prominent GOF critic who has surveyed the agency’s grant abstracts. (He says full proposals, which are typically not public, would verify his estimate.) They involve eight institutions in the United States, most studying flu, SARS, and MERS. His list includes a currently funded grant proposal by EcoHealth that describes plans for further bat coronavirus chimera work in Baric’s lab.

But a broader P3CO policy will affect “still a pretty small area” of research, suggests Lyric Jorgenson, acting director of the NIH Office of Science Policy. And this time, she does not expect another “crippling” shutdown of experiments while they are reviewed.

A U.S. CLAMPDOWN will have no sway over privately funded GOF research or what happens in other countries, which typically lack policies like the P3CO framework. In Japan and most of Europe, for example, oversight is limited to rules on biosafety and, sometimes, biosecurity along with voluntary self-regulation, say biosecurity experts Gregory Koblenz of George Mason University and Filippa Lentzos of King’s College London. It’s too soon to say how a 2020 Chinese biosafety law will affect PPP research, they say.

Such rules have not prevented GOF work that some researchers consider too risky. For example, since 2018 labs in China have published at least three papers in journals describing experiments with potential pandemic bird flu strains that Bloom thinks might have crossed the line because they added mutations for drug resistance or adaptation to mammals. None, however, was “as alarming as the earlier Fouchier or Kawaoka

[H5N1] studies,” says Bloom, who examined the papers for *Science*.

A study described in a June preprint by a team at the Pasteur Institute has also drawn concerns. The scientists passaged a bat coronavirus from Laos that is a distant cousin of SARS-CoV-2 through human cells and in mice to see whether it acquired a specific mutation that would help it infect people. The virus did not—a finding that some scientists said sheds light on how the COVID-19 pandemic began. But others told *The New York Times* that the work, which was reviewed by a local biosafety committee, might not have been worth the risk.

Meanwhile, a growing number of laboratories around the world are jumping into the field. In an interview with the *MIT Technology Review* last year, for example, Baric noted that just three or four labs were engineering bat coronaviruses before the pandemic, but that number has since multiplied. The expansion is “unsettling,” he said, because some “inexperienced” groups could proceed “with less respect for the inherent risk posed by this group of pathogens.” (Baric could not be reached for this story.)

Some GOF critics hope to launch a broader global dialogue about how to regulate high-risk pathogen studies. Bloom and Lentzos are part of the Pathogens Project, a 1-year taskforce launched in September by the *Bulletin of the Atomic Scientists*, best known for its Doomsday Clock warning of threats such as nuclear war. The project will gather international experts, including University of Cambridge microbiologist Ravindra Gupta, who has advised the United Kingdom’s COVID-19 response, and George Gao, former director of China’s Center for Disease Control and Prevention, to hammer out recommendations for working safely with risky pathogens.

Co-chair and microbiologist David Relman of Stanford University says, “The idea is to reach out and try to find a broad set of interested parties from across the globe and ask, what are the key questions? What are some possible actions? Is there an appropriate international entity right now that could take this on?” Those may be modest goals, he says, but it’s a start. ■

INSIGHTS

POLICY FORUM



With the internet and social media providing a vehicle for conspiracy theorists and snake-oil salesmen, education must provide tools to help make informed choices.

EDUCATION

Science, misinformation, and the role of education

“Competent outsiders” must be able to evaluate the credibility of science-based arguments

By **Jonathan Osborne** and **Daniel Pimentel**

Because of the limits to our knowledge and time, we all depend on the expertise of others. For example, most readers of *Science* accept the anthropogenic origin of climate change. Yet far fewer have actually read a report of the Intergovernmental Panel on Climate Change (IPCC), let alone evaluated the evidence and arguments. Nevertheless, we trust its claims because we rely on the credibility of its authors, the social practices of peer review used to vet any theoretical biases and errors, and the fact that it represents a consensus report of the relevant experts. Alternatively, we can choose to trust the media that report its findings. Amid increasing concern about trust in science being undermined by an ocean of misinformation (1–3), we consider how scientists, science curricula, and science educators must help equip individuals to evaluate the credibility of scientific information, even if the science is beyond their understanding (4).

The increasing complexity of modern society makes us ever more dependent on expertise (1). As outsiders to any domain of knowledge, we are forced to make judgments of credibility and expertise. Even being an expert in one scientific domain (e.g., cosmology) does not make one an expert in another (e.g., evolutionary biology). And though there have long been conspiracy theorists and snake-oil salesmen, the internet and social media have provided a much louder megaphone—and the means to avoid traditional gatekeepers (5). The acceptance of unfounded claims—e.g., the idea that vaccines cause autism, that the Earth is flat, or that climate change is a hoax—is of grave concern. For, though true knowledge is a collective good, information that is flawed, or fake, can be a danger—both individually and collectively. For instance, the idea that vaccines are harmful endangers not only the lives of those who hold this idea, but the whole community that depends on a high level of vaccination to ensure its health.

Why people choose to believe flawed or fake information is complex (6, 7). Studies in the public engagement with science have shown repeatedly that individuals tend to reject scientific information that threatens

their identity or worldview. Nevertheless, the task of a liberal education is to provide individuals with the knowledge required to critically evaluate claims. This is particularly important for young people before their ideologies and identities become entrenched. How they choose to then act is the individual's choice, but the function of education is to provide them with the best tools possible to make informed choices.

Research in the past 5 years has developed a range of approaches based on “inoculation,” “debunking,” or “lateral reading” (2). Education must, therefore, draw on this body of work if it is to be part of the solution to the challenge of scientific misinformation. Existing curricula, such as the US Next Generation Science Standards, place an emphasis on engaging in scientific practices such as arguing from evidence and analyzing and interpreting data. Although the inclusion of these practices in science education offers a valuable and innovative window into the internal workings of science, they sustain the belief that any individual can evaluate the evidence for themselves. Such a goal is misconceived. Formal science education can never provide all the knowledge that is needed—much less the knowledge that

Graduate School of Education, Stanford University,
Stanford, CA, USA. Email: osbornej@stanford.edu

might be required to evaluate the science that is yet to come. Hence, believing that all individuals might be capable of evaluating all scientific evidence for themselves is not a realistic response (8).

Rather, the goal of science education must be to make “competent outsiders” (9) of all students. Every one of us, when lacking detailed knowledge of any scientific topic (including scientists outside their own specialism), requires an understanding of three key concepts to evaluate any scientific claim successfully. These are (i) the social practices that the scientific community uses to produce reliable knowledge (10); (ii) the criteria of scientific expertise; and (iii) the basics of digital media literacy. Knowledge of the first two elements is central to developing the competency required to interrogate the trustworthiness of a source and evaluate claims of scientific expertise. It can only be taught in science, yet existing curricula do not offer any explanation of the vital social practices used by science for detecting and preventing error. In particular, neither the importance of consensus in establishing reliable knowledge, nor peer review, even in its narrowest sense, get a mention in K-12 standards. Moreover, these ideas should be addressed in middle school and high school, advanced placement, and undergraduate classes if they are to take hold and never wither.

Why is knowledge of the social practices of science so critical? First, as in the case of the IPCC report, our individual knowledge is bounded. We are all epistemically dependent on experts, whether they be doctors, lawyers, or bridge engineers (11). And, when confronted with claims by experts, the central challenge for the competent outsider becomes one of whom to trust. In the case of science, it is a knowledge of the mechanisms that science uses for establishing credibility—the credentials that enable anyone to claim expertise within a discipline and the social practices the scientific community uses to ensure the production of reliable knowledge (10).

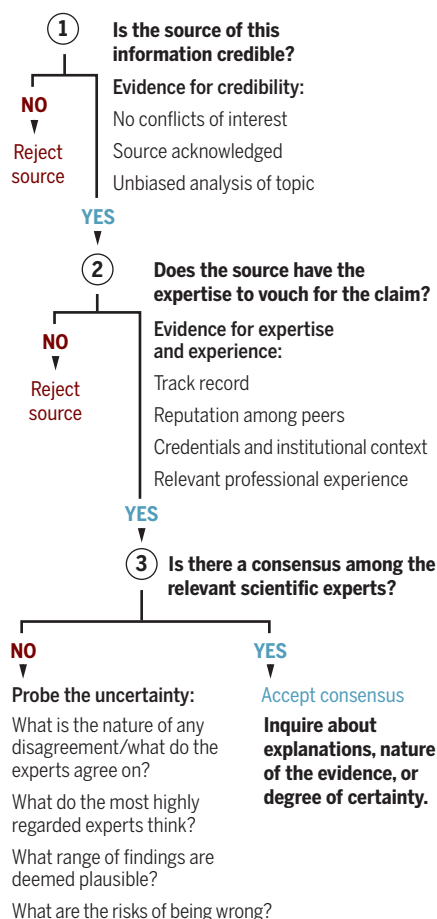
Our overview of the basic procedures that the competent outsider should adopt (see the figure) is synthesized from a large body of research (2, 12)—elements of which have been shown to be effective (13). The steps outlined in the figure offer a “fast and frugal” heuristic for evaluating scientific information for the competent outsider, capturing the three most important and effective filters—all of which must be applied.

Contrary to the intuitions of many, the first question to teach students to answer is not “what is the evidence?” nor “what are the arguments?” These are questions for those with relevant expertise—the scientists who can recognize sources of error,

cherry-picked data, or flaws in the methods. Instead, the first questions the competent outsider must ask are: Is the source of information credible? Is there a conflict of interest? To what extent is the source impartial? Does the author cite their sources of evidence? Here we have much to learn from the recent innovative work on civic online reasoning (13). When it comes to the internet, expert fact checkers commonly leave the webpage within 30 seconds. They employ

A “fast and frugal” heuristic

This process, with three important and effective filters, can help competent outsiders evaluate scientific information.



the technique of “lateral reading,” opening a new tab in their web browser to research who is making the claim (13). Students, by contrast, commonly attempt to evaluate the arguments and evidence on the page itself—a strategy that research shows leaves them none the wiser (13). Why? Because the evidence is often partial or picked to support misleading conclusions. Moreover, existing media literacy approaches to evaluating information such as the commonly used CRAAP checklist (Currency, Relevance,

Authority, Accuracy, and Purpose) have been shown to be of little value for helping students to detect flawed information. Why? Because (i) these tests do not start by asking about the source’s credibility; (ii) the focus on “accuracy” reflects a belief that the individual is capable of evaluating the evidence for themselves; and (iii) such resources commonly use only one of our three essential filters represented in the figure. Yet research shows that students can readily learn some of the basic skills used by fact checkers to improve their performance (13).

Establishing credibility alone—e.g., whether there are conflicts of interest or political bias—however well done, is not sufficient. Individuals need to understand something about the way science produces reliable knowledge. Thus, having passed the first filter, the second filter for the nonexpert is the question: Does the source have the scientific expertise to make this claim? Just as one would not trust a plumber to fix an automobile engine, why trust a physicist who claims to know about the effect of tobacco on health? Yet the mantra of being a “scientist” has been shown to endow a generic cloak of respectability (14). Hence, many scientists have been enlisted to cast doubt on the scientific consensus, even when they have no relevant expertise. Students need to know that science today is a highly specialized activity. Being an expert in one science does not make one an expert in all sciences.

If the source looks credible, the crucial third filter is the question: Is there a scientific consensus on this issue? In the case of climate change, evolution, or the origin of the Universe, the layperson can find that the answer is an unequivocal “yes.” In the case of threats posed by new virus variants or the long-term effects of new medical treatments, the answer may be less certain and more equivocal. In such cases, not surprisingly, nonexperts may be confused.

In the absence of a consensus, the competent outsider is well advised to doubt any lone voice who claims to know with absolute certainty (15). Scientific consensus is the public benchmark of reliability. Such knowledge is trustworthy because it is the product of extensive empirical work that has been examined critically from many perspectives. Although science-in-the-making may always be open to question, a decisive majority of experts is our best bet of what to trust. Notable exceptions (e.g., Galileo) are memorable because they are just that, exceptions. And, in most cases, dissenting voices turn out to be wrong. Knowing the importance of consensus, naysayers sometimes endeavor to project an alternate one, such as the Leipzig Declaration on Global Climate Change—essentially a “consensus” of nonexperts.

Yet, the knowledge needed to answer our three questions is rarely taught as a component of any science education—nor is it a feature of any teaching of digital media literacy. Even at the undergraduate level, discussions about the social nature of science are often absent. Given its importance then, scientists and science educators have a fundamental responsibility to teach about the social mechanisms and practices that science has for resolving disagreement and attaining consensus.

Undoubtedly, there is still more that the competent outsider needs to know. Peer-reviewed publication is often regarded as a threshold for scientific trust. Yet while peer review is a valuable step, it is not designed to catch every logical or methodological error, let alone detect deliberate fraud. A single peer-reviewed article, even in a leading journal, is just that—a single finding—and cannot substitute for a deliberative consensus. Even published work is subject to further vetting in the community, which helps expose errors and biases in interpretation. Again, competent outsiders need to know both the strengths and limits of scientific publications. In short, there is more to teach about science than the content of science itself.

Science textbooks, however, commonly traffic in the settled “facts” of yesterday’s science. Scientific misinformation capitalizes on this feature by appealing to the mythical ideal of science that such textbooks implicitly perpetuate. For instance, detractors may argue that “if scientists can’t even predict the weather next week, how can they predict the climate in 100 years?” This impossible standard erodes the cultural authority of science. Uncertainty is an inherent aspect of science, particularly for science-in-the-making. Teachers of science must acknowledge that uncertainty is normal and show how science has evolved standard ways to address or minimize it. This can be done just by getting a class to measure the length and breadth of a piece of paper, or the temperature in the room, and then asking what is the most accurate answer.

Science curricula that exist across the globe today, however, were written for a different era—one in which misinformation could not be circulated at the speed of a “retweet.” The threat to science from this new facility to disseminate misinformation so readily is, we argue, akin to the challenge posed by the launch of Sputnik in 1957. Likewise, it needs a similar coordinated response by scientists to acknowledge its importance. How the scientific community produces reliable knowledge is essential knowledge for a competent outsider. Such an omission from education—be it formal

or informal—not only fails our future citizens but also fails science itself.

There are at least four contributions that education can make to address scientific misinformation: adapting teacher training; developing curricular materials; revising standards and curricula; and improving assessment. The last of these is the most powerful and immediate lever. Assessments can be high stakes for both teachers and students. Hence they are read carefully as an important signal of the intent of the curriculum. The Programme for International Student Assessment (PISA) for 2025 will be innovative, as it will assess 15-year-old students’ competence to “research, evaluate and use scientific information for decision making and action...and evaluate its credibility, potential flaws and the implications for personal and communal decisions.” Asking students to identify the dubious nature of a scientific claim or the cherry-picked nature of the data represents a gestalt shift in assessment that commonly focuses on reproducing the right answers. However, it is readily achievable—it is just not something that examiners are used to doing.

Developing new curricula and materials is already underway, such as by the program on Civic Online Reasoning at Stanford University, and efforts in Finland, Israel, and elsewhere. For example, exercises can be used by students to evaluate claims made by different websites (4), such as co2science.org, which makes many misleading claims about climate change. Using “lateral reading,” students will find that this website has received funding from ExxonMobil, providing an opportunity to discuss conflicts of interest in science. Checking the “About Us” section, students will find only two staff listed, one of whom was the chair of the “Nongovernmental International Panel on Climate Change (NIPCC).” Further research shows NIPCC to have been supported by the Heartland Institute, a lobbying group set up to oppose the reports of the IPCC. This exercise would then afford opportunities to discuss what constitutes relevant expertise in science. In addition, a search for what the scientific consensus is on climate change reveals that 99% of scientists would disagree with the claims made on this website.

As for science standards, these are established at the country level or—in federal societies such as the United States, Germany, or Canada—at the state level. The problem is that most of these, including the influential Next Generation Science Standards, were drafted a decade ago before the current maelstrom of social-media-fueled misinformation swept the globe. In principle, they espouse the goal of educating students to be scientifically literate but commonly fail to de-

fine what such an outcome might look like, or what a student might be able to do as a result of such an education. Rather, what these standards tend to offer is a window into the internal workings of science. Although there is nothing wrong with that, it is inadequate if students are to become “competent outsiders.” Those who sit on the committees that draft these standards must recognize and address these weaknesses. Revising curriculum standards is the responsibility of scientific societies and academies, science teacher organizations, and science educators, all of whom need to take up the baton and address this issue through their existing structures. However, achieving such change can only be a medium-term goal.

Transforming preservice teacher training is a long-term goal. First, there is no uniform professional path to becoming a teacher of K-12 science, and neither are there any commonly agreed goals for training. Teacher training is ultimately responsive to what it sees to be the priorities in the standards and in the classrooms for which it prepares its students. Where others lead, it will follow.

It is time for scientists and science educators to step up to help address the complex problem posed by the plague of misinformation. Given that education standards define what knowledge counts, the primary goal must be to achieve a transformation in the limited curricula that students currently experience. More generally it means that all of those endowed with the label of being a scientist must accept the responsibility to explain why the fruits of their labor should be both valued and trusted. ■

REFERENCES AND NOTES

1. T. Nichols, *The Death of Expertise: The Campaign Against Established Knowledge and Why it Matters* (Oxford Univ. Press, 2017).
2. A. Kozyreva, S. Lewandowsky, R. Hertwig, *Psychol. Sci. Public Interest* **21**, 103 (2020).
3. S. Vosoughi, D. Roy, S. Aral, *Science* **359**, 1146 (2018).
4. J. F. Osborne et al., “Science Education in an Age of Misinformation,” Stanford University, 2022.
5. D. Höttercke, D. Allchin, *Sci. Educ.* **104**, 641 (2020).
6. D. Kahan, H. Jenkins-Smith, D. Braman, *J. Risk Res.* **14**, 147 (2011).
7. S. Lewandowsky, K. Oberauer, *Curr. Dir. Psychol. Sci.* **25**, 217 (2016).
8. L. Gierth, R. Bromme, *PLOS One* **15**, e0231387 (2020).
9. N. Feinstein, *Sci. Educ.* **95**, 168 (2011).
10. C. Z. Elgin, *True Enough* (Harvard Univ. Press, 2017).
11. J. Hardwig, *J. Philos.* **82**, 335 (1985).
12. S. Lewandowsky, S. van der Linden, *Eur. Rev. Soc. Psychol.* **32**, 348 (2021).
13. S. Wineburg et al., *J. Educ. Psychol.* **114**, 893 (2022).
14. N. Oreskes, E. M. Conway, *Merchants of Doubt* (Bloomsbury Press, 2010).
15. B. Russell, *Sceptical Essays* (George Allen & Unwin, 1928).

ACKNOWLEDGMENTS

We acknowledge the contributions of the following people to the arguments and points made in this article: B. Alberts, D. Allchin, S. Barzilai, C. Bergstrom, J. Coffey, B. Donovan, R. Dorph, K. Kivinen, A. Kozyreva, K. Perkins, S. Perlmutter, and S. Wineburg.

10.1126/science.abq8093

EVOLUTION

How butterfly wings got their pattern

Gene regulatory elements play a crucial role in the pattern formation of butterfly wings

By Marianne Espeland and
Lars Podsiadlowski

The development of morphological patterns and structures in organisms is the result of transcription factors and epigenetic regulation in different cells and tissues. Transcription factors, which are proteins that bind to DNA at sites called cis-regulatory elements (CREs), can turn gene expression on or off. The fine-tuned regulation of where, when, and to what extent a gene is expressed is also maintained by epigenetic processes, such as by modulating the accessibility of CREs to transcription factors. On an evolutionary time scale, variation in CREs may modify the expression of a neighboring gene and therefore the phenotype of the organism. On page 304 of this issue, Mazo-Vargas *et al.* (1) analyze the evolution of regulatory elements of the gene *WntA*, which is involved in wing pattern formation in Nymphalidae butterflies. Their results illustrate how gene regulatory elements can be conserved over a long time but sometimes quickly undergo adaptive changes.

Butterfly wing patterns provide a prominent model for studying the development and genetic regulation underlying evolutionary changes. This is because slight shifts in gene expression of a few master genes, such as *WntA*, affect the expression of several other genes, which can be directly observed as wing color and pattern variations (2–7). In the family Nymphalidae, which includes more than 6000 species, patterns from different species deviate from the idealized nymphalid ground plan pattern. This idealized pattern consists of color elements arranged in multiple parallel rows across the wings, known as symmetry systems (8). For butterflies of the fam-

ily Nymphalidae, the *WntA* gene modulates certain elements of these symmetry systems and, specifically, the black coloration in the rather atypically patterned genus *Heliconius* (2, 3, 5), which does not display any typical elements of the symmetry systems. Because the sequence of the protein-coding region of *WntA* is very similar even in Nymphalidae species with different wing patterns, it was assumed that noncoding CREs play a key role in the variation of wing patterns (2).



Evolutionary changes in wing patterns of Nymphalidae butterflies, such as that of the common buckeye butterfly (*Junonia coenia*), are mediated by regulatory elements associated with a few master genes.

Mazo-Vargas *et al.* used comparative sequence analysis and ATAC-seq (assay for transposase-accessible chromatin using sequencing). Combining the data from the two analytical methods, the authors identified CREs that might control *WntA* expression in five different Nymphalidae species. Many of the candidate CREs are located immediately upstream of the *WntA* gene and in the first intron. Mazo-Vargas *et al.* find that some of these candidates show sequence similarity among nymphalid butterflies, implying that the candidates were present in their last common ancestor, whereas other candidates evolved recently.

Gene-editing techniques have been use-

ful for understanding the function of genes in wing patterning. For example, after inactivating *WntA*, variations in colors and pattern elements can be observed, demonstrating that this gene is involved in wing pattern development (5, 9). Instead of inactivating the gene itself, Mazo-Vargas *et al.* inactivated regulatory elements that control the gene using CRISPR-Cas9 to excise small stretches of DNA from the genome. The effect of this deletion on the phenotype of the butterfly could then be studied. Mazo-Vargas *et al.* generated such deletions around 46 *WntA*-associated CREs in five butterfly species covering the diversity of the Nymphalidae family. A similar CRISPR-Cas9 approach has been used in butterfly studies before but only on a small taxonomic scale—e.g., for investigating the wing pattern-regulating master gene *optix* and its regulatory elements of butterflies from the genus *Heliconius*, which are also members of the Nymphalidae family (10).

The highly divergent wing patterns of members of the genus *Heliconius* do not display typical elements of the symmetry systems found in other Nymphalidae and have been proposed to either be derived from the nymphalid ground plan pattern or to have originated independently (11). If the former is true, one would expect to find the same CREs involved in wing pattern formation in *Heliconius* species as in other Nymphalidae species. If the latter is true, the CREs involved in pattern formation in *Heliconius* would not be found in other Nymphalidae species. Mazo-Vargas *et al.* confirm that both explanations are partly true—both conserved and recently evolved CREs play a role in wing pattern formation. Inactivation of each of the five selected deeply conserved CREs in the species *Heliconius himera* had broad effects on the black coloration. This indicates that although *Heliconius* color patterns look very different from those of other Nymphalidae species, they share the same regulatory elements as those butterflies displaying the nymphalid ground plan pattern. Furthermore, inactivation of CREs that are specific for *Heliconius* butterflies resulted in similar phenotypes, which indicates that recently evolved elements have adopted a role in wing patterning alongside the older, conserved CREs.

According to Mazo-Vargas *et al.*, the inactivation of another less-conserved CRE, which is only found in a single species (*Vanessa cardui*) but not in a close relative (*Vanessa tamerlana*), resulted in changes in multiple wing elements on both wings. This corroborates the idea of recently evolved CREs quickly becoming part of the regulatory

Leibniz Institute for the Analysis of Biodiversity Change, Museum Koenig, Bonn, Germany. Email: m.espeland@leibniz-lib.de; l.podsiadlowski@leibniz-lib.de

pathway in color pattern formation. In some cases, inactivation of a CRE expanded the wing area where *WntA* is expressed, demonstrating that some CREs may negatively control *WntA* transcription.

The five species analyzed by Mazo-Vargas *et al.* represent a large part of the diversity of the Nymphalidae family. The broadness of the sampling allows the authors to address the question of sequence similarity for regulatory elements at a larger scale than has been done by previous studies, which have largely restricted their experiments to a few closely related species. By choosing to study the monarch butterfly (*Danaus plexippus*), which is quite distantly related to the other four species in their experiment, the authors show that some regulatory elements are conserved even in species diverging almost 90 million years ago (12). So, how far across the order Lepidoptera does this similarity extend? *WntA* is apparently not expressed in the wings of a previously studied butterfly species from the Pieridae family (13). It would be interesting to see whether *WntA* plays a role in the formation of the wing patterns in other butterflies and moths that share similar wing patterns with unpalatable Nymphalidae species to avoid predation. It is worth investigating whether the patterns in these insects evolved through the same genetic pathways—for example, involving *WntA* and the conserved wing pattern master genes *cortex* and *optix* (4, 6, 14, 15)—or whether different pathways are involved.

Mazo-Vargas *et al.* demonstrate that although the regulatory landscape surrounding a gene may be stable over a long time, the loss or gain of CREs may suddenly enable evolutionary change. The approach to manipulate CREs and observe the phenotypic changes opens possibilities for examining other gene regulatory questions in developmental biology, such as those relevant for understanding invertebrate and vertebrate body plans. ■

REFERENCES AND NOTES

1. A. Mazo-Vargas *et al.*, *Science* **378**, 304 (2022).
2. A. Martin *et al.*, *Proc. Natl. Acad. Sci. U.S.A.* **109**, 12632 (2012).
3. A. Martin, R. D. Reed, *Dev. Biol.* **395**, 367 (2014).
4. A. E. van't Hof *et al.*, *Nature* **534**, 102 (2016).
5. A. Mazo-Vargas *et al.*, *Proc. Natl. Acad. Sci. U.S.A.* **114**, 10701 (2017).
6. N. J. Nadeau *et al.*, *Nature* **534**, 106 (2016).
7. J. R. Gallant *et al.*, *Nat. Commun.* **5**, 4817 (2014).
8. H. F. Nijhout, *The Development and Evolution of Butterfly Wing Patterns* (Smithsonian Institution Press, 1991).
9. C. Concha *et al.*, *Curr. Biol.* **29**, 3996 (2019).
10. J. J. Lewis *et al.*, *Proc. Natl. Acad. Sci. U.S.A.* **116**, 24174 (2019).
11. C. D. Jiggins, *The Ecology and Evolution of Heliconius Butterflies* (Oxford Univ. Press, 2017).
12. M. Espeland *et al.*, *Curr. Biol.* **28**, 770 (2018).
13. J. Fenner *et al.*, *Front. Ecol. Evol.* **8**, 197 (2020).
14. A. Prakash, C. Finet, T. D. Banerjee, V. Saranathan, A. Monteiro, *Cell Rep.* **40**, 111052 (2022).
15. L. Zhang, A. Mazo-Vargas, R. D. Reed, *Proc. Natl. Acad. Sci. U.S.A.* **114**, 10707 (2017).

10.1126/science.ade5689

SPECTROSCOPY

An ultraminiaturized spectrometer

Scaling down spectrometers could allow their application in consumer devices

By Jorge Quereda¹ and
Andres Castellanos-Gomez²

Optical spectrometers can measure the intensity of light with spectral resolution. Although laboratory benchtop spectrometer systems offer high resolution and wide spectral range, their large size hampers them from being more widely adopted for general consumer products, such as wearable electronics. The miniaturization of spectrometers is crucial to making them cheaper and easier to integrate with other devices, which can help expand the use of such a powerful analytical tool. There is a wide range of potential applications for cheap and small-sized spectrometers, from detecting counterfeit pharmaceuticals and banknotes to monitoring specific biosignals. On page 296 of this issue, Yoon *et al.* (1) present a design for an ultraminiaturized spectrometer with performance approaching that of benchtop systems.

Over the past decade, the miniaturization of spectrometers has advanced steadily. However, there are often performance trade-offs when miniaturizing them (2). For example, designs that are simply scaled-down versions of benchtop models tend to have relatively poor spectral resolution and light sensitivity. The recent development of “reconstructive-type” spectrometers holds promise to overcome these limitations by using a different operation principle, which could allow researchers to develop high-performance, ultraminiaturized spectrometers.

In conventional spectrometers, a dispersive element, such as a prism or a diffraction grating, is used to spread out the spectrum of a light source. Then, the intensity for the different wavelengths is measured using a large

array of identical detectors. By contrast, reconstructive spectrometers do not require the use of a dispersive element. Instead, their operation principle relies on a much smaller number of detectors, where each detector is designed to measure light of a different wavelength range. When measuring the light signal, the different detectors produce signals that can be “reconstructed” using software to produce the overall spectrum (2). Besides eliminating the need for dispersive elements, this design also reduces the number of sensors from millions to tens or even fewer, which further facilitates device miniaturization.

The recent discovery of semiconducting nanomaterials with strong light-matter interaction opened an avenue for further reducing the size of reconstructive-type spectrometers. An ultracompact microspectrometer (with a footprint of 10 μm by 150 μm) has been produced with a nanowire,

which is engineered to contain segments with different light-absorption spectral profiles (3). In addition to nanowires, two-dimensional (2D) semiconductors have also been used to make ultracompact microspectrometers. Because the optical absorption spectra of 2D semiconductors can be changed and controlled by an external electric field (4, 5), this enables a design with just a single detector, whose absorption spectrum can be adjusted to scan a range of wavelengths over time. Previously, 2D black phosphorus was used to build a reconstructive-type infrared spectrometer with a very small footprint of 10 μm by 20 μm (6). The device, however, did not work in the visible spectrum and required cryogenic temperatures to function, which limited its applications.

The 2D spectrometer presented by Yoon *et al.* works in the visible spectrum under ambient temperature. The ultraminiaturized spectrometer is created using an overlapping junction of two different semiconducting 2D materials—molybdenum disulfide (MoS_2) and tungsten diselenide (WSe_2). The device has a footprint of 22 μm by 8 μm , which is smaller than the average human skin cell.

“The device has a footprint of 22 μm by 8 μm , which is smaller than the average human skin cell.”

¹Grupo Interdisciplinar de Sistemas Complejos: Modelización Y Simulación, Departamento de Física de Materiales, Universidad Complutense de Madrid, Madrid, Spain. ²Materials Science Factory, Instituto de Ciencia de Materiales de Madrid, Consejo Superior de Investigaciones Científicas, Madrid, Spain. Email: jorquere@ucm.es; andres.castellanos@csic.es

In their design, an applied voltage is used to change the photon-to-electric current conversion mechanisms of the MoS₂-WSe₂ junction, that is, where the two layers overlap. By measuring the photon-generated current at different voltages, the spectrum of the incident light source can be determined with a spectral resolution of 3 nm. This is comparable with the resolution of a standard benchtop spectrometer and is unprecedented in spectrometers of this size. For comparison, the resolution for the miniature 2D black phosphorus-based spectrometer is 90 nm (6).

Yoon *et al.* also discuss where the performance of ultraminiaturized spectrometers can be enhanced. This can be done either by improving the software—for example, the reconstruction algorithm—or the hardware—for example, by designing heterojunctions with better spectral tunability. Because of the many ways in which their design can be fine-tuned, the authors predict that it should be possible to create a device that can surpass the already impressive performance of their proof-of-concept device.

It has only taken ~20 years for digital cameras to become a standard feature of mobile phones. The persistent popularity of wearable electronics, together with the ever-growing need for miniaturized devices, should offer plenty of market opportunities for integrated microspectrometers. Applications where weight and size are major constraints, such as aeronautics, can also benefit from ultraminiaturized spectrometers. For example, satellites or drones that are now used for monitoring the environment would benefit from this technology because it would reduce their carrying capacity for other sensors. Just as the popularization of digital cameras in mobile phones led to the creation of many unexpected applications [e.g., augmented reality, image recognition, quick response (QR) code reading, and so on], a similar effect may likewise result from the popularization of ultraminiaturized spectrometers. Only time will tell the extent to which this emerging technology will expand the utility of consumer electronics and wearable devices. ■

REFERENCES AND NOTES

1. H. H. Yoon *et al.*, *Science* **378**, 296 (2022).
2. Z. Yang *et al.*, *Science* **371**, eabe0722 (2021).
3. Z. Yang *et al.*, *Science* **365**, 1017 (2019).
4. R. Roldán, A. Castellanos-Gomez, *Nat. Photonics* **11**, 407 (2017).
5. X. Chen *et al.*, *Nat. Commun.* **8**, 1672 (2017).
6. S. Yuan *et al.*, *Nat. Photonics* **15**, 601 (2021).

ACKNOWLEDGMENTS

J.Q. and A.C.-G. acknowledge funding from the European Research Council (ERC) under the European Union's Horizon 2020 research and innovation program (grant agreement no. 755655 ERC-StG 2017, project 2D-TOPSENSE).

10.1126/science.ade6037

METABOLISM

The timing of eating controls energy use

Synchronizing food intake with the body clock boosts thermogenesis and limits obesity

By **Damien Lagarde**¹ and **Lawrence Kazak**^{1,2}

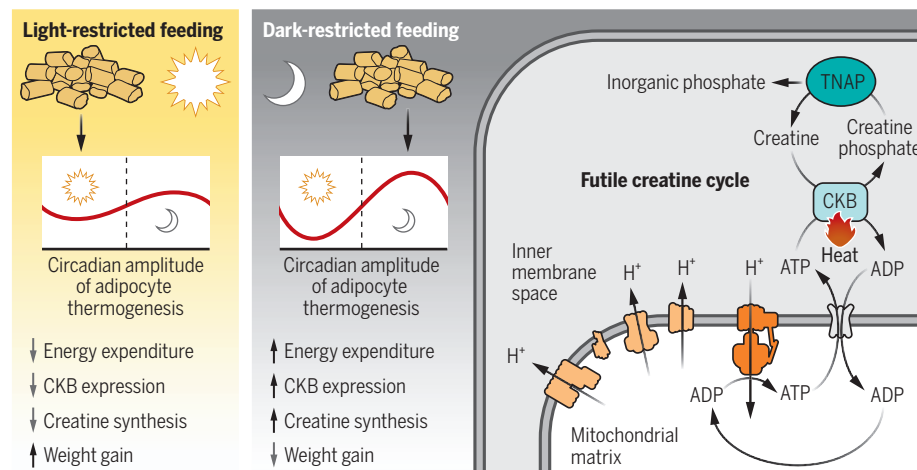
Obesity occurs when energy intake exceeds energy expenditure. Excess calories from food are stored by white adipocytes or dissipated by thermogenic (brown and beige) adipocytes. Molecular clocks control the rhythmic expression of numerous genes to regulate diverse physiological outputs such as energy intake and use during the day. This regulation is bidirectional because nutritional overload dampens circadian oscillations in gene expression and promotes mistimed feeding, which contributes to weight gain (1). Diet-induced obesity is modeled in mice by using energy-dense, high-fat diets. When the time window of high-fat food intake is restricted [time-restricted feeding (TRF)], weight gain is attenuated, but the underlying mechanisms are not resolved. On page 276 of this issue, Hepler *et al.* (2) reveal that TRF during the active period of the circadian clock (at night) protects mice from diet-induced obesity by enhancing adipocyte thermogenesis.

Light input is the principal trigger that drives circadian rhythms by the master clock that is situated in the suprachiasmatic nucleus (SCN) of the hypothalamus (3). Genetic interference with the circadian clock promotes a transition of food consumption toward the inactive period (during daylight for mice) and potentiates diet-induced obesity (4). SCN neurons project onto thermogenic brown adipose tissue. In mice, prolonged daily light exposure disturbs the circadian rhythm, reduces thermogenic activity, and promotes obesity (5), indicating that targeted activation of adipocyte thermogenesis may offset the relationship between disrupted circadian rhythm and excessive energy intake.

TRF involves deliberately restricting the time window during which energy is ingested, without any attempt to reduce calories or alter diet composition; the remaining time is spent fasting. TRF improves the rhythms of circadian clock components and promotes metabolic health in high-fat-fed wild-type mice and mice with disrupted circadian rhythms, without reducing caloric intake or

Mistimed feeding disrupts thermogenesis

In thermogenic adipocytes, creatine kinase B (CKB) and tissue-nonspecific alkaline phosphatase (TNAP) work in tandem to accelerate adenosine triphosphate (ATP) turnover to adenosine diphosphate (ADP) through the futile creatine cycle. This thermogenic pathway drives nutrient oxidation and oxygen consumption. The expression of CKB and creatine abundance are regulated in a circadian manner, peaking when energy expenditure is highest (at night in mice). When mice are fed during the night, when they are most active and thermogenic pathways are most highly expressed, they are more resistant to obesity than mice given light-restricted feeding.



increasing physical activity (6). This implies that the molecular mechanisms underpinning these effects may contain promising therapeutic targets during nutritional overload. Hepler *et al.* investigated the “optimal” time window of TRF, in the context of overnutrition, without the confounding effects of caloric restriction. They found that adipocyte thermogenesis at least partly underlies the beneficial effects associated with TRF during the active phase of the day in mice.

The presence of thermogenic brown adipose tissue, as quantified based on its glucose uptake, in humans is associated with cardiometabolic health (7). Thermogenesis can occur by stimulating futile cycles that either uncouple macronutrient oxidation from adenosine triphosphate (ATP) synthesis (proton leak) or accelerate ATP turnover. The conventional view posits that thermogenesis works exclusively through uncoupling protein 1 (UCP1), which promotes proton leak across the mitochondrial inner membrane, bypassing ATP production. An additional thermogenic pathway centers on the metabolite creatine. In most cells, creatine kinase catalyzes the reversible transfer of a phosphoryl group from ATP to creatine to balance cellular energy supply and demand. However, a UCP1-independent thermogenic pathway of energy dissipation, called the futile creatine cycle, accelerates ATP turnover through a cycle of creatine phosphorylation by creatine kinase B (CKB) and phosphocreatine hydrolysis by tissue-nonspecific alkaline phosphatase (TNAP) (8, 9) (see the figure).

Hepler *et al.* found that the expression of CKB and the production of creatine were regulated by the circadian clock when feeding was synchronized to nighttime, and their peak abundance was commensurate with increased energy expenditure (also at night). By contrast, mistimed feeding (food restricted to daytime) abrogated the rhythmicity of creatine abundance and CKB expression and resulted in susceptibility to diet-induced weight gain due to impaired adipocyte thermogenesis. The authors also discovered that mice with adipocytes that genetically lack zinc finger protein 423 (ZFP423), a transcriptional repressor of the thermogenic gene program (10), exhibited increased adipocyte thermogenesis and CKB expression and protection from obesity during mistimed feeding.

Mice that lack glycine amidinotransferase (GATM), which catalyzes the rate-limiting step in creatine biosynthesis, in adipocytes gain more weight than control mice (11). Hepler *et al.* reveal that in two mouse models that exhibit diminished adipocyte creatine

levels, energy expenditure could not be enhanced when TRF was synchronized with the circadian clock, causing similar weight gain as mistimed feeding. Notably, dietary creatine supplementation could offset this weight gain, indicating that creatine supplementation is beneficial when creatine levels in adipose tissue are limiting. It would be worth exploring whether creatine becomes limiting in the setting of nutritional overload where dietary creatine supplementation could promote adipocyte energy dissipation. If TRF regulates the abundance of creatine and the effectors of thermogenesis by the futile creatine cycle, perhaps this link is bidirectional, such that adipocyte-selective loss of the components that mediate the futile creatine cycle alter the time of eating when food is freely available. Whether such bidirectional control occurs through endocrine and/or sensory innervation of adipose tissue should also be investigated (12). Understanding this relationship could help elucidate the link between adipose tissue metabolism and energy intake.

TRF in humans appears to be a promising approach to decrease body weight and improve metabolic health with few side effects (13, 14). The work of Hepler *et al.* expands our knowledge about the mechanisms that underlie the benefits of TRF. However, the effects of TRF on human weight loss may be masked when combined with caloric restriction or become difficult to interpret if baseline feeding is not established. Similarly, the benefits of TRF can be difficult to discern if the eating window for food intake at baseline is similar to the TRF window (15). Additional challenges could arise from a lack of guidance for how to adhere to TRF or self-reporting bias. Moreover, given that eating and drinking often occurs in the evening, it will be critical to reflect on the social aspects of dining when designing a TRF intervention. ■

REFERENCES AND NOTES

1. A. Kohsaka *et al.*, *Cell Metab.* **6**, 414 (2007).
2. C. Hepler *et al.*, *Science* **378**, 276 (2022).
3. S. Panda *et al.*, *Science* **298**, 2213 (2002).
4. F. W. Turek *et al.*, *Science* **308**, 1043 (2005).
5. S. Kooijman *et al.*, *Proc. Natl. Acad. Sci. U.S.A.* **112**, 6748 (2015).
6. A. Chaix *et al.*, *Cell Metab.* **29**, 303 (2019).
7. T. Becher *et al.*, *Nat. Med.* **27**, 58 (2021).
8. J. F. Rahbani *et al.*, *Nature* **590**, 480 (2021).
9. Y. Sun *et al.*, *Nature* **593**, 580 (2021).
10. M. Shao *et al.*, *Genes Dev.* **35**, 1461 (2021).
11. L. Kazak *et al.*, *Cell Metab.* **26**, 660 (2017).
12. Y. Wang *et al.*, *Nature* **609**, 569 (2022).
13. E. F. Sutton *et al.*, *Cell Metab.* **27**, 1212 (2018).
14. M. J. Wilkinson *et al.*, *Cell Metab.* **31**, 92 (2020).
15. D. Liu *et al.*, *N. Engl. J. Med.* **386**, 1495 (2022).

ACKNOWLEDGMENTS

L.K. receives funding from the Canadian Institutes of Health Research (PJT-159529 and PJT-180557), the Natural Sciences and Engineering Research Council of Canada Discovery Grant, the Terry Fox Research Institute New Investigator Award, and the Canadian Foundation for Innovation John R. Evans Leaders Fund (37919). D.L. is supported by a Canderel postdoctoral fellowship.

¹Rosalind and Morris Goodman Cancer Institute, McGill University, Montreal, QC, Canada. ²Department of Biochemistry, McGill University, Montreal, QC, Canada. Email: lawrence.kazak@mcgill.ca

MEDICINE

Sex matters in liver fat regulation

Growth hormone orchestrates a complex, sex-dependent balancing act

By David J. Waxman¹ and Rhonda D. Kineman^{2,3}

Males are more susceptible than (premenopausal) females to diet-induced hepatic fat accumulation (steatosis) and progression to nonalcoholic fatty liver disease (NAFLD), liver fibrosis, and hepatocellular carcinoma, in both humans and rodents (1). Sex-specific differences in liver gene expression are primarily controlled by the sex-dependent temporal patterns of pituitary growth hormone (GH) secretion (2). However, the links between sex differences in GH-regulated gene expression and sex differences in liver metabolic disease, which are often ascribed to direct effects of gonadal steroids, are poorly understood. On page 290 of this issue, Nikkanen *et al.* (3) show that B cell lymphoma 6 (BCL6), a sex-dependent, GH-regulated hepatic transcription factor, drives the increased susceptibility of male mice to high-fat diet-induced NAFLD, compared to female mice. However, BCL6 also provides an unexpected benefit in the form of increased male survival after bacterial infection, suggesting an evolutionary trade-off.

Sex dimorphic hepatic gene expression is driven by the transcription factor signal transducer and activator of transcription 5b (STAT5B), which is activated by GH in a sex-dependent manner, with intermittent (pulsatile) STAT5B DNA binding activity seen in male liver versus persistent STAT5B activity in female liver (4). STAT5B controls sex-dependent gene expression directly and by regulating the expression of BCL6 (which is male specific) and cut-like 2 (CUX2, which is female specific), which reinforce sex differences through transcriptional and epigenetic repression mechanisms (5). Specifically, BCL6 competes for STAT5B binding sites in hepatocyte chromatin to repress female-specific genes in male liver (5). BCL6 also opposes the action of the transcriptional activator peroxisome proliferator-activated receptor- α (PPAR α), to limit hepatic lipid oxidation,

thereby promoting steatosis (6). Another important layer of regulation involves methyltransferase-like protein 14 (METTL14), which is repressed by BCL6 in male liver under conditions of excess dietary fat (7). METTL14 regulates hepatic triglyceride levels by N⁶-adenosine modification of lipogenic RNAs, which marks them for degradation, thereby suppressing lipogenesis (7). Together, these functions of BCL6 provide mechanistic insight into the male-specific predisposition to diet-induced NAFLD (see the figure).

Nikkanen *et al.* show that BCL6 plays a critical role in what is proposed to be an evolutionary trade-off. Female mice have low hepatic expression of BCL6 owing to the persistence of plasma GH stimula-

Sepsis is associated with substantial changes in circulating lipids and lipoproteins that can predict disease severity: Sepsis-induced hypertriglyceridemia correlates with mortality in some, but not all, clinical studies (10). The findings of Nikkanen *et al.* support the proposal that sex differences in hypertriglyceridemia in sepsis involves BCL6-mediated suppression of plasma concentrations of apolipoprotein C-III (APOC3), which has a role in inhibiting clearance of plasma triglycerides. Further, they showed that high triglycerides play a causal role in sepsis-induced mortality, because raising plasma triglycerides using a lipase inhibitor increased infection-induced mortality in hepatic BCL6-intact males, whereas preventing hypertri-

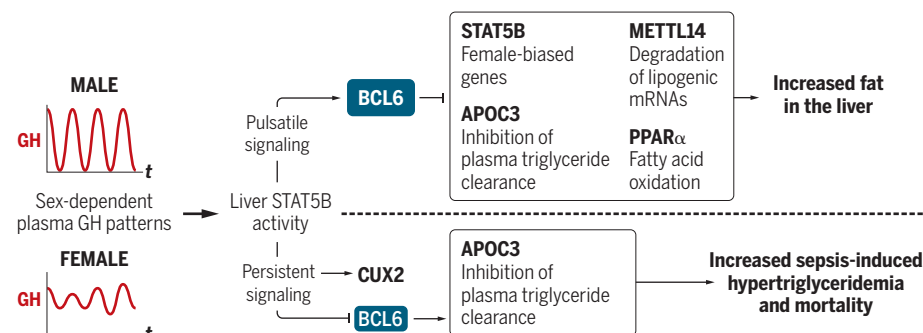
has been more difficult to assess. Human and mouse females generally mount stronger innate and adaptive immune responses to infection than males, but the robust nature of female immune responses can increase morbidity and mortality (14). Indeed, although sepsis mortality in the overall population is higher in men, women have a higher sepsis case fatality rate than men (15), consistent with the female bias in sepsis-induced mortality in mice reported by Nikkanen *et al.* Therefore, the increased susceptibility of females to sepsis could actually be the result of their heightened immune responsiveness.

The relevance of BCL6 for human sex differences in liver metabolism and responses to sepsis is still unknown. No sex differences in hepatic *BCL6* mRNA levels are apparent in a set of >200 human livers in the Genotype-Tissue Expression (GTEx) database. However, sex differences in expression could be masked by individual differences in age, health, and reproductive status. The timing of liver collection in relation to in vivo plasma GH peaks could add to variability, given that a single GH pulse can rapidly down-regulate *Bcl6* transcripts in rodent hepatocytes (8). Intriguingly, CUX2 expression does show human liver sex differences, with expression higher in males than females, which is opposite to what is found in mice.

Nikkanen *et al.* take an important first step in linking sex-dependent GH regulation of liver lipid metabolism and clearance to sex differences in the response to bacterial infection. Their findings highlight sex as a critical biological variable and the need to refine animal models to better match human conditions. Additionally, when considering sex-dependent traits, it is essential to think beyond genetic sex and the direct actions of androgens and estrogens, and to factor in complex downstream hormonal regulatory networks that may have more direct effects on health and disease. ■

Sex differences in responses to diet and sepsis

Gonadal steroids regulate the pattern of pituitary GH release. In male mice, pulsatile GH and thus pulsatile liver STAT5B activity promotes hepatic BCL6 expression, which represses female-specific genes and three genes that regulate fat metabolism. This increases susceptibility to high fat diet-induced fatty liver disease. The persistent GH pattern in females promotes expression of CUX2 and represses BCL6 expression, resulting in female-biased gene expression, higher APOC3 levels, and increased susceptibility to sepsis-induced mortality.



APOC3, apolipoprotein C-III; BCL6, B cell lymphoma 6; CUX2, cut-like 2; GH, growth hormone; METTL14, methyltransferase-like protein 14; PPARα, peroxisome proliferator-activated receptor-α; STAT5B, signal transducer and activator of transcription 5b.

tion and hepatic DNA binding STAT5B activity (8). As a result, they are protected from high fat diet-induced NAFLD, but this comes at the cost of higher mortality following intravenous injection of *Escherichia coli*, a model of Gram-negative sepsis, which is commonly associated with hyperlipidemia (9). Male mice, with higher expression of hepatic BCL6, are more susceptible to diet-induced NAFLD but are relatively resistant to hyperlipidemia and death after *E. coli* infection. The essential role of BCL6 was confirmed by the finding that hepatocyte-specific loss of *Bcl6* in males feminized gene expression and protected mice from diet-induced NAFLD, but also increased plasma triglyceride levels and mortality after *E. coli* infection.

glyceridemia improved postinfection survival in females. Therefore, at least in mice, GH-regulated sex differences in hepatocyte BCL6 expression, and consequently plasma lipid clearance, can impact host survival from sepsis. These findings point to BCL6 and APOC3 as potential therapeutic targets for improving hyperlipidemia associated with sepsis and could thereby increase survival.

The interconnection between sex-dependent diet-induced steatosis and infection-induced hypertriglyceridemia and mortality reported by Nikkanen *et al.* was most apparent under thermoneutral housing conditions (30°C). Under these conditions, mice do not need to burn fat to maintain body temperature and so this is a better mimic of the human condition for obesity-associated metabolic disease and immune function (11). Evidence is also mounting in both mice and humans for a connection between sex-dependent GH regulation of lipid metabolism and NAFLD progression (12, 13). However, the sex dependence of infection-induced mortality

REFERENCES AND NOTES

1. A. Lonardo *et al.*, *Hepatology* **70**, 1457 (2019).
2. D.J. Waxman, M. G. Holloway, *Mol. Pharmacol.* **76**, 215 (2009).
3. J. Nikkanen *et al.*, *Science* **378**, 290 (2022).
4. D. Lau-Corona *et al.*, *Endocrinology* **163**, bqac046 (2022).
5. A. Sugathan, D.J. Waxman, *Mol. Cell. Biol.* **33**, 3594 (2013).
6. M.A. Sommars *et al.*, *eLife* **8**, e43922 (2019).
7. D.A. Salisbury *et al.*, *Nat. Metab.* **3**, 940 (2021).
8. R.D. Meyer *et al.*, *Mol. Endocrinol.* **23**, 1914 (2009).
9. H.W. Harris *et al.*, *J. Endotoxin Res.* **6**, 421 (2000).
10. A. Cetinkaya, *Ther. Clin. Risk Manag.* **10**, 147 (2014).
11. D.A. Giles *et al.*, *Nat. Med.* **23**, 829 (2017).
12. L.E. Dichtel *et al.*, *J. Clin. Endocrinol. Metab.* **107**, 1812 (2022).
13. M.C. Vázquez-Borrego *et al.*, *Cells* **10**, 2532 (2021).
14. L.G. vom Steeg, S.L. Klein, *PLOS Pathog.* **12**, e1005374 (2016).
15. V.Y. Dombrovskiy *et al.*, *Crit. Care Med.* **35**, 1244 (2007).

ACKNOWLEDGMENTS

The authors receive support from the National Institutes of Health (grant DK121988 to D.J.W. and DK116878 to R.D.K.) and Veterans Administration (grant BX004448 to R.D.K.).

10.1126/science.ade7614

¹Department of Biology and Bioinformatics Program, Boston University, Boston, MA, USA. ²Department of Medicine, Section of Endocrinology, Diabetes, and Metabolism, University of Illinois at Chicago, Chicago, IL, USA. ³Jesse Brown VA Medical Center, Chicago, IL, USA. Email: djw@bu.edu



BOOKS *et al.*

MONITORING

Babbling bats and raucous reefs

Bioacoustics can aid in understanding and conserving species and ecosystems

By Benjamin Gottesman

In her new book, *The Sounds of Life*, Karen Bakker describes how it is possible to sense sound with no ears, reveals the noise that makes elephants cower in terror, and explains why coral reefs are as lively as city centers, all by introducing readers to the emerging field of digital bioacoustics. Each of the book's 10 chapters focuses on a different organism—from singing whales to dancing honeybees to growling turtles—and the scientists working to understand the meaning behind the sounds they make. These vignettes demonstrate how animal sounds, long relied on for tracking and hunting, have become key to understanding and conserving species and ecosystems.

The sounds emitted by bats, for example, are far more socially complex than we once thought. Beyond echolocation calls, some bat species babble like human babies in their early days, learn courtship songs from their fathers as juveniles, and have hundreds of call types for different contexts as adults. Meanwhile, real-time listening stations are drastically reducing the number of ship strikes of the North Atlantic right whale, one of North America's most endangered marine mammals. And in Southeast Asia, scientists-turned-DJs are broadcasting the spirited

sounds of healthy coral reefs to attract larval fish and coral to artificial reefs.

Just as fascinating are the stories Bakker tells of the humans who have made bioacoustics discoveries. The individuals she interviews all seem to have had a quirk or a talent that primed them to look (or listen) where no one else did. For zoologist Katy Payne, it was her training as a classical musician that enabled her to perceive the barely audible infrasonic rumbles of elephants. The sounds reminded her of the giant pipe organs at her local church. For Jacqueline Giles, it was her unmatched grit in the field. "It took Giles 230 days in the field and five hundred hours of recordings" to finally document the subtle vocalizations of turtles in the wild, notes Bakker. For school-skipper turned Nobel laureate Karl von Frisch, his obsessive and prolonged bouts in nature contributed to his curiosity about the elaborate dances performed by bees. For each of these researchers' breakthroughs, Bakker documents how initial skepticism from others in the field ultimately gave way to acceptance that animals and plants are capable of far more than we have previously been willing to accept.

Among the first people to use acoustic monitoring to assess animal populations were a group of Iñupiat living in Barrow, Alaska. In the late 1970s, they proposed that acoustics would provide a far more accurate census of the bowhead whale population than the vi-

Tomonari Akamatsu searches for acoustic signs of the baiji dolphin in the Yangtzi river in 2006.

sual surveys that were the standard method used at the time by Western scientists, which they believed were underestimating the population. Spearheaded by Iñupiat elder Harry (Kupaaq) Brower Sr., a team of Western scientists and Iñupiat hunters and knowledge holders confirmed the Iñupiat's hypothesis in 1984. Having demonstrated that the bowhead population was thriving rather than in decline, the Iñupiat were able to resume subsistence hunting. By including such stories, Bakker reveals the Indigenous knowledge that has informed many Western scientific discoveries—which may surprise even those who have worked in bioacoustics for some time—underscoring how much there is to learn from cultures that have long practiced deep listening.

Bakker also leaves space to consider what is to come. She imagines a future where artificial intelligence-enabled robots intermingle in animal worlds, where battery-less audio recording networks monitor biodiversity in real time across unprecedented spatial scales, and where animal languages are decoded into translatable dictionaries. Although

the road may be bumpier than Bakker acknowledges, her contemplation of where we are going is thoughtful and rigorous.

There have been a handful of other books that delve into bioacoustics, but Bakker's meticulously researched and colorfully presented offering is the first to integrate so many dimensions of the field in a way that is accessible to nonexperts. It is a wonderful mix of animal ecology, narratives of science-doing, futurism, and accounts of Indigenous knowledge that is as interdisciplinary as the field itself. ■

10.1126/science.ade1290



The Sounds of Life
Karen Bakker
Princeton University Press, 2022. 368 pp.

The reviewer is at the K. Lisa Yang Center for Conservation Bioacoustics, Cornell Lab of Ornithology, Cornell University, Ithaca, NY 14850, USA.
Email: ben.gottesman@cornell.edu

NEUROSCIENCE

A neurosurgeon's climate fight

Cutting greenhouse emissions will require less brain and more (collective) brawn

By Adam R. Aron

Although it is welcome, the recent passage of congressional and state-level climate policy in the United States is nowhere near strong enough to drive a large and quick reduction of greenhouse gas emissions. Against this backdrop comes *Minding the Climate*, a book by pediatric neurosurgeon Ann-Christine Duhaime, who is worried about the climate and ecological crisis, including the colossal energy footprint and material throughput of brain surgery. Taking her cue from the chair of the environmental science department at her alma mater—who advises, “Your best chance of having an impact is to work within your field”—she decides to approach the problem from a neuroscientific perspective.

The first part of the book summarizes key aspects and research on brain evolution and the reward system. The second part details the recent acceleration in the consumption of goods, describing how this is driven by electronic media that hijack our brains. The third part reviews the psychology of habits, behavior change, and nudges and discusses what kinds of emissions reductions are required and whose behavior must change.

Duhaime covers many issues in a thoughtful way, including the gap between people's stated intentions to perform pro-environmental behaviors and whether they actually do so; the limits of survey-based research about attitudes, beliefs, and behavior versus seldom-done field studies; and all the ways in which reward is pertinent for behavioral change. She succeeds in suggesting that neuroscience is indirectly relevant to understanding our current climate predicament. Yet her insistence on the primacy of reward for driving individual consumption change—it is a maxim, she writes, that if something

is not perceived as rewarding, we will not do it—overlooks the myriad reasons people have for behaving in certain ways. It is a stretch to argue, for example, that environmental justice advocates who invite prison time in the Global North and are killed by the hundreds each year in the Global South (1) do so because it is rewarding.

The Intergovernmental Panel on Climate Change (IPCC) Working Group III report of 2022 argues that consumption reduction is a key component in emissions reduction (2), but we need to identify a realistic



Hospitals generate substantial amounts of waste and greenhouse emissions.

level at which this must be done. Although Duhaime is correct in diagnosing overconsumption by the affluent as a crucial contributor to climate change—and we can hope that her advice might lead some of the highly affluent to reduce their private jet travel and some of the merely affluent to electrify their households and transportation—this is unlikely to be enough to address the problem at hand.

We need system-level policy changes such as ordinances to remove gas lines from new and existing buildings; low-interest loans so that many households can insulate and purchase electric appliances; mandates for public pensions to divest holdings in fossil fuel companies; bans on new, and even existing, oil and gas extraction; clean electricity standards; and regenerative agriculture policy. Such systemic change will only arise as a re-

**Minding the Climate:
How Neuroscience Can Help
Solve Our Environmental Crisis**
Ann-Christine Duhaime
Harvard University Press,
2022. 336 pp.



sult of a much wider advocacy movement—a social mobilization—that recognizes not only our individual foibles but also the powerful interests engaged in obfuscating, greenwashing, and retarding the transition away from fossil fuels. Although social science researchers are indeed working to help us better understand how to galvanize such advocacy efforts, that is not the topic of this book.

Duhaime is to be commended for jumping into the public fray to try to do something about a quickly deteriorating biosphere. But perhaps she might have interpreted the environmental scientist's advice to work within her own wheelhouse a bit differently. Instead of using the lens of neuroscience, she might instead have leveraged her position as a physician affiliated with various powerful institutions to exert change. It is possible, for example, that the year she spent delving into the climate problem at Harvard University's Radcliffe Institute for Advanced Study overlapped with the construction of a new fossil fuel-burning plant on campus (3). If that were the case, Duhaime could have sought to organize a mass movement of Harvard students, faculty, and staff (neurosurgeons included), who might have stopped the build-

ing of that plant and redirected the university to investing in renewable energy.

In the book's final chapter, she describes how we might create greener hospitals. Approximately 10% of all the greenhouse emissions in the US—along with a good proportion of toxins and wastes—come from the hospital sector, so this is a considerable exercise. There is a phrase in grassroots organizing: “Find your frontline.” Duhaime's frontline is medicine, and I am glad she is there. ■

REFERENCES AND NOTES

1. EJAtlas, The Global Atlas of Environmental Justice; <https://ejatlas.org>.
2. IPCC Sixth Assessment Report: Mitigation of Climate Change (2022); <https://www.ipcc.ch/report/ar6/wg3/>.
3. M. J. Lewis, “A statement of power at Harvard,” *Wall Street Journal*, 20 December 2021; <https://on.wsj.com/3SQKc20>.

The reviewer is at the Department of Psychology, University of California, San Diego, La Jolla, CA 92093, USA. Email: adamaron@ucsd.edu

10.1126/science.ade5672



Edited by Jennifer Sills

Regulatory insight from low-income countries

In their Policy Forum, “Transparency practices at the FDA: A barrier to global health” (5 August, p. 572), M. M. Lumpkin and colleagues call attention to the urgent need for the US Food and Drug Administration to share scientific assessments and manufacturing inspections with less resourced regulatory agencies in low- and middle-income countries. They explain that shared information can help relatively poorly resourced regulatory agencies pursue timely and effective reliance-based regulatory decisions. Historically, regulatory information has flowed either from well-resourced to less resourced agencies, as Lumpkin *et al.* suggest, or between well-resourced regulators (1). Insights from less well-resourced regulatory agencies in low- and middle-income countries could also benefit better-resourced regulatory agencies in high-income countries.

All regulators are resource-constrained, and addressing the full complexity of populations and contexts is challenging even for the best-resourced regulators. The varying salient characteristics of populations and contexts addressed by regulatory agencies in different countries have the potential to provide insights that might otherwise be missed. For example, the diversity of genetic biomarkers can inform pharmacovigilance and precision medicine efforts, and local patterns of antimicrobial resistance and transmission can inform global oversight (2–4).

Systematically amplifying regulatory insights from low- and middle-income

countries would have global benefits. Information from a variety of sources would deepen the understanding of the complexity across different contexts, including genetics, ethnicities, concurrent illnesses, concomitant medicines, microbiomes, socioeconomic, nutrition, and environmental exposures. A more diverse and comprehensive dataset would also strengthen the checks and balances across the global regulatory landscape.

Jackson K. Mukonzo¹, David A. Price²,
Thaddeus H. Grasela^{3,4*}

¹Department of Pharmacology & Therapeutics, Makerere University, College of Health Science, Uganda. ²DebateGraph, Somerset, UK. ³School of Pharmacy, University at Buffalo, Buffalo, NY 14260, USA. ⁴Azimuth Global Health Consulting, LLC, Amherst, NY 14226, USA.

*Corresponding author.

Email: ted.grasela@azimuthglobalhealth.com

REFERENCES AND NOTES

1. D. Drago, M. M. Lumpkin, “Reliance-based regulatory pathways—the key to smart(er) regulation?” (2021); <https://globalforum.diaglobal.org/issue/march-2022/reliance-based-regulatory-pathways-the-key-to-smarter-regulation>.
2. T. Hurrell, J. Naidoo, J. Scholefield, *Front. Genet.* **13**, 864725 (2022).
3. S. Muyambo *et al.*, *OMICS J. Integr. Biol.* **26**, 35 (2022).
4. O. O. Ikimiukor *et al.*, *Nat. Microbiol.* **7**, 757 (2022).

COMPETING INTERESTS

D.A.P. is a paid consultant for the Bill and Melinda Gates Foundation.

10.1126/science.ade9441

The challenge of open access incentives

In their Editorial “Public access is not equal access” (9 September, p. 1361), S. Parikh *et al.* explain that moving from a scientific publication model in which the subscriber pays to access content to a

model in which the author pays an article processing charge has the potential to affect publication quality. In subscriber-based models, journals have incentives to publish high-quality work because better articles should lead to more subscribers. In open access models based on author publication fees, the publishers make more money by publishing more articles. Quantity incentives increase while the relative importance of the quality declines. The publishing industry must work to counteract this potentially harmful incentive structure.

The impacts of quantity incentives can already be seen at the extremes in the rise of predatory (junk) journals, nearly all of which are open access (1), but the motivation to increase quantity at the expense of quality has the potential to affect even the most reputable journals. All open access journals must acknowledge this challenge and develop specific protocols to work against it. Parikh *et al.* rightly recognize the “temptation” to increase the quantity of accepted papers and promise that they have “made the costly decision to maintain editorial quality” for journals published by AAAS (the publisher of *Science*). Such declarations, while well-intentioned, are not sufficient. We have known since even before Adam Smith explored human behavior (2, 3) that incentives will trump intentions unless explicit guidelines are in place (4, 5).

One possible solution would be to allow authors to designate their submission as open access only after the review process and publication decision, to ensure that the journal evaluates the article for quality without the bias introduced by author fees. Authors would be motivated to opt for open access papers to maximize citations. This solution would not address the issue of equal access to all published work, and article fees would have to be fair to authors in more challenging funding environments. Even so, removing the incentive to focus on quantity over quality in the decision-making process would be a step forward.

Manuel Lerdau

Department of Environmental Sciences and Biology, University of Virginia, Charlottesville, VA 22903, USA. Email: mlerdau@virginia.edu

REFERENCES AND NOTES

1. M. Berger, J. Beals, *Coll. Res. Library News* **76**, 132 (2015).
2. Aristotle, *Nicomachean Ethics* (350 BCE), Book III; <http://classics.mit.edu/Aristotle/nicomachaen.3.iii.html>.
3. A. Smith, *The Theory of Moral Sentiments* (1759), 2002 Edition, K. Haakonssen, Ed. (Cambridge University Press, 2002).
4. C. F. Manski, J. V. Pepper, *Rev. Econ. Stat.* **100**, 232 (2018).
5. A. Agan, S. Starr, *Quart. J. Econ.* **133**, 191 (2018).

10.1126/science.ade7288

Preserving credibility of open access journals

In their Editorial “Public access is not equal access” (9 September, p. 1361), S. Parikh *et al.* explain how the open access model can compound inequities (1, 2) by charging article processing fees that early-career scientists and scientists in underfunded disciplines, teams, or regions (1) are unable to afford. They also acknowledge the perverse incentives of a business model based on volume of articles published, which has led to the proliferation of open access journals, many of which are predatory, and risks diluting the scientific literature (1, 3). However, they do not address another unintended consequence of open access policies: the erosion of trust in scientific publishing standards by institutions.

In Chinese universities, Science Citation Index and Social Science Citations Index publications are directly related to the salaries and titles of researchers, which creates an incentive for researchers to pay high article processing charges for open access journals. Given the risk that open access journals will sacrifice quality in the name of profit (4), at least one Chinese

university has declared that publication in open access journals will not be considered as part of a researcher's citation record (5). In the past decade, open access conference proceedings have lost credibility as well (6). China's Ministry of Science and Technology has reacted to concerns by limiting how much funding can be allocated to pay article processing charges (7). Chinese institutions' lack of confidence in the quality of open access articles will weaken the viability of legitimate open access journals and in turn hinder scientific research.

To balance the tensions between equitable content access for readers and equitable publishing access for authors, article processing fees should adhere to a standard proposed by credible international organizations such as the UN Educational, Scientific, and Cultural Organization, but they should also incorporate flexibility to take into account the author's country of residence, institution, team, and other financial circumstances. To protect against predatory publishers, a third-party evaluation system such as the Early Warning Journal List from the Chinese Academy of Sciences (8) should judge the quality control of open access publications by tracking article processing fees, volume of published

articles, and diversity of authors, and publicize the information for researchers.

Open access policy is not a scourge, but a challenge. Fair author fees and careful monitoring of the open access publication industry will allow better access for readers and affordable access for authors while maintaining the credibility of publications.

Baichang Zhong* and Xiaofan Liu

School of Information Technology in Education,
South China Normal University, Guangzhou
510631, China.

*Corresponding author. Email: zhongbc@163.com

REFERENCES AND NOTES

1. F. M. Cabrerizo, *Nature* **605**, 620 (2022).
2. J. Brainard, *Science* **371**, 16 (2021).
3. C. Aspesi, A. Brand, *Science* **368**, 574 (2020).
4. H. Else, R. Van Noorden, *Nature* **591**, 516 (2021).
5. Chengdu University of Technology, “The certification system on research projects, research achievements, and social services” (2018); www.cim.cdut.edu.cn/local/F/43/B3/B26DF93F67890FBAC04A4BF3C73_3E1F5763_F36F9.pdf [in Chinese].
6. L. Han *et al.*, *Sci. Technol. Inform. Dev. Econ.* **25**, 51 (2015); <https://doi.org/10.3969/j.issn.1005-6033.2015.04.024> [in Chinese].
7. Ministry of Science and Technology of the People's Republic of China, “Several measures to eliminate the bad orientation of ‘paper only’ in science and technology evaluation (trial implementation)” (2020); www.most.gov.cn/xgk/xinxifenlei/fdzdgknr/tgzc/gfxwj/gfxwj2020/202002/t20200223_151781.html [in Chinese].
8. Chinese Academy of Sciences, Early Warning Journal List (2021); <https://earlywarning.fenqubiao.com/#/en/>.

10.1126/science.ade8966

2023

AAAS MARTIN AND
ROSE WACHTEL
CANCER RESEARCH

AWARD

Recognizing the work of an early career scientist who has performed outstanding research in the field of cancer. Award nominees must have received their Ph.D. or M.D. within the last 10 years. The winner will deliver a public lecture on their research, receive a cash award of **\$25,000**, and publish a Focus article on their award-winning research in *Science Translational Medicine*.

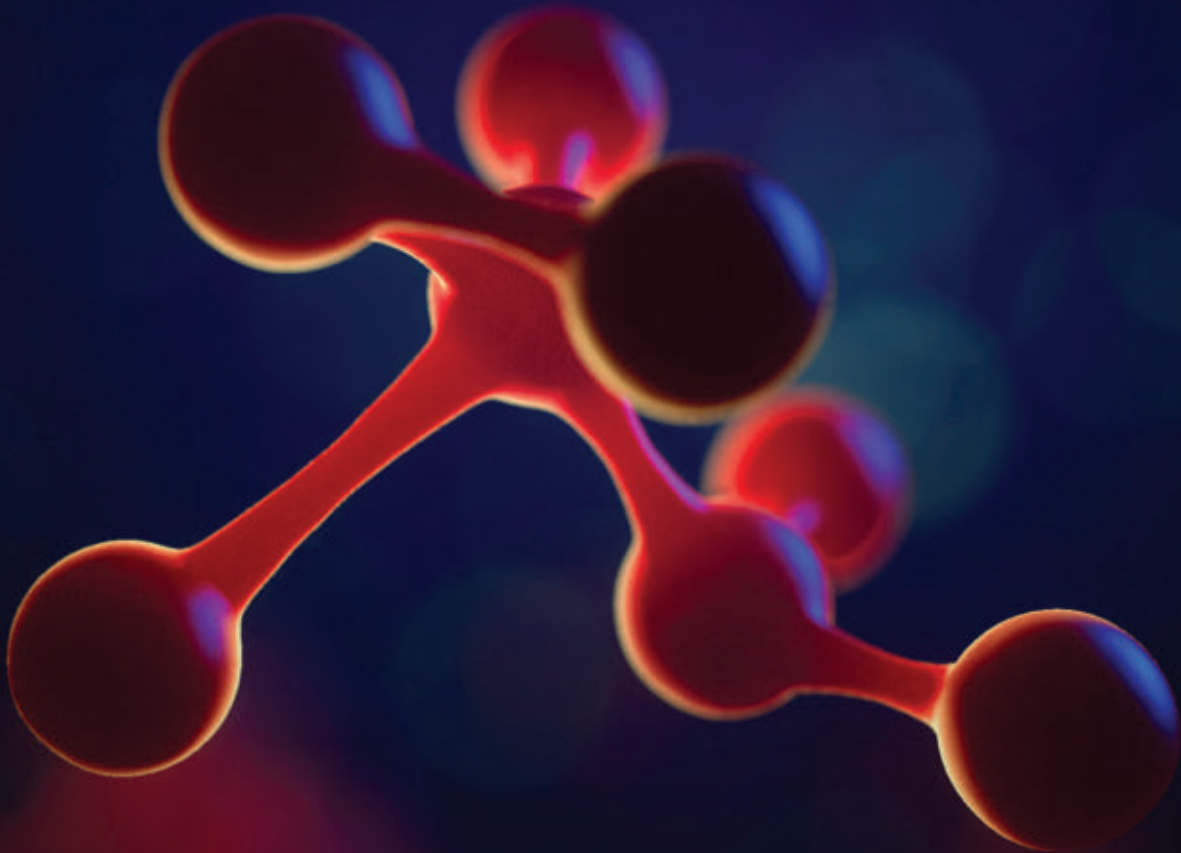
For more information visit www.aaas.org/aboutaaas/awards/wachtel or e-mail wachtelprize@aaas.org.

Deadline for submission: **February 1, 2023**.



Science Translational Medicine

Science
JOURNALS 



Publish your research in the *Science* family of journals

The *Science* family of journals (*Science*, *Science Advances*, *Science Immunology*, *Science Robotics*, *Science Signaling*, and *Science Translational Medicine*) are among the most highly-regarded journals in the world for quality and selectivity. Our peer-reviewed journals are committed to publishing cutting-edge research, incisive scientific commentary, and insights on what's important to the scientific world at the highest standards.

Submit your research today!

Learn more at **[Science.org/journals](https://www.science.org/journals)**

RESEARCH

IN SCIENCE JOURNALS

Edited by **Michael Funk**



WILDLIFE DISEASE

Black wolves' leg up

In North America, wolves generally have either gray or black coats, and the proportions of these colors vary across populations. The genetics of these coat colors have been revealed, and we now know that black wolves are either homozygous or heterozygous for a gene that is also related to resistance to canine distemper virus. Analyzing data from across North America, but especially from populations in Yellowstone National Park, Cubaynes *et al.* found that black coats were maintained through heterozygote advantage in, and mate choice preference for, black-coated wolves in areas where canine distemper is endemic even though gray-coated wolves have higher success when the virus is absent. —SNV *Science*, abi8745, this issue p. 300

CYSTIC FIBROSIS

How three drugs restore function

Cystic fibrosis is caused by defects in a chloride channel crucial for proper fluid balance

and secretion. Deletion of a single amino acid, phenylalanine 508 ($\Delta 508$), is the most common mutation and leads to misfolding and degradation of the protein before it can reach cell surfaces. Fiedorczuk and

Chen determined the structures of the $\Delta 508$ channel bound to three drugs that are given in combination therapy to correct folding and potentiate the channel. They uncovered a binding site for

one of the drugs, a dual function corrector and potentiator, that was not previously known. The structures showed only a partial correction of folding when only one corrector was provided, but full correction was achieved when type I and III correctors were bound.

—MAF

Science, ade2216, this issue p. 284

COMPUTER NETWORKS

Learning on the edge

Smart devices such as cell phones and sensors are low-power electronics operating on the edge of the internet. Although they are increasingly more powerful, they cannot perform complex machine learning tasks locally. Instead, such devices offload these tasks to the cloud, where they are performed by factory-sized servers in data centers, creating issues related to large power consumption, latency, and data privacy. Sludds *et al.* introduce an edge-computing architecture called NetCast that makes use of the strengths of photonics and electronics. In this method, smart transceivers periodically broadcast the weights of commonly used deep neural networks. The architecture allows low-power edge devices with minimal memory and processing to compute at teraflop rates otherwise reserved for high-power cloud computers.

—ISO

Science, abq8271, this issue p. 270

STRUCTURAL BIOLOGY

Focusing on the HCV target

The hepatitis C virus (HCV) causes chronic infection of the liver that can lead to cirrhosis or liver cancer. A prophylactic vaccine could ameliorate these long-term consequences for millions of people, but vaccine development is hampered by the lack of structural information on the vaccine target, a glycoprotein complex located on the surface of the virus.

Torrents de la Peña *et al.* determined the cryo-electron microscopy structure of the envelope glycoprotein E1E2 heterodimer in complex with three broadly neutralizing antibodies. The structure elucidates how the two subunits interact, describes three key neutralizing epitopes, and provides a blueprint for the design of vaccines and drugs that target HCV. —VV

Science, abn9884, this issue p. 263

MEMBRANES

Honeycomb channels enhance separations

Pervaporation membranes use a combination of permeation and evaporation for energy-efficient separations of volatile compounds from solutions. Xu *et al.* designed a strategy to fabricate defect-free superhydrophobic metal-organic framework (MOF) nanosheet membranes. Instead of dispersing the MOFs into a polydimethylsiloxane (PDMS) matrix, the authors grew a continuous and uniform layer of embedded MOF seeds on polymeric substrates that were then sealed with PDMS. This procedure results in a honeycomb-like structure with high flexibility and fast molecular transport channels, thus enhancing the separation of alcohols from water. —MSL

Science, abo5680, this issue, p. 308

MARINE CONSERVATION

Does the trick

Marine protected areas (MPAs) have been shown to protect local populations of fishes. Questions have remained, however, about whether they would also work to protect species that migrate or travel over large distances. Medoff *et al.* looked at the effectiveness of a recently established—and thus far the largest—fully protected MPA located near Hawai'i, and found clear evidence that the protections afforded to two migratory species, bigeye and yellowfin tuna, led to spillover

effects previously only seen for resident fish populations. —SNV
Science, abn0098, this issue p. 313

CELL BIOLOGY

How mitochondria handle helical proteins

The essential roles of mitochondria in metabolism and signaling depend on a functionally and structurally diverse class of alpha-helical proteins embedded in the outer mitochondrial membrane. Guna *et al.* identified the mitochondrial outer membrane protein MTCH2 (mitochondrial carrier homolog 2) and found that it is both necessary and sufficient for the insertion of mitochondrial alpha-helical proteins. MTCH2 is the defining member of a broadly conserved class of insertases that exploit a diverged ancestral solute transporter fold to mediate membrane protein insertion. MTCH2's role as a gatekeeper for outer mitochondrial membrane biogenesis rationalizes its pleiotropic phenotypes and association with human disease. —SMH

Science, add1856, this issue p. 317

PHYSIOLOGY

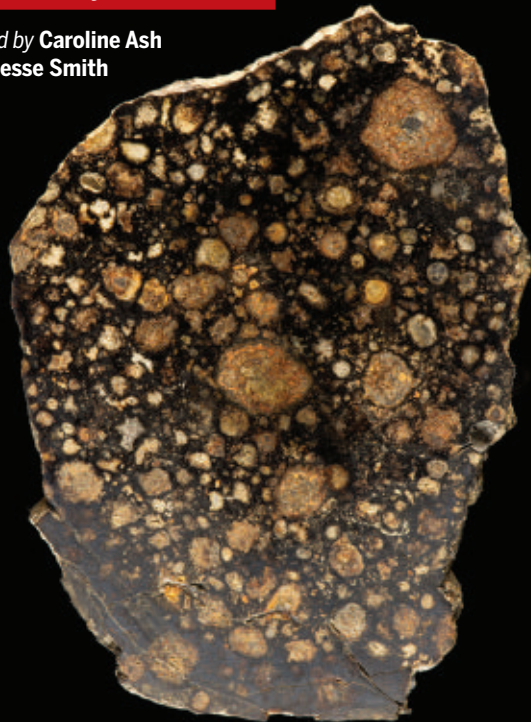
Differences of the heart

Physiological dimorphisms between men and women have the potential to reshape our understanding of both health and disease. Examining a cohort of healthy lean adults, Diaz-Canestro *et al.* found that systemic and peripheral cardiovascular parameters, including left ventricular size, diastolic function, and peripheral resistance, are associated with lean body mass in women but not in men. Although these relationships await investigation in other patient populations, the sex-specific relationship of lean body mass to cardiovascular capacity may have relevance for cardiovascular interventions and risk of heart failure. —CAC

Sci. Transl. Med. **14**, eabo2641 (2022).

IN OTHER JOURNALS

Edited by **Caroline Ash**
and **Jesse Smith**



ASTROCHEMISTRY

Complex origins of meteorite PAHs

Polycyclic aromatic hydrocarbons (PAHs) are molecules containing several adjacent benzene rings. Astronomical observations show that PAHs are common in the interstellar medium and that some carbonaceous meteorites contain PAHs; however, it is unclear whether these two observations are related. Lecasble *et al.* extracted PAHs from three meteorites and measured their carbon and hydrogen isotopes. They compared the isotope ratios with the expected values for formation in the interstellar medium or on meteorite parent bodies and with the degree of aqueous alteration of each meteorite. The authors propose that the PAHs formed in the interstellar medium were incorporated into the Solar System and then modified by reactions with liquid water. —KTS

Geochim. Cosmochim. Acta 10.1016/j.gca.2022.08.039 (2022).

The interstellar medium is the origin of the polycyclic aromatic hydrocarbons contained in carbonaceous chondrites, such as this one found in northwest Africa.

COMMUNITY ECOLOGY

Below ground, so above ground

Soil microorganisms can influence plants' response to herbivores or pathogens by activating or inhibiting plant defenses. Van Dijk *et al.* investigated whether soil communities can also influence aboveground

interactions between herbivores and pathogens that are affected by different plant defense pathways. Oak seedlings were grown with different experimental soil communities and exposed to powdery mildew, to aphids, or to both at once with or without caterpillar damage. Soil community affected seedling size and aboveground attack reduced

PHOTO: JOHN GANCALOS/ALAMY STOCK PHOTO

leaf size. The amount of mildew coverage of leaves depended on soil microbiome composition, and in turn the amount of mildew limited aphid populations. However, this effect only applied to caterpillar-bitten plants in certain soil types. Therefore, plants connect above- and belowground communities in ways that could be influenced by altering the soil microbiome. —BEL

Oikos 10.1111/oik.09366 (2022).

HUMAN GENETICS

The complicated genetics of sleep

Mendelian disorders are characterized by rare genetic variants causing disease. Historically, these disorders have been discovered through family studies in which they appear in patterns consistent with simple inheritance models. Weedon *et al.* examined the effects of 12 variants that had been associated with Mendelian sleep disorders in several large clinical cohorts. None of these variants was significantly associated with sleep disorders, although newly identified loss-of-function

mutations in some of them were associated with sleep timing. Monogenic diseases have revealed many facets of biology, but this study shows that proper controls must be used to ensure the correct identification of variants causing Mendelian disorders. —CNS

PLOS Genet. 10.1371/journal.pgen.1010356 (2022).

SURFACE SCIENCE

Robust oil-resistant surfaces

In marine environments, oil pollution from spills or manufacturing causes problematic surface fouling. Further, these are often physically and chemically harsh environments that can wear away structured surfaces or coatings that are designed to prevent fouling. Li *et al.* gel cast a high-concentration slurry of 200- to 300-nanometer-diameter aluminum oxide particles into an aqueous solution containing pluronic polymers. After drying and sintering, the aluminum oxide particles formed a highly textured film that was resistant to oil adhesion. Because it is ceramic based,

the films are resistant to acids, bases, and high salt concentrations. Further, when the surface is worn away, it naturally recovers a similar particle distribution size, thus retaining the surface properties. —MSL

ACS Appl. Mater. Interfaces 10.1021/acsami.2c13857 (2022).

CELL BIOLOGY

Liquid-liquid phase secretion

Insulin is a key regulator of human metabolism, and its dysfunction leads to diseases such as type 2 diabetes. How the precursor of insulin, proinsulin, is transferred within the cell from the trans-Golgi network (TGN) to secretory storage granules is unclear. However, chromogranin proteins are known central regulators of secretory granule biosynthesis. Parchure *et al.* found that chromogranins undergo liquid-liquid phase separation at the low pH levels seen in the TGN. The intrinsically disordered N-terminal domain of chromogranin B aids phase separation, which is critical for secretory granule formation. The

liquid chromogranin condensates can thus recruit and sort proinsulin and other cargo molecules in the TGN environment without any need for specific receptors. —SMH

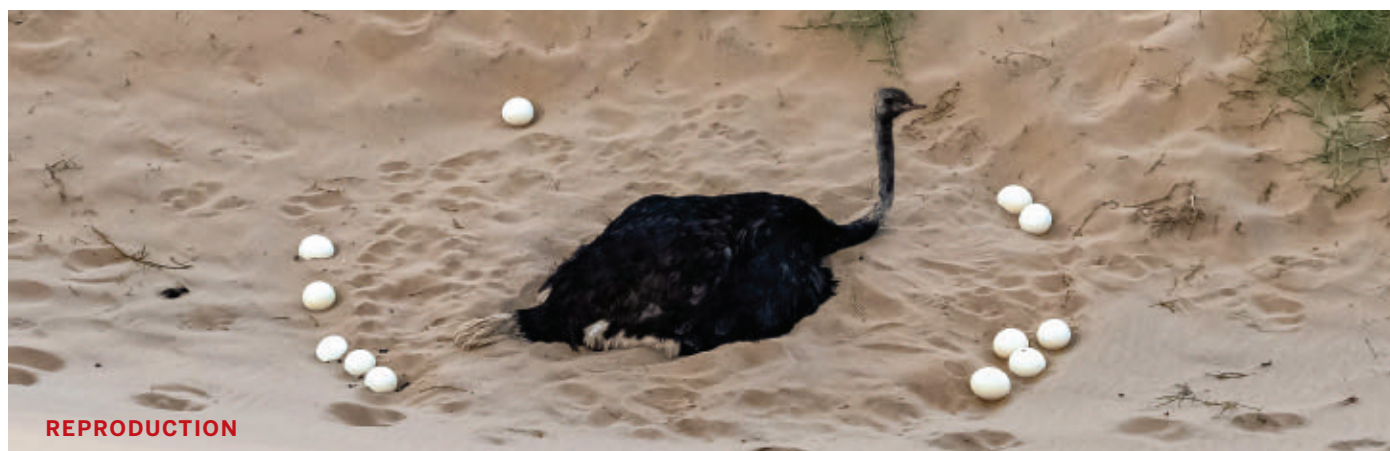
J. Cell Biol. 221, e202206132 (2022).

LITHIUM CHEMISTRY

A quick route to organolithium reagents

Organolithium compounds are essential reagents because of their extraordinarily potent basicity. They are also highly flammable and finicky and therefore a challenge to prepare. Crockett *et al.* report that recrystallization of lithium metal from liquid ammonia ahead of time enhances the rate and reliability of its subsequent reaction with halocarbons to produce these bases. Gradual evaporation of the ammonia resulted in a high-surface-area dendritic morphology of the semicrystalline metal, which reacted readily with a wide range of alkyl, aryl, and vinyl chlorides and bromides. —JSY

J. Am. Chem. Soc. 144, 16631 (2022).



REPRODUCTION

Cooperative ostriches

Many birds breed cooperatively in various ways to reduce the costs of looking after eggs and chicks. For example, as many as 12 unrelated female ostriches may lay eggs in one nest brooded by either sex. Melgar *et al.* investigated what drives the variability in the number of partner adults in an experimental comparison of captive and wild ostriches living under similar conditions. They found that males

needed to ally with about four females to maximize breeding success. Females gained more from cooperation and were most successful when clubbing together in larger groups of up to six individuals. Intermediate group sizes tended to reduce reproductive success in both males and females because of conflicts in the timing of egg laying and incubation and the risk of eggs being trampled by ardent males. —CA *eLife* 11, e77170 (2022).

Ostriches breed cooperatively, with variable numbers of females contributing eggs to one nest.

ALSO IN *SCIENCE* JOURNALS

Edited by Michael Funk

METABOLISM

Why it matters when mice eat

The timing of feeding relative to daily cycles of activity and sleep can determine whether mice fed the same high-fat diet (HFD) become obese. Hepler *et al.* clarified the mechanism behind such differential energy handling (see the Perspective by Lagarde and Kazak). In their experiments, mice fed an HFD consumed during the active phase of their daily cycle (nighttime for a mouse) had greater energy expenditure resulting from the metabolism of food to produce heat. Such thermogenesis depended on the circadian clock of adipocytes and on increased synthesis of creatine, fueling a futile cycle of ATP turnover in the mitochondria of adipocytes. These results help to explain the benefits of time-restricted feeding and how circadian disruption can contribute to metabolic disease. —LBR

Science, ab18007, this issue p. 276;
see also ade6720, p. 251

EVOLUTIONARY BIOLOGY

One cannot have everything

It is well known that there are sex-specific differences in the incidence of various diseases. It is likewise understood that some genes associated with metabolic disease and other medical conditions were likely selected during evolution because they were adaptive under other circumstances. In an example that ties together both of these concepts, Nikkanen *et al.* used mice to show that the hepatic transcription factor BCL6 plays a key role in determining the genetic program active in male versus female mice and hence their survival in different conditions (see the Perspective by Waxman and Kineman). Male mice had a high expression of BCL6, resulting in protection from infection

but vulnerability to metabolic disease, and the opposite was observed in the female mice. —YN

Science, abn9886, this issue p. 290;
see also ade7614, p. 252

CELL BIOLOGY

Oocytes store mRNAs around mitochondria

Mammalian oocytes stop transcribing DNA into messenger RNA (mRNA) during the final stages of their development. The oocyte's meiotic divisions and early embryo development occur in the absence of transcription and rely instead on maternal mRNAs that are stored in the oocyte. However, where and how mammalian oocytes store mRNAs has remained elusive. Cheng *et al.* discovered that mammalian oocytes, including those in humans, store maternal mRNAs around the mitochondria in a membraneless compartment with hydrogel-like properties. The RNA-binding protein ZAR1 drives the assembly of this compartment, which clusters the mitochondria and protects the mRNAs against degradation. —SMH

Science, abq4835, this issue p. 262

OPTICS

Miniaturizing spectrometers

High-resolution spectrometry tends to be associated with bench-sized machines. Recent efforts on computational spectrometers have shown that this physical footprint can be shrunk by using nanowires and two-dimensional (2D) materials, but these devices are often associated with limited performance. Yoon *et al.* developed a single-detector computational spectrometer using an electrically tunable spectral response of a single junction comprising 2D van der Waal materials (see the Perspective by Quereda and

Castellanos-Gomez). The electrically tunable spectral response and high performance of the tiny detector are promising for the further development of computational spectrometers. —ISO

Science, add8544, this issue p. 296;
see also ade6037, p. 250

EVOLUTION

The butterfly's grand ground plan

In the 1920s, biologists proposed that butterfly wing pattern diversity evolved as variations of a ground plan of pattern elements that vary in color, shape, and position between different species. Mazo-Vargas *et al.* found that major aspects of this ground plan are determined by an ancient array of deeply conserved noncoding DNA sequences (see the Perspective by Espeland and Podsiadlowski). These regulatory sequences can have both positive and negative effects, and nuanced interactions between noncoding regions sculpt wing patterns. Deep homology of complex, rapidly evolving traits can thus be reflected in noncoding genomic sequences. —LMZ and DJ

Science, abi9407, this issue p. 304;
see also ade5689, p. 249

CANCER MICROBIOME

A tumorigenic infection

The tumor-associated microbiome can contribute to tumor development and progression. Udayasuryan *et al.* found that *Fusobacterium nucleatum*, an oral commensal that can become an opportunistic pathogen, promotes tumor progression—associated activity in pancreatic ductal adenocarcinoma (PDAC) cells. Infection with *F. nucleatum* induced the release of cytokines that promoted proliferation, migration, and invasion in human PDAC cell lines, but not in normal human pancreatic epithelial cells. An antibody targeting one of the

secreted cytokines inhibited the proliferation of PDAC cells. —LKF
Sci. Signal. **15**, eabn4948 (2022).

IMMUNOTHERAPY

Flipping graft-versus-tumor effects

Allogeneic bone marrow transplantation (alloBMT) is a potentially curative treatment for blood-related cancers, but patients are prone to tumor relapse due to escape from graft-versus-tumor effects, especially when accompanied by systemic immunosuppression. Using a mouse model of myeloma resistant to treatment with alloBMT, Minnie *et al.* found that alloBMT-derived donor T cells became functionally exhausted from exposure to alloantigen rather than tumor antigen. Post-transplant cyclophosphamide depleted alloantigen-driven exhausted T cells, leaving a population bearing a stem cell memory-like gene signature. In leukemia-bearing mice receiving a haploidentical transplant, agonist immunotherapy with an engineered interleukin-18 resistant to endogenous inhibitors enhanced antitumor immunity and improved survival. These results demonstrate that immunotherapy targeting residual T cell populations can improve the graft-versus-tumor response of alloBMT during systemic immunosuppression. —CO

Sci. Immunol. **7**, eabo3420 (2022).

Pushing the Boundaries of Knowledge

As AAAS's first multidisciplinary, open access journal, *Science Advances* publishes research that reflects the selectivity of high impact, innovative research you expect from the *Science* family of journals, published in an open access format to serve a vast and growing global audience. Check out the latest findings or learn how to submit your research: **[ScienceAdvances.org](https://www.scienceadvances.org)**

Science
Advances
AAAS

GOLD OPEN ACCESS, DIGITAL, AND FREE TO ALL READERS

RESEARCH ARTICLE SUMMARY

CELL BIOLOGY

Mammalian oocytes store mRNAs in a mitochondria-associated membraneless compartment

Shiya Cheng[†], Gerrit Altmeyen[†], Chun So, Luisa M. Welp, Sarah Penir, Torben Ruhwedel, Katerina Menelaou, Katarina Harasimov, Alexandra Stützer, Martyn Blayney, Kay Elder, Wiebke Möbius, Henning Urlaub, Melina Schuh*

INTRODUCTION: Mammalian oocytes accumulate a large number of messenger RNAs (mRNAs) through active transcription as they grow. Transcription ceases during the final stages of oocyte growth and only resumes when the embryonic genome is activated after fertilization. During this period, the oocyte and the embryo can only use the stored mRNAs to synthesize new proteins. Proper storage of maternal mRNAs is thus critical for the maturation of oocytes into fertilizable eggs through meiosis and for early embryonic development after fertilization. However, where and how maternal mRNAs are stored in mammalian oocytes, including human oocytes, has remained elusive.

RATIONALE: RNAs are often stored in membraneless compartments that form by spontaneous phase separation of proteins and/or nucleic acids. Previous studies identified different types of membraneless compartments that store mRNAs in non-mammalian oocytes, such as P granules in *Caenorhabditis elegans* and Polar granules in *Drosophila*. We thus set out to identify potential RNA storage compartments in mammalian oocytes.

RESULTS: We analyzed the localization of RNA-binding proteins that were highly expressed in mouse oocytes. We found that the

RNA-binding proteins ZAR1, YBX2, DDX6, LSM14B, and 4E-T (EIF4ENIF1) co-localized with mitochondria, forming clusters throughout the cytoplasm. By contrast, they did not co-localize with the Golgi apparatus, recycling endosomes, or lysosomes, and only partially co-localized with the endoplasmic reticulum. Additionally, we stained mRNAs using RNA fluorescence in situ hybridization and found that they were stored in this mitochondria-associated domain. This domain was also present in oocytes of other mammalian species, including humans. Because this domain was distinct from any known RNA-containing compartment, we named it mitochondria-associated ribonucleoprotein domain, or MARDO for short.

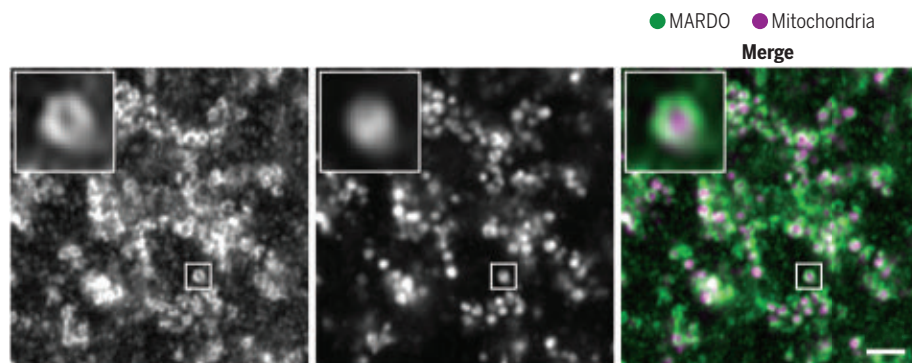
MARDO assembly around mitochondria was directed by an increase in mitochondrial membrane potential during oocyte growth. The MARDO gradually appeared as oocytes grew and became most prominent in full-grown oocytes, the mitochondria of which are also the most active. Among the MARDO-localized RNA-binding proteins, ZAR1 played a major role in the assembly of the MARDO. ZAR1, but not other RNA-binding proteins, promoted the coalescence of MARDO foci into hydrogel-like matrices when overexpressed. MARDO coalescence drove the aggregation of mitochondria into giant clusters. Through a series of

in vivo and in vitro experiments, we found that the unstructured N-terminal domain of ZAR1 was essential for MARDO assembly and its association with mitochondria. We depleted ZAR1 by gene knockout, RNA interference, and Trim-Away and found that both MARDO formation and mitochondrial clustering were impaired. MARDO formation and mitochondrial clustering were restored by expressing ZAR1 in *Zar1*-knockout oocytes. These results confirmed that ZAR1 is essential for MARDO assembly and mitochondrial clustering. Furthermore, live-cell imaging analyses showed that loss of ZAR1 caused severe defects in spindle assembly, chromosome alignment, and cytokinesis during oocyte meiotic maturation.

The MARDO stored translationally repressed mRNAs, some of which are known to become translationally activated during the maturation of oocytes into fertilizable eggs or after fertilization. Loss of ZAR1 not only disrupted the MARDO, but also caused a premature loss of MARDO-localized mRNAs. Maternal mRNAs need to be progressively degraded and replaced by mRNAs transcribed from the embryonic genome to ensure proper embryonic development. The MARDO dissolved during the transition from meiosis I to meiosis II because of proteasomal degradation of ZAR1, which was essential for the timely degradation of maternal mRNAs.

CONCLUSION: In this study, we identified the MARDO, a mitochondria-associated membraneless compartment that stores maternal mRNAs in oocytes of various mammalian species, including humans. Our data reveal how the MARDO coordinates maternal mRNA storage, translation, and degradation to ensure fertility in mammals. The RNA-binding protein ZAR1 promotes MARDO assembly and coalescence into clusters. The MARDO stores translationally repressed mRNAs, some of which are translated during later stages of development. Proteasomal degradation of ZAR1 drives MARDO dissolution in mature eggs to ensure the timely degradation of maternal mRNAs.

Our data also reveal physical and functional interactions between the membraneless MARDO and membrane-bound mitochondria, both of which are maternally contributed compounds that accumulate during oocyte growth. ■



The MARDO in a mouse oocyte. The MARDO (ZAR1, green) assembles around mitochondria (cytochrome c, magenta), where it stores maternal mRNAs. Insets are magnifications of outlined regions showing the accumulation of the MARDO around an individual mitochondrion. Scale bar, 2 μ m.

The list of author affiliations is available in the full article online.

*Corresponding author. Email: melina.schuh@mpinat.mpg.de

[†]These authors contributed equally to this work.

Cite this article as S. Cheng et al., *Science* 378, eabq4835 (2022). DOI: 10.1126/science.abq4835

S READ THE FULL ARTICLE AT
<https://doi.org/10.1126/science.abq4835>

RESEARCH ARTICLE

CELL BIOLOGY

Mammalian oocytes store mRNAs in a mitochondria-associated membraneless compartment

Shiya Cheng^{1†}, Gerrit Altmeyen^{1†}, Chun So¹, Luisa M. Welp², Sarah Penir¹, Torben Ruhwedel³, Katerina Menelaou^{1,4}, Katarina Harasimov¹, Alexandra Stützer², Martyn Blayney⁴, Kay Elder⁴, Wiebke Möbius^{3,5}, Henning Urlaub^{2,6}, Melina Schuh^{1,5*}

Full-grown oocytes are transcriptionally silent and must stably maintain the messenger RNAs (mRNAs) needed for oocyte meiotic maturation and early embryonic development. However, where and how mammalian oocytes store maternal mRNAs is unclear. Here, we report that mammalian oocytes accumulate mRNAs in a mitochondria-associated ribonucleoprotein domain (MARDO). MARDO assembly around mitochondria was promoted by the RNA-binding protein ZAR1 and directed by an increase in mitochondrial membrane potential during oocyte growth. MARDO foci coalesced into hydrogel-like matrices that clustered mitochondria. Maternal mRNAs stored in the MARDO were translationally repressed. Loss of ZAR1 disrupted the MARDO, dispersed mitochondria, and caused a premature loss of MARDO-localized mRNAs. Thus, a mitochondria-associated membraneless compartment controls mitochondrial distribution and regulates maternal mRNA storage, translation, and decay to ensure fertility in mammals.

In mammals such as humans and mice, transcription ceases during the final stages of oocyte growth and only resumes when the embryonic genome is activated after fertilization (1–3). During this period, the oocyte and the embryo can only use stored mRNAs to synthesize new proteins. The proper storage of maternal mRNAs is thus critical for generating mature, haploid eggs through meiosis and for early embryonic development after fertilization (4).

RNAs often accumulate in membraneless compartments that form by phase separation (5–8). Membraneless RNA storage compartments have been well characterized in non-mammalian oocytes, but less so in oocytes from mammals. For instance, P granules have been described in *Caenorhabditis elegans* oocytes (9, 10), polar granules in *Drosophila* oocytes (11–13), and the Balbiani body in *Xenopus* and zebrafish oocytes (14, 15). The Balbiani body is present in the early stages of human oocyte development but is absent at later stages (16). Mouse oocytes contain large, P-body-like granules during the early stages of development, but these are dispersed as oocytes grow larger

(17, 18). Thus, it is still unknown where and how maternal mRNAs are stored in full-grown human and mouse oocytes. Previous studies had established that RNA-binding proteins such as YBX2 (17, 19, 20) and ZAR1 (21) are required for maternal mRNA storage in full-grown mouse oocytes. Several RNA-binding proteins have been suggested to be enriched in the cortex of mouse oocytes (17). Nevertheless, the exact localization of maternal mRNAs and the mechanism that stores them remain elusive.

Results

Identification of a mitochondria-associated RNA storage compartment in mammalian oocytes

To identify an mRNA storage compartment in mammalian oocytes, we performed a localization screen in full-grown mouse oocytes. First, we analyzed the potential co-localization between highly expressed RNA-binding proteins and different types of membrane-bound organelles, including mitochondria, endoplasmic reticulum (ER), Golgi apparatus, recycling endosomes, and lysosomes (Fig. 1, A to V, and fig. S1, A to I). We found that the RNA-binding proteins ZAR1 (21–24), YBX2 (19, 20, 25, 26), DDX6 (18), LSM14B (27), and 4E-T (EIF4ENIF1) (28) co-localized with mitochondria, forming clusters that were distributed throughout the oocyte cytoplasm (Fig. 1, A and B, and fig. S1, B to I). High-resolution images revealed that ZAR1 accumulated around mitochondria (Fig. 1, C and D).

Next, we investigated whether mRNAs co-localize with RNA-binding proteins in proximity to mitochondria. Indeed, RNA-fluorescence in situ hybridization (RNA-FISH) indicated that ZAR1 also co-localized with mRNAs that contain a poly(A) tail (Fig. 1, E and F, and fig. S1,

J and K). Consistent with this observation, ZAR1 co-localized with the poly(A)-binding protein PABPCIL (29, 30) (fig. S1, L and M). ZAR1 also co-localized with the other four RNA-binding proteins, YBX2, DDX6, LSM14B, and 4E-T (Fig. 1, G to N). Collectively, these results indicate that both mRNAs and RNA-binding proteins accumulate around mitochondria in mouse oocytes.

By contrast, ZAR1 did not associate with the Golgi apparatus, recycling endosomes, or lysosomes, and associated with only a fraction of ER tubules (Fig. 1, O to V, and fig. S1N). The specific association between ZAR1 and mitochondria was further confirmed by a proximity ligation assay (PLA): Many more PLA spots were observed when ZAR1 was ligated to a mitochondrial marker than to a recycling endosome marker (Fig. 1, W and X).

ZAR1 and other RNA-binding proteins also accumulated around mitochondria in human, porcine, and bovine oocytes (Fig. 1Y and fig. S2). Similar to mouse oocytes, RNA-binding proteins and mitochondria formed clusters throughout the cytoplasm in these mammalian oocytes.

Thus, maternal mRNAs and RNA-binding proteins are mainly deposited around mitochondria in oocytes of various mammalian species, including humans. Because this domain is distinct from any known RNA-containing compartment (31, 32), we named it “mitochondria-associated ribonucleoprotein domain” (MARDO).

MARDO formation depends on an increase in mitochondrial membrane potential during oocyte growth

To investigate when the MARDO forms, we performed immunostaining for ZAR1 and mitochondria on oocytes at different growth stages. The MARDO gradually appeared as oocytes grew larger and was most prominent in full-grown “surrounded nucleolus” (SN) oocytes, so called because their nucleoli are surrounded by chromatin (Fig. 2, A to I, and fig. S3, A and B). PLA confirmed that the association of ZAR1 with mitochondria increased during oocyte growth (fig. S3, C and D). Coincidentally, the mitochondrial membrane potential also increased during oocyte growth and reached a maximum in SN oocytes (Fig. 2, J and K). We thus investigated whether MARDO formation required the increased mitochondrial membrane potential by treating oocytes with different mitochondrial inhibitors. Mitochondria were completely or partially depolarized in oocytes treated with antimycin A, carbonyl cyanide *p*-trifluoromethoxyphenylhydrazone (FCCP), or oligomycin A (fig. S3, E to G). Moreover, the MARDO was disrupted when oocytes were treated with any of these inhibitors (Fig. 2, L and M, and fig. S3, H and I), implying that the increase in mitochondrial membrane potential during oocyte growth is essential for

¹Department of Meiosis, Max Planck Institute for Multidisciplinary Sciences, Göttingen, Germany.

²Bioanalytical Mass Spectrometry Group, Max Planck Institute for Multidisciplinary Sciences, Göttingen, Germany.

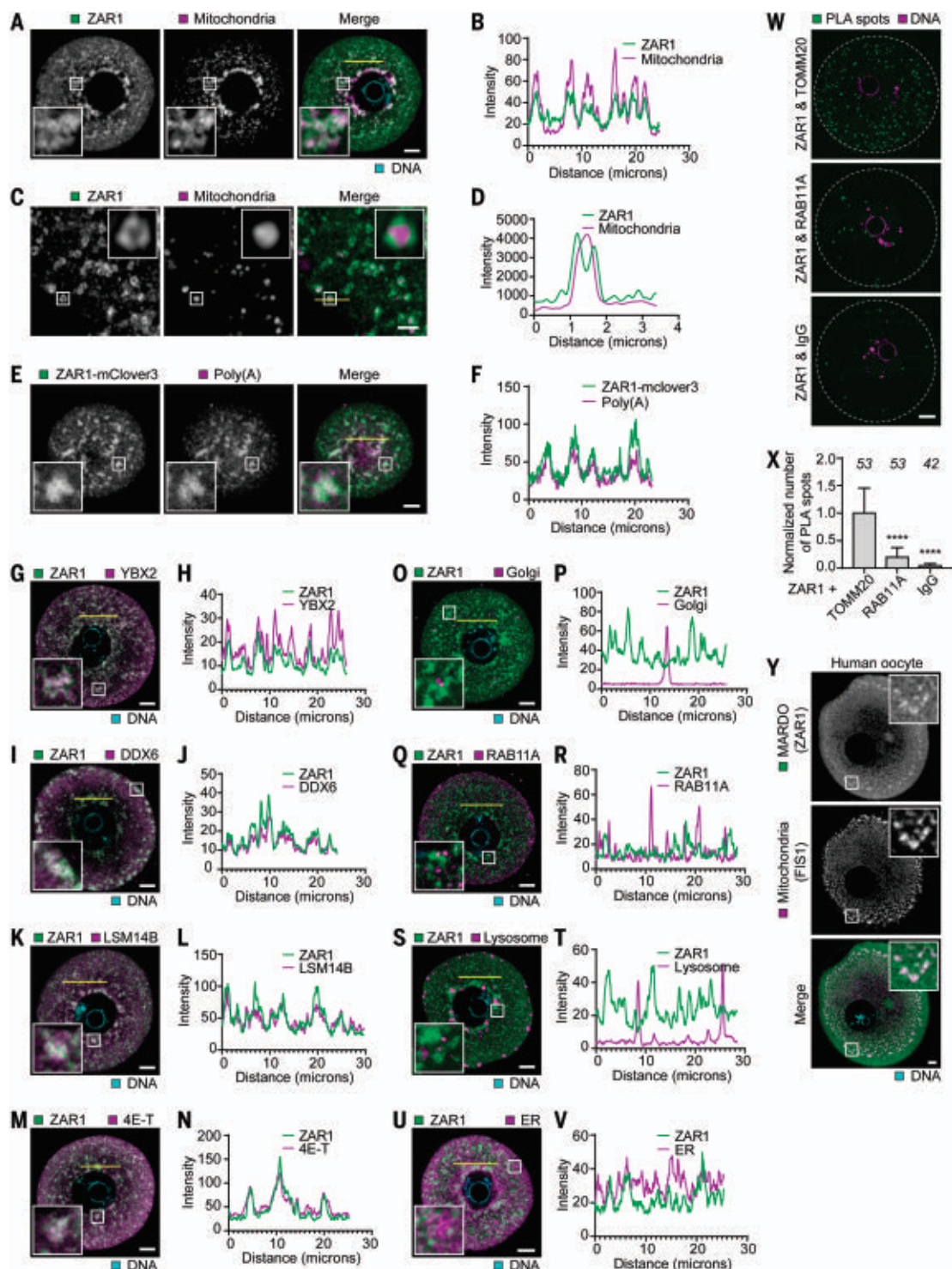
³Electron Microscopy City Campus, Department of Neurogenetics, Max Planck Institute for Multidisciplinary Sciences, Göttingen, Germany. ⁴Bourn Hall Clinic, Cambridge, UK. ⁵Cluster of Excellence “Multiscale Bioimaging: from Molecular Machines to Networks of Excitable Cells” (MBExC), University of Göttingen, Göttingen, Germany. ⁶Bioanalytics Group, Institute for Clinical Chemistry, University Medical Center Göttingen, Göttingen, Germany.

*Corresponding author. Email: melina.schuh@mpinat.mpg.de

†These authors contributed equally to this work.

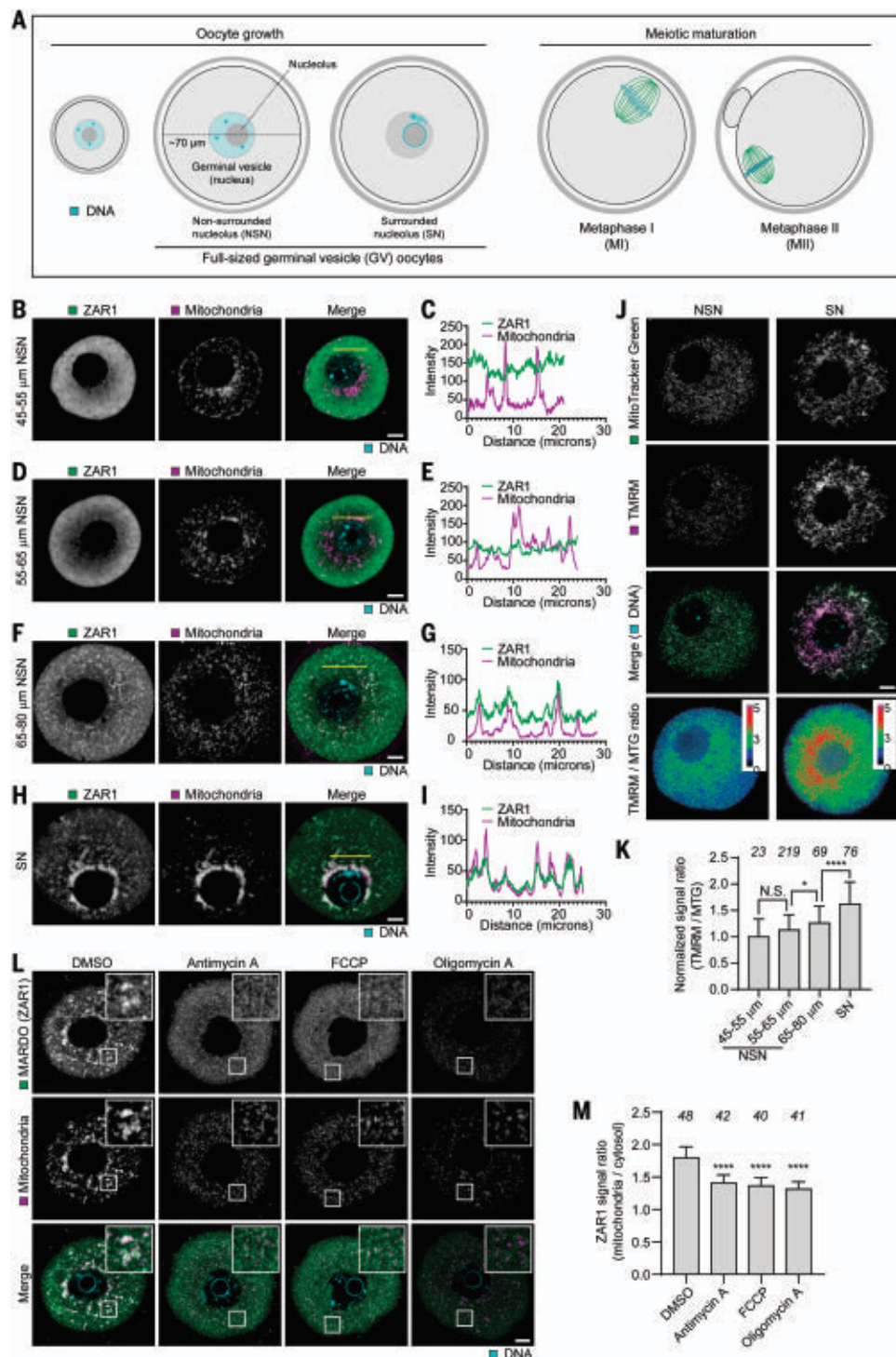
Fig. 1. Identification of a mitochondria-associated RNA storage compartment in mammalian oocytes.

(A) Representative immunofluorescence images of mouse GV oocytes. Green, ZAR1; magenta, mitochondria (cytochrome c); cyan, DNA (Hoechst 33342). Insets are magnifications of out-lined regions. (B) Intensity profiles of ZAR1 and mitochondria (cytochrome c) along the yellow line in (A). (C) Representative immunofluorescence Airyscan images of mouse GV oocytes. Green, ZAR1; magenta, mitochondria (cytochrome c). Insets are magnifications of outlined regions. Scale bar, 2 μ m. (D) Intensity profiles of ZAR1 and mitochondria (cytochrome c) along the yellow line in (C). (E) Representative RNA-FISH images of mouse GV oocytes. Green, ZAR1-mClover3; magenta, mRNAs with a poly(A) tail [5'-Cy5-Oligo d(T)30]. Insets are magnifications of outlined regions. (F) Intensity profiles of ZAR1-mClover3 and mRNAs [5'-Cy5-Oligo d(T)30] along the yellow line in (E). (G to N) Representative immunofluorescence images of mouse GV oocytes [(G), (I), (K), and (M)]. Green, ZAR1; magenta, YBX2 (G), DDX6 (I), LSM14B (K), 4E-T (M); cyan, DNA (Hoechst 33342). Insets are magnifications of outlined regions. Intensity profiles along the yellow lines are shown in (H), (J), (L), and (N), respectively. (O to V) Representative immunofluorescence images of mouse GV oocytes [(O), (Q), (S), and (U)]. Green, ZAR1; magenta, Golgi apparatus (GM130) (O), RAB11A-positive recycling endosomes (Q), lysosomes (LAMP1) (S), ER (BCAP31) (U); cyan, DNA (Hoechst 33342). Insets are magnifications of outlined regions. Intensity profiles along the yellow lines are shown in (P), (R), (T), and (V), respectively. (W) Representative images of in situ PLA performed with antibody pairs anti-ZAR1 and anti-TOMM20, anti-ZAR1 and anti-RAB11A, or anti-ZAR1 and IgG control in mouse GV oocytes. Green, PLA spots; magenta, DNA (Hoechst 33342). Dashed lines demarcate the oocytes.



(X) Quantification and normalization of the number of PLA spots. The data were normalized by dividing the values of each group by the mean of the first group (ZAR1 and TOMM20). (Y) Representative immunofluorescence images of human GV oocytes. Green, MARD0 (ZAR1); magenta, mitochondria (FIS1); cyan, DNA (Hoechst 33342). Insets are magnifications of outlined regions. The number of analyzed oocytes is specified in *italics* in (X). Data are shown as mean \pm SD. *P* values were calculated using one-way ANOVA with Tukey's post hoc test. Scale bars, 10 μ m unless otherwise specified.

Fig. 2. MARDO formation is directed by an increase in mitochondrial membrane potential during oocyte growth. (A) Schematic representation of oocyte growth and meiotic maturation. (B to I) Representative immunofluorescence images of mouse oocytes at different growth stages. Representative nonsurrounded nucleolus (NSN) oocytes with diameters between 45 and 55, 55 and 65, and 65 and 80 μm are shown in (B), (D), and (F), respectively. A representative SN oocyte is shown in (H). Green, ZAR1; magenta, mitochondria (cytochrome c); cyan, DNA (Hoechst 33342). Intensity profiles along the yellow lines are shown in (C), (E), (G), and (I), respectively. (J) Representative fluorescence images of similarly sized NSN and SN mouse oocytes stained with MitoTracker Green (MTG, green), the membrane potential-sensitive dye TMRM (magenta), and SIR-DNA (cyan). Fluorescence intensity ratios of TMRM to MitoTracker Green are shown with rainbow RGB pseudocolors. (K) Quantification of the fluorescence intensity ratio of TMRM to MitoTracker Green on mitochondria in mouse oocytes at different growth stages. The data were normalized by dividing the values of each group by the mean of the first group (NSN oocytes, 45 to 55 μm). (L) Representative immunofluorescence images of mouse GV oocytes treated with DMSO, 5 $\mu\text{g}/\text{ml}$ antimycin A, 5 μM FCCP, or 5 $\mu\text{g}/\text{ml}$ oligomycin A. Green, MARDO (ZAR1); magenta, mitochondria (COX17); cyan, DNA (Hoechst 33342). Insets are magnifications of outlined regions. (M) Quantification of the ratio of mean ZAR1 intensity on mitochondria to that in the cytosol under different treatments. The number of analyzed oocytes is specified in italics. Data are shown as mean \pm SD. *P* values were calculated using one-way ANOVA with Tukey's post hoc test. Scale bars, 10 μm .



MARDO formation. To further investigate the requirement of mitochondrial polarization in MARDO assembly, we tracked the accumulation of newly synthesized mScarlet-tagged ZAR1 around mitochondria labeled with mitochondria-targeted enhanced green fluorescent protein (Mito-EGFP). The accumulation of ZAR1 around mitochondria was significantly lower in FCCP-treated oocytes than in control oocytes, with similar total levels of ZAR1 (fig. S3, J to M). Thus,

MARDO formation is directed by an increase in mitochondrial membrane potential during oocyte growth.

ZAR1 promotes MARDO coalescence and mitochondrial clustering

The MARDO and mitochondria form clusters throughout the cytoplasm (Fig. 1, A to D and Y, and figs. S1, B to I, and S2). To investigate which MARDO component can promote clus-

ter formation, we overexpressed mScarlet fusions of the RNA-binding proteins with Mito-EGFP in mouse oocytes. By comparing the ratio of signal on mitochondria to signal in the cytosol, we found that ZAR1 was the most highly enriched protein on mitochondria, followed by LSM14B (Fig. 3, A to D, and fig. S4). ZAR1-mScarlet and mitochondria coalesced into huge clusters, whereas YBX2-Scarlet, DDX6-Scarlet, LSM14B-mScarlet, 4E-T-mScarlet, and

Fig. 3. ZAR1 drives MARDO coalescence and mitochondrial clustering.

(A) Representative fluorescence images of mouse GV oocytes expressing Mito-EGFP (mitochondria, green) and ZAR1-mScarlet (magenta). The dashed line demarcates the oocyte.

(B) Representative Airyscan fluorescence images of mouse GV oocytes expressing Mito-EGFP (mitochondria, green) and ZAR1-mScarlet (magenta). Scale bar, 2 μ m.

(C) Representative fluorescence images of mouse GV oocytes expressing Mito-EGFP (mitochondria, green) and mScarlet (magenta).

(D) Quantification of the signal ratio of indicated proteins on mitochondria (Mito-EGFP) to that in the cytosol.

(E) Quantification of the mitochondrial (Mito-EGFP) clustering index when the indicated proteins are overexpressed in mouse GV oocytes.

(F) Representative stills from time-lapse movies of mouse GV oocytes expressing Mito-EGFP (mitochondria, green) and ZAR1-mScarlet (magenta). Arrows highlight fusing MARDO-mitochondria clusters. Dashed lines highlight fused MARDO-mitochondria clusters. Scale bar, 2 μ m.

(G) Partial bleaching of ZAR1-mScarlet in the MARDO in mouse GV oocytes. The bleached area is outlined by the dashed box. Scale bar, 2 μ m.

(H) FRAP analysis of ZAR1-mScarlet in the MARDO. Scale bar, 2 μ m.

(I) Quantification of the FRAP experiment in (H). (J) Domain organization of mouse ZAR1 showing the disordered region predicted by IUPred2.

(K) Representative fluorescence images of mouse GV oocytes expressing Mito-EGFP (mitochondria, green) and ZAR1(1-263)-mScarlet (magenta).

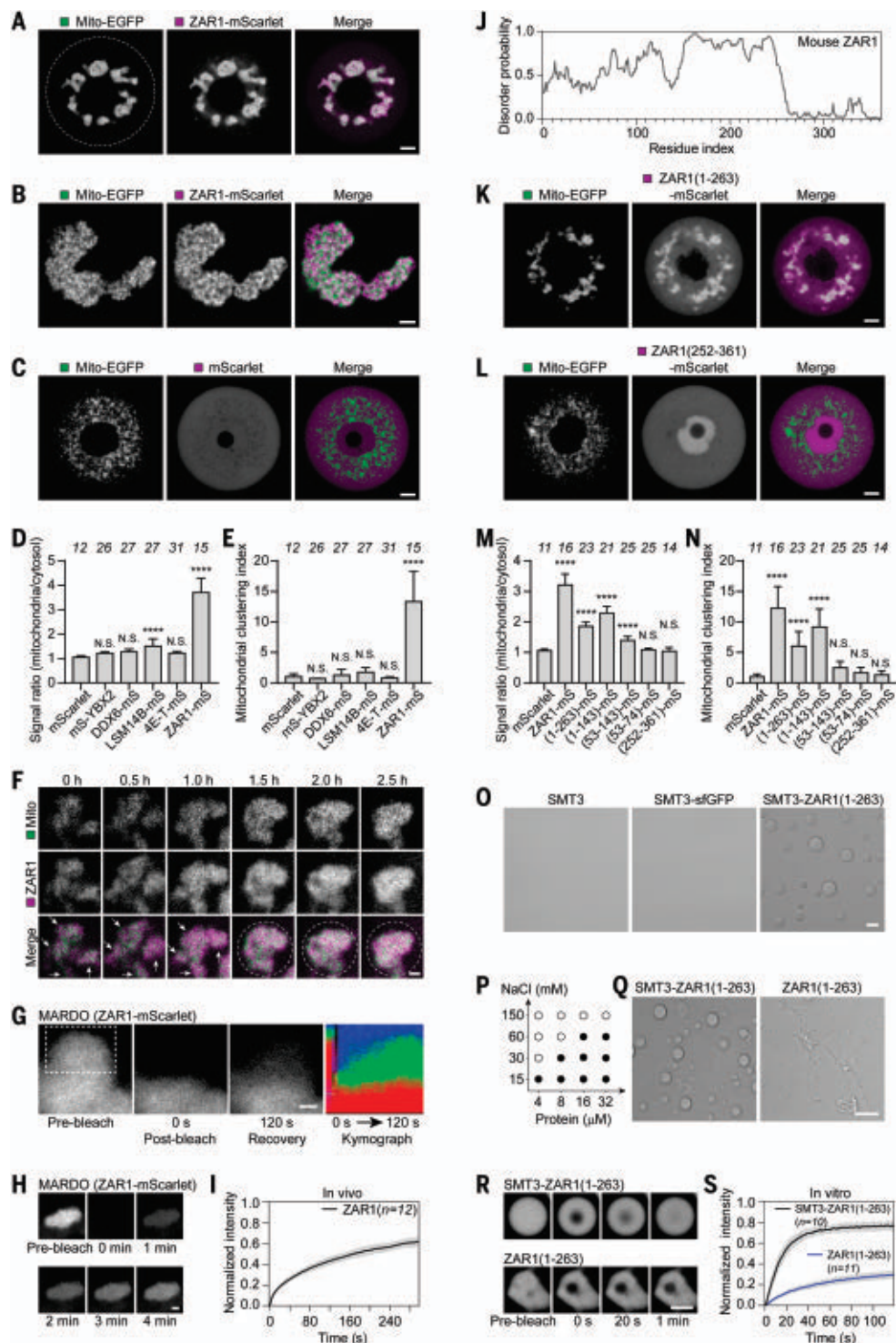
(L) Representative fluorescence images of mouse GV oocytes expressing Mito-EGFP (mitochondria, green) and ZAR1(252-361)-mScarlet (magenta).

(M) Quantification of the signal ratio of indicated proteins on mitochondria (Mito-EGFP) to that in the cytosol.

(N) Quantification of the mitochondrial (Mito-EGFP) clustering index when the indicated proteins are overexpressed in mouse GV oocytes.

(O) Representative bright-field images of SMT3 or SMT3-sfGFP solutions and SMT3-ZAR1(1-263) droplets formed by phase separation in vitro.

The protein concentrations of SMT3 and SMT3-sfGFP are both 32 μ M. The protein concentration of SMT3-ZAR1(1-263) is 8 μ M. The buffer is 50 mM HEPES, pH 7.4, 30 mM NaCl, and 2 mM DTT. (P) Phase separation of SMT3-ZAR1(1-263) at different protein concentrations and under different salt conditions. Solid dot represents phase separation. Hollow dot represents no phase separation. The buffer contains 50 mM HEPES, pH 7.4, and 2 mM DTT. (Q) Representative bright-field images of SMT3-ZAR1(1-263) droplets and ZAR1(1-263) hydrogels. The nonspherical morphology of ZAR1(1-263) condensate is due to incomplete fusion. The protein concentrations are



both 40 μ M. The buffer is 50 mM HEPES, pH 7.4, 150 mM NaCl, 2 mM DTT, and 10% Ficoll 400. (R) FRAP analysis of SMT3-ZAR1(1-263) droplets and ZAR1(1-263) hydrogels. The protein concentrations are both 40 μ M, with 2% of proteins conjugated by Alexa Fluor 488. The buffer is 50 mM HEPES, pH 7.4, 150 mM NaCl, 2 mM DTT, and 10% Ficoll 400. Scale bar, 2 μ m. (S) Quantification of the FRAP experiment in (R). The number of analyzed oocytes [(D), (E), (M), and (N)] or FRAP experiments [(I) and (S)] is specified in italics. Data are shown as mean \pm SD. *P* values were calculated using one-way ANOVA with Tukey's post hoc test. Scale bars, 10 μ m unless otherwise specified.

mScarlet alone had no significant effect on mitochondrial clustering, which was measured by calculating the reciprocal of cluster number (Fig. 3, A to C and E; fig. S4; and movie S1). High-resolution images revealed that ZAR1 intermingled with mitochondria (Fig. 3B and movie S2). Prominent mitochondrial clusters were also observed by electron microscopy of oocytes overexpressing ZAR1 (fig. S5, A and B). ZAR1 localization to interstitial spaces within the mitochondrial cluster was confirmed by immunoelectron microscopy (fig. S5, C to F). Thus, ZAR1 can promote MARDO coalescence and mitochondrial clustering in mouse oocytes.

The coalesced MARDO in ZAR1-overexpressing oocytes also contained mitochondria (fig. S6, A and B) but was largely devoid of other organelles such as the Golgi apparatus, recycling endosomes, lysosomes, and ribosomes (fig. S6, C to F). Some ER tubules were localized in the coalesced MARDO in association with mitochondria, but most were outside of the MARDO (figs. S5B and S6G). These results further suggest that the MARDO is a mitochondria-associated compartment. In addition, randomly localized cytoplasmic proteins were not enriched in the coalesced MARDO but rather were partially excluded from this region (fig. S6, H and I).

The disordered N-terminal region of ZAR1 drives MARDO coalescence

Given that MARDO foci had the capacity to coalesce and promote mitochondrial clustering (Fig. 3F and movie S3), we considered that this process occurs through phase separation. When ZAR1-mScarlet was partially photobleached in the coalesced MARDO, nonbleached ZAR1-mScarlet diffused into the bleached region (Fig. 3G). This diffusion indicates internal rearrangement, which is a hallmark of a phase-separated compartment. MARDO coalescence and the signal recovery of ZAR1-mScarlet after photobleaching were both slow (Fig. 3, F to I), consistent with hydrogel-like rather than liquid-like properties. The MARDO was destroyed in oocytes treated with 1,6-hexanediol (fig. S7, A to C), suggesting that MARDO formation requires weak hydrophobic interactions.

It was previously reported that RNA reduces, whereas RNase treatment enhances, the phase separation behavior of prion-like RNA-binding proteins (33). We found that injecting RNase promoted MARDO coalescence and mitochondrial clustering (fig. S7, D and E), similar to ZAR1 overexpression. Mitochondrial clustering occurred within 4 minutes after RNase injection, which excludes the possibility that RNase acted by affecting translation and the amounts of intracellular proteins (fig. S7F and movie S4). This result further suggests that the MARDO is a phase-separated compartment, and its coalescence is regulated by RNA levels.

On the basis of our findings that MARDO coalescence is driven by ZAR1 and that the MARDO shows some characteristics of phase-separated compartments, we considered that ZAR1 drives phase separation. ZAR1 has an unstructured domain at the N terminus and a structured RNA-binding domain at the C terminus (21–23, 34) (Fig. 3J). We expressed truncation mutants of ZAR1 in mouse oocytes and found that the unstructured N-terminal domain of ZAR1 was both necessary and sufficient for promoting MARDO coalescence and mitochondrial clustering (Fig. 3, K to N, and fig. S7H). We then purified the N-terminal domain of ZAR1 [ZAR1(1–263)], and found that it could phase-separate on its own in vitro (Fig. 3, O and P). ZAR1(1–263) formed hydrogel-like condensates with slow recovery after photobleaching, which resembled the behavior of coalesced MARDO in vivo (Fig. 3, Q to S). By contrast, ZAR1(1–263) fused to the small ubiquitin-related modifier (SUMO) tag SMT3, which increases protein solubility, formed liquid-like condensates with rapid signal recovery after photobleaching (Fig. 3, Q to S). Together, our data indicate that the N-terminal region of ZAR1, which can undergo phase separation, promotes the coalescence of the MARDO into a hydrogel-like matrix that sequesters mitochondria.

Proteasomal degradation of ZAR1 underlies MARDO dissolution during oocyte meiotic maturation

Full-grown oocytes contain a large nucleus referred to as germinal vesicle (GV) and are arrested in prophase I of meiosis until a surge of luteinizing hormone initiates the resumption of meiosis (Fig. 2A). Subsequently, the GV oocyte matures into a fertilizable egg by undergoing the first meiotic division, a process referred to as oocyte meiotic maturation (Fig. 2A). To investigate the dynamics of the MARDO when oocytes resume meiosis, we stained ZAR1 in oocytes at different stages of meiotic maturation (Fig. 2A). ZAR1 was progressively depleted from the mitochondria during oocyte meiotic maturation, suggesting that the MARDO was progressively disassembled (Fig. 4, A and B). Consistent with previous studies (35, 36), mitochondria were clustered around the spindle during metaphase I (MI) but were dispersed during metaphase II (MII) (Fig. 4, A and C). Moreover, we found that mitochondrial dispersion was concomitant with MARDO dissolution in MII oocytes (Fig. 4, A to C).

Phosphorylation is a well-known mechanism for regulating the assembly and disassembly of membraneless compartments (37). Through mass spectrometry (MS) analysis of GV and MI oocytes, we established a dataset of protein phosphorylation during this transition. Many more phosphorylated proteins were identified in MI oocytes than in GV oocytes, implying that

phosphorylation is critical for meiotic progression (data S1). We found that MARDO proteins such as DDX6, 4E-T, LSM14B, YBX2 [also reported in (38)], and ZAR1 were phosphorylated when oocytes resumed meiosis (fig. S8A and data S2). Phosphorylation of ZAR1 in oocytes that resumed meiosis was further confirmed by lambda protein phosphatase treatment using a universal ZAR1 antibody and an antibody that only recognizes nonphosphorylated ZAR1 (fig. S8, B to G). Moreover, treating oocytes with the CDK1 inhibitor RO-3306 just after nuclear envelope breakdown affected ZAR1 phosphorylation (fig. S8H), whereas the proteasome inhibitor MG-132 or the MEK1/2 inhibitor U0126 had no effect (fig. S8I), suggesting that ZAR1 is phosphorylated by CDK1 during oocyte meiotic maturation. Phosphorylation of ZAR1 by CDK1 was confirmed by an in vitro phosphorylation assay (fig. S9A). Two phosphorylation sites, T154 and S161, were identified both in vivo and in vitro (figs. S8A and S9A and data S2), and mutations at these two sites fully blocked the electrophoretic mobility shift of ZAR1 when oocytes resumed meiosis (fig. S9, B to D). However, similar to wild-type ZAR1, the phosphomimetic variants of ZAR1 [ZAR1(T154D, S161D)] still triggered MARDO coalescence in GV oocytes (fig. S9, E and F), suggesting that phosphorylation does not regulate MARDO dynamics.

We then observed that dissolution of the MARDO was accompanied by a decrease in ZAR1 protein levels (Fig. 4, A, D, and E). The decrease of ZAR1 protein during oocyte meiotic maturation was also observed in a previous study (27). Live imaging analysis indicated that MARDO dissolution occurred during the transition from MI to MII (Fig. 4F and movie S5). Furthermore, when ZAR1 was overexpressed, MARDO dissolution was delayed, whereas polar body extrusion was not significantly affected (Fig. 4F, movie S6, and fig. S10A). We hypothesized that the decrease in ZAR1 protein levels and MARDO dissolution require proteasome-mediated degradation of ZAR1. Consistent with this hypothesis, treating oocytes with the proteasome inhibitor MG-132 blocked both ZAR1 degradation and MARDO dissolution (Fig. 4, E, G, and H). To exclude the possibility that impaired MARDO dissolution was caused by MI arrest upon MG-132 treatment (39), we also treated oocytes with nocodazole, which depolymerizes microtubules and impairs spindle assembly, causing a cell cycle arrest before reaching MI. We found that nocodazole treatment had no effect on MARDO dissolution (Fig. 4, G and H), indicating that MARDO dissolution occurs independently of cell cycle progression. In addition, we artificially delayed MARDO dissolution by overexpressing ZAR1 (Fig. 4F) and added MG-132 only upon completion of the first meiotic division. In contrast to LSM14B,

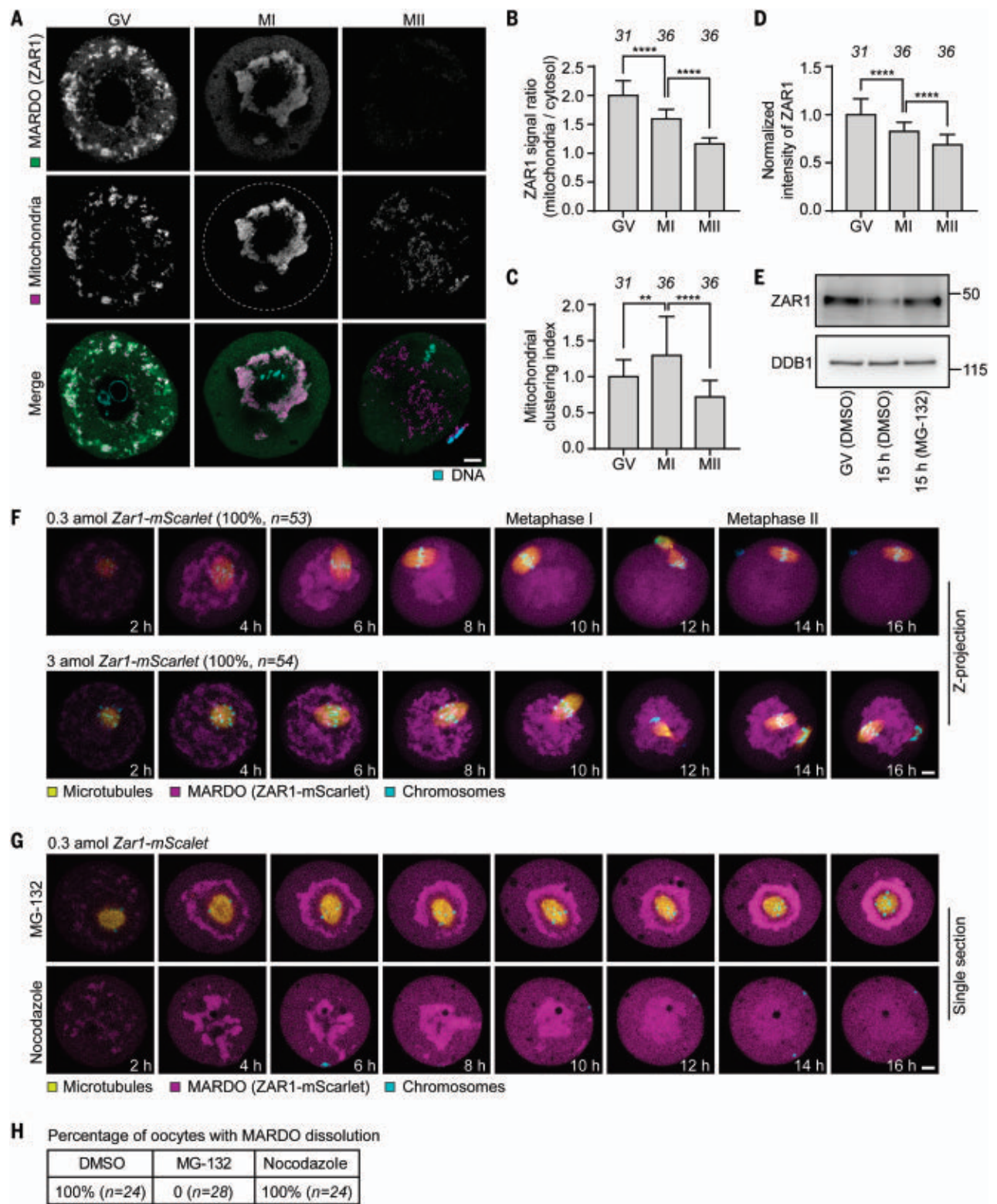


Fig. 4. Proteasome-mediated degradation of ZAR1 promotes MARDO dissolution during oocyte meiotic maturation. (A) Representative immunofluorescence images of mouse oocytes at different stages of meiosis. Green, MARDO (ZAR1); magenta, mitochondria (COX17); cyan, DNA (Hoechst 33342). The dashed line demarcates the oocyte. (B) Quantification of the ratio of mean ZAR1 intensity on mitochondria to that in the cytosol. (C) Quantification of the mitochondrial clustering index (D) Quantification of the mean fluorescence

intensity of ZAR1 (E) Western blot analyses showing the expression of ZAR1 at different stages of meiosis. GV (DMSO), oocytes were kept with dbcAMP and DMSO for 15 hours; 15 h (DMSO), oocytes were treated with DMSO for 15 hours after washout of dbcAMP; 15 h (MG-132), oocytes were treated with 10 μ M MG-132 for 15 hours after washout of dbcAMP. DDB1 was used as a loading control. (F) Representative stills from time-lapse movies of mouse oocytes microinjected with 0.3 or 3 amol *Zar1-mScarlet* mRNA. Brightness of scans was individually

adjusted. Yellow, microtubules (mClover3-MAP4-MTBD); magenta, MARDO (ZAR1-mScarlet); cyan, chromosomes (H2B-miRFP670). Time is given as hours after washout of dbcAMP. The percentage of oocytes with representative pattern is shown in brackets. “*n*” indicates the number of analyzed oocytes. Z projections, 11 sections every 6 μm . **(G)** Representative stills from time-lapse movies of mouse oocytes with 0.3 amol ZAR1-mScarlet mRNA injected. DMSO, MG-132, or

nocodazole was added to the culture medium 2 hours after washout of dbcAMP. Time is given as hours after washout of dbcAMP. **(H)** Percentage of oocytes with MARDO dissolution treated with DMSO, 10 μM MG-132, or 10 μM nocodazole. “*n*” indicates the number of analyzed oocytes. The number of analyzed oocytes is specified in italics in (B), (C), and (D). Data are shown as mean \pm SD. *P* values were calculated using one-way ANOVA with Tukey’s post hoc test. Scale bars, 10 μm .

the levels of which remained largely constant after reaching a maximum, overexpressed ZAR1 was still gradually reduced in MII oocytes, and MG-132 treatment of MII oocytes blocked the degradation of overexpressed ZAR1 and the dissolution of the MARDO (fig. S10, B to E). Thus, proteasomal degradation of ZAR1 promotes MARDO dissolution during the MI-MII transition, and this degradation is independent of cell cycle progression.

Loss of ZAR1 disrupts MARDO formation and mitochondrial clustering

To confirm that ZAR1 is essential for MARDO assembly and mitochondrial clustering in oocytes, we established *Zar1*-knockout mice (Fig. 5A and fig. S11, A and B). The ratio of YBX2 on mitochondria to that in the cytosol was reduced in *Zar1*-knockout oocytes compared with wild-type controls, suggesting that MARDO is disrupted (Fig. 5, A and B). In addition, mitochondria were more dispersed in the knockout oocytes (Fig. 5, A and C). These phenotypes were most prominent in MI oocytes: The MARDO and mitochondria were clustered around the MI spindle in controls but completely dispersed in the absence of ZAR1 (Fig. 5, D to F).

Using Mito-EGFP to label mitochondria and LSM14B-mScarlet to label the MARDO, we also observed MARDO disruption and mitochondrial dispersion in live *Zar1*-knockout oocytes (fig. S11, C to F). Disruption of the MARDO in *Zar1*-knockout oocytes was further confirmed by a PLA. The association of MARDO-localized DDX6 with the mitochondrial outer membrane protein TOMM20 was significantly diminished in *Zar1*-knockout oocytes (Fig. 5, G and H). Moreover, we found that poly(A)-positive mRNAs no longer accumulated around mitochondria in *Zar1*-knockout oocytes compared with controls, suggesting that mRNA accumulation around mitochondria requires the MARDO (Fig. 5, I and J). MARDO disruption and mitochondrial dispersion were also observed when *Zar1* mRNA or ZAR1 protein were depleted by RNA interference (RNAi) or Trim-Away (40), respectively (fig. S12, A to G). By contrast, depletion of DDX6 by Trim-Away did not affect MARDO formation and mitochondrial clustering (fig. S12, H to K).

Finally, RNase treatment promoted mitochondrial clustering in wild-type oocytes but not in *Zar1*-knockout oocytes (fig. S12, L to O). Together, our data establish that ZAR1 is es-

sential for MARDO formation and mitochondrial clustering.

To identify the protein domains within ZAR1 that promote MARDO formation, we expressed full-length and truncation mutants of ZAR1 in *Zar1*-knockout oocytes. Both the full-length ZAR1 and the unstructured N-terminal domain of ZAR1 restored mitochondrial clustering (Fig. 5, K and L), consistent with our observation that the N-terminal domain of ZAR1 promoted MARDO coalescence and mitochondrial clustering (Fig. 3, K to S). Full-length ZAR1 was more efficient than the N terminus of ZAR1 in concentrating YBX2 (Fig. 5, K and M), the recruitment of which to the MARDO was RNA dependent (fig. S7G). These results suggest that the unstructured N-terminal domain of ZAR1 forms the scaffold for MARDO assembly around mitochondria, whereas the C-terminal RNA-binding domain of ZAR1 (21–23) promotes the recruitment of mRNAs to the MARDO.

The MARDO stores mRNAs and represses translation

Given that RNA-binding proteins and mRNAs accumulate in the MARDO, we investigated whether loss of ZAR1 and disruption of the MARDO affects mRNA levels. RNA sequencing (RNA-seq) of *Zar1*-knockout oocytes revealed that >1000 mRNAs were reduced by at least 50% (Fig. 6A and data S3), consistent with a previous study in *Zar1/Zar2* double-knockout mice (21). Reverse transcription quantitative polymerase chain reaction (RT-qPCR) confirmed the decreased levels of several of these mRNAs in *Zar1*-knockout oocytes (Fig. 6, A and B). Using single-molecule RNA-FISH (smRNA-FISH), we found that these mRNAs were relatively enriched in the MARDO, unlike the control mRNA *Actin beta* (Fig. 6, C to F, and movie S7). These results suggest that many distinct mRNAs are stored in the MARDO, and that loss of ZAR1 not only disrupts the MARDO but also causes mRNA reduction.

The RNA-seq results also revealed an increase in certain classes of transcripts, including transcripts involved in translation and mitochondrial function (fig. S13 and data S3). Many of the RNA-binding proteins that accumulate in the MARDO are implicated in translational repression (Fig. 1, A and B, and fig. S1, B to I) (19, 22, 23, 28, 41). This, together with the up-regulation of translation-related transcripts in *Zar1*-knockout oocytes, implied a function of ZAR1 and the MARDO in repress-

ing mRNA translation. To further investigate this potential role, we labeled translating ribosomes assembled on mRNAs by performing proximity ligation of RPL24 and phosphor-RPS6 (42). We found that translating ribosomes were mostly excluded from the MARDO (Fig. 6G and fig. S14A). Similarly, electron microscopy showed that polysomes were readily detected throughout the cytoplasm but largely excluded from the MARDO (Fig. 6H). Previous studies showed that ZAR1 repressed translation in *Xenopus* and zebrafish oocytes (22, 23). To confirm that ZAR1 represses translation in mouse oocytes, we performed a translation reporter assay by using the PP7 hairpin-PP7 coat protein (PCP) interaction (43) (Fig. 6I). A reporter mRNA (*mClover3-2 \times PP7*) and the control mRNA *mScarlet* were coinjected with either tandem dimer of PCP (*tdPCP*) (44) or *tdPCP-Zar1*, and the translation of the reporter mRNA was assessed by the signal ratio of mClover3 to mScarlet (Fig. 6, I and J). *tdPCP-Zar1* substantially reduced the translation of the reporter mRNA compared with *tdPCP* in GV oocytes (Fig. 6, J and K), indicating that ZAR1 represses the translation of bound mRNA. Similarly, *tdPCP-LSM14B* also represses translation (Fig. 6L). Collectively, these data indicate that maternal mRNAs stored in the MARDO are translationally repressed.

Many mRNAs are known to be stored in a dormant state during oocyte growth and are translationally activated when the oocyte resumes meiosis or after fertilization (45–47). We found that some of these known mRNAs were prematurely lost in *Zar1*-knockout oocytes (fig. S14B and data S4). Previous work established that *Zar1*-knockout oocytes progress through meiosis with defects and arrest soon after fertilization, resulting in female infertility (21, 48, 49). We performed live-cell imaging and found that *Zar1*-knockout oocytes have severe defects in spindle assembly, chromosome alignment, and cytokinesis (fig. S14, C to I, and movies S8 to S10). The premature loss of mRNAs in *Zar1*-knockout oocytes may contribute to these meiotic and embryonic developmental defects (21, 48, 49).

MARDO dissolution is essential for timely maternal mRNA degradation during oocyte meiotic maturation

Approximately 79% of maternal mRNAs are degraded during oocyte meiotic maturation (Fig. 2A), which may be achieved through translational activation of mRNA decay factors

Fig. 5. ZAR1 is essential for MARDO assembly and mitochondrial clustering.

(A) Representative immunofluorescence images of GV oocytes collected from *Zar1*^{+/+} and *Zar1*^{-/-} mice. Yellow, ZAR1; magenta, MARDO (YBX2); cyan, mitochondria (cytochrome c). Insets are magnifications of outlined regions. The dashed line demarcates the oocyte.

(B) Quantification of the ratio of mean YBX2 intensity on mitochondria to that in the cytosol.

(C) Quantification of the mitochondrial clustering index.

(D) Representative immunofluorescence images of MI oocytes collected from *Zar1*^{+/+} and *Zar1*^{-/-} mice. Yellow, ZAR1; magenta, MARDO (YBX2); cyan, mitochondria (cytochrome c). Insets are magnifications of outlined regions. Dashed lines demarcate the oocyte.

(E) Quantification of the ratio of mean YBX2 intensity on mitochondria to that in the cytosol.

(F) Quantification of the mitochondrial clustering index.

(G) Representative images of in situ PLA performed with antibody pairs anti-TOMM20 and anti-DDX6 or anti-TOMM20 and IgG control in GV oocytes collected from *Zar1*^{+/+} and *Zar1*^{-/-} mice. Green, PLA spots; magenta, DNA (Hoechst 33342). Dashed lines demarcate the oocytes.

(H) Quantification and normalization of the number of PLA spots. The data were normalized by dividing the values of each group by the mean of the first group (PLA of TOMM20 and DDX6 in *Zar1*^{+/+} oocytes).

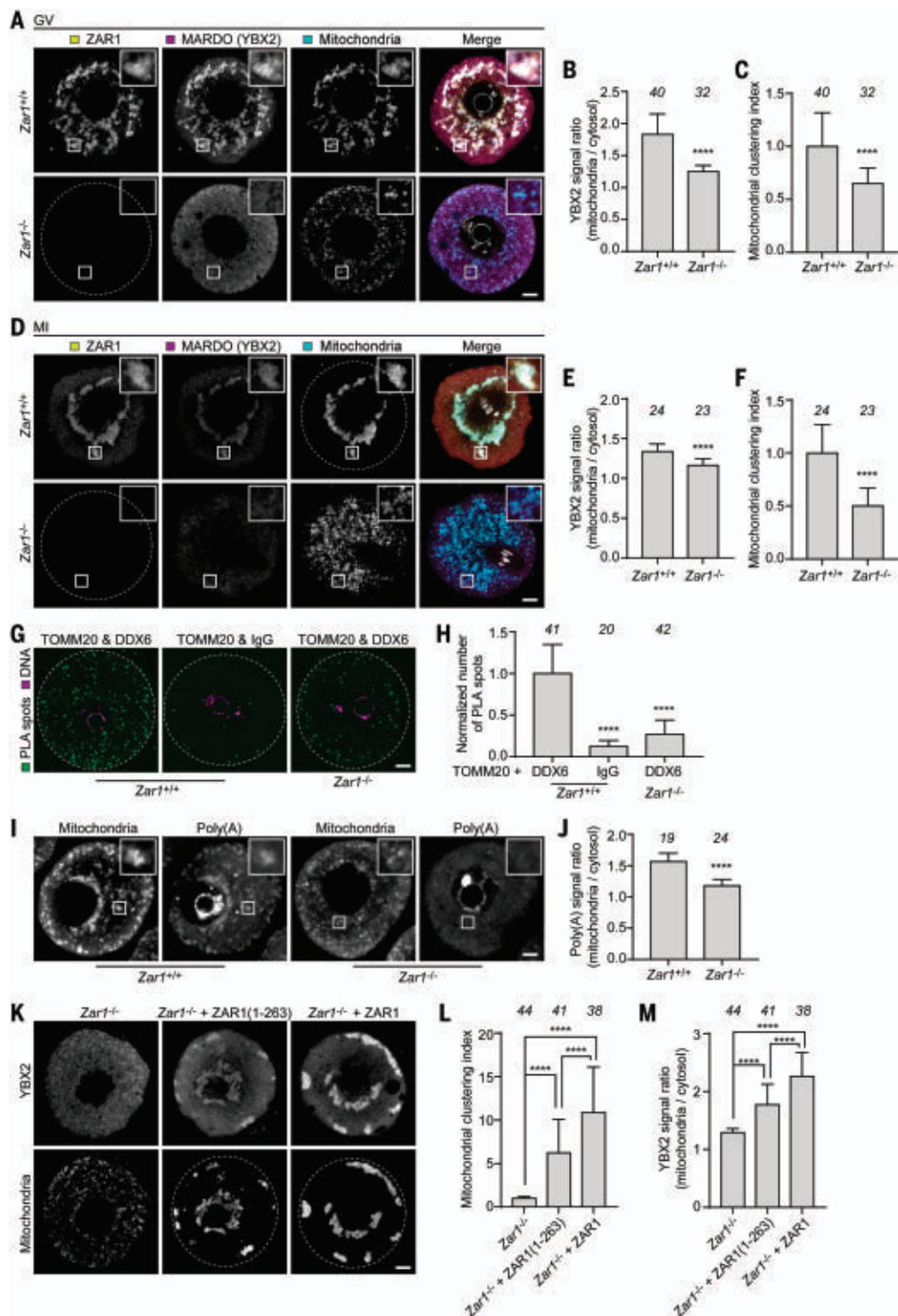
(I) Representative RNA-FISH images of GV oocytes collected from *Zar1*^{+/+} and *Zar1*^{-/-} mice. Oocytes were further stained with anti-COX17 antibody after FISH. Mitochondria, COX17; mRNAs with a poly(A) tail, 5'-Cy5-Oligo d(T)30. Insets are magnifications of outlined regions.

(J) Quantification of the ratio of mean 5'-Cy5-Oligo d(T)30 intensity on mitochondria to that in the cytosol.

(K) Representative immunofluorescence images of *Zar1*^{-/-} GV oocytes stained with anti-YBX2 and anti-cytochrome c (mitochondria) antibodies. Either ZAR1(1-263) or ZAR1 was overexpressed in oocytes before fixation. Non-injected oocytes were used as a control.

(L) Quantification of the mitochondrial clustering index.

(M) Quantification of the ratio of mean YBX2 intensity on mitochondria to that in the cytosol. The number of analyzed oocytes is specified in italics. Data are shown as mean ± SD. *P* values were calculated using unpaired two-tailed Student's *t* test [(B), (C), (E), (F), and (J)] or one-way ANOVA with Tukey's post hoc test [(H), (L), and (M)]. Scale bars, 10 μm.



in mouse oocytes (50–55). MARDO dissolution (Fig. 4F) and maternal mRNA decay (50–55) both occur at the MI-MII transition, which motivated us to investigate whether MARDO dissolution is necessary for timely mRNA decay. RNA-FISH revealed that maternal mRNAs were

enriched in the MARDO in prophase-arrested oocytes but dispersed in the cytoplasm in MII oocytes (Fig. 7A). ZAR1 overexpression retained both the MARDO and a significant fraction of MARDO-localized mRNAs in MII oocytes (Fig. 7B). Consistent with this observation, RT-qPCR

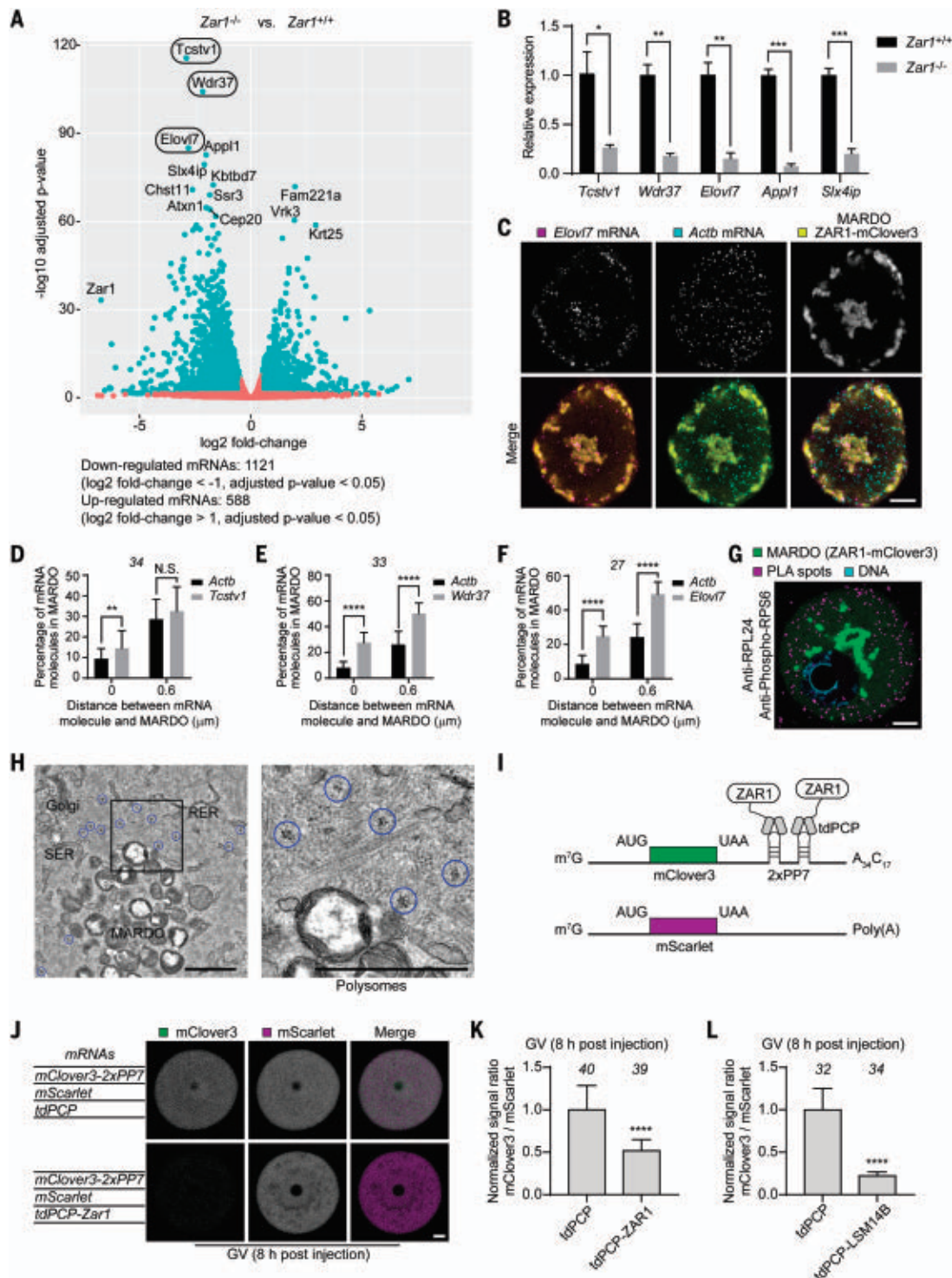
analyses revealed that the degradation of mRNAs stored in the MARDO was compromised when MARDO dissolution was delayed by ZAR1 overexpression (Fig. 7C). By contrast, those mRNAs that were not down-regulated in *Zar1*-knockout oocytes (fig. S15), and thus

Fig. 6. The MARDO stores mRNA and represses mRNA translation. (A) RNA-seq analyses reveal differentially expressed genes (DEGs; cyan dots in the volcano plot, adjusted P value < 0.05, average log2 fold change > 0.5 or < -0.5) in $Zar1^{-/-}$ oocytes versus $Zar1^{+/+}$ oocytes.

(B) RT-qPCR results showing expression of five genes (*Tcstv1*, *Wdr37*, *Elovl7*, *Appl1*, and *Slx4ip*) in $Zar1^{+/+}$ and $Zar1^{-/-}$ oocytes. Three biological replicates were used in the experiment.

(C) Representative smRNA-FISH images of mouse GV oocytes expressing ZAR1-mClover3. Yellow, MARDO (ZAR1-mClover3); magenta, Alexa Fluor 647-conjugated *Elovl7* mRNA probes; cyan, Alexa Fluor 546-conjugated *Actb* mRNA probes.

(D to F) Quantification of the percentage of the indicated mRNA molecules inside or associated with the MARDO. If the distance between an mRNA molecule and the MARDO is 0 μ m, it means that the mRNA molecule is inside of the MARDO. If the distance between mRNA molecule and the MARDO is <0.6 μ m, it means that the mRNA molecule is either inside of the MARDO or associated with the MARDO. (G) Representative image of in situ PLA performed with the antibody pair anti-RPL24 and anti-phospho-RPS6 in mouse GV oocytes expressing ZAR1-mClover3. Green, MARDO (ZAR1-mClover3); magenta, PLA spots; cyan, DNA (Hoechst 33342). (H) Representative transmission electron microscopy image of mouse GV oocytes expressing ZAR1-mClover3 showing that polysomes (marked with blue circles) are excluded from the MARDO. The outlined region is magnified on the right. SER, smooth ER; RER, rough ER. Scale bar, 1 μ m. (I) Schematic representation of *mClover3-2xPP7* reporter mRNA and *mScarlet* control mRNA. The signal ratio of mClover3 to mScarlet can be used to assess whether tdPCP fusion proteins regulate translation of tethered reporter mRNA. (J) Representative fluorescence images of mouse GV oocytes expressing *mClover3-2xPP7*, *mScarlet*, and *tdPCP* or



unlikely to be stored in the MARDO, were not affected (Fig. 7D). Therefore, MARDO dissolution is essential for timely mRNA degradation during the MI-MII transition.

Discussion

Where and how maternal mRNAs are stored in mammalian oocytes has remained elusive. Here, we identified the MARDO, a mitochondria-associated membraneless compartment that stores maternal mRNAs in mouse, bovine, porcine, and human oocytes (Fig. 7E). MARDO assembly around mitochondria is directed by an increase in mitochondrial membrane potential during oocyte growth. Expression of ZAR1 promotes MARDO coalescence and mitochondrial clustering, whereas proteasomal degradation of ZAR1 drives MARDO dissolution and mRNA decay during oocyte meiotic maturation.

Oocytes accumulate both the MARDO and mitochondria during growth. Maternal mitochondria provide energy for oocyte meiotic maturation and early embryonic development (56, 57), but they also generate reactive oxygen species (ROS) that can compromise the integrity of genetic material in mitochondria and the nucleus (58, 59). Emerging evidence has revealed that interactions between membrane-bound and membraneless compartments play fundamental roles in cellular organization and function (15, 60–69). Our study reveals physical and functional interactions between the membraneless MARDO and membrane-bound mitochondria. Mitochondria serve as a platform for MARDO assembly, and in return, the MARDO can modulate the distribution of mitochondria (Fig. 7E). MARDO formation depends on an increase in mitochondrial membrane potential during oocyte growth. During the long growth phase of oocytes, mitochondria maintain relatively low levels of activity. Low mitochondrial activity results in less ROS production and less DNA damage. This is beneficial for maintaining the stability of genetic material in oocytes. The complete polarization of mitochondria occurs only in full-grown SN oocytes, which ensures the energy supply for oocyte meiotic maturation and subsequent embryogenesis. Concomitantly, the MARDO becomes the most prominent in SN oocytes. In mouse, bovine, porcine, and human oocytes, the MARDO acts like a glue that holds the mitochondria together. Disruption of the MARDO leads to the dispersion of mitochondria. The exact function of the clustered mitochondria is not yet clear. During oocyte meiotic maturation, mitochondria tend to cluster around the MI spindle (35, 36). Moreover, the mitochondria around the spindle have a higher membrane potential (70). Concentrating active mitochondria in areas of high energy demand, rather than increasing the activity of all mitochondria, may help to minimize ROS production.

Beyond the central role of ZAR1 in promoting MARDO formation and mitochondrial clustering, interactions between the ER and mitochondria may also contribute to mitochondrial clustering (71). In contrast to the colocalization of mitochondria and the MARDO, only a fraction of ER tubules are localized in the MARDO, potentially indirectly, through interactions with mitochondria. However, when an ER tubule interacts with two or more mitochondria, this contributes to the formation of the mitochondrial cluster.

MARDO dissolution depends on the proteasome-mediated degradation of ZAR1. This is reminiscent of the disassembly of stress granules, which requires ubiquitination of G3BP1, the central protein within the RNA-protein network of stress granules (72, 73). Ubiquitinated G3BP1 is extracted by the segregase p97/valosin-containing protein (VCP) through the VCP adapter FAF2 and is then targeted to the proteasome for degradation (72, 73). A previous study in *Xenopus* revealed that Zar1 interacts with VCP (74). Further studies are required to verify whether MARDO dissolution requires FAF2-VCP-mediated extraction of ZAR1.

The MARDO co-localizes with mitochondria and is therefore distinct from P bodies, stress granules, P granules, and polar granules, which do not or only partially co-localize with mitochondria (31, 32). The MARDO shares some features with the Balbiani body: The MARDO and the Balbiani body both cluster mitochondria and both may favor active mitochondria. The Balbiani body is thought to be involved in the selection of active and healthy mitochondria (75, 76). It is interesting in this context that MARDO formation depends on the increase in mitochondrial membrane potential during oocyte growth. However, the MARDO and Balbiani body differ in three aspects. First, they appear at different stages of oocyte development. The Balbiani body is formed in early oocytes, whereas the MARDO is formed at later stages of oocyte growth. Injected RNAs have been reported to associate with mitochondria in full-grown *Xenopus* oocytes in which Balbiani bodies had dispersed at an earlier developmental stage (77). Further studies are required to test for the presence of the MARDO and the function of ZAR1 in MARDO assembly in *Xenopus* oocytes. Second, the MARDO and the Balbiani body have different material properties. The Balbiani body is held together by an amyloid-like matrix (15, 78), whereas the coalesced MARDO has hydrogel-like properties and still exchanges with the cytosol. Finally, the MARDO and the Balbiani body have different compositions. The Balbiani body contains Golgi apparatus, whereas the MARDO does not interact with the Golgi. Nevertheless, the MARDO and other RNA-containing membraneless compartments share

some common components. For example, the DDX6-LSM14B-4E-T complex (79) is present in the MARDO, as well as in P bodies and stress granules in some cell types, where it is involved in translational regulation. Whether the DDX6-LSM14B-4E-T complex has similar functions in the MARDO remains to be explored in mammalian oocytes.

Materials and Methods

Preparation and culture of mouse oocytes and follicles

All mice were maintained in a specific pathogen-free environment according to the Federation of European Laboratory Animal Science Association guidelines and recommendations. *Zar1*-knockout mice were generated through CRISPR/Cas9-mediated genome engineering (80) in a C57BL/6N background by Cyagen Biosciences. The guide RNA (gRNA1, matches forward strand of gene, GCCGCCTATTTAAC-GCAGCGTGG; gRNA2, matches reverse strand of gene, CCACACAAGTCTTGCCGATGGGG) for mouse *Zar1* and *Cas9* mRNA were co-injected into fertilized mouse eggs to generate targeted knockout offspring. F0 founder animals were identified by PCR followed by sequence analysis and subsequently bred with wild-type mice to test for germline transmission and to generate F1 animals. As a result, 3782 base pairs (bp) of the *Zar1* gene were removed, which caused complete removal of exons 1, 2, and 3 and partial removal of exon 4. For both gRNA-targeting sequences, five potential off-target sites were identified by PCR and sequence analysis, and the result indicated that no unwanted modifications occurred on these sites.

For most experiments, oocytes were isolated from ovaries of 7- to 10-week-old CD1 or C57BL/6N female mice. CD1 mice were used in the experiments shown in Figs. 1 to 3 and Fig. 6, J to L, and in fig. S1; figs. S3 to S6; fig. S7, D to H; fig. S8A; and fig. S9, E and F. C57BL/6J × CBA F1 female mice were used for follicle culture and RNAi shown in fig. S12, A to D. C57BL/6N mice were used in all other mouse experiments. Cortical enrichment of mitochondria was more prominent in C57BL/6N oocytes than in CD1 oocytes. Full-grown oocytes with a centered GV were kept arrested in prophase in homemade phenol red-free M2 medium supplemented with 250 μ M dibutyryl cyclic AMP (dbcAMP) under paraffin oil (NidaCon, catalog no. NO-400K) at 37°C. To collect oocytes at all growth stages, ovaries from 4-week-old female mice were washed in phosphate-buffered saline (PBS) and then dissected into pieces in 2 ml TrypLE Express Enzyme (1×) (Thermo Fisher Scientific, catalog no. 12604013) supplemented with 2 mg/ml collagenase IV (Thermo Fisher Scientific, catalog no. 17104019) and 250 μ M dbcAMP. After incubating at 37°C for 20 min, 2 ml of M2-dbcAMP medium was added, and oocytes were released by gentle

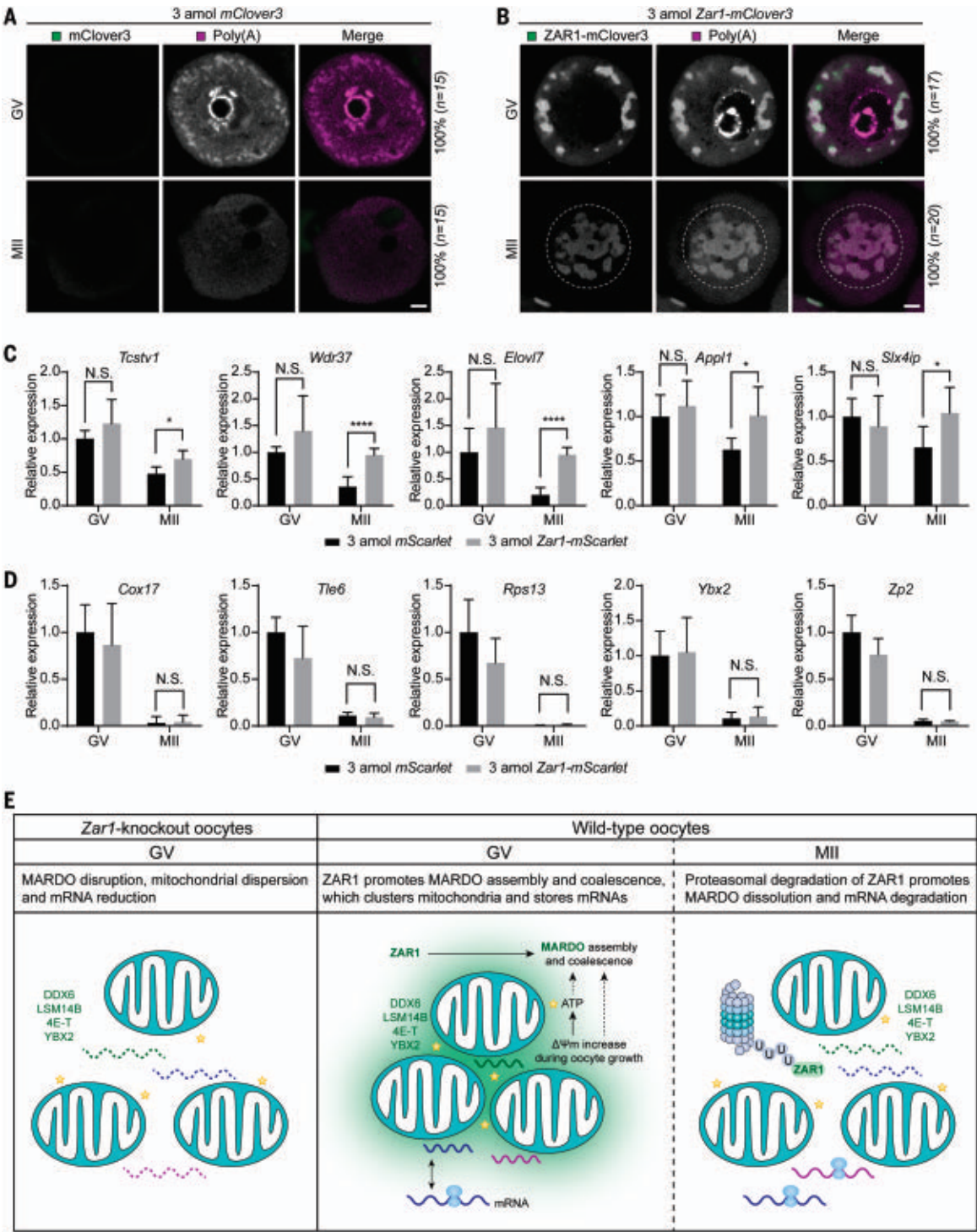


Fig. 7. MARDO dissolution is essential for timely maternal mRNA degradation during the MI-MII transition. (A and B) Representative RNA-FISH images of mouse GV oocytes and MII oocytes expressing mClover3 (A) or ZAR1-mClover3 (B). First, 3 amol mClover3 or Zar1-mClover3 mRNA was injected into GV oocytes. Four hours later, half of the oocytes were transferred to dbcAMP-free medium for in vitro maturation. Seventeen hours later, in vitro-matured MII oocytes and the remaining GV oocytes were fixed for RNA-FISH. mRNAs with a poly(A) tail were labeled with 5'-Cy5-Oligo d(T)30. Dashed lines demarcate the MARDO. The percentage of oocytes with a representative pattern is shown. "n" indicates the number of analyzed oocytes. (C and D) RT-qPCR results showing the expression of two groups of genes in GV oocytes and MII oocytes

with or without ZAR1 overexpression. First, 3 amol mScarlet or Zar1-mScarlet mRNA was injected into GV oocytes. Four hours later, half of the oocytes were transferred to dbcAMP-free medium for in vitro maturation. Seventeen hours later, in vitro-matured MII oocytes and the remaining GV oocytes were used to prepare cDNA libraries for RT-qPCR analyses. Six biological replicates were used in the experiment. (E) Model showing the mechanism of MARDO assembly, coalescence, and dissolution and how maternal mRNA storage, translation, and degradation are coupled to meiotic progression. The gradient green indicates the MARDO around mitochondria. $\Delta\Psi m$ is the mitochondrial membrane potential. Data are shown as mean \pm SD. P values were calculated using unpaired two-tailed Student's *t* test. Scale bars, 10 μm .

pipetting. The released oocytes were transferred to M2-dbcAMP medium and recovered for 30 min at 37°C before use. Day 14, 16, 18, and 21 oocytes were isolated from ovaries of 14-, 16-, 18- or 21-day-old female mice, and oocytes covered with loose granulosa cells were cleaned and collected. Culture of follicles was performed as previously described (87).

Preparation of bovine and porcine oocytes

All ovaries were obtained from local slaughterhouses. Bovine and porcine ovaries were transported in a ThermoFisher to the laboratory within 1 to 3 hours after retrieval and washed extensively with warm 0.9% NaCl. Cumulus-oocyte complexes were recovered by aspiration of antral follicles with an 18-gauge needle mounted on a 1-ml syringe. Additionally, 140 µl of 5000 IU/ml heparin (Merck Millipore, catalog no. 375095-100KU) was added to every 20 ml of aspirates from bovine ovaries. Bovine and porcine cumulus-oocyte complexes were allowed to sediment and then washed extensively with prewarmed HEPES-buffered medium 199 (Sigma-Aldrich, catalog no. M2520) and POE-CM (Cosmo Bio, catalog no. CSR-CK020), respectively. Only full-grown oocytes with a homogeneous cytoplasm and several layers of compact cumulus cells were selected for experiments. Bovine and porcine oocytes were maintained in prophase arrest in dbcAMP-containing medium at 39°C. The cumulus cells surrounding bovine and porcine oocytes were removed by vortex.

Source of human oocytes

The use of immature unfertilized human oocytes in this study was approved by the UK's National Research Ethics Service under the REC reference 11/EE/0346 [Integrated Research Application System (IRAS) project ID 84952]. Oocytes were sourced from women undergoing assisted reproduction treatment at Bourn Hall Clinic (Cambridge, UK). Only oocytes that were immature and thus unsuitable for intracytoplasmic sperm injection were used. All patients gave informed consent for their immature oocyte(s) to be used in this study.

Immunofluorescence

To obtain mouse MI and MII oocytes, oocytes were incubated at 37°C for ~7 and ~15 hours, respectively, upon release into dbcAMP-free medium. Oocytes from different sources were all fixed with 4% methanol-free formaldehyde in PBS for 1 hour at room temperature. Fixed oocytes were washed and extracted with PBT buffer (0.5% Triton X-100 in PBS) for 1 hour at room temperature or overnight at 4°C. Permeabilized oocytes were blocked with PBT-BSA buffer (PBS containing 3% bovine serum albumin and 0.1% Triton X-100) for 1 hour at room temperature or overnight at 4°C. Lipid droplets in bovine and porcine oocytes were

cleared with 4000 U/ml lipase from *Candida rugosa* (Sigma-Aldrich, catalog no. L8525) in lipase buffer (50 mM Tris pH 7.2, 400 mM NaCl, 5 mM CaCl₂, and 0.2% sodium taurocholate supplemented with cOmplete, EDTA-free Protease Inhibitor Cocktail; Roche, catalog no. 11873580001) for 1 hour at 37°C. Cleared oocytes were washed with PBT-BSA and subsequently incubated with antibodies. Oocytes were incubated with primary antibodies in PBT-BSA for 1.5 hours at room temperature. After washing three times with PBT-BSA, oocytes were incubated with secondary antibodies and Hoechst 33342 (Thermo Fisher Scientific, catalog no. H3570) for 1.5 hours at room temperature. Oocytes were then washed three times again and imaged in 2 to 3 µl of PBS with 10% fetal bovine serum (Gibco, catalog no. 16000-044) under paraffin oil in a 35-mm dish with a #1.0 coverslip.

Primary antibodies used were goat anti-ZAR1 (Santa Cruz Biotechnology, catalog no. sc-55994), mouse anti-cytochrome c (Santa Cruz Biotechnology, catalog no. sc-13561), rabbit anti-YBX2 (Abcam, catalog no. ab33164), rabbit anti-DDX6 (Abcam, catalog no. ab174277), mouse anti-DDX6 (Sigma-Aldrich, catalog no. SAB4200837), rabbit anti-LSM14B (Thermo Fisher Scientific, catalog no. PA5-66371), rabbit anti-4E-T (Thermo Fisher Scientific, catalog no. PA5-51680), mouse anti-PABPCIL (Santa Cruz Biotechnology, catalog no. sc-515476), mouse anti-KDEL (Enzo Life Sciences, catalog no. ADI-SPA-827), rabbit anti-BCAP31 (Proteintech, catalog no. 11200-1-AP), mouse anti-GM130 (BD Biosciences, catalog no. 610822), rabbit anti-RAB11A (Thermo Fisher Scientific, catalog no. 71-5300), rat anti-LAMP1 (Thermo Fisher Scientific, catalog no. 14-1071-82), mouse anti-TOMM20 (Novus Biologicals, catalog no. H00009804-M01), rabbit anti-FIS1 (Sigma-Aldrich, catalog no. HPA017430), rabbit anti-COX17 (Sigma-Aldrich, catalog no. HPA042226), rabbit anti-RPL24 (Thermo Fisher Scientific, catalog no. PA5-30157), mouse anti-phospho-RPS6 (Cell Signaling Technology, catalog no. 62016), mouse anti-phospho-ERK1/2 (Cell Signaling Technology, catalog no. 9106), guinea pig anti-nonphosphorylated-ZAR1 (made by Cambridge Research Biochemicals). All primary antibodies were diluted at 1:100 except for rabbit anti-YBX2 (Abcam, catalog no. ab33164), which was diluted at 1:500. Secondary antibodies used were Alexa Fluor 488-, 568-, or 647-conjugated anti-goat immunoglobulin G (IgG), anti-rabbit IgG, anti-mouse IgG, anti-rat IgG, or anti-guinea pig IgG highly cross-adsorbed secondary antibodies (Thermo Fisher Scientific). All secondary antibodies were raised in donkey or goat.

smRNA-FISH

Oocytes were fixed with 4% methanol-free formaldehyde in PBS for 30 min and then per-

meabilized with fresh 70% ethanol for 20 min at room temperature. Permeabilized oocytes were rehydrated with Wash Buffer A (Biosearch Technologies, catalog no. SMF-WA1-60) containing 10% formamide and then incubated with 200 nM Cy5-conjugated oligo (dT)30 (Integrated DNA Technologies) in hybridization buffer (Biosearch Technologies, catalog no. SMF-HB1-10) supplemented with 10% formamide for 16 hours at 37°C. After probe incubation, oocytes were washed with Wash Buffer A for 30 min at 37°C and then stained with Hoechst in Wash Buffer A for another 30 min at 37°C. After sequential washing with Wash Buffer A and Wash Buffer B (Biosearch Technologies, catalog no. SMF-WB1-20) for 30 min each at 37°C and room temperature, respectively, oocytes were mounted for imaging or immunofluorescence.

smRNA-FISH

The ViewRNA Cell Plus Assay-Kit (Thermo Fisher Scientific, catalog no. 88-19000-99) was used for smRNA-FISH. The assay was performed as previously described with some optimizations (82). Oocytes expressing ZAR1-mClover3 were fixed with 4% methanol-free formaldehyde in PBS for 20 min at room temperature. After extensive washing with homemade wash buffer containing 1% polyvinylpyrrolidone (Sigma-Aldrich, catalog no. P0930), 0.1% Triton X-100, and 1× RNase inhibitor (provided in the kit) in PBS, oocytes were permeabilized with homemade permeabilization solution (PBS containing 1% Triton X-100 and 1× RNase inhibitor) for 30 min at room temperature. After washing with the homemade wash buffer again, oocytes were treated with 1:8000 diluted Protease QS (Thermo Fisher Scientific, catalog no. QVC0001) for 5 min at room temperature. Probe sets of mRNAs of interest (Tbstv1, catalog no. VB6-3203791-VCP; Wdr37, catalog no. VB6-3215318-VCP; or Elov17, catalog no. VB6-3209719-VCP) and control probe set (Actb, catalog no. VB1-10350-VCP) were mixed and diluted 1:100 with prewarmed probe set diluent supplemented with 0.1% Triton X-100. After protease treatment and washing with homemade wash buffer, oocytes were incubated with the diluted probe sets for 3 hours at 40°C. Hybridization and all following steps were performed in a six-well dish (Agtech, catalog no. 3926909910). After probe set hybridization, oocytes were washed five times with ViewRNA Cell Plus RNA Wash Buffer Solution supplemented with 0.5% BSA, and then subjected to sequential hybridization with pre-amplifier mix, amplifier mix, and label probe mix, all of which were diluted 1:25 with prewarmed provided diluent supplemented with 0.1% Triton X-100. Hybridizations with pre-amplifier, amplifier, and label probe were performed at 40°C for 1 hour. Oocytes were washed five times with the ViewRNA Cell Plus

RNA Wash Buffer Solution containing 0.5% BSA between every hybridization step. Finally, oocytes were stained with Hoechst 33342 in PBT-BSA solution (PBS containing 0.1% Triton X-100 and 3% BSA) for 1.5 hours at room temperature to label DNA.

PLA

PLA was performed with the Duolink In Situ Red Starter Kit Mouse/Rabbit (Sigma-Aldrich, catalog no. DUO92101). Oocytes with or without ZAR1-mClover3 were fixed with 4% methanol-free formaldehyde in PBS for 20 min at room temperature. Fixed oocytes were washed and extracted with PBT buffer (1% Triton X-100 in PBS) for 1 hour at room temperature and then blocked with PBT-BSA (0.1% Triton X-100 and 3% BSA in PBS) overnight at 4°C. All of the following steps, including primary antibody incubation, PLA probe incubation, ligation, amplification, and final washes, were performed according to the protocol provided with the kit except that primary antibodies were diluted 1:50 or 1:100 with PBT-BSA. Oocytes can be further stained with other antibodies and/or Hoechst 33342 before imaging.

Primary antibody pairs used include goat anti-ZAR1 (Santa Cruz Biotechnology, catalog no. sc-55994) and mouse anti-TOMM20 (Novus Biologicals, catalog no. H00009804-M01), rabbit anti-RAB11A (Thermo Fisher Scientific, catalog no. 71-5300), or normal rabbit IgG (Merck Millipore, catalog no. 12-370); mouse anti-TOMM20 and rabbit anti-DDX6 (Abcam, catalog no. ab174277) or normal rabbit IgG; rabbit anti-RPL24 (Thermo Fisher Scientific, catalog no. PA5-30157) and mouse anti-phosphor-RPS6 (Cell Signaling Technology, catalog no. 62016). Corresponding PLA probes were all purchased from Sigma-Aldrich.

Expression constructs, mRNA synthesis, protein expression, and purification

Primers used for plasmid construction are shown in data S5. To generate constructs for mRNA synthesis, pGEMHE-mClover3-N1, pGEMHE-mScarlet-N1, pGEMHE-mClover3-C1, and pGEMHE-mScarlet-C1 were built first for subcloning of other constructs. To generate pGEMHE-mClover3-N1 and pGEMHE-mScarlet-N1, published coding sequences of mClover3 (83) and mScarlet (84) were amplified using primers P1 and P2 and then ligated into pGEMHE through BamHI/XbaI. To build pGEMHE-mClover3-C1 and pGEMHE-mScarlet-C1, mClover3 and mScarlet were amplified using primers P3 and P4 and then ligated into pGEMHE through NheI/XhoI. To construct pGEMHE-Mito-EGFP, MitoTimer was first amplified from pMitoTimer (Addgene, catalog no. 52659) (85) and then subcloned into pGEMHE through NheI/NotI to get pGEMHE-MitoTimer. Timer was then replaced with EGFP(L221K) that was amplified using primers

P5 and P6. To generate pGEMHE-ZAR1-mScarlet and pGEMHE-ZAR1-mClover3, ZAR1 was amplified from a mouse cDNA library using primers P7 and P8 and assembled with linearized pGEMHE-mScarlet-N1(NheI/NcoI) and pGEMHE-mClover3-N1(NheI/NcoI) through Gibson assembly (NEB, catalog no. E2621S). To build pGEMHE-mScarlet-YBX2, YBX2 was amplified from a mouse cDNA library using primers P9 and P10 and then assembled with linearized pGEMHE-mScarlet-C1(XhoI/BamHI) through Gibson assembly. To build pGEMHE-LSM14B-mScarlet, pGEMHE-DDX6-mScarlet, and pGEMHE-4E-T-mScarlet, LSM14B, DDX6 and 4E-T were amplified from mouse cDNA libraries using primers P11 and P12, P13 and P14, and P15 and P16, respectively, and then assembled with linearized pGEMHE-mScarlet-N1(NheI/NcoI) through Gibson assembly. To generate pGEMHE-ZAR1(1-263)-mScarlet and pGEMHE-ZAR1(1-143)-mScarlet, site-directed mutagenesis (86) on pGEMHE-ZAR1-mScarlet was performed using primers P17 and P18 and P19 and P20, respectively. To build pGEMHE-ZAR1(53-143)-mScarlet, site-directed mutagenesis on pGEMHE-ZAR1(1-143)-mScarlet was performed using primers P21 and P22. To construct pGEMHE-ZAR1(53-74)-mScarlet, ZAR1(53-74) was synthesized (Integrated DNA Technologies) and assembled with linearized pGEMHE-mScarlet-N1(NheI/NcoI) through Gibson assembly. To generate pGEMHE-ZAR1(252-361)-mScarlet, site-directed mutagenesis on pGEMHE-ZAR1-mScarlet was performed using primers P23 and P24. To build pGEMHE-mClover3-2×PP7, 2×PP7 was amplified from pHAGE-CMV-CFP-24×PP7 (Addgene, catalog no. 40652) (44) using primers P25 and P26 and then assembled with linearized pGEMHE-mClover3-N1(XbaI) through Gibson assembly. To build pGEMHE-tdPCP and pGEMHE-tdPCP-ZAR1, pGEMHE-tdPCP-mscarlet was generated first. tdPCP was amplified from pHAGE-UBC-NLS-HA-tdPCP-GFP (Addgene, catalog no. 40650) (44) using primers P27 and P28 and ligated into pGEMHE-mScarlet-N1 through XhoI/NcoI. To generate pGEMHE-tdPCP, site-directed mutagenesis on pGEMHE-tdPCP-mScarlet was performed using primers P29 and P30. To construct pGEMHE-tdPCP-ZAR1, ZAR1 with a linker (74, 87) was amplified from pGEMHE-ZAR1-mScarlet using primers P31 and P32 and then assembled with linearized pGEMHE-tdPCP acquired by digesting pGEMHE-tdPCP-mScarlet with NcoI/XbaI. To construct pGEMHE-tdPCP-LSM14B, LSM14B with a linker was amplified from pGEMHE-LSM14B-mScarlet using primers P33 and P34 and then assembled with linearized pGEMHE-tdPCP acquired by digesting pGEMHE-tdPCP-mScarlet with NcoI/XbaI. To generate pGEMHE-FLAG-ZAR1(1-263), pGEMHE-FLAG-ZAR1 was built first. FLAG-ZAR1 was amplified from pGEMHE-ZAR1-mScarlet using

primers P35 and P36 and ligated into pGEMHE through NheI/XbaI. To build pGEMHE-FLAG-ZAR1(1-263), site-directed mutagenesis on pGEMHE-FLAG-ZAR1 was performed using primers P17 and P18. To generate pGEMHE-FLAG-ZAR1(1-263)(T154A) and pGEMHE-FLAG-ZAR1(1-263)(S161A), site-directed mutagenesis on pGEMHE-FLAG-ZAR1(1-263) was performed using primers P37 and P38 and P39 and P40, respectively. To generate pGEMHE-FLAG-ZAR1(1-263)(T154A, S161A), site-directed mutagenesis on pGEMHE-FLAG-ZAR1(1-263)(T154A) was performed using primers P39 and P40. To construct pGEMHE-FLAG-ZAR1(1-263)(S124A, S161A) and pGEMHE-FLAG-ZAR1(1-263)(S161A, S244A), site-directed mutagenesis on pGEMHE-FLAG-ZAR1(1-263)(S161A) was performed using primers P41 and P42 and P43 and P44, respectively. To build pGEMHE-ZAR1(T154D)-mScarlet and pGEMHE-ZAR1(S161D)-mScarlet, site-directed mutagenesis on pGEMHE-ZAR1-mScarlet was performed using primers P45 and P46 and P47 and P48, respectively. To generate pGEMHE-ZAR1(T154D, S161D)-mScarlet, site-directed mutagenesis on pGEMHE-mZAR1(S161D)-mScarlet was performed using primers P45 and P46. To build pGEMHE-PPP2R1A-mClover3, PPP2R1A was amplified from a mouse cDNA library using P49 and P50 and then assembled with linearized pGEMHE-mClover3-N1 (NheI/NcoI) through Gibson assembly. Constructs pGEMHE-mClover3-MAP4-MTBD, pGEMHE-H2B-mRFP, pGEMHE-H2B-miRFP670, and pGEMHE-TRIM21 were generated in previous studies (88, 89). All mRNAs were synthesized using the HiScribe T7 ARCA mRNA Kit (with tailing) (NEB, catalog no. E2060S) and then purified with the RNeasy Mini Kit (Qiagen, catalog no. 74104).

To generate constructs for protein expression, codon optimization (Integrated DNA Technologies) was performed on all genes for better expression in *E. coli*. To generate pET-21c(+)-6xHis-SMT3, 6xHis-SMT3 was synthesized and ligated into pET-21c(+) through NdeI/BamHI. To build pET-21c(+)-6xHis-SMT3-sfGFP, superfolder GFP (sfGFP) was synthesized and ligated into pET-21c(+)-6xHis-SMT3 through BamHI/HindIII. To generate pET-21c(+)-6xHis-SMT3-ZAR1(1-263), ZAR1(1-263) was amplified from synthesized ZAR1 using primers P51 and P52 and then ligated into pET-21c(+)-6xHis-SMT3 through BamHI/HindIII. All constructs were expressed in BL21(DE3) Competent *E. coli* (NEB, catalog no. C2527H). Proteins were purified first using Ni-NTA resin (Qiagen, catalog no. 30210), followed by size-exclusion chromatography on a HiLoad 16/600 Superdex 200 pg column (Sigma-Aldrich, catalog no. GE28-9893-35) performed with the ÄKTA pure 25 system (Cytiva). SMT3 tag was removed by cutting with SUMO protease (Thermo Fisher Scientific, catalog no. 12588018) when necessary.

Short-interfering RNAs

All short interfering RNAs (siRNAs) were purchased from Qiagen. For knockdown of *Zar1* by RNAi, a mix of siRNAs targeting the following sequences were used: 5'-CACCACTAAGGTGTACTTCA-3', 5'-CCGAGTGTGTGAGAAATCCTA-3', 5'-CAGCTTCAATACATCATTTA-3', and 5'-TTC-CAAATCTTCATGACAGA-3'. AllStars Negative Control (Qiagen, catalog no. 1027281) was used as a control.

Microinjection of mouse oocytes

Mouse oocytes were microinjected with 6 pl of mRNAs as previously described (89, 90). For ZAR1, YBX2, LSM14B, DDX6, 4E-T, and their truncation or point mutants, mRNAs were injected at a concentration of 0.5 μ M in the injection solution unless otherwise specified. To minimize the effect of ZAR1 on MARDO dissolution when following MARDO dynamics, mRNAs were injected at 0.05 μ M. *Mito-EGFP* was injected at 0.2 μ M. *mClover3-Map4-MTBD*, *H2B-mRFP*, and *H2B-mRFP670* were injected at 50 ng/ μ l. In the tdPCP-PP7 tethering assay, *mClover3-2 \times PP7* and *mScarlet* were injected at 0.2 and 0.1 μ M respectively, whereas *tdPCP*, *tdPCP-Zar1*, and *tdPCP-Lsm14b* were injected at 0.5 μ M. In the RNase injection assay, 6 pl of 10% RNase Cocktail Enzyme Mix (Thermo Fisher Scientific, catalog no. AM2286) in PBS was injected into each oocyte. Mouse follicles were microinjected with 6 pl of siRNAs at a concentration of 2 μ M, as previously described (87).

Confocal microscopy

For confocal imaging, oocytes were imaged in 2 to 3 μ l of M2 medium (for live mouse oocytes) or PBS with 10% fetal bovine serum (Gibco, catalog no. 16000-044) or 5 mg/ml UltraPure BSA (Thermo Fisher Scientific, catalog no. AM2616) (for fixed oocytes) under paraffin oil in a 35-mm dish with a #1.0 coverslip. Images were acquired with LSM 880 confocal laser scanning microscopes (Zeiss) equipped with an environmental incubator box and a 40 \times C-Apochromat 1.2 numerical aperture water-immersion objective. Airyscan images were acquired using the Airyscan module on LSM880 confocal laser scanning microscopes (Zeiss) and processed in ZEN software (Zeiss) after acquisition. Images of the control and experimental groups were acquired under identical imaging conditions on the same microscope. Movies S8 to S10 were smoothened with a Gaussian filter (sigma = 1.3) in ZEN and aligned using HyperStackReg in Fiji (NIH) (91). Care was taken that the imaging conditions (laser power, pixel-dwell time, and detector gain) did not cause phototoxicity (for live imaging), photobleaching, or saturation.

Electron microscopy and immunogold labeling

Mouse oocytes with or without ZAR1-mClover3 overexpression were fixed in 100 mM HEPES

(pH 7.0, titrated with KOH), 50 mM EGTA (pH 7.0, titrated with KOH), 10 mM MgSO₄, 3% EM-grade glutaraldehyde, and 0.5% methanol-free formaldehyde at 37°C for 1 hour. All of the following processing steps were performed in a microwave (Ted Pella) and oocytes were washed three times with water for 40 s at 250 W between every staining step. Oocytes were first stained with 2% osmium tetroxide in water for 12 min at 100 W (microwave cycling between on and off every 2 min). Oocytes were then stained with 1% uranyl acetate in water for 12 min at 100 W (microwave cycling between on and off every 2 min). Oocytes were subsequently dehydrated in a graded ethanol series (10, 30, 50, 75, 90, 100, and 100%) for 40 s at 250 W and infiltrated in a graded series (25, 50, 75, 90, 100, and 100%) of Epon resin in ethanol for 3 min at 250 W. Samples were then cured overnight at 60°C. Ultrathin sections (50 to 70 nm) were cut using a diamond knife (Diatome) on an EM UC7 ultramicrotome (Leica) and placed on copper grids.

For immunogold labeling, grids were incubated with 1% BSA in PBS (PBS-BSA) for 5 min, followed by 10 μ g/ml goat anti-GFP (Rockland Immunochemicals, catalog no. 600-101-215) in PBS-BSA for 30 min. Samples that were not incubated with primary antibody were used as negative controls to assess the specificity of immunogold labeling. Grids were then washed with PBS and incubated with 10 nm gold-conjugated donkey anti-goat antibody (Aurion, catalog no. 810.333) in PBS-BSA at a 1:20 dilution for 30 min. Grids were further washed with PBS, contrast enhanced using UranylLess (Electron Microscopy Sciences, catalog no. 22400), and air-dried. Grids were visualized on a LEO 912 transmission electron microscope (Zeiss) operated at 120 kV.

In vitro phase separation assay

To investigate phase separation of SMT3-ZAR1(1-263), proteins and negative controls dissolved in buffer containing 50 mM HEPES, pH 7.4, 300 mM NaCl, and 2 mM dithiothreitol (DTT) were diluted with 50 mM HEPES, pH 7.4, and 2 mM DTT to reach different protein concentrations and different salt conditions. Protein dilution was performed on a collagen IV-coated μ -Slide 18-well slide (Ibidi, catalog no. 81822), and the samples were kept in a humidifying chamber for 30 min before imaging. To check phase separation of SMT3-ZAR1(1-263) and ZAR1(1-263) at physiological salt concentration, proteins were diluted to 40 μ M in a buffer containing 50 mM HEPES, pH 7.4, 150 mM NaCl, 2 mM DTT, and 10% Ficoll 400 and then imaged immediately. To perform the fluorescence recovery after photobleaching (FRAP) assay in condensates of SMT3-ZAR1(1-263) and ZAR1(1-263) at physiological salt concentration, proteins were dialyzed with 50 mM HEPES, pH 7.4, 300 mM

NaCl, and 0.5 mM tris (2-chloroethyl) phosphate (TCEP) to remove DTT and then conjugated with Alexa Fluor 488 C₅ maleimide (Thermo Fisher Scientific, catalog no. A10254). Excess dyes were removed by passing through an NAP-5 desalting column (Sigma-Aldrich, catalog no. GE17-0853-01). The 98% nonlabeled proteins and 2% labeled proteins were mixed and diluted as above.

FRAP

Oocytes expressing ZAR1-mScarlet or condensates labeled by Alexa Fluor 488 were used to perform FRAP assays. Rectangular or circular regions of interest (ROIs) were marked and photobleached using the corresponding excitation laser line at maximum power after the third time point. Images were captured every 4 s (in vivo) or 1 s (in vitro) and mean intensities of ROIs over time were recorded. Intensities were normalized by subtracting the remaining signal after photobleaching and then normalized to the mean intensity of the first three time points before photobleaching.

tdPCP-PP7 tethering assay

For the tdPCP-PP7 tethering assay, 0.2 μ M reporter mRNA *mClover3-2 \times PP7* and 0.1 μ M injection control *mScarlet* were coinjected with either 0.5 μ M *tdPCP*, 0.5 μ M *tdPCP-Zar1* or 0.5 μ M *tdPCP-Lsm14b* mRNA into GV oocytes. Reporter mRNA contains an oligo(A) tail followed by oligo(C) (A₃₄C₁₇), whereas all of the other mRNAs contain an ~150-bp poly(A) tail. The expression of reporter mRNA was assessed by the signal ratio of mClover3 to mScarlet at 8 hours after mRNA injection.

Vital stain labeling and drug treatment

The fluorescence intensity ratio of tetramethylrhodamine methyl ester (TMRM) to MitoTracker Green was used to monitor mitochondrial membrane potential. TMRM was diluted in anhydrous dimethyl sulfoxide (DMSO) (Thermo Fisher Scientific, catalog no. D12345) to make a 25 μ M stock. MitoTracker Green and SiR-DNA were diluted in DMSO to make 1 mM stocks. Culture medium containing 400 nM MitoTracker Green, 25 nM TMRM, and 2 μ M SiR-DNA was freshly prepared and prewarmed for 30 min at 37°C. Oocytes were stained for 30 min at 37°C and then washed with culture medium without dyes. Antimycin A (Sigma-Aldrich, catalog no. A8674) was diluted in ethanol to make a 10 mg/ml stock. FCCP (Sigma-Aldrich, catalog no. C2920) and oligomycin A (Sigma-Aldrich, catalog no. 75351) were diluted in DMSO to make a 10 mM stock and a 5 mg/ml stock, respectively. Antimycin A and oligomycin A were used at a final concentration of 5 μ g/ml in culture medium. FCCP was used at a 5 μ M concentration unless specified otherwise. Oocytes were treated for 1 hour at 37°C before fixation. To perform drug treatment simultaneously

with TMRM and MitoTracker Green staining, oocytes were incubated with 200 nM MitoTracker Green, 12.5 nM TMRM, and the drug for 1 hour at 37°C and then imaged as quickly as possible. RO-3306 (Sigma-Aldrich, catalog no. SML0569), MG-132 (Selleckchem, catalog no. S2619), and nocodazole (Sigma-Aldrich, catalog no. M1404) were diluted in DMSO to make 10 mM stocks and added to treat oocytes at a final concentration of 10 μ M. U0126 (Calbiochem, catalog no. 662005) was diluted in DMSO to make a 50 mM stock and used at a 20 μ M concentration. For 1,6-hexanediol treatment, 10% 1,6-hexanediol (Sigma-Aldrich, catalog no. 240117) in culture medium was freshly prepared and diluted to 5% for use. Oocytes were treated for 5 min at 37°C before fixation.

Trim-Away in mouse oocytes

An anti-ZAR1 antibody was raised in guinea pig against a synthetic peptide corresponding to amino acids 152 to 168 of mouse ZAR1 and further purified by affinity purification (Cambridge Research Biochemicals). Ultrafiltration (Merck Millipore, catalog no. UFC510024) was performed to change the buffer of the anti-ZAR1 antibody, the anti-DDX6 antibody (Sigma-Aldrich, catalog no. SAB4200837), and control IgG (Merck Millipore, catalog no. 12-371) to PBS. Then, 2 μ l of *Trim* mRNA and 4 μ l of antibody containing 0.1% NP-40 were coinjected as previously described (92). For depletion of ZAR1, injected oocytes were kept in M2 medium supplemented with 250 μ M dbcAMP for 16 hours before fixation. For depletion of DDX6, injected oocytes were kept in M2 medium supplemented with 10 μ M RO-3306 for 5 hours before fixation.

RNA-seq and data analysis

GV oocytes were collected from three *Zar1*^{+/+} and three *Zar1*^{-/-} mice. Ten oocytes collected from the same mouse were pooled together to prepare RNA-seq libraries using the QIAseq FX Single Cell RNA Library Kit (Qiagen, catalog no. 180733). Libraries were prepared according to the handbook of the kit with the following changes. The zona pellucida of oocytes was removed in acidic Tyrode's solution (Merck Millipore, catalog no. MR-004-D) before cell lysis. The adapters in the kit were replaced with xGen UDI-UMI adapters (Integrated DNA Technologies, catalog no. 10006914). Sequencing of multiplexed libraries with paired-end reads (PE75) was performed using a NextSeq 550 system (Illumina) at an average sequencing depth of 50 million reads per library. Adapters were trimmed with cutadapt 2.8 (93) using the “-q 20 -m 35 -j 15” parameters. Reads were mapped against the Gencode GRCm39 reference genome with the STAR 2.7.8a (94) aligner using the default settings. Counting of reads mapping to features in the Gencode vM26 annotation file was

performed with HTSeq 0.13.5 (95). Differentially expressed genes (adjusted *P* value < 0.05, average log2 fold change > 0.5) were identified with the DESeq2 v1.32.0 (96) package in R. Down-regulated or up-regulated phenotype-associated pathways were identified with gene set enrichment analysis using the fgsea v1.18.0 (97) package in R and the MSigDB (98, 99) C5 (ontology) gene set. The RNA-seq data were then compared with published mRNAs that are translationally activated during oocyte meiotic maturation or at the MII–zygote transition (45, 46). To identify mRNAs that are translationally activated during oocyte meiotic maturation, TMM-normalized CPM values from the RiboTag/RNA-seq experiments with Gene Expression Omnibus (GEO) accession number GSE135525 (45) were re-analyzed with the Bioconductor packages edgeR v3.34.1 (100) and Limma v3.48.3 (101).

RT-qPCR

GV oocytes were collected from three *Zar1*^{+/+} and three *Zar1*^{-/-} mice. Ten oocytes collected from the same mouse were pooled together to do reverse transcription and whole transcriptome amplification using the QIAseq FX Single Cell RNA Library Kit (Qiagen, catalog no. 180733). The cDNA was diluted 1:100 and 5 μ l was used for a 25- μ l reaction. qPCR was performed on the Rotor-Gene Q (Qiagen) system using the PowerUp SYBR Green Master Mix (Thermo Fisher Scientific, catalog no. A25742). Endogenous *Actin* (*Actb*) was used as an internal control to calculate relative transcript levels in *Zar1*^{-/-} versus *Zar1*^{+/+} oocytes. Three cDNA libraries were built for each genotype.

To quantify transcript levels with or without ZAR1 overexpression, 3 amol *mScarlet* or *Zar1-mScarlet* mRNA was injected into GV oocytes. Four hours later, half of the oocytes were transferred to dbcAMP-free medium for in vitro maturation. After 17 hours, in vitro-matured MII oocytes and the remaining GV oocytes were used to prepare cDNA libraries. RT-qPCR was performed using the same method as above. Six cDNA libraries each containing five oocytes were built for each experimental condition (*mScarlet* GV, *mScarlet* MII, *Zar1-mScarlet* GV, and *Zar1-mScarlet* MII). Primers used for RT-qPCR are listed in data S6.

Immunoblotting

Oocytes were quickly washed in PBS, resuspended in 10 μ l of PBS, and immediately snap-frozen in liquid nitrogen. Then, 10 μ l of 2 \times NuPAGE LDS Sample Buffer (Thermo Fisher Scientific, catalog no. NP0007) with 100 mM DTT was added, followed by heating at 95°C for 10 min. Samples were resolved on a 10-well NuPAGE 10% Bis-Tris protein gel of 1.0-mm thickness (Thermo Fisher Scientific, catalog no. NP0301BOX) with NuPAGE MOPS SDS run-

ning buffer (Thermo Fisher Scientific, catalog no. NP0001). Proteins were then transferred onto a 0.45- μ m polyvinylidene difluoride membrane (Thermo Fisher Scientific, catalog no. LC2005) with NuPAGE transfer buffer (Thermo Fisher Scientific, catalog no. NP0006). Blocking and antibody incubations were performed in PBS with 5% skim milk and 0.1% Tween-20. Primary antibodies used were goat anti-ZAR1 diluted at 1:200 (Santa Cruz Biotechnology, catalog no. sc-55994), guinea pig anti-non-phosphorylated-ZAR1 diluted at 1:200 (made by Cambridge Research Biochemicals), mouse anti-FLAG diluted at 1:200 (Sigma-Aldrich, catalog no. F3165), and rabbit anti-DDB1 diluted at 1:4000 (Abcam, catalog no. ab109027). Secondary antibodies used were HRP-conjugated anti-goat (Santa Cruz Biotechnology, catalog no. sc-2020), anti-guinea pig (Thermo Fisher Scientific, catalog no. A18775), anti-mouse (Dako, catalog no. P0260), and anti-rabbit (Abcam, catalog no. ab205718). All secondary antibodies were diluted 1:1000 for use. Blots were developed with SuperSignal West Femto Maximum Sensitivity Substrate (Thermo Fisher Scientific, catalog no. 34095) and documented with an Amersham Imager 600 (Cytiva). Care was taken that the exposure time did not cause saturation.

In vitro phosphorylation assay

For the in vitro phosphorylation assay, 8 μ l of 80 μ M HIS-SMT3-ZAR1(1-263) in 50 mM HEPES, pH 7.4, 300 mM NaCl, and 2 mM DTT was mixed with 2 μ l of 30 mM MgCl₂, 6 mM ATP, 1 μ l of 100 mM DTT, and 1 μ l of 0.255 mg/ml CDK1-CCNB1 (Enzo Life Sciences, catalog no. BML-SE295-0010). The reaction mixture was kept at 25°C for 1.5 hours.

MS analysis

Sample preparation

Phosphorylated HIS-SMT3-ZAR1(1-263) was denatured with 1% RapiGest. Reduction and alkylation of cysteine residues were performed using 25 mM DTT and 33 mM iodoacetamide (IAA), respectively. Proteins were then digested with trypsin (Promega, catalog no. V5111) at a 1:20 enzyme-to-protein ratio in 25 mM ammonium bicarbonate overnight at 37°C. Digestion was quenched with 2% formic acid (FA) at 37°C for 2 hours. Precipitated RapiGest was removed by centrifugation. Phosphopeptides were enriched using TiO₂ spin columns packed in-house as described previously (102). In brief, the column was equilibrated with buffer B [80% acetonitrile (ACN) and 5% trifluoroacetic acid (TFA)] and buffer A (5% glycerol in buffer B). Peptides were loaded onto the TiO₂ column in buffer A and washed several times with buffer A, buffer B, and buffer BII (60% ACN and 0.1% TFA). Enriched phosphopeptides were eluted with 0.3 M NH₄OH and dried in a SpeedVac evaporator. Phosphopeptides were dissolved in 2% ACN and 0.05% TFA

and ten subjected to liquid chromatography-electrospray ionization-tandem MS (LC-ESI-MS/MS) measurements.

Identical numbers of GV oocytes were incubated at 37°C for 7 hours in medium supplemented with either 10 μ M RO-3306 or with DMSO. Prophase arrested oocytes and in vitro matured MI oocytes were collected and resuspended in 150 μ l of lysis buffer (50 mM HEPES, pH 7.5, 150 mM NaCl, 4% SDS, 2 mM DTT, and 0.5% NP-40). The cells were mechanically disrupted by a Bioruptor (Diagenode) for 10 min with cycles of 30 s off/30 s on at the highest output level. Samples were then heated to 99°C for 10 min and diluted to 1% SDS with 50 mM HEPES, pH 7.5. Then, 500 U of universal nuclease (Thermo Fisher Scientific, catalog no. 88700) and 1 mM MgCl₂ were added, followed by 30 min of incubation at 37°C. Proteins were reduced and alkylated with 5 mM DTT and 20 mM IAA, respectively. Residual IAA was quenched by adding another 5 mM DTT. Protein cleanup was performed using the SP3 method as described previously (103). On-bead protein digestion and phosphopeptide enrichment were performed as described above.

LC-ESI-MS/MS

All peptide samples were measured on an Orbitrap Exploris 480 mass spectrometer (Thermo Fisher Scientific) coupled to a Dionex Ultimate 3000 RSLCnano system. Peptides were loaded on a Pepmap 300 C18 column (Thermo Fisher Scientific) at a flow rate of 10 μ l/min in buffer A (0.1% FA) and then separated on an C18 column (30 cm; ReproSil-Pur 120Å, 1.9 μ m, C18-AQ; inner diameter, 75 μ m) packed in-house at a flow rate of 300 nl/min.

ZAR1 phosphopeptides from the in vitro phosphorylation assay were analyzed over 58 min. A linear gradient from 10 to 45% buffer B (80% ACN and 0.08% FA) over 44 min was applied to elute peptides, followed by 5 min in 90% buffer B and 6 min in 5% buffer B. Eluting peptides were analyzed in positive mode using a data-dependent top 20 acquisition method. MS1 and MS2 resolution were set to 120,000 and 30,000 full width at half maximum (FWHM), respectively, and AGC targets were 10⁶ and 10⁵. Precursors selected during MS1 scans [scan range, mass/charge ratio (m/z) 350 to 1600] were fragmented using 30% normalized, higher-energy collision-induced dissociation (HCD) fragmentation. Further MS/MS parameters were set as follows: isolation width, 1.6 m/z ; dynamic exclusion, 9 s; and maximum injection times (MS1/MS2), 60 ms/120 ms.

The phosphopeptides from mouse oocytes were analyzed over 88 min. A linear gradient from 10 to 40% buffer B over 70 min was applied, followed by 5 min in 90% buffer B and 5 min in 5% buffer B. Eluting peptides were analyzed in positive mode using a data-dependent

top 30 acquisition method. MS1 and MS2 resolution were set to 120,000 and 15,000 FWHM, respectively, and AGC targets were 3 \times 10⁶ and 5 \times 10⁴. Precursors (scan range, m/z 350 to 1600) were fragmented using 28% normalized HCD fragmentation. Further MS/MS parameters were set as follows: isolation width, 1.6 m/z ; dynamic exclusion, 30 s; maximum injection times (MS1/MS2), 50 ms/54 ms. For all measurements, the lock mass option (m/z 445.120025) was used for internal calibration.

MS data analysis

MS data analysis was performed using MaxQuant (software version 1.6.5.0) and a reviewed database of canonical protein sequences from *Mus musculus* (downloaded from UniProt on October 9th, 2021 containing 17,077 entries) (104, 105). For phosphorylation site identification, carbamidomethylation was set as a fixed modification; oxidation of methionine and phosphorylation of serine, threonine, and tyrosine were set as variable modifications. Default settings were used apart from those mentioned above.

Image analysis and quantification

Images were analyzed in Fiji (NIH) (97), Imaris (Bitplane), or ZEN (Zeiss) software. The exported data were further processed in Excel and Graphpad Prism 9.

Time-lapse movies of live oocytes were analyzed in three dimensions (3D) using Imaris. Nuclear envelope breakdown was defined as the time point when the sharp boundary between the nucleus and cytoplasm disappeared in the differential interference contrast image. Anaphase onset was defined as the time point before chromosome separation was first observed. To score for chromosome misalignment, chromosomes that failed to congress on the metaphase plate at anaphase onset were classified as misaligned chromosomes. Oocytes that entered into anaphase, extruded the first polar body, but soon refused with the polar body were categorized as cytokinesis failure. Two spindles or one united spindle could be observed in the fused cell. To quantify spindle volume, the spindle labeled by mClover3-MAP4-MTBD was segmented using the “surface” function of Imaris (surfaces detail: 2.5; background subtraction: 1.5). A suitable threshold was selected to detect the spindle as accurately as possible. Surfaces were further filtered with “number of voxels Img=1.” Falsely detected structures were removed manually, and the data were exported into Excel.

Z stacks of smRNA-FISH were also analyzed with Imaris. Images were processed with “normalize layers” before analysis. The MARDO labeled by ZAR1-mClover3 was segmented using the “surface” function of Imaris (surfaces detail: 0.165; background subtraction: 0.62). A suitable threshold was selected to detect the MARDO

as accurately as possible. Surfaces were further filtered with “number of voxels Img=1.” Spots of mRNA were detected with an estimated diameter of 1.2 μ m in x - y and 2.4 μ m in z , and with “background subtraction.” A suitable threshold was selected to detect mRNA spots as accurately as possible. Falsely detected spots were removed manually. “Distance transformation” was then performed to calculate the shortest distance of each spot to the surface (MARDO). If the distance is 0, it means that the mRNA spot is inside of the MARDO; if the distance is >0 but <0.6 μ m, it means that the mRNA spot is attached to the MARDO.

Quantification of signal on mitochondria and in the cytosol was performed in Fiji as described below. The channel that labels mitochondria was duplicated and then processed with a band-pass filter (filter_large = 40, filter_small = 1, suppress = none, tolerance = 5, autoscale, saturate). Mitochondria were segmented by setting auto threshold (Li dark). Particles in the range of 0.10 μ m² to infinity were added to ROI manager. All nonspecific particles outside of the cell were removed. Multimeasure of all channels was applied, and data were exported for further analysis. Mitochondria were then removed to measure the fluorescence intensity in the cytosol. The remaining cytosol was segmented by setting auto threshold (default). The mean fluorescence intensity on mitochondria was measured by dividing the total intensity by the total area of all objects >0.10 μ m². The ratio of mean intensities between two channels (TMRM/MitoTracker Green) or between mitochondria and cytosol was then calculated and normalized. The number of objects (>0.10 μ m²) is also the number (N) of mitochondrial clusters. 1/ N was applied as the mitochondrial clustering index and normalized to assess mitochondrial clustering.

To quantify total fluorescence intensity change of ZAR1-mScarlet or LSM14B-mScarlet over time, Z projection (sum slices) was performed first and then all time points were measured by applying “measure stack” in Fiji. Except for this experiment, all other fluorescence intensity measurements refer to measurements of the mean fluorescence intensity. To measure the mean fluorescence intensity in oocytes, oocytes were segmented by applying a suitable threshold or were manually outlined on the basis of the differential interference contrast image if there was no marker labeling the entire oocyte. To quantify the number of PLA spots, Watershed was applied to separate connected spots after thresholding. The data were normalized by dividing the values of each group by the mean of the control group in each experiment.

Statistical analysis

SD was used as y -axis error bars for bar charts and curves plotted from the mean value of the

data. Statistical significance based on unpaired, two-tailed Student's *t* test (for comparison of two groups) was calculated in Excel. Statistical significance based on one-way ANOVA followed by Tukey's post hoc test (for comparison of three or more groups) or two-tailed Fisher's exact test was calculated in Graphpad Prism 9. All data are from at least two independent experiments. In the figures, significance is designated as follows: *****P* < 0.0001, ****P* < 0.001, ***P* < 0.01, **P* < 0.05. Nonsignificant values are indicated as N.S.

REFERENCES AND NOTES

- G. P. Moore, S. Lintern-Moore, H. Peters, M. Faber, RNA synthesis in the mouse oocyte. *J. Cell Biol.* **60**, 416–422 (1974). doi: [10.1083/jcb.60.2.416](#); pmid: [4813213](#)
- J. N. Dumdie *et al.*, Chromatin modification and global transcriptional silencing in the oocyte mediated by the mRNA decay activator ZFP36L2. *Dev. Cell* **44**, 392–402.e7 (2018). doi: [10.1016/j.devcel.2018.01.006](#); pmid: [29408237](#)
- D. Jukam, S. A. M. Shariati, J. M. Skotheim, Zygotic genome activation in vertebrates. *Dev. Cell* **42**, 316–332 (2017). doi: [10.1016/j.devcel.2017.07.026](#); pmid: [28829942](#)
- L. Li, P. Zheng, J. Dean, Maternal control of early mouse development. *Development* **137**, 859–870 (2010). doi: [10.1242/dev.039487](#); pmid: [20179092](#)
- Y. Lin, D. S. Protter, M. K. Rosen, R. Parker, Formation and maturation of phase-separated liquid droplets by RNA-binding proteins. *Mol. Cell* **60**, 208–219 (2015). doi: [10.1016/j.molcel.2015.08.018](#); pmid: [26412307](#)
- M. Ferlic *et al.*, Coexisting liquid phases underlie nucleolar subcompartments. *Cell* **165**, 1686–1697 (2016). doi: [10.1016/j.cell.2016.04.047](#); pmid: [27212236](#)
- J. Y. Youn *et al.*, Properties of stress granule and P-body proteomes. *Mol. Cell* **76**, 286–294 (2019). doi: [10.1016/j.molcel.2019.09.014](#); pmid: [31626750](#)
- D. L. J. Lafontaine, J. A. Riback, R. Bascetin, C. P. Brangwynne, The nucleolus as a multiphase liquid condensate. *Nat. Rev. Mol. Cell Biol.* **22**, 165–182 (2021). doi: [10.1038/s41580-020-0272-6](#); pmid: [32873929](#)
- G. Seydoux, The P granules of *C. elegans*: A genetic model for the study of RNA-protein condensates. *J. Mol. Biol.* **430**, 4702–4710 (2018). doi: [10.1016/j.jmb.2018.08.007](#); pmid: [30096346](#)
- C. P. Brangwynne *et al.*, Germline P granules are liquid droplets that localize by controlled dissolution/condensation. *Science* **324**, 1729–1732 (2009). doi: [10.1126/science.1172046](#); pmid: [19460965](#)
- T. Trcek, R. Lehmann, Germ granules in *Drosophila*. *Traffic* **20**, 650–660 (2019). doi: [10.1111/tra.12674](#); pmid: [31218815](#)
- K. E. Kistler *et al.*, Phase transitioned nuclear Oskar promotes cell division of *Drosophila* primordial germ cells. *eLife* **7**, e37949 (2018). doi: [10.7554/eLife.37949](#); pmid: [30260314](#)
- M. Bose, M. Lampe, J. Mahamid, A. Ephrussi, Liquid-to-solid phase transition of oskar ribonucleoprotein granules is essential for their function in *Drosophila* embryonic development. *Cell* **185**, 1308–1324.e23 (2022). doi: [10.1016/j.cell.2022.02.022](#); pmid: [35325593](#)
- A. Jamieson-Lucy, M. C. Mullins, The vertebrate Balbiani body, germ plasm, and oocyte polarity. *Curr. Top. Dev. Biol.* **135**, 1–34 (2019). doi: [10.1016/bbs.ctdb.2019.04.003](#); pmid: [31155356](#)
- E. Boke *et al.*, Amyloid-like self-assembly of a cellular compartment. *Cell* **166**, 637–650 (2016). doi: [10.1016/j.cell.2016.06.051](#); pmid: [27471966](#)
- A. T. Hertig, E. C. Adams, Studies on the human oocyte and its follicle. I. Ultrastructural and histochemical observations on the primordial follicle stage. *J. Cell Biol.* **34**, 647–675 (1967). doi: [10.1083/jcb.34.2.647](#); pmid: [4292010](#)
- M. Flemr, J. Ma, R. M. Schultz, P. Svoboda, P-body loss is concomitant with formation of a messenger RNA storage domain in mouse oocytes. *Biol. Reprod.* **82**, 1008–1017 (2010). doi: [10.1095/biolreprod.109.082057](#); pmid: [20075394](#)
- Y. Kato *et al.*, ELAVL2-directed RNA regulatory network drives the formation of quiescent primordial follicles. *EMBO Rep.* **20**, e48251 (2019). doi: [10.15252/embr.201948251](#); pmid: [31657143](#)
- J. Yu, N. B. Hecht, R. M. Schultz, RNA-binding properties and translation repression in vitro by germ cell-specific MSY2 protein. *Biol. Reprod.* **67**, 1093–1098 (2002). doi: [10.1095/biolreprod.67.4.1093](#); pmid: [12297523](#)
- S. Medvedev, H. Pan, R. M. Schultz, Absence of MSY2 in mouse oocytes perturbs oocyte growth and maturation, RNA stability, and the transcriptome. *Biol. Reprod.* **85**, 575–583 (2011). doi: [10.1095/biolreprod.111.091710](#); pmid: [21613634](#)
- Y. Rong *et al.*, ZAR1 and ZAR2 are required for oocyte meiotic maturation by regulating the maternal transcriptome and mRNA translational activation. *Nucleic Acids Res.* **47**, 11387–11402 (2019). doi: [10.1093/nar/gkz863](#); pmid: [31598710](#)
- T. M. Yamamoto *et al.*, Zar1 represses translation in *Xenopus* oocytes and binds to the TCS in maternal mRNAs with different characteristics than Zar2. *Biochim. Biophys. Acta* **1829**, 1034–1046 (2013). doi: [10.1016/j.bbagr.2013.06.001](#); pmid: [23827238](#)
- L. Miao *et al.*, Translation repression by maternal RNA binding protein Zar1 is essential for early oogenesis in zebrafish. *Development* **144**, 128–138 (2017). pmid: [27913641](#)
- V. E. Deuschmeyer, A. M. Richter, The ZAR1 protein in cancer; from epigenetic silencing to functional characterisation and epigenetic therapy of tumour suppressors. *Biochim. Biophys. Acta Rev. Cancer* **1874**, 188417 (2020). doi: [10.1016/j.bbcan.2020.188417](#); pmid: [32828887](#)
- P. Bouvet, A. P. Wolffe, A role for transcription and FRGY2 in masking maternal mRNA within *Xenopus* oocytes. *Cell* **77**, 931–941 (1994). doi: [10.1016/0092-8674\(94\)90141-4](#); pmid: [8004679](#)
- J. Yu, N. B. Hecht, R. M. Schultz, Expression of MSY2 in mouse oocytes and preimplantation embryos. *Biol. Reprod.* **65**, 1260–1270 (2001). doi: [10.1095/biolreprod.65.4.1260](#); pmid: [11566752](#)
- T. Zhang *et al.*, RNA-associated protein LSM family member 14 controls oocyte meiotic maturation through regulating mRNA pools. *J. Reprod. Dev.* **63**, 383–388 (2017). doi: [10.1262/jrd.2017-018](#); pmid: [28458300](#)
- F. Rasch, R. Weber, E. Izaurralde, C. Igreja, 4E-T-bound mRNAs are stored in a silenced and deadenylated form. *Genes Dev.* **34**, 847–860 (2020). doi: [10.1101/gad.336073.119](#); pmid: [32354837](#)
- E. Seli *et al.*, An embryonic poly(A)-binding protein (ePAB) is expressed in mouse oocytes and early preimplantation embryos. *Proc. Natl. Acad. Sci. U.S.A.* **102**, 367–372 (2005). doi: [10.1073/pnas.0408378102](#); pmid: [15630085](#)
- O. Guzeloglu-Kayisli *et al.*, Embryonic poly(A)-binding protein (EPAB) is required for oocyte maturation and female fertility in mice. *Biochem. J.* **446**, 47–58 (2012). doi: [10.1042/BJ2010467](#); pmid: [22621333](#)
- P. Ivanov, N. Kedersha, P. Anderson, Stress granules and processing bodies in translational control. *Cold Spring Harb. Perspect. Biol.* **11**, a032813 (2019). doi: [10.1101/cshperspect.a032813](#); pmid: [30082464](#)
- C. So, S. Cheng, M. Schuh, Phase separation during germline development. *Trends Cell Biol.* **31**, 254–268 (2021). doi: [10.1016/j.tcb.2020.12.004](#); pmid: [33455855](#)
- S. Maharana *et al.*, RNA buffers the phase separation behavior of prion-like RNA binding proteins. *Science* **360**, 918–921 (2018). doi: [10.1126/science.aar7366](#); pmid: [29650702](#)
- B. Mészáros, G. Erdos, Z. Dosztányi, IUPred2A: Context-dependent prediction of protein disorder as a function of redox state and protein binding. *Nucleic Acids Res.* **46** (W1), W329–W337 (2018). doi: [10.1093/nar/gky384](#); pmid: [29860432](#)
- Y. Yu, R. Dumollard, A. Rossbach, F. A. Lai, K. Swann, Redistribution of mitochondria leads to bursts of ATP production during spontaneous mouse oocyte maturation. *J. Cell. Physiol.* **224**, 672–680 (2010). doi: [10.1002/jcp.22171](#); pmid: [20578238](#)
- C. M. Dalton, J. Carroll, Biased inheritance of mitochondria during asymmetric cell division in the mouse oocyte. *J. Cell Sci.* **126**, 2955–2964 (2013). pmid: [23659999](#)
- W. T. Snead, A. S. Gladfelter, The control centers of biomolecular phase separation: How membrane surfaces, PTMs, and active processes regulate condensation. *Mol. Cell* **76**, 295–305 (2019). doi: [10.1016/j.molcel.2019.09.016](#); pmid: [31604601](#)
- S. Medvedev, J. Yang, N. B. Hecht, R. M. Schultz, CDC2A (CDK1)-mediated phosphorylation of MSY2 triggers maternal mRNA degradation during mouse oocyte maturation. *Dev. Biol.* **321**, 205–215 (2008). doi: [10.1016/j.ydbio.2008.06.016](#); pmid: [18606161](#)
- L. B. Y. Josefsberg, D. Galiani, A. Dantes, A. Amsterdam, N. Dekel, The proteasome is involved in the first metaphase-to-anaphase transition of meiosis in rat oocytes. *Biol. Reprod.* **62**, 1270–1277 (2000). doi: [10.1095/biolreprod.62.5.1270](#); pmid: [10775176](#)
- D. Clift *et al.*, A method for the acute and rapid degradation of endogenous proteins. *Cell* **171**, 1692–1706.e18 (2017). doi: [10.1016/j.cell.2017.10.033](#); pmid: [29153837](#)
- K. J. Tanaka *et al.*, RAP55, a cytoplasmic mRNP component, represses translation in *Xenopus* oocytes. *J. Biol. Chem.* **281**, 40096–40106 (2006). doi: [10.1074/jbc.M609059200](#); pmid: [17074753](#)
- D. Jansova, A. Tetkova, M. Koncicka, M. Kubelka, A. Susor, Localization of RNA and translation in the mammalian oocyte and embryo. *PLOS ONE* **13**, e0192544 (2018). doi: [10.1371/journal.pone.0192544](#); pmid: [29529035](#)
- F. Lim, T. P. Downey, D. S. Peabody, Translational repression and specific RNA binding by the coat protein of the *Pseudomonas* phage PP7. *J. Biol. Chem.* **276**, 22507–22513 (2001). doi: [10.1074/jbc.M102411200](#); pmid: [11306589](#)
- B. Wu, J. A. Chao, R. H. Singer, Fluorescence fluctuation spectroscopy enables quantitative imaging of single mRNAs in living cells. *Biophys. J.* **102**, 2936–2944 (2012). doi: [10.1016/j.bpj.2012.05.017](#); pmid: [22735544](#)
- X. G. Luong, E. M. Daldello, G. Rajkovic, C. R. Yang, M. Conti, Genome-wide analysis reveals a switch in the translational program upon oocyte meiotic resumption. *Nucleic Acids Res.* **48**, 3257–3276 (2020). doi: [10.1093/nar/gkaa010](#); pmid: [31970406](#)
- C. Zhang, M. Wang, Y. Li, Y. Zhang, Profiling and functional characterization of maternal mRNA translation during mouse maternal-to-zygotic transition. *Sci. Adv.* **8**, eab3967 (2022). doi: [10.1126/sciadv.abj3967](#); pmid: [35108058](#)
- Z. Xiong *et al.*, Ultrasensitive Ribo-seq reveals translational landscapes during mammalian oocyte-to-embryo transition and pre-implantation development. *Nat. Cell Biol.* **24**, 968–980 (2022). doi: [10.1038/s41556-022-00928-6](#); pmid: [35697785](#)
- X. Wu *et al.*, Zygote arrest 1 (Zar1) is a novel maternal-effect gene critical for the oocyte-to-embryo transition. *Nat. Genet.* **33**, 187–191 (2003). doi: [10.1038/ng1079](#); pmid: [12539046](#)
- D. Bai *et al.*, Genome transfer for the prevention of female infertility caused by maternal gene mutation. *J. Genet. Genomics* **47**, 311–319 (2020). doi: [10.1016/j.jgg.2020.06.002](#); pmid: [32893179](#)
- J. Ma, M. Flemr, H. Strnad, P. Svoboda, R. M. Schultz, Maternally recruited DCPIA and DCP2 contribute to messenger RNA degradation during oocyte maturation and genome activation in mouse. *Biol. Reprod.* **88**, 11 (2013). doi: [10.1095/biolreprod.112.105312](#); pmid: [23136299](#)
- J. Ma, Y. Fukuda, R. M. Schultz, Mobilization of dormant Cnot7 mRNA promotes deadenylation of maternal transcripts during mouse oocyte maturation. *Biol. Reprod.* **93**, 48 (2015). doi: [10.1095/biolreprod.115.130344](#); pmid: [26134871](#)
- M. Pasternak, S. Pfender, B. Santhanam, M. Schuh, The BTG4 and CAF1 complex prevents the spontaneous activation of eggs by deadenylating maternal mRNAs. *Open Biol.* **6**, 160184 (2016). doi: [10.1098/rsob.160184](#); pmid: [27605379](#)
- C. Yu *et al.*, BTG4 is a meiotic cell cycle-coupled maternal-zygotic-transition licensing factor in oocytes. *Nat. Struct. Mol. Biol.* **23**, 387–394 (2016). doi: [10.1038/nsmb.3204](#); pmid: [27065194](#)
- Q. Q. Sha *et al.*, CNOT6L couples the selective degradation of maternal transcripts to meiotic cell cycle progression in mouse oocyte. *EMBO J.* **37**, e99333 (2018). doi: [10.15252/emboj.201899333](#); pmid: [30478191](#)
- L. W. Zhao *et al.*, PABPNIL mediates cytoplasmic mRNA decay as a placeholder during the maternal-to-zygotic transition. *EMBO Rep.* **21**, e49956 (2020). doi: [10.15252/embr.201949956](#); pmid: [32558204](#)
- A. J. Harvey, Mitochondria in early development: Linking the microenvironment, metabolism and the epigenome. *Reproduction* **157**, R159–R179 (2019). doi: [10.1530/REP.18-0431](#); pmid: [30870807](#)
- D. Adhikari *et al.*, Depletion of oocyte dynamin-related protein 1 shows maternal-effect abnormalities in embryonic development. *Sci. Adv.* **8**, eabl8070 (2022). doi: [10.1126/sciadv.abl8070](#); pmid: [35704569](#)
- H. Sasaki *et al.*, Impact of oxidative stress on age-associated decline in oocyte developmental competence. *Front. Endocrinol. (Lausanne)* **10**, 811 (2019). doi: [10.3389/fendo.2019.00811](#); pmid: [31824426](#)
- A. Rodríguez-Nuevo *et al.*, Oocytes maintain ROS-free mitochondrial metabolism by suppressing complex I. *Nature*

- 607, 756–761 (2022). doi: [10.1038/s41586-022-04979-5](https://doi.org/10.1038/s41586-022-04979-5); pmid: 35859172
60. W. Ma, C. Mayr, A membraneless organelle associated with the endoplasmic reticulum enables 3'UTR-mediated protein-protein interactions. *Cell* **175**, 1492–1506.e19 (2018). doi: [10.1016/j.cell.2018.10.007](https://doi.org/10.1016/j.cell.2018.10.007); pmid: 30449617
 61. M. Zacharogianni, A. Aguilera-Gomez, T. Veenendaal, J. Smout, C. Rabouille, A stress assembly that confers cell viability by preserving ERES components during amino-acid starvation. *eLife* **3**, e04132 (2014). doi: [10.7554/eLife.04132](https://doi.org/10.7554/eLife.04132); pmid: 25386913
 62. Y. Fujioka *et al.*, Phase separation organizes the site of autophagosome formation. *Nature* **578**, 301–305 (2020). doi: [10.1038/s41586-020-1977-6](https://doi.org/10.1038/s41586-020-1977-6); pmid: 32025038
 63. J. E. Lee, P. I. Cathey, H. Wu, R. Parker, G. K. Voeltz, Endoplasmic reticulum contact sites regulate the dynamics of membraneless organelles. *Science* **367**, eaay7108 (2020). doi: [10.1126/science.aay7108](https://doi.org/10.1126/science.aay7108); pmid: 32001628
 64. Y. C. Liao *et al.*, RNA granules hitchhike on lysosomes for long-distance transport, using annexin A11 as a molecular tether. *Cell* **179**, 147–164.e20 (2019). doi: [10.1016/j.cell.2019.08.050](https://doi.org/10.1016/j.cell.2019.08.050); pmid: 31539493
 65. G. Zhang, Z. Wang, Z. Du, H. Zhang, mTOR regulates phase separation of PGL granules to modulate their autophagic degradation. *Cell* **174**, 1492–1506.e22 (2018). doi: [10.1016/j.cell.2018.08.006](https://doi.org/10.1016/j.cell.2018.08.006); pmid: 30173914
 66. A. Yamasaki *et al.*, Liquidity is a critical determinant for selective autophagy of protein condensates. *Mol. Cell* **77**, 1163–1175.e9 (2020). doi: [10.1016/j.molcel.2019.12.026](https://doi.org/10.1016/j.molcel.2019.12.026); pmid: 31995729
 67. D. Milovanovic, Y. Wu, X. Bian, P. De Camilli, A liquid phase of synapsin and lipid vesicles. *Science* **361**, 604–607 (2018). doi: [10.1126/science.aat5671](https://doi.org/10.1126/science.aat5671); pmid: 29976799
 68. X. Yu *et al.*, The STING phase-separator suppresses innate immune signalling. *Nat. Cell Biol.* **23**, 330–340 (2021). doi: [10.1038/s41556-021-00659-0](https://doi.org/10.1038/s41556-021-00659-0); pmid: 33833429
 69. Y. G. Zhao, H. Zhang, Phase separation in membrane biology: The interplay between membrane-bound organelles and membraneless condensates. *Dev. Cell* **55**, 30–44 (2020). doi: [10.1016/j.devcel.2020.06.033](https://doi.org/10.1016/j.devcel.2020.06.033); pmid: 32726575
 70. U. Al-Zubaidi *et al.*, The spatio-temporal dynamics of mitochondrial membrane potential during oocyte maturation. *Mol. Hum. Reprod.* **25**, 695–705 (2019). doi: [10.1093/molehr/gaz055](https://doi.org/10.1093/molehr/gaz055); pmid: 31579926
 71. A. A. Rowland, G. K. Voeltz, Endoplasmic reticulum-mitochondria contacts: Function of the junction. *Nat. Rev. Mol. Cell Biol.* **13**, 607–615 (2012). doi: [10.1038/nrm3440](https://doi.org/10.1038/nrm3440); pmid: 22992592
 72. B. A. Maxwell *et al.*, Ubiquitination is essential for recovery of cellular activities after heat shock. *Science* **372**, eaabc3593 (2021). doi: [10.1126/science.abc3593](https://doi.org/10.1126/science.abc3593); pmid: 34739326
 73. Y. Gwon *et al.*, Ubiquitination of G3BP1 mediates stress granule disassembly in a context-specific manner. *Science* **372**, eaab6548 (2021). doi: [10.1126/science.aab6548](https://doi.org/10.1126/science.aab6548); pmid: 34739333
 74. J. M. Cook, Master's thesis, University of Colorado at Denver (2015).
 75. L. Lei, A. C. Spradling, Mouse oocytes differentiate through organelle enrichment from sister cyst germ cells. *Science* **352**, 95–99 (2016). doi: [10.1126/science.aad2156](https://doi.org/10.1126/science.aad2156); pmid: 26917595
 76. M. Colnaghi, A. Pomiankowski, N. Lane, The need for high-quality oocyte mitochondria at extreme ploidy dictates mammalian germline development. *eLife* **10**, e69344 (2021). doi: [10.7554/eLife.69344](https://doi.org/10.7554/eLife.69344); pmid: 34279226
 77. S. Nijjar, H. R. Woodland, Localisation of RNAs into the germ plasm of vitellogenic *Xenopus* oocytes. *PLOS ONE* **8**, e61847 (2013). doi: [10.1371/journal.pone.0061847](https://doi.org/10.1371/journal.pone.0061847); pmid: 23626739
 78. E. F. Roovers *et al.*, Tdrd6a regulates the aggregation of Buc into functional subcellular compartments that drive germ cell specification. *Dev. Cell* **46**, 285–301.e9 (2018). doi: [10.1016/j.devcel.2018.07.009](https://doi.org/10.1016/j.devcel.2018.07.009); pmid: 30086300
 79. T. Brandmann *et al.*, Molecular architecture of LSM14 interactions involved in the assembly of mRNA silencing complexes. *EMBO J.* **37**, e97869 (2018). doi: [10.15252/emboj.201797869](https://doi.org/10.15252/emboj.201797869); pmid: 29510985
 80. B. Shen *et al.*, Generation of gene-modified mice via Cas9/RNA-mediated gene targeting. *Cell Res.* **23**, 720–723 (2013). doi: [10.1038/cr.2013.46](https://doi.org/10.1038/cr.2013.46); pmid: 23545779
 81. S. Pfender *et al.*, Live imaging RNAi screen reveals genes essential for meiosis in mammalian oocytes. *Nature* **524**, 239–242 (2015). doi: [10.1038/nature14568](https://doi.org/10.1038/nature14568); pmid: 26147080
 82. F. Xie, K. A. Timme, J. R. Wood, Using single molecule mRNA fluorescent in situ hybridization (RNA-FISH) to quantify mRNAs in individual murine oocytes and embryos. *Sci. Rep.* **8**, 7930 (2018). doi: [10.1038/s41598-018-26345-0](https://doi.org/10.1038/s41598-018-26345-0); pmid: 29785002
 83. B. T. Bajar *et al.*, Improving brightness and photostability of green and red fluorescent proteins for live cell imaging and FRET reporting. *Sci. Rep.* **6**, 20889 (2016). doi: [10.1038/srep20889](https://doi.org/10.1038/srep20889); pmid: 26879144
 84. D. S. Bindels *et al.*, mScarlet: A bright monomeric red fluorescent protein for cellular imaging. *Nat. Methods* **14**, 53–56 (2017). doi: [10.1038/nmeth.4074](https://doi.org/10.1038/nmeth.4074); pmid: 27869816
 85. R. C. Laker *et al.*, A novel MitoTimer reporter gene for mitochondrial content, structure, stress, and damage in vivo. *J. Biol. Chem.* **289**, 12005–12015 (2014). doi: [10.1074/jbc.M113.530527](https://doi.org/10.1074/jbc.M113.530527); pmid: 24644293
 86. H. Liu, J. H. Naismith, An efficient one-step site-directed deletion, insertion, single and multiple-site plasmid mutagenesis protocol. *BMC Biotechnol.* **8**, 91 (2008). doi: [10.1186/1472-6750-8-91](https://doi.org/10.1186/1472-6750-8-91); pmid: 19055817
 87. J. M. Cook, A. Charlesworth, Insertion of inter-domain linkers improves expression and bioactivity of Zygote arrest (Zar) fusion proteins. *Protein Eng. Des. Sel.* **30**, 313–319 (2017). doi: [10.1093/protein/gzx002](https://doi.org/10.1093/protein/gzx002); pmid: 28130327
 88. C. So *et al.*, A liquid-like spindle domain promotes centrosomal spindle assembly in mammalian oocytes. *Science* **364**, eaat9557 (2019). doi: [10.1126/science.aat9557](https://doi.org/10.1126/science.aat9557); pmid: 31249032
 89. M. Schuh, J. Ellenberg, Self-organization of MTOCs replaces centrosome function during centrosomal spindle assembly in live mouse oocytes. *Cell* **130**, 484–498 (2007). doi: [10.1016/j.cell.2007.06.025](https://doi.org/10.1016/j.cell.2007.06.025); pmid: 17693257
 90. L. A. Jaffe, M. Terasaki, Quantitative microinjection of oocytes, eggs, and embryos. *Methods Cell Biol.* **74**, 219–242 (2004). doi: [10.1016/S0091-679X\(04\)74010-8](https://doi.org/10.1016/S0091-679X(04)74010-8); pmid: 15575609
 91. J. Schindelin *et al.*, Fiji: An open-source platform for biological-image analysis. *Nat. Methods* **9**, 676–682 (2012). doi: [10.1038/nmeth.2019](https://doi.org/10.1038/nmeth.2019); pmid: 22743772
 92. D. Clift, C. So, W. A. McEwan, L. C. James, M. Schuh, Publisher Correction: Acute and rapid degradation of endogenous proteins by Trim-Away. *Nat. Protoc.* **14**, 2596–2596 (2019). doi: [10.1038/s41596-018-0092-8](https://doi.org/10.1038/s41596-018-0092-8); pmid: 30504914
 93. M. Martin, Cutadapt removes adapter sequences from high-throughput sequencing reads. *EMBnet J.* **17**, 10 (2011). doi: [10.14806/ej.17.1.200](https://doi.org/10.14806/ej.17.1.200)
 94. A. Dobin *et al.*, STAR: Ultrafast universal RNA-seq aligner. *Bioinformatics* **29**, 15–21 (2013). doi: [10.1093/bioinformatics/bts635](https://doi.org/10.1093/bioinformatics/bts635); pmid: 23104886
 95. S. Anders, P. T. Pyl, W. Huber, HTSeq—A Python framework to work with high-throughput sequencing data. *Bioinformatics* **31**, 166–169 (2015). doi: [10.1093/bioinformatics/btu638](https://doi.org/10.1093/bioinformatics/btu638); pmid: 25260700
 96. M. I. Love, W. Huber, S. Anders, Moderated estimation of fold change and dispersion for RNA-seq data with DESeq2. *Genome Biol.* **15**, 550 (2014). doi: [10.1186/s13059-014-0550-8](https://doi.org/10.1186/s13059-014-0550-8); pmid: 25516281
 97. G. Korotkevich *et al.*, Fast gene set enrichment analysis. *bioRxiv*, 060012 (2021).
 98. A. Subramanian *et al.*, Gene set enrichment analysis: A knowledge-based approach for interpreting genome-wide expression profiles. *Proc. Natl. Acad. Sci. U.S.A.* **102**, 15545–15550 (2005). doi: [10.1073/pnas.0506580102](https://doi.org/10.1073/pnas.0506580102); pmid: 16199517
 99. A. Liberzon *et al.*, Molecular signatures database (MSigDB) 3.0. *Bioinformatics* **27**, 1739–1740 (2011). doi: [10.1093/bioinformatics/btr260](https://doi.org/10.1093/bioinformatics/btr260); pmid: 21546393
 100. M. D. Robinson, D. J. McCarthy, G. K. Smyth, edgeR: A Bioconductor package for differential expression analysis of digital gene expression data. *Bioinformatics* **26**, 139–140 (2010). doi: [10.1093/bioinformatics/btp616](https://doi.org/10.1093/bioinformatics/btp616); pmid: 19910308
 101. M. E. Ritchie *et al.*, limma powers differential expression analyses for RNA-sequencing and microarray studies. *Nucleic Acids Res.* **43**, e47 (2015). doi: [10.1093/nar/gkv007](https://doi.org/10.1093/nar/gkv007); pmid: 25605792
 102. I. Fukuda *et al.*, Optimization of enrichment conditions on TiO2 chromatography using glycerol as an additive reagent for effective phosphoproteomic analysis. *J. Proteome Res.* **12**, 5587–5597 (2013). doi: [10.1021/pr400546u](https://doi.org/10.1021/pr400546u); pmid: 24245541
 103. C. S. Hughes *et al.*, Single-pot, solid-phase-enhanced sample preparation for proteomics experiments. *Nat. Protoc.* **14**, 68–85 (2019). doi: [10.1038/s41596-018-0082-x](https://doi.org/10.1038/s41596-018-0082-x); pmid: 30464214
 104. S. Tyanova, T. Temu, J. Cox, The MaxQuant computational platform for mass spectrometry-based shotgun proteomics. *Nat. Protoc.* **11**, 2301–2319 (2016). doi: [10.1038/nprot.2016.136](https://doi.org/10.1038/nprot.2016.136); pmid: 27809316
 105. J. Cox, M. Mann, MaxQuant enables high peptide identification rates, individualized p.p.b.-range mass accuracies and proteome-wide protein quantification. *Nat. Biotechnol.* **26**, 1367–1372 (2008). doi: [10.1038/nbt.1511](https://doi.org/10.1038/nbt.1511); pmid: 19029910
 106. R. Edgar, M. Domrachev, A. E. Lash, Gene Expression Omnibus: NCBI gene expression and hybridization array data repository. *Nucleic Acids Res.* **30**, 207–210 (2002). doi: [10.1093/nar/30.1.207](https://doi.org/10.1093/nar/30.1.207); pmid: 11752295
 107. Y. Perez-Riverol *et al.*, The PRIDE database resources in 2022: a hub for mass spectrometry-based proteomics evidences. *Nucleic Acids Res.* **50**, D543–D552 (2022). doi: [10.1093/nar/gkab1038](https://doi.org/10.1093/nar/gkab1038); pmid: 34723319

ACKNOWLEDGMENTS

We thank the staff of the animal facility, proteomics facility, and live-cell imaging facility of the Max Planck Institute for Multidisciplinary Sciences for technical assistance; the patients who participated in this study; the clinicians, nurses, and embryologists at Bourn Hall Clinic for support of this study; K. Maier and P. Cramer for help with RNA-seq; M. Daniel and L. Wartusch for coordination of animal experiments; K. Rentsch and L. Timm for genotyping; J. Uraji for help with the optimization of human oocyte fixation; M. Boiani for the goat anti-ZAR1 antibody; P. Lénárt, A. Politi, and E. Mönlich for advice on image analysis; M. Raabe, T. Dehne, and R. Pflanz for help with MS sample processing and analyses; Z. Yan for the plasmid pMitoTimer; R. Singer for the plasmids pHAGE-CMV-CFP-24×PP7 and pHAGE-UBC-NLS-HA-tdPCP-GFP; and Life Science editors for critical comments on the manuscript. **Funding:** The research leading to these results received financial support from the Max Planck Society and Deutsche Forschungsgemeinschaft (DFG, German Research Foundation) under Germany's Excellence Strategy (EXC 2067/1-390729940) and a DFG Leibniz Prize to M.S. (SCHU 3047/1-1). S.C. was further supported by a European Molecular Biology Organization (EMBO) long-term postdoctoral fellowship. **Author contributions:** S.C. and M.S. conceived the study. S.C. and M.S. designed the experiments and methods for data analysis. S.C. performed all experiments and analyzed the data with the following exceptions. G.A. performed the experiments described in Figs. 1W, 2J, 4A, 5G, and 6, C and G; analyzed the data shown in Fig. 2K and Fig. 6, D to F; and collected oocytes for the MS analysis shown in fig. S8A. C.S. performed electron microscopy experiments with T.R. L.M.W. performed the MS experiments described in figs. S8A and S9A. S.P. analyzed the RNA-seq data. K.M. collected and fixed human oocytes. K.H. and A.S. performed the MS experiments shown in fig. S1A and participated in the optimization of MS analysis of mouse oocytes. M.B. and K.E. supervised the collection of human oocytes. W.M. supervised the electron microscopy experiments. H.U. supervised the MS experiments. S.C. and M.S. wrote the manuscript and prepared the figures with input from all authors. M.S. supervised the study. **Competing interests:** The authors declare no competing interests. **Data and materials availability:** The RNA-seq datasets have been deposited in the National Center for Biotechnology Information (NCBI) GEO database (106) under accession number GSE213351. The phosphoproteomics data have been deposited to the ProteomeXchange Consortium via the PRIDE partner repository with the dataset identifier PXD036974 (107). Plasmids are available from M.S. under a material transfer agreement with the Max Planck Society. All data needed to evaluate the conclusions in the study are present in the main text or the supplementary materials. **License information:** Copyright © 2022 the authors, some rights reserved; exclusive licensee American Association for the Advancement of Science. No claim to original US government works. <https://www.science.org/about/science-licenses-journal-article-reuse>

SUPPLEMENTARY MATERIALS

science.org/doi/10.1126/science.abq4835

Figs. S1 to S15
Movies S1 to S10
Data S1 to S6
MDAR Reproducibility Checklist

Submitted 16 April 2022; accepted 22 September 2022
10.1126/science.abq4835

RESEARCH ARTICLES

STRUCTURAL BIOLOGY

Structure of the hepatitis C virus E1E2 glycoprotein complex

Alba Torrents de la Peña^{1†}, Kwinten Sliepen^{2,3,*}, Lisa Eshun-Wilson^{1†}, Maddy L. Newby⁴, Joel D. Allen⁴, Ian Zon^{2,3}, Sylvie Koekoek^{2,3}, Ana Chumbe^{2,3}, Max Crispin⁴, Janke Schinkel^{2,3}, Gabriel C. Lander¹, Rogier W. Sanders^{2,3,5*}, Andrew B. Ward^{1*}

Hepatitis C virus (HCV) infection is a leading cause of chronic liver disease, cirrhosis, and hepatocellular carcinoma in humans and afflicts more than 58 million people worldwide. The HCV envelope E1 and E2 glycoproteins are essential for viral entry and comprise the primary antigenic target for neutralizing antibody responses. The molecular mechanisms of E1E2 assembly, as well as how the E1E2 heterodimer binds broadly neutralizing antibodies, remain elusive. Here, we present the cryo-electron microscopy structure of the membrane-extracted full-length E1E2 heterodimer in complex with three broadly neutralizing antibodies—AR4A, AT1209, and IGH505—at ~3.5-angstrom resolution. We resolve the interface between the E1 and E2 ectodomains and deliver a blueprint for the rational design of vaccine immunogens and antiviral drugs.

Despite the need for a hepatitis C virus (HCV) prophylactic vaccine, vaccine development has been limited by the extensive sequence diversity of the virus and the lack of structural information on the vaccine target: the envelope glycoprotein E1E2 complex (1, 2). Previous studies suggest that eliciting broadly neutralizing antibodies (bNAbs), which target E1E2 during infection, correlates with viral clearance and protection in humans (3–5), whereas passively administered bNAbs protect against infection in animal models (6–8). These observations provide a motivation for the development of an HCV vaccine aimed at inducing bNAbs (1).

HCV is an enveloped, single-strand, positive-sense RNA virus from the Flaviviridae family. The RNA genome encodes a single polypeptide that is processed by host and viral proteases into three structural and seven nonstructural proteins (9). The E1 and E2 envelope proteins associate to form a glycoprotein complex located on the outside of the virus that drives entry into hepatocytes (9). The E2 subunit includes the receptor-binding domain and engages scavenger-receptor class B1 (SR-B1) and the tetraspanin CD81, whereas E1 is assumed to be the fusogenic subunit because it contains the putative fusion peptide (pFP) (10–12).

Because the E1E2 complex is the only viral protein on the surface of the virus, it is the sole target for bNAbs and thus an attractive candidate for structure-based immunogen design.

High-resolution structure determination of the full-length E1E2 heterodimer has been hindered by intrinsic flexibility, conformational heterogeneity, disulfide-bond scrambling, and extensive glycosylation (2, 13–16). The glycan shield not only protects E1E2 from immune recognition but also facilitates assembly and viral infection (16–18). At the present time, structural information is limited to truncated versions of recombinant E1 or E2, or small peptides (20–28). Moreover, antigenic region 4 (AR4), which includes the epitopes of several broad and potent HCV bNAbs such as AR4A and AT1618, has eluded structural characterization (5, 28). Whereas membrane-associated E1E2 displays AR4 and binds bNAb AR4A efficiently, soluble HCV E1E2 glycoprotein complex usually does not, suggesting that AR4 represents a metastable domain (18, 29–31). Using an optimized expression and purification scheme, we discovered that the coexpression and binding of AR4A stabilized the assembly of the full-length E1E2 heterodimer, producing a promising sample for structure determination. We subsequently determined the cryo-electron microscopy (cryo-EM) structure of the E1E2 heterodimer in complex with the fragment antigen binding (Fab) domain of AR4A and the Fabs of the bNAbs IGH505 and AT1209, providing a molecular description of three key neutralizing epitopes that pave the way for structure-based vaccine design.

Results

Purification and overall fold of E1E2

The full-length HCV envelope glycoprotein complex E1E2 described here is derived from

the genotype 1a strain AMS0232, which was obtained from an HCV-infected individual enrolled in the MOSAIC cohort (32). The AMS0232-based pseudovirus (HCVpp) was more resistant to neutralization by polyclonal HCV-positive sera than the reference strain H77 but was sensitive to AR4A, making it suitable for pursuing a complex with this bNAb (Fig. 1A and fig. S1A).

We coexpressed StrepII-tagged AR4A Fab with the E1E2 heterodimer and used StrepTactin purification to produce E1E2 in complex with AR4A (Fig. 1B). Negative-stain electron microscopy (NS-EM) revealed that E1E2 glycoprotein in complex with AR4A is more homogeneous than unbound E1E2 glycoprotein complexes, making AR4A-bound E1E2 more suitable for high-resolution structural characterization using cryo-EM (fig. S1, B and C). Binding of monoclonal antibodies and CD81 to E1E2, unbound or in complex with AR4A, was tested by enzyme-linked immunosorbent assay (ELISA) (fig. S1, D and E). Antibody binding correlated with neutralization of the parental pseudovirus, suggesting that AR4A-extracted E1E2 glycoprotein complex is antigenically analogous to functional E1E2 (fig. S1F). Additionally, we observed low binding of non-neutralizing monoclonal antibodies CBH-4B, CBH-4D, and CBH-4G in AR4A-extracted E1E2 glycoprotein complex, likely because of the steric blockage of AR4A (33).

For cryo-EM studies, we coexpressed the full-length E1E2 glycoprotein complex with the AT1209 Fab (34) and the StrepII-tagged AR4A Fab to increase E1E2 stability. The complex was extracted from the membrane and reconstituted into peptidiscs before the addition of the IGH505 Fab (Fig. 1B) (35, 36). To prevent mispairing of the AR4A and AT1209 heavy and light chains during synthesis, we used a CrossMab version of the AT1209 Fab (CrossFab) (37).

Although we were able to isolate a biochemically well-behaved complex of E1E2 bound to Fabs, the relatively small size and flexibility of the complex presented substantial challenges for high-resolution reconstruction. To overcome these challenges, we used 3D Variability Analysis in cryoSPARC (38) to resolve both discrete and flexible conformations of the E1E2 heterodimer bound to three Fabs. This strategy allowed us to determine the structures of the ectodomains at 3.5-Å resolution and the flexible domains at 3.8-Å resolution (fig. S2). This structure was sufficient to model 51% of E1 and 82% of E2, including the interface of these two envelope glycoproteins; the epitopes of bNAbs AR4A, AT1209, and IGH505; and the glycan shield (Fig. 1, C to E, and fig. S3). Regions that were not modeled in the E1E2 heterodimer bound to three Fabs included the disordered hypervariable region 1 (HVR1) in E2 (amino acids 384 to 410), amino acids 412 to 419 in antigenic site 412 (AS412, amino

¹Department of Integrative Structural Biology and Computational Biology, The Scripps Research Institute, La Jolla, CA 92037, USA.

²Department of Medical Microbiology and Infection Prevention, Laboratory of Experimental Virology, Amsterdam UMC, University of Amsterdam, 1105 AZ Amsterdam, Netherlands. ³Amsterdam Institute for Infection and Immunity, Infectious Diseases, 1105 AZ Amsterdam, Netherlands. ⁴School of Biological Sciences, University of Southampton, Southampton SO17 1BJ, UK. ⁵Weill Medical College of Cornell University, New York, NY 10065, USA.

*Corresponding author. Email: andrew@scripps.edu (A.B.W.); r.w.sanders@amsterdamumc.nl (R.W.S.); k.h.sliepen@amsterdamumc.nl (K.S.)

†These authors contributed equally to this work.

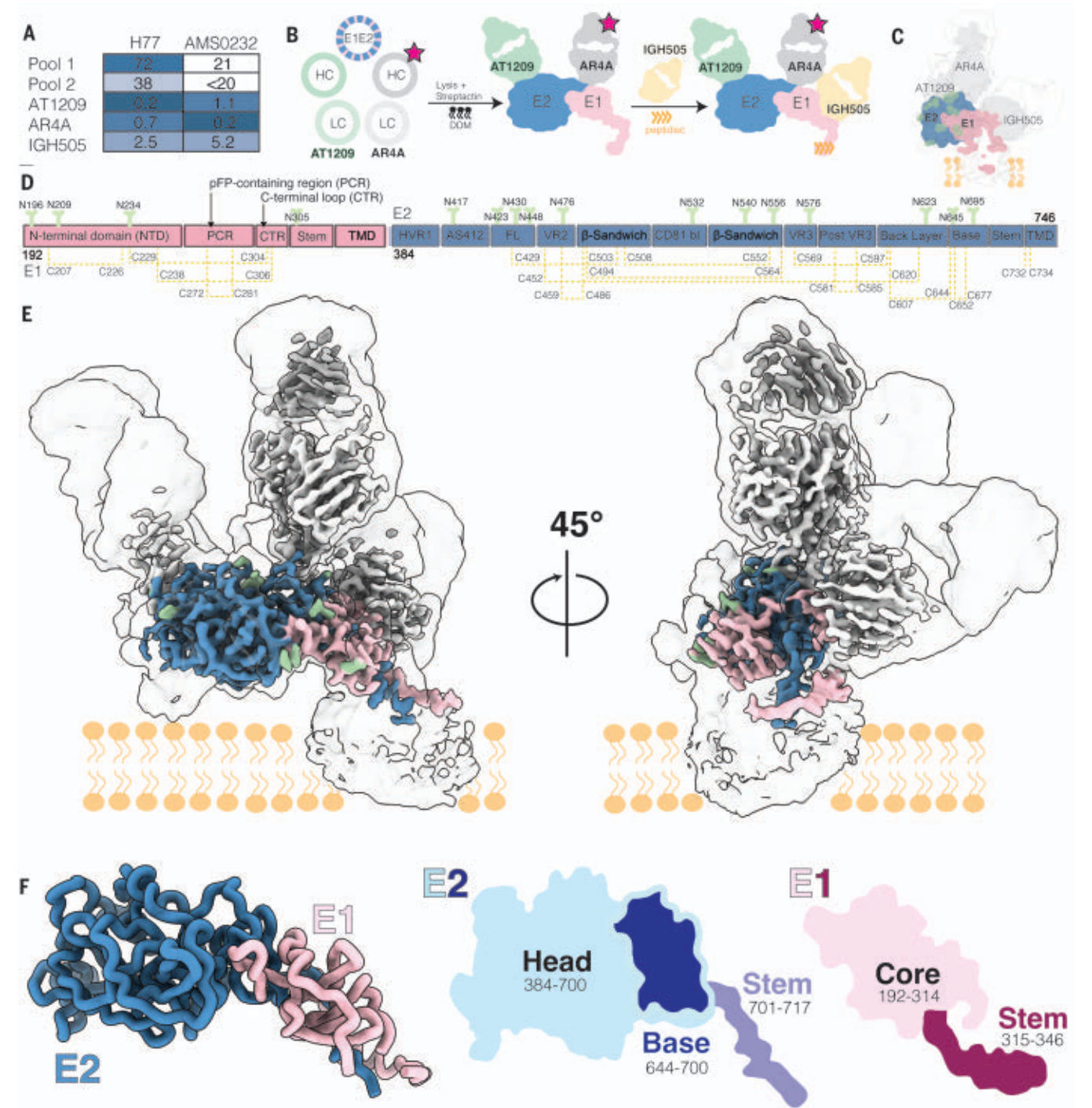


Fig. 1. Cryo-EM structure of the HCV E1E2 heterodimer in complex with bNAbs AT1209, IGH505, and AR4A. (A) Sensitivity of AMS0232 and H77 pseudovirus to neutralization by polyclonal serum pools and bNAbs AT1209, IGH505, and AR4A. The serum dilutions and antibody concentrations (in $\mu\text{g/ml}$) at which HCV infectivity is inhibited by 50% (ID_{50} and IC_{50} , respectively) are listed. Values are the mean of two or three independent experiments. Darker shading indicates increased sensitivity. (B) Schematic representation of the purification of full-length HCV E1E2. The stars indicate StrepII-tag. DDM, dodecyl- β -D-maltoside; HC, heavy chain; LC, light chain. (C) Cartoon representation of the cryo-EM map density of E1 and E2

in complex with AT1209, IGH505, and AR4A Fabs overlaid with the low-resolution cryo-EM map at a threshold of 0.1 in ChimeraX. (D) Schematic representation of the full-length E1E2 AMS0232 construct. The E1 and E2 subunits are shown in pink and blue, respectively, with the different subdomains indicated. N-linked glycans are shown in green and disulfide bonds in yellow. The same color coding is used in (E) and (F). (E) Cryo-EM map showing the density of the full-length E1E2 in complex with the three bNAbs. (F) View of E1E2 heterodimer. A cartoon representation of the head and stem regions of E2 with the newly resolved base region are highlighted.

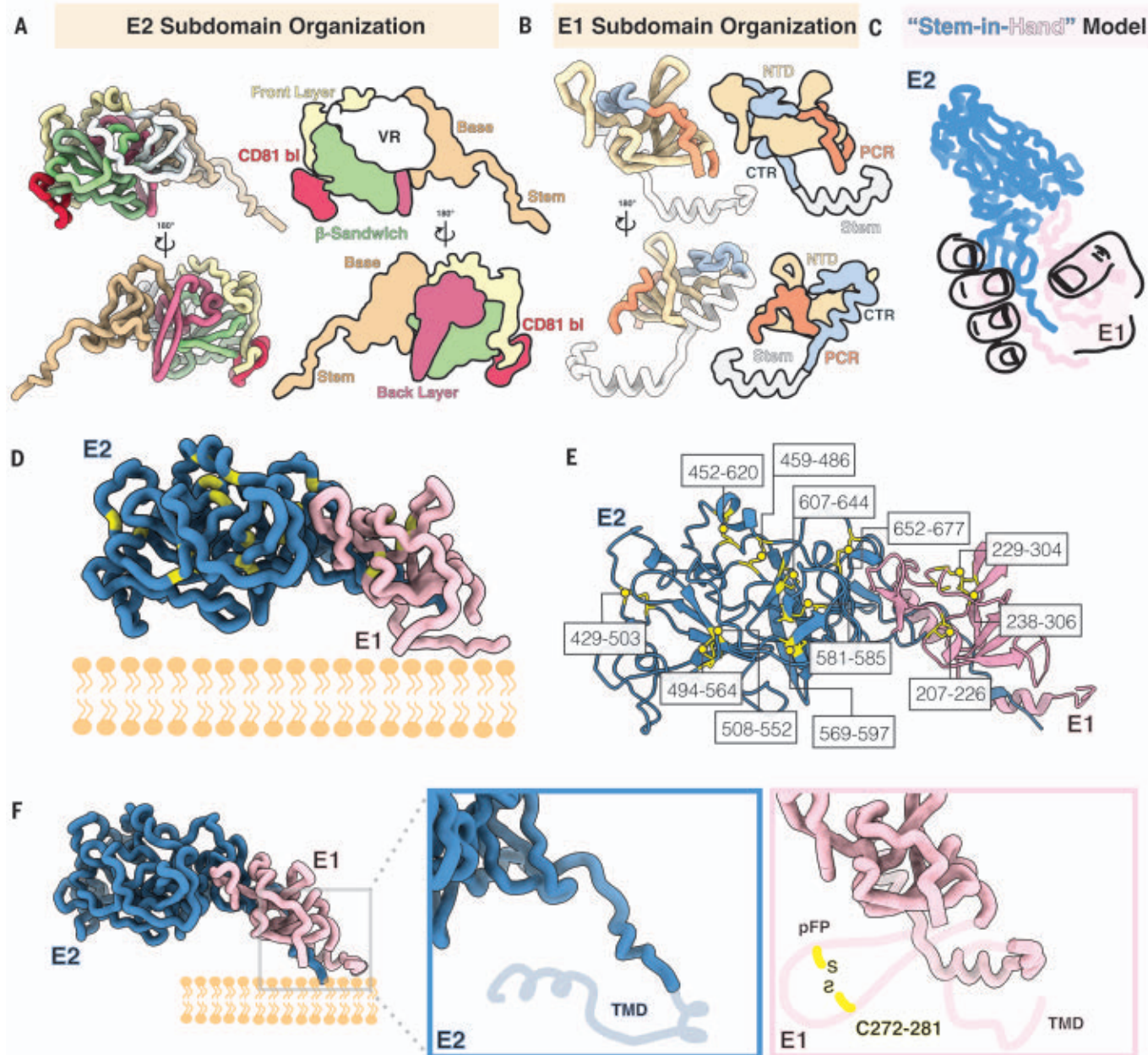


Fig. 2. Subdomain organization and disulfide bonds of E1 and E2. (A to F) View of E1E2 subdomains. In (A), each domain in E2 is colored and represented as licorice and cartoon. The E2 stem and base are shown in tan, followed by the back layer in magenta, the β sandwich in green, the front layer in yellow, and the CD81 binding site in red; all variable regions (VR) are shown in white. In (B), the E1 NTD is shown in yellow, whereas the PCR is shown in orange, the CTR in shown in blue, and the stem region is colored white. Shown in (C) is a stem-in-hand model of

E1 (hand) grasping the stem of E2. In (D), the location of each cysteine in E1E2 is highlighted in yellow and further outlined and numbered in (E). Shown in (F) are close-ups of the E1E2 C-terminal region to highlight the missing regions in this highly flexible region: the TMD in E2 and two helices in E1 that comprise the E1 pFP-containing region and contain a conserved disulfide bond as well as a TMD in E1 (indicated by the light pink cartoon line). The missing regions are depicted according to AlphaFold predictions.

acids 412 to 423) in E2, the transmembrane domains (TMDs) in E1 and E2 (amino acids 350 to 382 and 718 to 746, respectively), and lastly, the pFP-containing region (PCR) in E1 (residues 257 to 294) (figs. S3 and S4A). Although the E1 and E2 TMDs were unresolved, we combined the AlphaFold-predicted structure of these domains with our experimentally derived model to gain insight into the

positioning of E1E2 relative to the membrane (fig. S4D).

Subdomain organization of E1 and E2

E2 contains three subdomains—the head, stem, and TMD. Our structure of the E2 head domain in the E1E2 complex agrees well with previously reported crystal structures of recombinant E2, including the most complete crystal structure

[root mean square deviation (RMSD) of 0.805 Å, Protein Data Bank (PDB) ID 6MEI] (fig. S4A). However, our E1E2 structure reveals two previously unresolved regions of E2: (i) an extended loop interrupted by a small antiparallel β sheet in the E2 head that we term the “base” (residues 645 to 700) and (ii) the stem (residues 701 to 717), which connects the base with the TMD (amino acids 718 to 746; Figs. 1F

and 2A). The E2 head consists of a central β -sandwich core (residues 484 to 517 and 535 to 568), a front layer and a back layer (residues 420 to 458 and 596 to 643, respectively), the apical CD81 binding site (amino acids 518 to 534), HVR1 (residues 384 to 410), AS412 (residues 412 to 423), variable regions 2 and 3 (VR2, residues 459 to 483; VR3, residues 569 to 579), and the newly resolved base (residues 645 to 700).

In E1, our structure contains well-resolved density for the core (residues 192 to 314) and the stem (residues 315 to 346) (Fig. 1F). The E1 core includes the N-terminal domain (NTD; residues 192 to 248), the PCR (residues 249 to 299), and a C-terminal loop region (CTR; residues 300 to 314) that connects the PCR to the stem (Figs. 1F and 2B). The conformation of the E1 NTD differs substantially from that of a prior crystal structure of the soluble E1 NTD (25) (PDB ID 4UOI), suggesting that the presence of E2 is required for proper E1 folding. However, a prior crystal structure of 10 residues within the E1 stem (residues 314 to 324) aligns well with our atomic model of the E1 stem (residues 310 to 328) (RMSD = 0.254 Å) (fig. S4A) (27) (Figs. 1F and 2B and fig. S4, A and C).

Disulfide bond networks of E1 and E2

The cysteine residues in E1E2 are highly conserved, but disulfide-bond patterns differ between recombinant E2 structures (19–21, 39), whereas the disulfide bond network in E1 has remained largely elusive (40). In our cryo-EM structure, E2 is stabilized by nine disulfide bonds: C429–C503, C452–C620, C459–C486, C494–C564, C508–C552, C569–C597, C581–C585, C607–C644, and C652–C677 (Fig. 2, D to F) (C, Cys). Meanwhile, E1 is held together by four disulfide bonds: C207–C226, C229–C304, C238–C306, and C272–C281 (Fig. 2, D to F). The E2 disulfide network is consistent with that in previous crystal structures of the E2 ectodomain in complex with HEPC3 or HEPC74, although the C652–C677 cysteine pair in the E2 base was missing from these structures (21). By contrast, in most recombinant E2 structures and a structure of E2 core in complex with AR3C (PDB ID 4MWF), the cysteines at positions C569, C581, C585, and C597 are paired differently (fig. S3). We directly observed three disulfide bonds in E1 (C207–C226, C229–C304, and C238–C306), and AlphaFold predicted the presence of a fourth disulfide bridge between C272 and C281, which would connect two amphipathic helices of the pFP. The proximity of the cysteine pairs C494–C564 to C508–C552, C452–C620 to C459–C486, and C581–C585 to C569–C597 and C607–C644 in E2, as well as the close proximity of the three observed disulfide bonds in E1, likely allows disulfide scrambling resulting in heterogeneous E1E2 proteins (Fig. 2, E and F) (19, 20, 39, 41, 42).

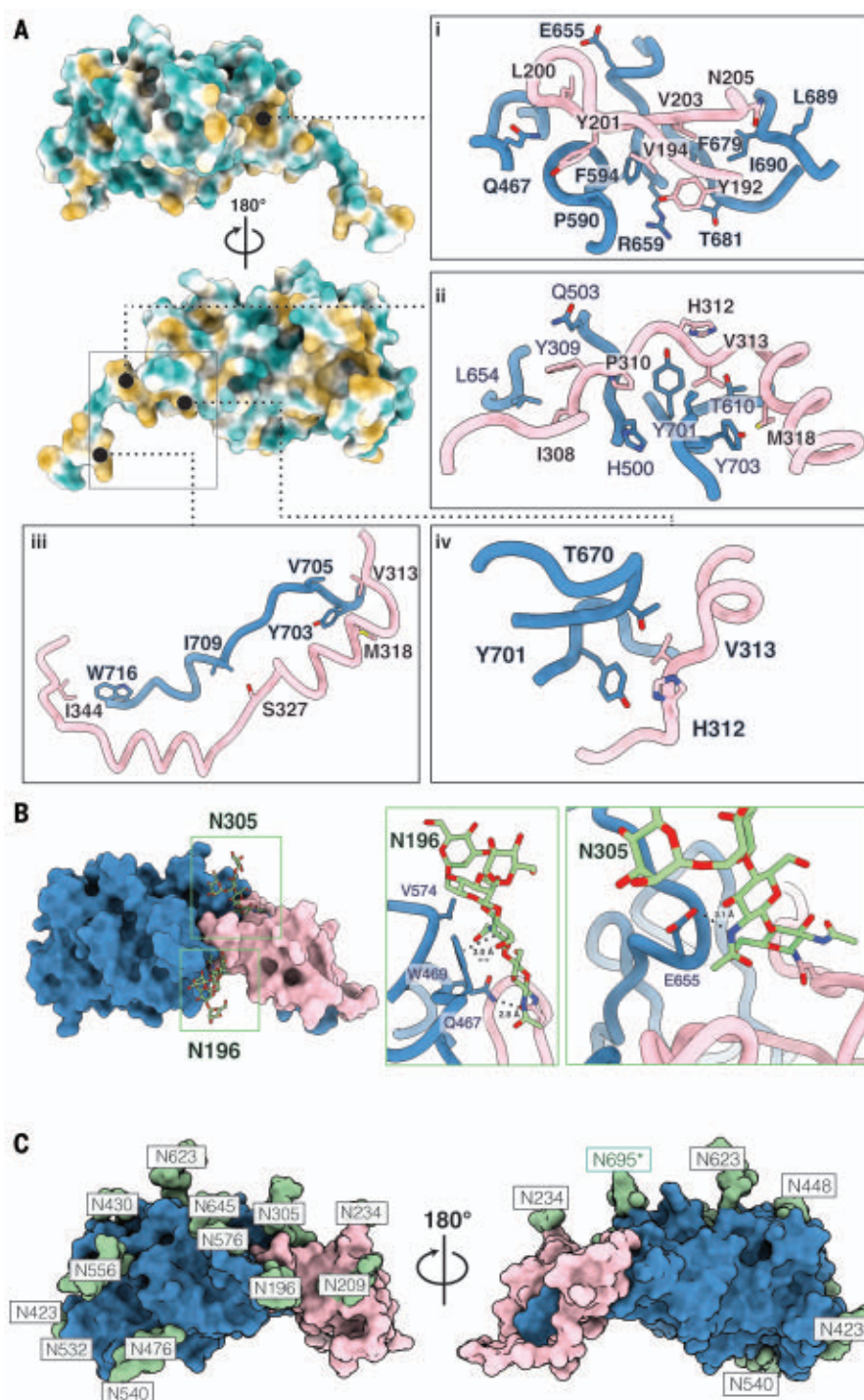


Fig. 3. The E1E2 interface and glycan shield. (A) The newly characterized E1E2 interface is stabilized by hydrophobic interactions. E2 is colored by hydrophobicity, with green representing hydrophilic regions and yellow signifying hydrophobic patches. The first panel (i) showcases a deep hydrophobic cavity in the base of E2 against which E1 packs. The following panels (ii to iv) highlight additional hydrophobic interactions that we assert further stabilize the E1E2 interface. (B) Glycans buttress the E1E2 interface. Key interactions between glycans N196 and N305 are showcased. Glycan N196 is involved in hydrophobic interactions, including a π - π stacking interaction with W469, as well as a salt bridge with Q467. N305 forms a stabilizing salt bridge with E655. (C) Surface representation of the E1 and E2 model showing the glycan sites in green with their respective asparagine residues. The predominant glycoform identified by LC-MS at each PNGS was modeled using Coot (59). An asterisk indicates that the glycan at position N695 uses a noncanonical N-glycosylation motif, NXV. Single-letter abbreviations for the amino acid residues are as follows: A, Ala; C, Cys; D, Asp; E, Glu; F, Phe; G, Gly; H, His; I, Ile; K, Lys; L, Leu; M, Met; N, Asn; P, Pro; Q, Gln; R, Arg; S, Ser; T, Thr; V, Val; W, Trp; and Y, Tyr.

The E1E2 interface

To illustrate the E1E2 interface, we posit the “stem-in-hand” model, wherein the E1 ectodomain wraps around the E2 stem and interacts with the base of E2 with a total shared buried surface area of $\sim 1879 \text{ \AA}^2$ (Fig. 2C). Consistent with earlier studies on intracellular E1E2 (43, 44), the interface interactions are non-covalent, comprising residues that mediate hydrophobic interactions or form hydrogen bonds. A highly conserved hydrophobic patch lines the E2 stem to stabilize the E1E2 heterodimer interface (Fig. 3 and fig. S5A). The E2 base contains a hydrophobic cavity involving residues F586, P590, F679, T681, L689, and I690, which interact with Y192, V194, Y201, and V203 on E1, whereas E655 and R659 form hydrogen bonds with L200 and G199 (Fig. 3A, i) (F, phenylalanine; I, isoleucine; L, leucine; P, proline; T, threonine; V, valine; Y, tyrosine). Within the hydrophobic stretch in the E2 stem, a region consisting of L654, Y701, and Y703 interacts with I308, Y309, P310, H312, V313, and M318 in E1 (Fig. 3A, ii and iv) and the stretch of residues Y703, V705, I709, and W716 pair with E1 residues V313, M318, S327, and I344 (Fig. 3A, iii) (H, histidine; M, methionine; S, serine; W, tryptophan).

The E1E2 interaction is further buttressed by two highly conserved glycans at N196 and N305 in E1 (Fig. 3B) (N, asparagine). The N305 glycan forms a salt bridge with E655 in E2, whereas the N196 glycan forms multiple interactions, including a salt bridge with Q467, π - π stacking interactions with the aromatic ring of W469, and hydrophobic packing interactions with V574 (Fig. 3B) (E, glutamate; Q, glutamine). To assess the relevance of this interface in infectivity, we measured viral entry of HCV pseudoparticles that contain amino acid mutations in the E1 NTD, E2 base, and E2 stem [Tyr²⁰¹→Ala (Y201A), N205A, R659A, F679A, L689A, and Y703A; R, arginine] or glycan interface (N196 and/or N305: T198A, S307A, and T198A+S307A) (figs. S5A, and S6). Most viral mutants were noninfectious (<5% infectivity compared with wild type) except for T198A ($\sim 31\%$ compared with wild type) (fig. S6). These data are consistent with and provide a structural basis for the results of a recent alanine scanning mutagenesis study on E1E2 pseudovirus (45), which also reported that amino acids R657, D658, L692, and Q700 in E2 and Y201, T204, N205, and D206 in E1 are crucial for infectivity (fig. S5, B to F) (D, aspartate).

The E1E2 glycan shield

All potential N-glycosylation sites (PNGSs) are located on one face of the E1E2 glycoprotein complex. The opposite face is hydrophobic and highly conserved (fig. S7A), consistent with an exposed neutralizing face subject to immune pressure and a non-neutralizing face that is

likely inaccessible on the surface of the virion (22, 23, 46). We detected density for glycans at all PNGSs except N325 in E1, which is not glycosylated because of a proline at the fourth position within the N325 sequon (47) (fig. S7D). Interestingly, although N-glycans are usually located at NXT and NXS sequons, we also identified an N-glycan attached to a noncanonical NXV motif at N695 in E2 (Fig. 3C and fig. S7B) (X, any amino acid except for proline). Site-specific glycan analysis of the E1E2 heterodimer in complex with AR4A and AT1209 using liquid chromatography-mass spectrometry (LC-MS) confirmed the presence of glycans at all canonical PNGSs except N325, as well as at the noncanonical N695 site, which was glycan-occupied in 25% of the sample (Fig. 3C and fig. S7B). Further glycan analysis revealed that the occupancy of N695 remained unchanged when the E1E2 glycoprotein complex was not bound to AR4A and AT1209 Fabs (fig. S7, B and C). Additionally, the antigenicity of N695 mutants (N695A, N695Q, and V697T) was not substantially affected, whereas viral infectivity was slightly increased when the 695 glycan was removed (N695A and N695Q) (fig. S8, A and B). Moreover, the E1E2 heterodimer was highly enriched in oligomannose-type glycans (Man₅₋₉GlcNAc₂), except for N234 (fig. S7B). The oligomannose content is high likely because the transmembrane domain of E1 is a signal for static retention in the endoplasmic reticulum, where glycans remain oligomannose-type species, combined with purification from intracellular compartments, including the endoplasmic reticulum (48, 49).

Definition of three bNAb epitopes

Importantly, our full-length E1E2 structure delivers a structural description of three bNAb epitopes in their full quaternary context, including the previously ill-defined epitopes in AR4. Previous alanine-scanning mutagenesis studies suggested that AR4A recognizes an epitope on both E1 and E2 (28, 50). However, our model shows that AR4A targets the back layer and base regions of E2 but does not engage E1 (Fig. 4A). AR4A contacts E2 almost exclusively using its 25-amino acid-long CDRH3 through five hydrophobic interactions and four hydrogen bonds (AR4A - E2: T100c - G649, F100d - I696; L100e - D698, W646, P676; W100f - L667, Q671, I696) (Fig. 4A and figs. S9A and S12). AR4A contains a nine-amino acid insert in the CDRH2 (fig. S9), and this allows Y52i to electrostatically interact with R648 in the back layer of E2 (Fig. 4). Notably, one glycan in E2 (N623) interacts with the NTD of the light chain of the Fab (fig. S10A). Analysis of E1E2 glycoprotein mutants revealed that AR4A binding not only relied on direct amino acid contacts in E2 (R648 and D698) but was also affected by amino acid changes in the interface between E1 (Y201A, N205A, T198A, S307A, and

T198A+S305A) and E2 (R659A, F679A, and L689A) (fig. S6, B and C). Moreover, the same mutants in a pseudovirus context were not infectious (fig. S6, A and C). Together, these data indicate that the epitope of AR4A on E2 is metastable and requires E1 for stable presentation (fig. S11). Hence, AR4A may neutralize the virus by stabilizing the prefusion state of E1E2 and impeding conformational changes needed for infection.

The bNAb IGH505 targets the surface-exposed conserved α helix in E1, which is positioned against the CDRH3 loop and inserted between the CDRH1, CDRH2, CDRL1, and CDRL3 loops with these five CDR loops making contact with the epitope (36). IGH505 targets H316 and W320 in E1, which bind to CDRH3, CDRL1, and CDRL3, likely through hydrogen bonds to D95 and π - π interactions with Y98, F100e (CDRH3), F32 (CDRL1), and W91 (CDRL3) (Fig. 4B and fig. S12). Also, M323 and M324, located at the C-terminal domain of the α helix in E1, are within hydrogen-bonding distance of A33 in CDRH1 and W50 and K58 in CDRH2 (K, lysine) (Fig. 4B and fig. S12). Although the latter interactions are not seen in the crystal structure of the E1 helix in complex with IGH526, both antibodies share similar footprints, indicating that they target an overlapping epitope at a very similar angle (figs. S9B and S10B) (27). Given the location of the IGH505 and IGH526 epitopes on E1, these antibodies likely neutralize the virus by impeding conformational changes of E1E2.

The bNAb AT1209 targets AR3, which involves the front layer and the CD81 binding loop in E2. AT1209 contains the longest CDRH3 loop among all known AR3-targeting bNAbs (25 amino acids) and shares a similar footprint with the previously described antibodies HEPC3, HEPC74, AR3C, AR3A, HCl1, and AR3X (Fig. 4C and fig. S10C). The sequence signature of these VH1-69-derived bNAbs is a CDRH3 that contains a β hairpin-like structure stabilized by a disulfide bond (CXGGXC motif; G, glycine) (fig. S10D). The β -hairpin conformation adopted by the CDRH3 of AT1209 involves four hydrogen bond interactions between its CDRH3 and the front layer of E2 and the CD81 binding loop: I97-A248, R99-T435, C100a-C429, and G100c-W529 (Fig. 4C and figs. S10D and S12).

Although the CDRH3 dominates the paratope of most of the AR3-targeting bNAbs isolated to date, the unusually 32-residue-long CDRH2 (Kabat numbering) contributes substantially to the interaction of AT1209 with the front layer of E2, with nine residues within hydrogen-bonding distance (E52f, G52l, G52m, L52h, and I53) and burying similar surface area (493 \AA^2) to the CDRH3 (526 \AA^2) (Fig. 4C, figs. S10E and S12, and table S2). A similarly ultra-long CDRH2 (31 residues) is present in AR3X (27). Additionally, functional and structural

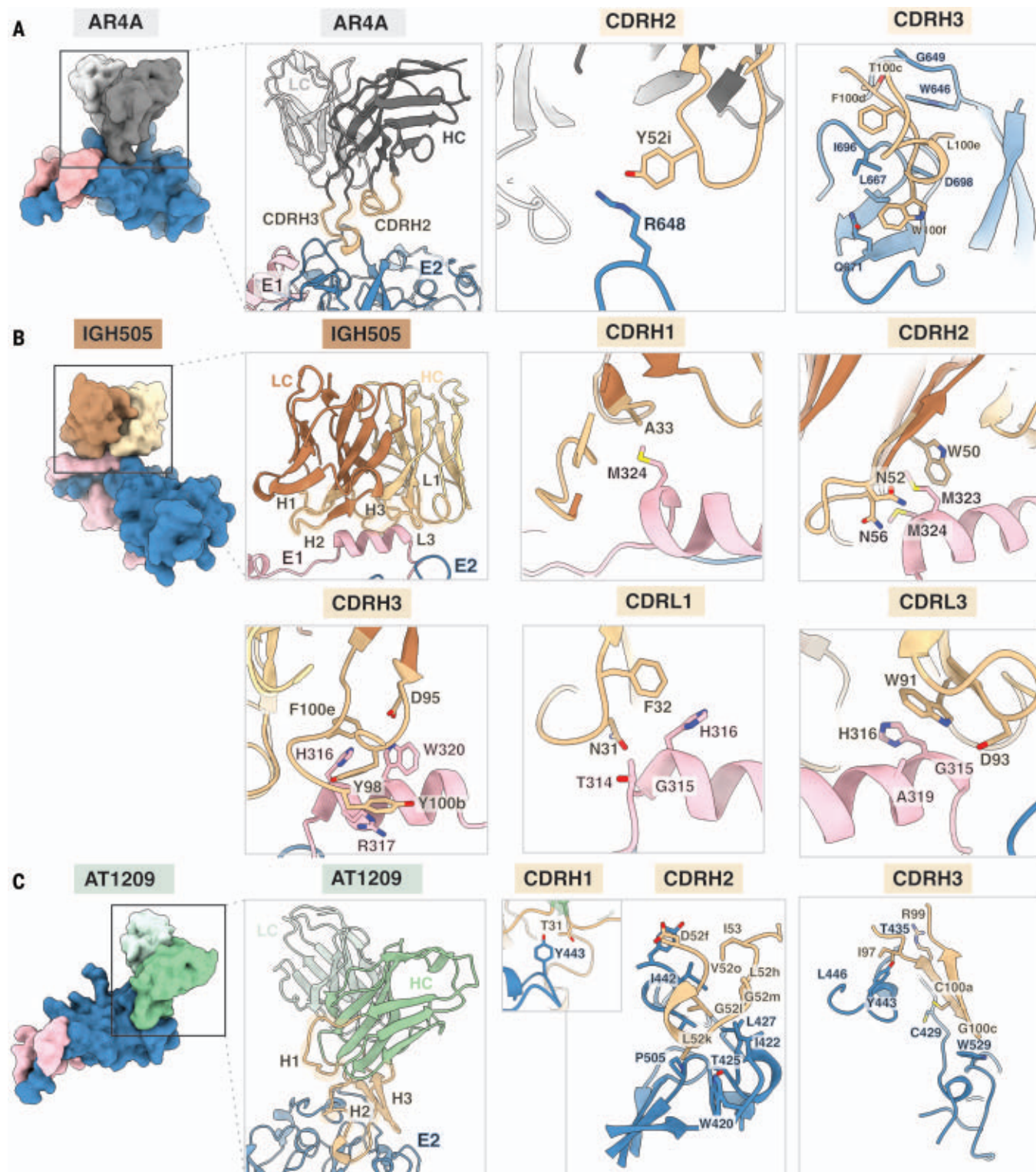


Fig. 4. Structural definition of the AR4A, IGH505, and AT1209 epitopes. (A) The AR4A Fab recognizes protein elements in E2 (blue) near the interface with the E1 subunit (pink). Heavy and light chains are shown in dark and light gray, respectively, and CDRH2 and CDRH3 are highlighted in tan. Whereas the CDRH2 only interacts with the stem region of E2, the CDRH3 loop targets both the back layer and stem of E2. (B) The IGH505 Fab interacts with the surface-exposed α helix in E1 (pink). Heavy and light chains are shown in brown and yellow, respectively, and CDRH1 to CDRH3 and CDRL1 and CDRL3 are

highlighted in tan. IGH505 encases the conserved α helix in E1 (amino acids 310 to 328) using the CDRH1 to CDRH3 and CDRL1 and CDRL3 regions of the Fab. (C) The AT1209 Fab binds the front layer of E2 (blue). Heavy and light chains are represented in green and light green, respectively, and CDRH1 to CDRH3 are highlighted in tan. All of the CDRH loops interact with the front layer of E2, near the CD81 binding site. Epitopes on E1 and E2 were defined as residues containing an atom within 4 Å of the bound Fab, and the amino acids present in the epitope are shown as sticks representations.

analyses reveal that the amino acids that are critical for host receptor CD81 engagement by E2 (I422, S424, L427, N430, S432, G436, W437, L438, G440, L441, F442, Y443, V515, T519, T526, Y527, W529, and W616) overlap with those located in the epitope of the AT1209 antibody (fig. S13). Collectively, these data give us comprehensive insights into the neutralizing face of E1 and E2 and facilitate structure-based vaccine design (fig. S14).

Discussion

The structure of the HCV envelope glycoprotein complex E1E2 proved challenging to resolve because of the need to coexpress E1 and E2 and their propensity to form heterogeneous complexes (29, 51–53). Previous studies showed that the E1E2 glycoprotein complex is a non-covalent heterodimer in infected cells and that it selectively forms disulfide-linked complexes on virions (48). Whether these disulfide-linked complexes present infectious E1E2 or misfolded noninfectious forms is unknown at the present time. Interestingly, a previous study showed that the neutralizing antibody AR4A only captures a small fraction of available virions (13), suggesting that a substantial portion of virion-associated E1E2 might be nonfunctional. Our studies demonstrate that the E1E2 interface is stabilized by glycans and hydrophobic patches as opposed to covalent disulfide bonds, providing insight into how to engineer stable immunogens for structure-based vaccine design (54–56).

Coexpression of the bNAb AR4A was key to stabilizing the metastable E1E2 complex, which we surmise is arrested in the prefusion conformation. Similarly, structures of prefusion HIV-1 Env and respiratory syncytial virus (RSV) F were solved using conformational prefusion-specific antibodies (54, 57). The viral entry pathway after CD81 binding likely involves a multistep process in which the interface of the E1E2 glycoprotein complex is destabilized and opens up upon low pH and/or receptor binding, triggering downstream conformational changes that expose the fusion peptide on E1 and induce viral fusion (24, 45). Neutralizing antibodies can therefore either block CD81 binding by direct competition—for example, AT1209—or, if bound outside the receptor binding site, can impede entry by blocking conformational changes required for fusion, for example, AR4A and IGH505.

Our cryo-EM structure elucidates the HCV E1E2 glycan shield that includes a rare glycan addition to a noncanonical NXV sequon at position 695. This glycan did not have a substantial impact on E1E2 function *in vitro*. However, it may have a role *in vivo*, for example, by creating additional heterogeneity and/or by shielding underlying protein epitopes. Where glycans usually play minor roles in the stability

between interfaces in protein complexes, two glycans are critical for stabilizing the E1E2 interface. The E1E2 region that lacks glycans is primarily hydrophobic and therefore may be involved in oligomerization and/or interaction with the viral lipid bilayer (58). Overall, our cryo-EM study elucidates a full molecular description of E1E2, including three bNAb epitopes, and provides a long-sought-after blueprint for the design of a new generation of HCV glycoprotein immunogens and antiviral drugs.

REFERENCES AND NOTES

1. T. R. Fuerst, B. G. Pierce, Z. Y. Keck, S. K. H. Fong, *Front. Microbiol.* **8**, 2692 (2018).
2. S. A. Yost, Y. Wang, J. Marcotrigiano, *Front. Immunol.* **9**, 1917 (2018).
3. V. J. Kinchen *et al.*, *Cell Host Microbe* **24**, 717–730.e5 (2018).
4. J. M. Pestka *et al.*, *Proc. Natl. Acad. Sci. U.S.A.* **104**, 6025–6030 (2007).
5. S. J. Merat *et al.*, *J. Hepatol.* **71**, 14–24 (2019).
6. M. Law *et al.*, *Nat. Med.* **14**, 25–27 (2008).
7. D. O'Shea *et al.*, *Liver Transpl.* **22**, 324–332 (2016).
8. Y. P. de Jong *et al.*, *Sci. Transl. Med.* **6**, 254ra129 (2014).
9. B. D. Lindenbach, C. M. Rice, *Nat. Rev. Microbiol.* **11**, 688–700 (2013).
10. P. Pileri *et al.*, *Science* **282**, 938–941 (1998).
11. E. Scarselli *et al.*, *EMBO J.* **21**, 5017–5025 (2002).
12. H. E. Drummer, I. Boo, P. P. Pountourios, *J. Gen. Virol.* **88**, 1144–1148 (2007).
13. M. T. Catanese *et al.*, *Proc. Natl. Acad. Sci. U.S.A.* **110**, 9505–9510 (2013).
14. G. Vieyres, J. Dubuisson, T. Pletschmann, *Viruses* **6**, 1149–1187 (2014).
15. L. Stejskal *et al.*, *PLOS Comput. Biol.* **16**, e1007710 (2020).
16. M. Lavie, X. Hanouille, J. Dubuisson, *Front. Immunol.* **9**, 910 (2018).
17. A. Goffard *et al.*, *J. Virol.* **79**, 8400–8409 (2005).
18. J. Prentoe *et al.*, *Proc. Natl. Acad. Sci. U.S.A.* **116**, 10039–10047 (2019).
19. L. Kong *et al.*, *Science* **342**, 1090–1094 (2013).
20. I. Khan *et al.*, *J. Virol.* **88**, 12276–12295 (2014).
21. A. I. Flyak *et al.*, *Cell Host Microbe* **24**, 703–716.e3 (2018).
22. N. Tzarum *et al.*, *Sci. Adv.* **5**, eaav1882 (2019).
23. N. Tzarum, I. A. Wilson, M. Law, *Front. Immunol.* **9**, 1315 (2018).
24. A. Kumar *et al.*, *Nature* **598**, 521–525 (2021).
25. K. El Omari *et al.*, *Nat. Commun.* **5**, 4874 (2014).
26. J. A. Potter *et al.*, *J. Virol.* **86**, 12923–12932 (2012).
27. L. Kong *et al.*, *J. Mol. Biol.* **427**, 2617–2628 (2015).
28. E. Giang *et al.*, *Proc. Natl. Acad. Sci. U.S.A.* **109**, 6205–6210 (2012).
29. T. B. Ruwona, E. Giang, T. Nieuwsma, M. Law, *J. Virol.* **88**, 10459–10471 (2014).
30. L. Cao *et al.*, *PLOS Pathog.* **15**, e1007759 (2019).
31. J. D. Guest *et al.*, *Proc. Natl. Acad. Sci. U.S.A.* **118**, e2015149118 (2021).
32. X. V. Thomas *et al.*, *AIDS* **29**, 2287–2295 (2015).
33. B. G. Pierce *et al.*, *Proc. Natl. Acad. Sci. U.S.A.* **113**, E6946–E6954 (2016).
34. S. J. Merat *et al.*, *PLOS ONE* **11**, e0165047 (2016).
35. M. L. Carlson *et al.*, *eLife* **7**, e34085 (2018).
36. J. C. Meunier *et al.*, *J. Virol.* **82**, 966–973 (2008).
37. W. Schaefer *et al.*, *Proc. Natl. Acad. Sci. U.S.A.* **108**, 11187–11192 (2011).
38. A. Punjani, D. J. Fleet, *J. Struct. Biol.* **213**, 107702 (2021).
39. M. Castelli *et al.*, *Drug Discov. Today* **19**, 1964–1970 (2014).
40. A. Wahid *et al.*, *J. Virol.* **87**, 1605–1617 (2013).
41. T. Krey *et al.*, *PLOS Pathog.* **6**, e1000762 (2010).
42. M. Q. Marín *et al.*, *Vaccines* **8**, 440 (2020).
43. W. Wang *et al.*, *Virology* **448**, 229–237 (2014).
44. V. Deleersnyder *et al.*, *J. Virol.* **71**, 697–704 (1997).
45. J. M. Pfaff-Kilgore *et al.*, *Cell Rep.* **39**, 110859 (2022).
46. C. Di Lorenzo, A. G. N. Angus, A. H. Patel, *Viruses* **3**, 2280–2300 (2011).
47. J. C. Meunier *et al.*, *J. Gen. Virol.* **80**, 887–896 (1999).
48. G. Vieyres *et al.*, *J. Virol.* **84**, 10159–10168 (2010).
49. L. Cocquerel *et al.*, *J. Virol.* **73**, 2641–2649 (1999).
50. R. Gopal *et al.*, *PLOS Pathog.* **13**, e1006735 (2017).
51. J. P. Michalak *et al.*, *J. Gen. Virol.* **78**, 2299–2306 (1997).
52. J. Patel, A. H. Patel, J. McLauchlan, *Virology* **279**, 58–68 (2001).
53. M. Brazzoli *et al.*, *Virology* **332**, 438–453 (2005).
54. J. S. McLellan *et al.*, *Science* **340**, 1113–1117 (2013).
55. S. W. de Taeye *et al.*, *Cell* **163**, 1702–1715 (2015).
56. J. Juraszek *et al.*, *Nat. Commun.* **12**, 244 (2021).
57. J. H. Lee, G. Ozorowski, A. B. Ward, *Science* **351**, 1043–1048 (2016).
58. P. Falsen *et al.*, *J. Virol.* **89**, 10333–10346 (2015).
59. P. Emsley, M. Crispin, *Acta Crystallogr. D Struct. Biol.* **74**, 256–263 (2018).

ACKNOWLEDGMENTS

We thank B. Anderson, H. L. Turner, and M. Wu for cryo-EM data collection support; C. Bowman and J. C. Ducom for computational support; and A. Antanasijevic, G. Ozorowski, P. Sauer, D. Montiel-Garcia, E. Watson, B. Basanta, and J. Yang for supportive discussions. We thank J. Koopsen for the sequence alignment used for generating fig. S5A, N. Zandhuis for performing pilot experiments on AR4A coexpression, and M. J. van Gils for supervising HCVpp assays. We also acknowledge the Scripps Research Institute Cryo-EM Facility and additional scientific resources at the Scripps Research Institute. We thank S. Fong for donating the 212.10 and 212.15 antibodies and T. Beaumont and S. Merat for donating the AT1209 and AT1618 antibodies and antibody plasmids. We also thank V. Eshun-Wilson for grammar and editing expertise. **Funding:** R.W.S. is a recipient of a Vici grant from the Netherlands Organization for Scientific Research (NWO). J.S. is a recipient of a Vidi and Aspasia grant from the NWO (grant numbers 91719372 and 015.015.042). This work was supported by National Science Foundation grant 2109312 to L.E.-W., NWO Rubicon grant 45219118 to A.T.d.I.P., and an Amsterdam Institute for Infection and Immunity Postdoctoral grant to K.S. Mass spectrometry was supported by Bill & Melinda Gates Foundation grant INV-008352/OPP1153692 to M.C. M.C. is a supernumerary fellow of Oriol College, Oxford, and professor adjunct at the Scripps Research Institute, CA. G.C.L. is supported by the National Institutes of Health, grants GM143805 and GM142196. **Author contributions:** A.T.d.I.P. optimized sample preparation for cryo-EM analysis and collected cryo-EM data. L.E.-W. assisted in cryo-EM data collection and processed the data. A.T.d.I.P. and L.E.-W. built and refined the atomic models into the cryo-EM maps. K.S. conceived the protein purification strategy and designed the constructs. K.S., S.K., I.Z., and A.C. performed protein purifications, ELISA experiments, and neutralization assays. J.D.A. and M.L.N. ran site-specific glycosylation analysis. J.S. provided crucial materials. A.B.W., G.C.L., K.S., and R.W.S. provided guidance. A.T.d.I.P., L.E.-W., K.S., G.C.L., R.W.S., and A.B.W. wrote the paper. All authors contributed to the manuscript text by assisting in writing or providing feedback. R.W.S. and A.B.W. supervised the research. **Competing interests:** The authors declare that they have no competing interests. **Data and materials availability:** The GenBank entry for AMS0232 is OL855837.1. The PDB IDs and Electron Microscopy Data Bank (EMDB) IDs for the E1E2 maps have been deposited into the RCSB PDB (<https://www.rcsb.org>) under accession number 7T6X and to the EMD database (<https://www.ebi.ac.uk/emdb/>) under the accession number EMD-25730. The EMDB for the NS-EM map has been deposited into the EMD database under the accession number EMD-27578. The mass spectrometry RAW files have been deposited in the MassIVE server (<https://massive.ucsd.edu>) with accession number (MSV000088553). Materials are available from A.B.W. or R.W.S. upon request. **License information:** Copyright © 2022 the authors, some rights reserved; exclusive licensee American Association for the Advancement of Science. No claim to original US government works. <https://www.science.org/about/science-licenses-journal-article-reuse>

SUPPLEMENTARY MATERIALS

science.org/doi/10.1126/science.abn9884

Materials and Methods

Figs. S1 to S14

Tables S1 and S2

References

MDAR Reproducibility Checklist

Submitted 5 January 2022; resubmitted 14 July 2022

Accepted 27 September 2022

10.1126/science.abn9884

COMPUTER NETWORKS

Delocalized photonic deep learning on the internet's edge

Alexander Sludds^{1*}, Saamil Bandyopadhyay¹, Zaijun Chen^{1†}, Zhizhen Zhong², Jared Cochrane^{1,3}, Liane Bernstein¹, Darius Bunandar^{1‡}, P. Ben Dixon³, Scott A. Hamilton³, Matthew Streshinsky^{4§}, Ari Novack^{4§}, Tom Baehr-Jones^{4§}, Michael Hochberg^{4§}, Manya Ghobadi², Ryan Hamerly^{1,5*}, Dirk Englund^{1*}

Advanced machine learning models are currently impossible to run on edge devices such as smart sensors and unmanned aerial vehicles owing to constraints on power, processing, and memory. We introduce an approach to machine learning inference based on delocalized analog processing across networks. In this approach, named Netcast, cloud-based “smart transceivers” stream weight data to edge devices, enabling ultraefficient photonic inference. We demonstrate image recognition at ultralow optical energy of 40 attojoules per multiply (<1 photon per multiply) at 98.8% (93%) classification accuracy. We reproduce this performance in a Boston-area field trial over 86 kilometers of deployed optical fiber, wavelength multiplexed over 3 terahertz of optical bandwidth. Netcast allows milliwatt-class edge devices with minimal memory and processing to compute at teraFLOPS rates reserved for high-power (>100 watts) cloud computers.

Advances in deep neural networks (DNNs) are transforming science and technology (1–4). However, the increasing computational demands of the most powerful DNNs limit deployment on low-power devices, such as smartphones and sensors—and this trend is accelerated by the simultaneous move toward Internet of Things (IoT) devices. Numerous efforts are underway to

lower power consumption, but a fundamental bottleneck remains because of energy consumption in matrix algebra (5), even for analog approaches including neuromorphic (6), analog memory (7), and photonic meshes (8). In all these approaches, memory access and multiply-accumulate (MAC) functions remain a stubborn bottleneck near 1 pJ per MAC (5, 9–12). Edge devices typically use chip-scale sensors, occupy

millimeter-scale footprints, and consume milliwatts of power. Their small footprint and low power budget mean that performance is limited by the size, weight, and power (SWaP) of computing systems integrated on the device.

To make advanced DNNs at all feasible on low-power devices, industry has resorted to offloading computationally heavy DNN inference to cloud servers. For instance, a smart home device may send a voice query as a vector U to a cloud server, which returns the inference result V to the client (Fig. 1). This offloading architecture adds a ~200-ms latency to voice commands (13), which makes services such as self-driving impossible. Moreover, offloading poses security risks in both the edge and the cloud: Hacking of the communication

¹Research Laboratory of Electronics, Massachusetts Institute of Technology, Cambridge, MA 02139, USA. ²Computer Science and Artificial Intelligence Laboratory, Massachusetts Institute of Technology, Cambridge, MA 02139, USA. ³Lincoln Laboratory, Massachusetts Institute of Technology, Lexington, MA 02421, USA. ⁴Nokia Corporation, New York, NY 10016, USA. ⁵Physics and Informatics Laboratories, NTT Research Inc., Sunnyvale, CA 94085, USA.

*Corresponding author. Email: asludds@mit.edu (A.S.); rhamerly@mit.edu (R.H.); englund@mit.edu (D.E.)

†Present address: Ming Hsieh Department of Electrical and Computer Engineering, University of Southern California, Los Angeles, CA 90089, USA. ‡Present address: Lightmatter Inc., Boston, MA 02110, USA. §Present address: Luminous Computing Inc., Mountain View, CA 94041, USA.

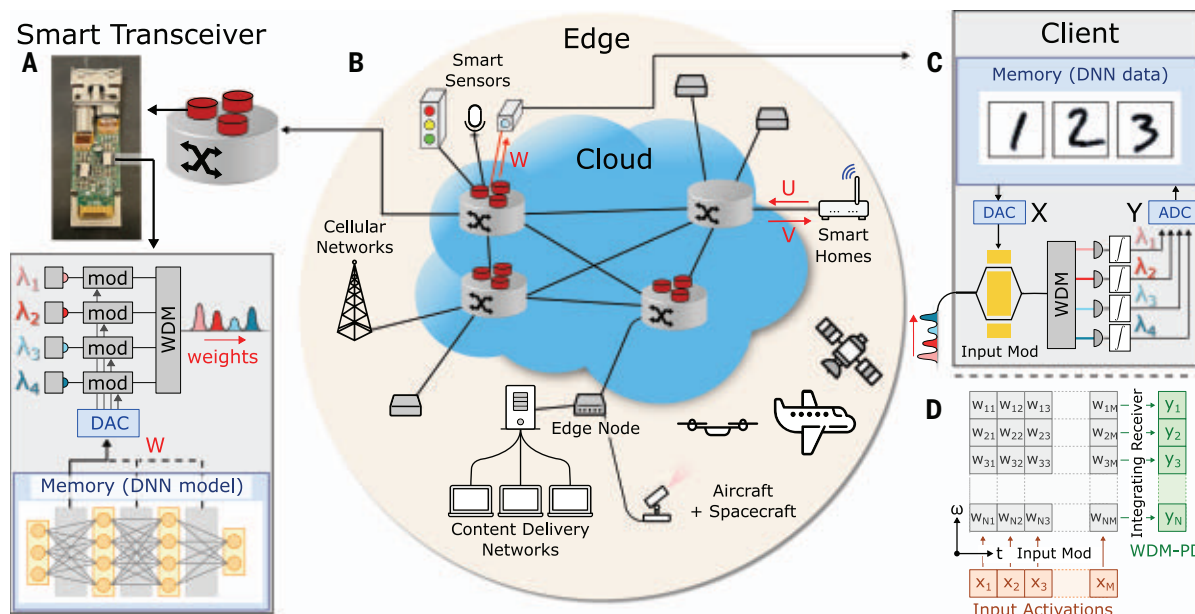


Fig. 1. Netcast concept. (A) Smart transceivers integrated alongside cloud computing infrastructure including servers, data storage, network switches, and edge nodes. The smart transceiver sequentially encodes layers of a neural network model onto the intensity of distinct optical wavelengths using digital-to-analog converters (DACs), optical modulators (mod), and lasers. Wavelength-division multiplexers (WDMs) combine the separate wavelengths from each modulator to the smart transceiver output. (B) U and V highlight current solutions to large model deployments on the edge, with edge device data communicated back to cloud computers. In our solution, smart transceivers

have connections to many devices at the edge of the communications network, including cellular networks, smart sensors, content delivery networks, and aircraft. (C) The edge client encodes input activation data onto a single broadband optical modulator, modulating all weight wavelengths simultaneously. Wavelengths are separated with a WDM, and the result of matrix-vector multiplication is computed on time-integrating receivers. (D) Matrix-vector products between an M -element input vector and (M,N) weight matrix are time-frequency (t - ω) encoded, with each wavelength accumulating its results on a time-integrating receiver.

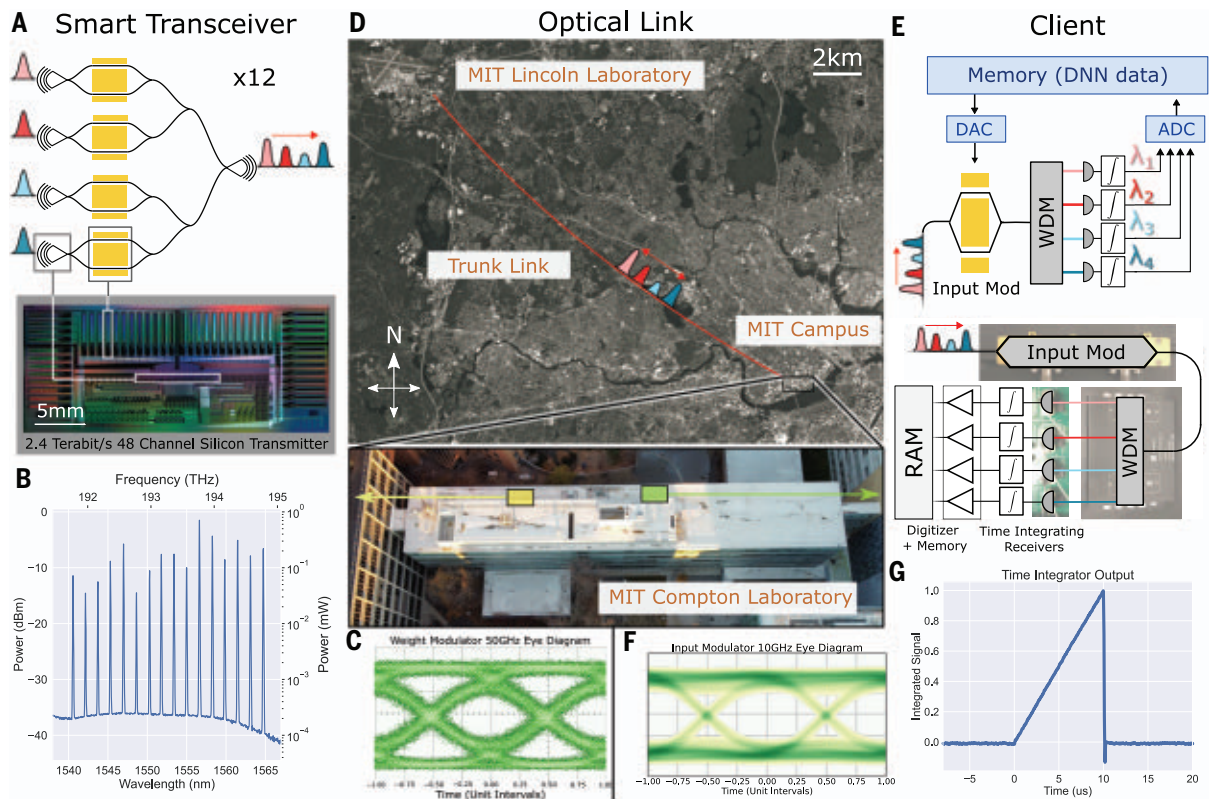


Fig. 2. Experimental demonstration of Netcast system. (A) Smart transceiver composed of a 48-modulator silicon photonic transmitter with 2.4 Tbps of total bandwidth. (B) Optical spectrum of smart transceiver output, showing 16 laser sources across 3 THz of bandwidth with >25 dB optical SNR. (C) An example of high-speed operation of the smart transceiver modulators, with a 50 GHz open eye. (D) Weights are sent over 86 km of deployed optical fiber

connecting the smart transceiver to the client. (E) Client receiver composed of a broadband, high-speed optical modulator, a WDM demultiplexer, and custom time-integrating receivers. (F) The client input modulator also achieves an open eye of 10 GHz (test equipment limited). (G) Example time-integrating receiver waveform showing constant optical power being accumulated over 10 μ s and resetting. Satellite imagery in (D) taken using a deployed satellite (Planet.com).

of client data (in vector U) has led to security breaches of private data.

To address these problems, we introduce here a photonic edge computing architecture, named Netcast, to minimize the energy and latency of large linear algebra operations such as general matrix-vector multiplication (GEMV) (5). In the Netcast architecture, cloud servers stream DNN weight data (W) to edge devices in an analog format for ultraefficient optical GEMV that eliminates all local weight memory access (14).

Servers containing a “smart transceiver” (15)—which may be in the standard pluggable transceiver format represented in Fig. 1A—periodically broadcast the weights (W) of commonly used DNNs to edge devices, using wavelength division multiplexing (WDM) to leverage the large spectrum available at the local access layer. Specifically, the (M, N)-sized weight matrix of one DNN layer may be encoded in a time-frequency basis by the amplitude-modulated field $W_n(t) = \sum_{j=1}^M w_{nj} e^{-i\omega_n t} \delta(t - j\Delta T)$, where the optical amplitude w_{nj} at frequency ω_n and time step j

represents the n th row of the weight matrix (Fig. 1D), and δ is the impulse response function.

Suppose now that a camera in Fig. 1 requires inference on an image X . To do so, it waits for the server to stream the “image recognition” DNN weights, which it modulates with $X(t) = \sum_{j=1}^M x_j \delta(t - j\Delta T)$ using a broadband optical modulator and subsequently separates the wavelengths to N time-integrating detectors to produce the vector-vector dot product $Y_n(t) = \sum_{j=1}^M w_{nj} x_j \delta(t - j\Delta T)$. This architecture minimizes the active components at the client, requiring only a single optical modulator, digital-to-analog converter (DAC), and analog-to-digital converter (ADC).

Experimental implementation of Netcast

We demonstrate the Netcast protocol with a smart transceiver (Fig. 2A), made in a commercial silicon-photonic CMOS foundry (OpSIS/IME, described in supplementary text section 2). The smart transceiver is composed of 48 Mach-Zehnder modulators (MZMs), each capable of modulation up to 50 Gbps for a total band-

width of 2.4 Tbps (16). The smart transceiver supports WDM, with Fig. 2B showing 16 WDM lasers simultaneously transmitting through the chip with ~ 10 dBm (100 μ W) power per wavelength. Figure 2C shows an open eye diagram at 50 GHz (supplementary text section 8). Weights are transmitted over 86 km of deployed optical fiber from the Massachusetts Institute of Technology (MIT) main campus to MIT Lincoln Laboratory and back to the main campus (Fig. 2D). The client (Fig. 2E) applies input activation values to the incoming weight data using a high-speed (20-GHz) broadband lithium niobate MZM, with Fig. 2F showing an open eye diagram at 10 GHz (limited by testing equipment). A passive wavelength demultiplexer separates each wavelength channel for detection onto an array of custom time-integrating receivers, with an example of time integration shown in Fig. 2G (supplementary text section 6). After integration, the generated voltages from the receivers are measured by a digitizer and stored in memory. Additional postprocessing steps, such as the non-linear activation function, are performed using a computer. Multiple neural network layers

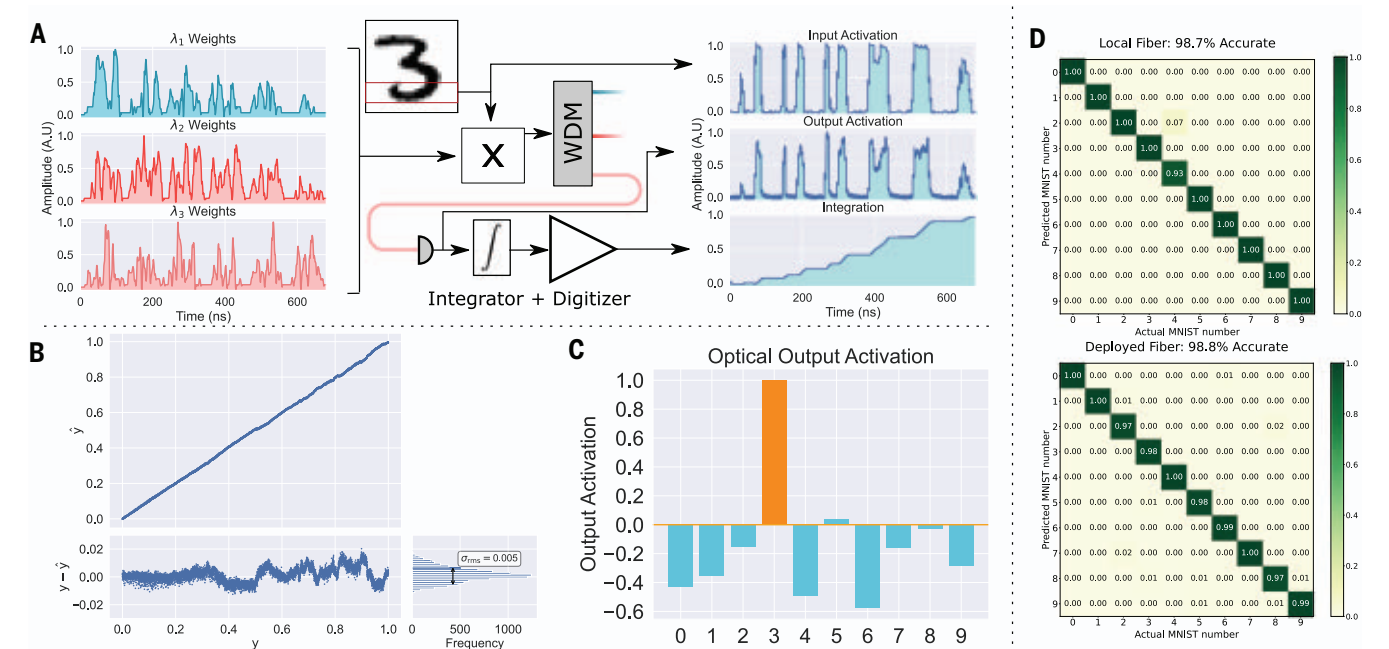


Fig. 3. Computational accuracy of Netcast system. (A) Weight data from multiple wavelength channels is simultaneously modulated by input data. After wavelength multiplexing, the generated photocurrent is time-integrated. (B) Floating-point computing accuracy comparing the results of 10,000 scalar-scalar floating point multiplications. Electrical floating point results are designated as y and optical results are designated as \hat{y} . The difference $y - \hat{y}$ has a standard deviation of $\sigma_{rms} = 0.005$ or ≈ 8 -bit accuracy. (C) Example output activation data from the optical setup correctly classifying the digit “3.” (D) Computing results of image classification over both local links and the 86-km deployed fiber link.

Table 1. Device contributions to receiver performance assuming conventional technology.
Device energy consumption is amortized by either a spatial fan-out factor (N) or time-domain fan-out factor (M). We assume a carrier depletion modulator in silicon is used and that a single high-speed (gigahertz) ADC reads out from an array of N slow integrators. See supplementary text section 19 for derivation of nonlinearity energy consumption.

Netcast client energy consumption				
Device	Number of devices	Fan-out	Energy per device	Energy per MAC
Modulator (16)	1	N	~ 1 pJ	$\sim (1/N)$ pJ
DAC (37)	1	N	~ 1 pJ	$\sim (1/N)$ pJ
ADC (38)	1	M	~ 1 pJ	$\sim (1/M)$ pJ
Integrator (39)	N	M	~ 1 fJ	$\sim (1/M)$ fJ
Nonlinearity	N	M	< 100 fJ	$\sim (1/M)$ fJ
Total	—	—	—	$\sim (1/N)$ pJ

are run by taking the resulting output activations of the previous layer and encoding them onto the input modulator while the next layer’s weights are transmitted.

We show the flow of data through the experimental setup and the accuracy it can achieve in Fig. 3A. Weight data are encoded to multiple modulators simultaneously. For clarity, we show a single row of the digit “3” being encoded and the resulting time trace from a single wavelength. We demonstrate computing with high accuracy, with Fig. 3B showing 8 bits of precision, more than the ≈ 5 bits of precision required for neural network computation (17, 18).

After calibrating the system, we perform image classification by running a benchmark handwritten digit classification task [Modified National Institute of Standards and Technology (MNIST)], which was trained on a digital computer (supplementary text sections 14 and 16). Figure 3C illustrates an example of the system’s computing result for classifying the digit “3.” We then test the system’s performance both locally and over deployed fiber using a benchmark three-layer MNIST model with 100 neurons per hidden layer (supplementary text section 14). Using 1000 test images locally, we demonstrate 98.7% accurate computation, compa-

rable with the model’s baseline accuracy of 98.7%. Using the same test images, we utilize 3 THz of bandwidth over the deployed fiber and classify MNIST digits with 98.8% accuracy. This result shows the potential for this architecture to support ultrahigh bandwidths in real-world deployed systems using conventional components.

Energy efficiency

Netcast is designed to minimize the power used at the client. To enable this, we make sure every component at the client is performing a large number of MACs (M or N) for modulation and electrical readout, respectively. Only a single MZM and DAC are used to encode input data across N wavelengths, enabling N MACs of work for every voltage applied to the modulator. While the energy costs of these individual components can be high, they have high parallelism, performing many MACs of work per time step. For encoding input activations, the client only uses a single broadband optical modulator, allowing for $\sim (1/N)$ pJ per MAC of energy consumption using standard components. Furthermore, the integrator and ADC can be much slower than the speed of modulated weights, because readout occurs after M timesteps. As a result, the integrator and ADC can be M times slower, decreasing the cost of electrical readout components to $\sim (1/M)$ pJ per MAC. Assuming near-term values of $N = M = 100$, client energy consumption can reach

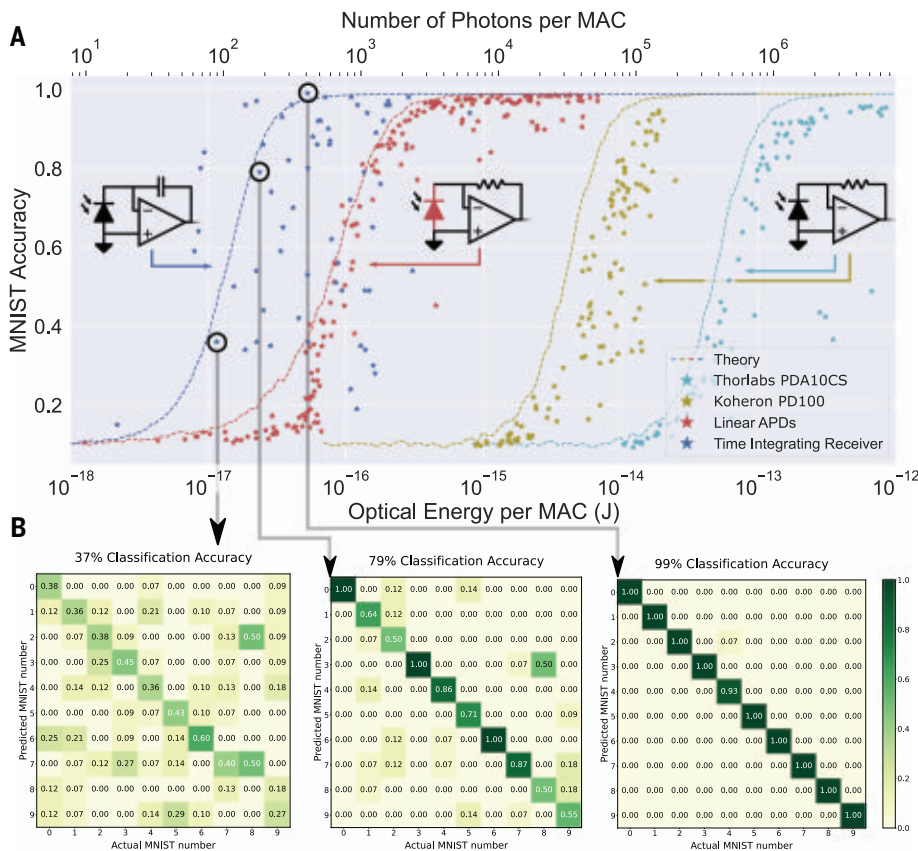


Fig. 4. Thermal noise limited optical sensitivity of Netcast system. (A) Experimentally measured sensitivity of optical receivers. Standard amplified photoreceivers are shown on the right side of the plot, with performance limited by electrical amplifier thermal noise, giving a typically optical energy of 10 to 100 fJ per MAC. The center of the plot shows linear avalanche photodiodes, which use intrinsic gain to lower the energy per MAC, but at the cost of increased energy consumption and lower-bandwidth time-integrating receivers, which lower the effective thermal noise floor by performing many MAC operations for each readout. Time-integrating receivers using off-the-shelf technology can achieve high accuracy with <100 aJ per MAC of optical sensitivity on the benchmark neural network task. (B) Confusion matrices for labeled points in (A), showing how each digit in the MNIST dataset is classified by the optical hardware (on-diagonal elements correspond to correct classification; columns add to 1, but rows do not have to).

≈10 fJ per MAC, which is three orders of magnitude lower than is possible in existing digital CMOS. The scaling of the client energy consumption is summarized in Table 1.

In our experimental demonstration, we have fabricated a 48-channel silicon smart transceiver to deploy weights to the client. The modulators used in this smart transceiver can operate at a data rate of 50 Gbps. The client uses a fiber lithium niobate modulator with a bandwidth of 20 GHz and energy efficiency of 18 pJ per bit (supplementary text section 1). Sharing this input modulator over 48 wavelengths, we find that our input modulator uses 370 fJ per MAC of energy. Simple changes to the client, such as making use of the same modulator at the client as we do at the smart transceiver (≈450 fJ per bit), would enable <10 fJ per MAC energy efficiency. Our integrating receivers have a 20 mW power consumption per channel, leading to an energy efficiency of 1 pJ per MAC and the potential to

improve orders of magnitude with commercial technology (see Discussion section).

Receiver sensitivity

Applications of Netcast, including free-space deployment to drones or spacecraft, can operate in deeply photon-starved environments. For example, recent satellite optical communication demonstrations, such as NASA's Lunar Laser Communication Demonstration, have shown ≈100 Mbps communications to satellites orbiting the Moon with link losses in excess of 70 dB (19). To enable high-speed and energy-efficient machine learning on these deployments, optical receivers must have the lowest possible noise floor, ideally operating at the shot noise limit with ≈1 photon per MAC. Modern photoreceivers are limited by either thermal noise of readout electronics [also called Johnson-Nyquist noise (20)], shot noise, flicker (1/f) noise, or relative intensity noise of the

laser; of these, for integrated optoelectronics, thermal and shot noise are dominant in Netcast (see supplementary text sections 13 and 23). We overcome this problem with time-integrating receivers, which accumulate partial results from vector-matrix multiplication. We compare the sensitivity of different photoreceivers. Amplified photoreceivers (Fig. 4A, right) have typical sensitivities of ≈10 to 100 fJ per MAC. Amplified linear mode avalanche photodetectors (Fig. 4A, middle) overcome some of the thermal noise of the amplifier and achieve ≈1 fJ per MAC. Our custom time-integrating receivers (Fig. 4A, left) perform M MACs per measurement window before readout, lowering the required optical power per readout by M . Amplified photodetectors, in contrast, read out after each MAC, acquiring thermal noise for each measurement and adding the results of each MAC together to create the resulting output activation value. For time-integrating receivers, the resulting output activation signal is measured while measuring thermal noise once, giving a $\frac{1}{M}$ optical energy per MAC scaling. For amplified photodetectors, the partial-product signal terms add together linearly, while thermal noise adds in quadrature, giving a $\frac{\sqrt{M}}{M} = \frac{1}{\sqrt{M}}$ scaling. In our experiment, we demonstrate that with $M = 100$, only 10 aJ per MAC (100 photons) of optical energy is required (two orders of magnitude less than for similar amplified photodetectors). This result brings Netcast close to the fundamental quantum limit of optical computation (21, 22), which we can reach by engineering the receiver to lower thermal noise.

Thermal noise is a hardware-dependent noise source, originating from the thermal motion of charge carriers in an electrical conductor. In a resistor-capacitor (RC) circuit, thermal noise manifests in a fluctuation in the number of readout electrons in a circuit given by $\sigma_{\text{th}} = \sqrt{k_B T C} / q$, where k_B is the Boltzmann constant, T is temperature, q is the electron charge, and C is the capacitance of the receiver (23). Conventional amplified photodetectors read out on every MAC operation and add partial-product results to generate an output activation value. Adding together each MAC adds together the measured signal linearly, and noise terms add in quadrature. This results in a signal-to-noise ratio (SNR) of

$$\begin{aligned} \text{SNR} &= \frac{\text{Signal Electrons}}{\text{Noise Electrons}} \\ &= MP_{\text{opt}} \eta T_{\text{clk}} / \sqrt{\sum_{i=1}^M \sigma_{\text{th}}^2} \\ &= MP_{\text{opt}} \eta T_{\text{clk}} / \sqrt{M \sigma_{\text{th}}^2} \\ &= \sqrt{M} P_{\text{opt}} \eta T_{\text{clk}} / \sigma_{\text{th}} \end{aligned}$$

where P_{opt} is photon flux incident on the detector (units of photons per second), η is detector quantum efficiency, and T_{clk} is the time period for each MAC. In contrast, our

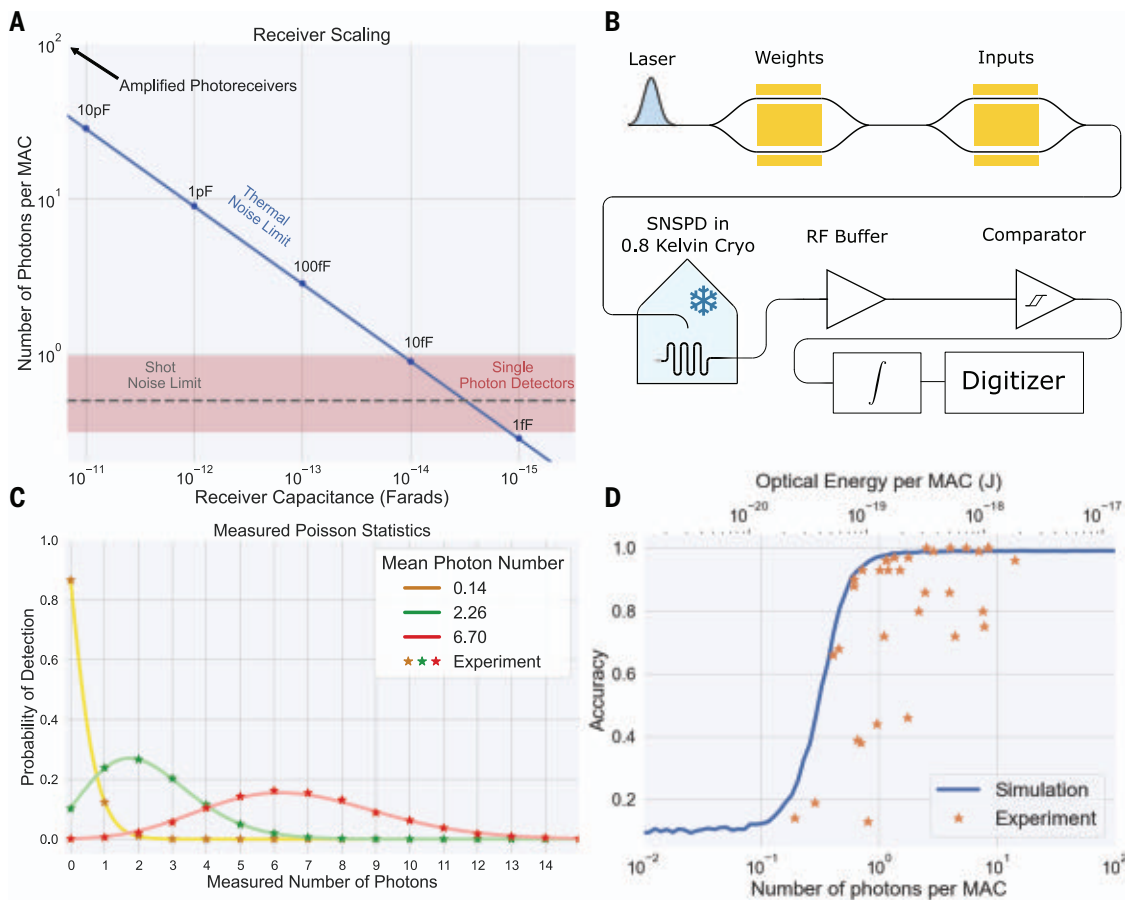


Fig. 5. Forward looking performance of Netcast. (A) Fundamental noise bounds of time-integrating receivers from thermal noise of an integrator and shot noise to achieve 50% accuracy on MNIST task. Decreasing the capacitance of the time integrator lowers thermal readout noise, enabling access to the single photon-per-MAC regime. (B) Proof-of-concept experimental setup consisting of input and weight

modulators and superconducting nanowire single-photon detectors (SNSPDs), allowing us to probe this fundamental single-photon bound. (C) We experimentally validate the single-photon detectors by measuring shot noise on the detector over many integration windows. (D) Using a three-layer MNIST model, we experimentally measure computation with <1 photon per MAC with high accuracy.

time-integrating receivers only see thermal noise once per measurement window

$$\text{SNR} = \frac{\text{Signal Electrons}}{\text{Noise Electrons}} = MP_{\text{opt}} \eta T_{\text{clk}} / \sigma_{\text{th}}$$

As a result, we see that the required number of photons per MAC is \sqrt{M} times lower than for standard amplified photoreceivers.

Improvements to time-integrating receivers are possible by minimizing the integration capacitance of the receiver. Figure 5A shows the thermal noise limit of time-integrating receivers as integration capacitance is decreased. This noise floor is fundamentally connected to the size scale of photodetectors, readout electronics, and their proximity of integration (10). Modern foundry processes enable ≈ 1 fF-scale receivers, lowering the thermal readout noise to the single photon-per-MAC level (24, 25). This single photon-per-MAC regime is fundamentally limited by the quantum nature of light, where precision is determined by the Poissonian distribution of photons that arrive within a measurement window. Poissonian noise, also

called shot noise, can be observed in experimentally measured data in Fig. 5C. We investigate this fundamental bound of the Netcast system through a proof-of-concept experiment using superconducting nanowire single-photon detectors (SNSPDs) as shown in Fig. 5B. These photodetectors are ideal, demonstrating pure shot noise-limited performance. We show that the fundamental shot noise bound on the same benchmark digit classification problem from Fig. 4 allows the receiver to operate with high accuracy with <1 photon per MAC (0.1 aJ per MAC). This result may at first seem surprising given that less than a single photon per MAC is counterintuitive. We can understand this measurement better by noting that at readout, we have performed a vector-vector product with $M = 100$ MACs. Each MAC can have less than a single photon in it, but the measured signal will have many photons in it. A graphical explanation is given in supplementary text section 18. This single photon-per-MAC regime enables many new applications. The realization of computing with less than one photon

per MAC could enable a new class of computing systems that protect both client input and server weight data. Another application that benefits from less than one photon per MAC is deployed spacecraft that operate in a strongly photon-starved environment. Weight data from a directional base station could be transmitted to the spacecraft and classified on the craft, before the results are transmitted to Earth.

Discussion

The system-level demonstration shown here is one example of an implementation of Netcast. The cloud-based smart transceiver can reside inside of existing networking hardware such as network switches, servers, or edge nodes. Our ideas can be extended to the case where the user data are streamed through programmable network switches with smart transceivers, enabling in-network optical inference (15). Modern network switches, such as Intel's Tofino switch, are an ideal platform for developing Netcast commercially, as they are programmable, enabling multiple streams of weights

to be deployed at line rate (100 Gbps), and can support 64 GB of memory, reaching the storage requirements of modern neural networks. Prior work has demonstrated the feasibility of using programmable switches to perform layer-by-layer inference with smart transceivers (15). The large data storage of these network switches enables multiple models to be stored and queried. The client device could use its broadband modulator to allow for reflection-mode communication back to the server, where the client modulates received light and sends it back along the fiber link for communication. This querying communication can be slow and lossy, as only a few bits are required to request that a new model be sent.

Emerging photonic technologies, such as low-power static phase shifters (26–28) and high-speed phase shifters (29–32), can reduce receiver electrical energy consumption to ~ 10 aJ per MAC. This energy can be further decreased by making use of the tight integration of transistors and photonics in silicon using technologies such as receiverless detectors (10), photonic DACs (33), and photonic ADCs (34). Detectors such as avalanche detectors could be incorporated with a time integrator to provide a benefit to the optical sensitivity of the receiver, but at the cost of added electrical power consumption (supplementary text section 21). Further improvements in optical sensitivity are possible by using coherent detection, which boosts the received signal using a strong local oscillator (21). Two examples of a Netcast system using coherent detection to substantially improve optical energy per MAC are detailed in supplementary text section 12.

A number of companies have designed custom edge computing application-specific integrated circuits (ASICs) with reduced SWaP (7, 35), but these ASICs are hampered by the same energy and bandwidth constraints as larger CMOS processors. Analog accelerators, such as memristive crossbar arrays and meshes of photonic interferometers, hold promise for lowering the power consumption of neural networks compared with electronic counterparts, but existing commercial demonstrations still consume watts of power (8, 36).

One obstacle to scaling bandwidth in traditional optical communication systems is dispersion in optical fiber. For a single smart transceiver and client, techniques such as wavelength-dependent delays can compensate for dispersion at the smart transceiver. However, in systems where weights are deployed to multiple clients from one smart transceiver with different lengths of fiber, this technique cannot be used. We discuss the effects of dispersion in supplementary text section 22 and show that it is possible to make use of the optical O-band to enable terahertz of bandwidth at clock rates of 10 GHz per wavelength over more than 10 km of optical fiber.

Outlook

We have described an edge computing architecture that makes use of the strengths of photonics and electronics to achieve orders of magnitude in energy efficiency and optical sensitivity improvements over existing digital electronics. We have demonstrated scalable photonic edge computing using WDM, time-integrating receivers, scalability to milliwatt-class power consumption, <1 photon-per-MAC receiver sensitivity, and computing over deployed fiber using 3 THz of bandwidth. On image classification tasks, we show 98.8% accurate image classification. The hardware shown in this paper is readily mass-producible from existing CMOS foundries, allowing for near-term impact on our daily lives. Our approach removes a fundamental bottleneck in edge computing, enabling high-speed computing on deployed sensors and drones.

REFERENCES AND NOTES

1. T. B. Brown *et al.*, arXiv:2005.14165 [cs.CL] (2020).
2. O. Vinyals *et al.*, *Nature* **575**, 350–354 (2019).
3. A. Krizhevsky, I. Sutskever, G. E. Hinton, *Adv. Neural Inf. Process. Syst.* **25**, 1097–1105 (2012).
4. J. Deng *et al.*, 2009 IEEE Conference on Computer Vision and Pattern Recognition (IEEE, 2009), pp. 248–255.
5. V. Sze, Y.-H. Chen, T.-J. Yang, J. S. Emer, *Proc. IEEE* **105**, 2295–2329 (2017).
6. M. Davies *et al.*, *IEEE Micro* **38**, 82–99 (2018).
7. Mythic, M1076 Analog Matrix Processor; <https://mythic.ai/products/m1076-analog-matrix-processor/>.
8. C. Demirkiran *et al.*, arXiv:2109.01126 [cs.AR] (2021).
9. M. Horowitz, 2014 IEEE International Solid-State Circuits Conference Digest of Technical Papers (ISSCC) (IEEE, 2014), pp. 10–14.
10. D. A. Miller, *J. Lightwave Technol.* **35**, 346–396 (2017).
11. L. Bernstein *et al.*, *Sci. Rep.* **11**, 3144 (2021).
12. Y.-H. Chen, T. Krishna, J. S. Emer, V. Sze, *IEEE J. Solid-State Circuits* **52**, 127–138 (2016).
13. M. Satyanarayanan, *Computer* **50**, 30–39 (2017).
14. R. Hamerly *et al.*, *Proc. SPIE* **11804**, 118041R (2021).
15. Z. Zhong *et al.*, *Proceedings of the ACM SIGCOMM 2021 Workshop on Optical Systems (OptSys '21)* (Association for Computing Machinery, 2021), pp. 18–22.
16. M. Streshinsky *et al.*, *J. Lightwave Technol.* **32**, 4370–4377 (2014).
17. T. Gokmen, M. J. Rasch, W. Haensch, 2019 IEEE International Electron Devices Meeting (IEDM) (IEEE, 2019), pp. 22.3.1–22.3.4.
18. S. Garg, J. Lou, A. Jain, M. Nahmias, arXiv:2102.06365 [cs.LG] (2021).
19. D. M. Boroson, J. J. Scozzafava, D. V. Murphy, B. S. Robinson, M. I. T. Lincoln, 2009 Third IEEE International Conference on Space Mission Challenges for Information Technology (IEEE, 2009), pp. 23–28.
20. J. B. Johnson, *Phys. Rev.* **32**, 97–109 (1928).
21. R. Hamerly, L. Bernstein, A. Slud, M. Soljačić, D. Englund, *Phys. Rev. X* **9**, 021032 (2019).
22. T. Wang *et al.*, *Nat. Commun.* **13**, 123 (2022).
23. J. Pierce, *Proceedings of the IRE* **44**, 601–608 (1956).
24. M. Rakowski *et al.*, 2020 Optical Fiber Communication Conference (OFC), OSA Technical Digest (Optica Publishing Group, 2020), paper T3H–3.
25. C. Sun *et al.*, *IEEE J. Solid-State Circuits* **51**, 893–907 (2016).
26. G. Liang *et al.*, *Nat. Photonics* **15**, 908–913 (2021).
27. R. Baghdadi *et al.*, *Opt. Express* **29**, 19113–19119 (2021).
28. M. Dong *et al.*, *Nat. Photonics* **16**, 59–65 (2022).
29. E. Timurdogan *et al.*, *Nat. Commun.* **5**, 4008 (2014).
30. C. Wang *et al.*, *Nature* **562**, 101–104 (2018).
31. M. Xu *et al.*, *Optica* **9**, 61 (2022).
32. W. Heni *et al.*, *Nat. Commun.* **10**, 1694 (2019).
33. S. Moazeni *et al.*, *IEEE J. Solid-State Circuits* **52**, 3503–3516 (2017).
34. A. Zazzi *et al.*, *IEEE Open J. Solid State Circuits Soc.* **1**, 209–221 (2021).
35. A. Yazdanbakhsh, K. Seshadri, B. Akin, J. Laudon, R. Narayanaswami, arXiv:2102.10423 [cs.LG] (2021).
36. D. Fick, M. Henry, “Analog computation in flash memory for datacenter-scale AI inference in a small chip,” *Hot Chips 2018 (HC30)*, Cupertino, California, 19–21 August 2018.
37. B. M. Pietro Caragiulo, C. Daigle, B. Murmann, Dac performance survey 1996–2020, GitHub (2022); <https://github.com/pietro-caragiulo/survey-DAC>.
38. B. Murmann, ADC performance survey 1997–2021, Stanford University (2022); <http://web.stanford.edu/~murmman/adcsurvey.html>.
39. E. Yang, T. Lehmann, “High gain operational amplifiers in 22 nm CMOS,” 2019 IEEE International Symposium on Circuits and Systems (ISCAS) (IEEE, 2019).
40. A. Sludds, alexsludds/Delocalized_Photonic_Deep_Learning_on_the_Internets_Edge: Zenodo Added, Zenodo (2022); <https://doi.org/10.5281/zenodo.6982196>.

ACKNOWLEDGMENTS

We acknowledge D. Lewis and A. Pennes for assistance in machining laboratory equipment and E. Allen for discussions related to using squeezed light to further reduce photon counts. We are grateful to E. Bersin and B. Dixon for assistance in coordinating usage of the deployed fiber and A. Rizzo for help in converting and plotting eye diagram data as well as proofreading the manuscript. We thank C. Panuski and S. Krastanov for informative discussions on single-photon operation of Netcast. We thank A. Pyke of Micro-Precision Technologies for wire bonding the electrical connections from the printed circuit board to the 48-channel transmitter. We appreciate help from F. Wong for the use of his SNSPDs and acknowledge M. Prabhu and C. Errando Herranz for facilitating the usage of the SNSPDs, C. Freeman for help in taking drone photography, NVIDIA for supplying a Tesla K40 GPU that was used for simulations shown in the main text and supplementary materials, and Planet.com for allowing us to take custom satellite imagery. **Funding:** A.S. and S.B. are supported by National Science Foundation Graduate Research Fellowship 1745302. L.B. is supported by the Natural Sciences and Engineering Research Council of Canada (PGSD3-517053-2018). This research was funded by a collaboration with NTT-Research and NSF Eager (CNS-1946976). This material is based on research sponsored by the Air Force Office of Scientific Research (AFOSR) under award FA9550-20-1-0113, the Air Force Research Laboratory (AFRL) under agreement FA8750-20-2-1007, the Army Research Office (ARO) under agreement W911NF-17-1-0527, NSF RAISE-TAQs grant 1936314, NSF C-Accel grant 2040695, NSF grant ASCENT-2023468, NSF grant CAREER-2144766, and ARPA-E grant ENLITENED PINE DE-AR0000843. The work was further supported by funding from the Alfred P. Sloan foundation (FG-2022-18504) and DARPA grant FastNICs 4202290027. Distribution Statement A. Approved for public release. Distribution is unlimited. This material is based upon work supported by the Under Secretary of Defense for Research and Engineering under Air Force Contract No. FA8702-15-D-0001. Any opinions, findings, conclusions or recommendations expressed in this material are those of the authors and do not necessarily reflect the views of the Under Secretary of Defense for Research and Engineering. **Author contributions:** A.S. created the experimental setup and conducted the experiment. S.B. assisted in fiber-to-chip coupling and discussions on the project. Z.C. assisted with high-speed measurements of the setup and discussions. M.S., A.N., T.B.-J., and M.H. designed and taped out the smart transceiver. D.B. packaged the 48-channel silicon transceiver. J.C. packaged the time-integrating receivers and assisted in calibration. D.E. established the fiber link between MIT and MIT Lincoln Laboratory, and S.A.H. and P.B.D. helped with its use. L.B. helped in discussion of fundamental noise sources. M.G. and Z.Z. assisted with discussions on modern telecommunication networks. R.H. conceived of the project idea. S.B., Z.C., L.B., M.S., A.N., T.B.-J., M.H., Z.Z., J.C., S.A.H., P.B.D., and M.G. provided feedback on the manuscript. A.S., D.E., and R.H. wrote the manuscript. **Competing interests:** M.H. is president of Luminous Computing. A.N. is vice president of system hardware design at Luminous Computing. T.B.-J. is vice president of engineering at Luminous Computing. M.S. is vice president of packaging, photonics, and mixed-signal at Luminous Computing. M.H., A.N., T.B.-J., and M.S. own stock in Luminous Computing. D.B. is chief scientist at Lightmatter and holds stock in the company. A.S. has interned at Lightmatter, receiving a wage. D.E. is an adviser to and holds shares in Lightmatter but received no support for this work.

S.B. has received consulting fees from Nokia Corporation. M.G. owns stock in companies with telecommunication interests (Google and Microsoft). R.H. and D.E. have filed a patent related to Netcast: PCT/US21/43593. M.G., Z.Z., L.B., A.S., R.H., and D.E. have filed a provisional patent related to Netcast: 63/191,120. The other authors declare that they have no competing interests. **Data and materials availability:** Data required to recreate results in the main text are available in Zenodo (40). **License information:**

Copyright © 2022 the authors, some rights reserved; exclusive licensee American Association for the Advancement of Science. No claim to original US government works. <https://www.science.org/about/science-licenses-journal-article-reuse>

SUPPLEMENTARY MATERIALS

science.org/doi/10.1126/science.abq8271

Materials and Methods
Supplementary Text
Figs. S1 to S26
Table S1
References (41–88)

Submitted 3 May 2022; accepted 23 September 2022
10.1126/science.abq8271

METABOLISM

Time-restricted feeding mitigates obesity through adipocyte thermogenesis

Chelsea Hepler¹, Benjamin J. Weidemann¹, Nathan J. Waldeck¹, Biliana Marcheva¹, Jonathan Cedernaes¹, Anneke K. Thorne¹, Yumiko Kobayashi¹, Rino Nozawa¹, Marsha V. Newman¹, Peng Gao², Mengle Shao³, Kathryn M. Ramsey¹, Rana K. Gupta³, Joseph Bass^{1*}

Misalignment of feeding rhythms with the light-dark cycle leads to disrupted peripheral circadian clocks and obesity. Conversely, restricting feeding to the active period mitigates metabolic syndrome through mechanisms that remain unknown. We found that genetic enhancement of adipocyte thermogenesis through ablation of the zinc finger protein 423 (ZFP423) attenuated obesity caused by consumption of a high-fat diet during the inactive (light) period by increasing futile creatine cycling in mice. Circadian control of adipocyte creatine metabolism underlies the timing of diet-induced thermogenesis, and enhancement of adipocyte circadian rhythms through overexpression of the clock activator brain and muscle Arnt-like protein-1 (BMAL1) ameliorated metabolic complications during diet-induced obesity. These findings uncover rhythmic creatine-mediated thermogenesis as an essential mechanism that drives metabolic benefits during time-restricted feeding.

Fundamental to the development of obesity is the imbalance between energy intake and expenditure in the setting of over-nutrition. Overconsumption of food is also associated with disrupted endogenous circadian rhythms in meal timing and metabolism (1). Genetic disruption of the circadian clock leads to increased consumption of food during the light period when animals are typically sleeping and exaggerated diet-induced obesity (2). Feeding at the wrong time of day exacerbates diet-induced obesity (3), whereas restricting a calorie-dense diet to the normal active period (night for nocturnal rodents and day for humans) improves metabolic health (4, 5). This indicates that misalignment of feeding rhythms with autonomous energetic cycles contributes to diet-induced obesity and metabolic syndrome, but the mechanisms remain unknown.

Results

Within 1 week of exposure to a high-fat diet (HFD) provided exclusively during the inactive (light) period, mice exhibit increased weight

gain compared with mice provided an isocaloric HFD during the active (dark) period (3). We sought to determine whether this initial effect of weight gain during restriction of feeding to the inactive period resulted from altered energy expenditure. We placed mice at thermoneutrality (30°C), which is defined as the temperature at which mice expend minimal energy on maintaining body temperature (6). Monitoring mice at 30°C unmasks the contribution of diet-induced thermogenesis to energy balance by emphasizing pathways independent of body temperature maintenance that contribute to whole-body metabolic rate (6). We provided a HFD to mice ad libitum, either restricted to the inactive (light) period (Zeitgeber time 0 to 12, or ZT0-12) or restricted to the active (dark) period (ZT12-24) for 1 week (Fig. 1A). Mice fed the HFD ad libitum displayed increased weight gain over the course of 1 week, with ~30% of their feeding extending into the light period (Fig. 1, B and C). However, mice fed a HFD restricted to the inactive (light) period showed increased weight gain and altered respiratory exchange ratio (RER) rhythms as compared with mice fed a HFD restricted to the active (dark) period, despite similar cumulative food intake and digestive efficiency (Fig. 1, B to D). Mice fed a HFD restricted to the light period had lower oxygen consumption during the active (dark) period than animals fed during the dark period, despite similar activity rhythms (Fig. 1, E and F). Analysis of

energy expenditure with body mass as a covariate [analysis of covariance (ANCOVA)] revealed that the slope of total energy expenditure versus body mass was higher in mice fed only in the active (dark) period as compared with mice fed only in the inactive (light) period (Fig. 1G). This is consistent with enhanced thermogenesis in mice fed during the active (dark) period compared with mice fed during the inactive (light) period (7). These results suggest that feeding during the inactive phase of the environmental light-dark cycle leads to weight gain that results, at least in part, from reduced diet-induced energy expenditure.

The increase in energy expenditure in mice fed during the active phase led us to investigate whether metabolism of adipose tissue, a key organ for diet-induced thermogenesis, differed depending on feeding time. We used in vivo isotope tracing with glucose to investigate the incorporation of glucose carbons into glycolytic and tricarboxylic acid (TCA) cycle metabolites in adipose tissue. We administered U-¹³C-glucose orally at the onset of the feeding period in mice adjusted to time-restricted feeding (TRF) (ZT0 in light-fed mice and at ZT12 in dark-fed mice). Labeled glucose was rapidly taken up by inguinal white adipose tissue (iWAT) and brown adipose tissue (BAT) and peaked 15 min after feeding (Fig. 1H and fig. S1A). iWAT and BAT from mice fed in the active (dark) phase had increased labeling of pyruvate and lactate from glucose compared with iWAT and BAT from mice fed in the inactive (light) phase, indicating enhanced glycolysis and likely uptake of labeled lactate (8). TCA cycle intermediates were also enriched in labeled carbons from glucose in iWAT of mice fed in the active phase compared with iWAT from mice fed in the inactive phase. This indicates that the time of feeding relative to the light-dark cycle influences carbon flux in adipose tissue. Thus, alignment of feeding with the active period leads to enhanced incorporation of glucose into glycolytic and TCA cycle metabolites in adipose tissue.

Insight into the link between overnutrition and circadian disruption originated with the discovery that mice fed a HFD have abnormal circadian behavioral rhythms and inhibition of core clock and metabolic genes in WAT (7). To evaluate whether TRF affected the clock in adipose tissue, we analyzed gene expression at ZT0 and ZT12, corresponding to the peak and trough of *Bmal1* RNA expression, in iWAT and

¹Department of Medicine, Division of Endocrinology, Metabolism, and Molecular Medicine, Feinberg School of Medicine, Northwestern University, Chicago, IL 60611, USA.

²Robert H. Lurie Cancer Center Metabolomics Core, Feinberg School of Medicine, Northwestern University, Chicago, IL 60611, USA.

³Touchstone Diabetes Center, Department of Internal Medicine, University of Texas Southwestern Medical Center, Dallas, TX 75390, USA.

*Corresponding author. Email: j-bass@northwestern.edu

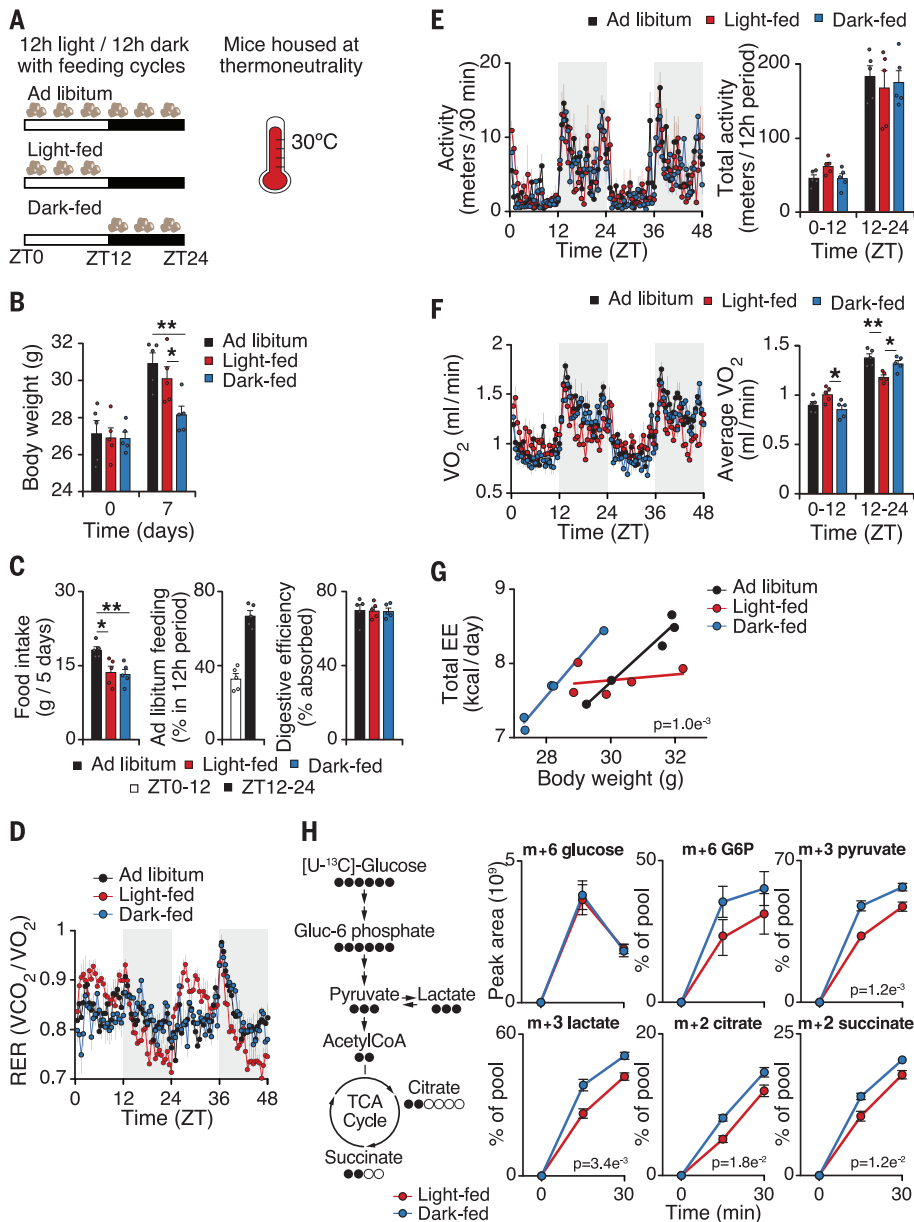


Fig. 1. Circadian mistiming of feeding promotes obesity through reducing energy expenditure.

(A) Experimental design depicting the timing of HFD access as ad libitum, restricted to the light period (ZT0-12; "light-fed") or restricted to the dark period (ZT12-24; "dark-fed") in wild-type male mice at thermoneutrality (30°C). (B) Body weight of mice fed an ad libitum, light-fed, or dark-fed HFD at days 0 and 7 of the HFD ($n = 5$). (C) Cumulative 5-day food intake of mice, average feeding distribution for ad libitum HFD-fed mice from days 5 to 7 of the HFD, and digestive efficiency at days 6 and 7 of the HFD ($n = 5$). (D to F) RER rhythms (D), activity rhythms and average total activity over 12 hours (E), and VO_2 rhythms and average VO_2 levels over 12 hours (F) during days 5 to 7 of the HFD ($n = 5$). The shaded regions indicate the active (dark) time periods. (G) Total energy expenditure (EE) over 24 hours versus body weight during day 7 of the HFD ($n = 5$). Each dot represents one mouse. The p value shown is the analysis of variance (ANOVA) interaction effect. (H) Labeling schematic for $U^{13}C$ -glucose tracing into glycolysis and the TCA cycle (left) and $U^{13}C$ -glucose labeling of indicated metabolites in iWAT at designated times in mice adjusted to TRF for 10 days after oral gavage of 2.5 g of $U^{13}C$ -glucose per kg of body weight at ZT0 (time point 0) for light-fed mice or ZT12 (time point 0) for dark-fed mice (right) ($n = 4$). The ^{13}C isotopologue is depicted by mass (m) plus the number of carbons labeled with ^{13}C . The p value shown is the ANOVA interaction effect. Data are represented as mean \pm SEM. Statistical significance was calculated by two-way ANOVA for multiple comparisons [(B) and (C), (E) and (F), and (H)] or ANCOVA (G) (* $p < 0.05$ and ** $p < 0.01$).

BAT (1, 9). Mice fed a HFD exclusively during the dark period had the highest amplitude of core clock gene expression, whereas mice fed a HFD ad libitum and restricted to the light period had reduced amplitude of clock gene expression in iWAT and BAT (fig. S1, B and C). Furthermore, expression of uncoupling protein 1 (UCP1) was reduced in iWAT and BAT in mice fed during the light period. Thus, disrupted adipocyte circadian and thermogenic rhythms may underlie the negative metabolic consequences of feeding during the inactive (light) period.

The adipocyte circadian clock is required for maintenance of thermogenic rhythms in body temperature (9). To determine whether increasing adipocyte thermogenesis could prevent weight gain and improve health during

mistimed feeding, we used mice with genetically enhanced thermogenesis. Inducible deletion of adipocyte zinc finger protein 423 (ZFP423) in adult mice represents a stronger thermogenic stimulus compared with overexpression of the transcriptional thermogenic activators early B cell factor-2 (EBF2), PRDM1-RIZ (PR) domain-containing 16 (PRDM16), or zinc finger protein 516 (ZFP516), with the strongest activation of thermogenesis occurring at standard housing temperature (22° to 25°C) as compared with thermoneutrality (10). Therefore, we performed TRF in mice with inducible pan adipocyte-specific deletion of the anti-thermogenic transcription factor ZFP423 [Zfp423-knockout (KO) mice] at room temperature, which leads to widespread accumulation of beige adipocytes in WAT and activation

of thermogenesis (Fig. 2A) (11). Adipocyte-specific deletion of Zfp423 prevented weight gain and improved glucose tolerance in mice fed a HFD during the inactive (light) phase compared with control mice fed during the light phase (Fig. 2, B and C, and fig. S2). This indicates that enhancing adipocyte thermogenesis can decrease weight gain during feeding in the inactive (light) period, similar to its role during ad libitum feeding (11).

ZFP423 acts as a co-repressor of EBF2 activity and inhibits the thermogenic transcriptional program, including the pathway that leads to adrenergic activation of UCP1 (11). However, the metabolic mechanisms through which deletion of Zfp423 promotes thermogenesis remain unknown. The major adipocyte thermogenic mechanisms include proton leak

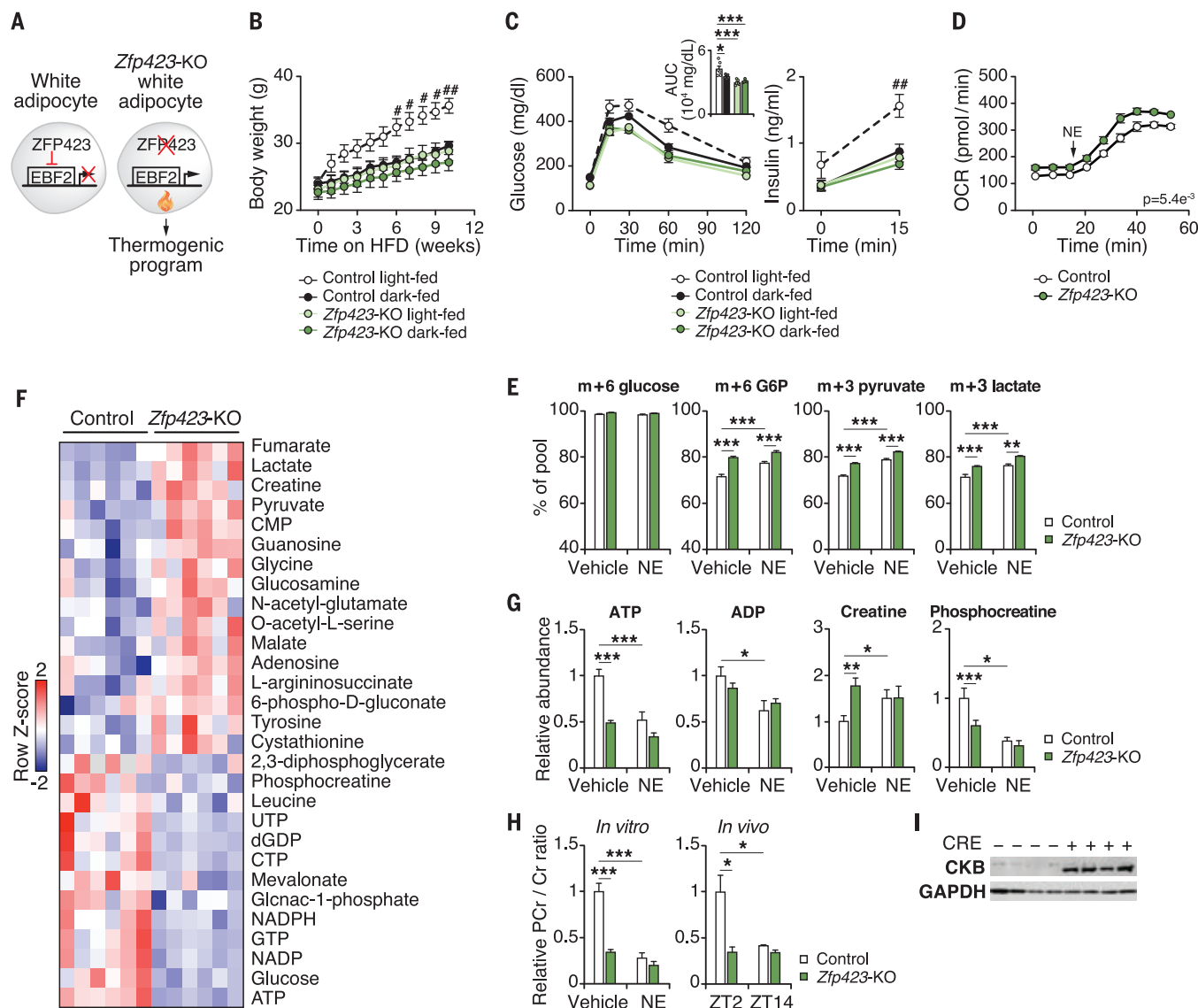


Fig. 2. Genetic disinhibition of adipocyte thermogenesis improves metabolic health during mistimed feeding through enhancing glycolytic flux and creatine metabolism. (A) Model of adipocyte-specific deletion of ZFP423 to drive thermogenic programming in white adipocytes. (B) Body weight during an isocaloric light-fed or dark-fed HFD for 10 weeks in control (*Adiponectin-rtTA;Zfp423^{fllox/fllox}*) and *Zfp423*-KO (*Adiponectin-rtTA;TRE-Cre;Zfp423^{fllox/fllox}*) male mice ($n = 5$ or 6). The # symbol denotes significance between control light-fed and control dark-fed groups. (C) Glucose tolerance test (GTT), area under curve (AUC) during the GTT (inset), and insulin during the GTT at ZT2 at 10 weeks of a HFD ($n = 5$ or 6). For insulin, the # symbol denotes significance between control light-fed versus all other groups. (D) Oxygen consumption rate (OCR) of adipocytes differentiated from inguinal WAT stromal vascular cells from control and adipocyte *Zfp423*-KO mice. After three basal recordings, 100 nM NE was added onto the cells ($n = 5$). The p value shown is the ANOVA interaction effect. (E) Labeling of indicated metabolites after addition of U-¹³C-glucose in the presence or absence of 100 nM NE for 5 hours in differentiated adipocytes from control and adipocyte *Zfp423*-KO mice ($n = 6$).

(F) Heatmap of differentially abundant metabolites [$p < 0.05$ and false discovery rate < 0.10 , calculated using the two-step Benjamini, Krieger, and Yekutieli multiple comparison adjustment approach] in differentiated adipocytes ($n = 6$). CMP, cytidine monophosphate; CTP, cytidine triphosphate; dGDP, deoxyguanosine diphosphate; GTP, guanosine triphosphate; NADH, reduced nicotinamide adenine dinucleotide; NADPH, reduced nicotinamide adenine dinucleotide phosphate; UTP, uridine triphosphate. (G) Relative abundance of ATP, adenosine diphosphate (ADP), creatine, and phosphocreatine in differentiated adipocytes ($n = 6$). (H) PCr/Cr ratio in differentiated adipocytes (left) from control and *Zfp423*-KO mice and iWAT (right) from 3-month-old male control and adipocyte *Zfp423*-KO mice after 4 weeks of dox-chow harvested at ZT2 (light period) and ZT14 (dark period) ($n = 4$). (I) Western blot of CKB and glyceraldehyde phosphate dehydrogenase (GAPDH) in iWAT from control and adipocyte *Zfp423*-KO mice after 4 weeks of a doxycycline-containing HFD at ZT4. Data are represented as mean \pm SEM. Statistical significance was calculated by two-way ANOVA for multiple comparisons [(B) to (E), (G), and (H)] (* $p < 0.05$, ** $p < 0.01$, and *** $p < 0.001$).

through UCP1, creatine-substrate cycling, calcium-dependent adenosine triphosphate (ATP) hydrolysis, and lipid cycling (12). To explore the metabolic mechanisms underlying enhanced thermogenesis in adipocyte

Zfp423-KO mice, we performed bioenergetic and metabolomic analyses in primary adipocytes differentiated from the stromal vascular fraction of the inguinal WAT depot. *Zfp423*-KO adipocytes had increased thermogenic

gene expression, increased basal oxygen consumption due to uncoupling of oxygen consumption from ATP production, and enhanced norepinephrine (NE)-stimulated respiration (Fig. 2D and fig. S3). Isotopic tracing with

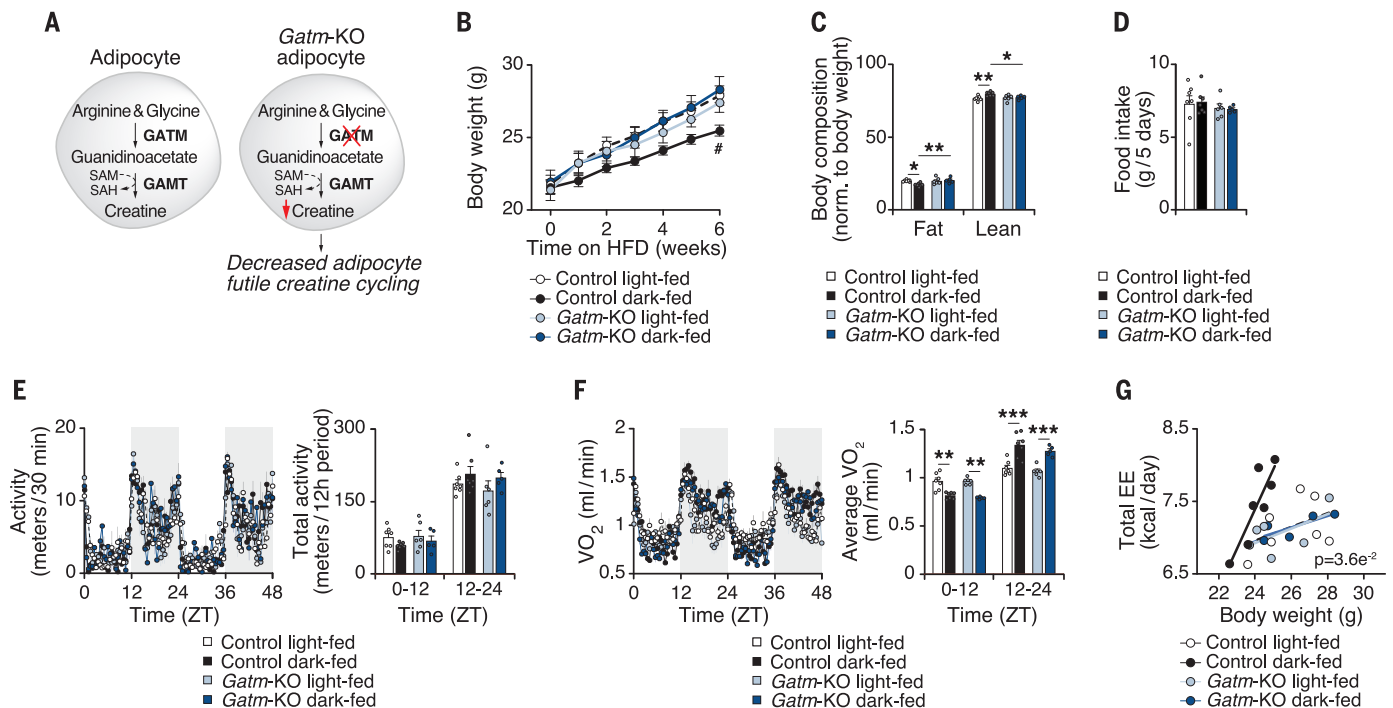


Fig. 3. Genetic depletion of adipocyte creatine levels impairs metabolic benefits driven by TRF. (A) Model of adipocyte-specific deletion of GATM to ablate creatine synthesis in adipocytes. GATM, guanidinoacetate methyltransferase; SAH, S-adenosylhomocysteine; SAM, S-adenosylmethionine. (B) Body weight during an isocaloric light-fed or dark-fed HFD for 6 weeks in control (*Gatm*^{flx/flx}) and *Gatm*-KO (*Adiponectin-Cre;Gatm*^{flx/flx}) male mice ($n = 5$ to 7). The # symbol denotes significance between control dark-fed and control light-fed groups. (C and D) Body

composition (C) and 5-day cumulative food intake (D) during week 6 of a HFD ($n = 5$ to 7). (E and F) Activity rhythms and average total activity over 12 hours (E) and VO_2 rhythms and average VO_2 levels over 12 hours (F) during week 6 of a HFD ($n = 5$ to 7). (G) Total energy expenditure over 24 hours versus body weight after 6 weeks of a HFD ($n = 5$ to 7). The p value shown is the ANOVA interaction effect. Data are represented as mean \pm SEM. Statistical significance was calculated by two-way ANOVA for multiple comparisons [(B) to (F)] or ANCOVA (G) (* $p < 0.05$, ** $p < 0.01$, and *** $p < 0.001$).

U - ^{13}C -glucose indicated that adipocytes stimulated with NE had increased glycolytic flux (Fig. 2E), as do brown adipocytes stimulated with a β_3 adrenergic receptor agonist (13). *Zfp423*-KO adipocytes also showed increased incorporation of U - ^{13}C -glucose into glycolytic intermediates and end products from U - ^{13}C -glucose, including pyruvate and lactate (Fig. 2E). The enhanced glycolytic flux in *Zfp423*-KO adipocytes mirrored the response to pharmacological activation of the β_3 adrenergic receptor.

We used unbiased metabolomic profiling to assess whether steady-state metabolites differ after adipocyte-specific ablation of *Zfp423*. We identified 29 differentially abundant metabolites in *Zfp423*-KO adipocytes compared with control adipocytes, including increased amounts of creatine, pyruvate, and lactate and decreased amounts of phosphocreatine and ATP (Fig. 2, F and G). Increasing creatine synthesis, import, and cycling fuels a futile cycle of mitochondrial ATP turnover in thermogenic cells (12). The phosphocreatine/creatine (PCr/Cr) ratio was lower in *Zfp423*-KO adipocytes, mirroring the response of adrenergic stimulus with NE (Fig. 2H). Additionally, the PCr/Cr ratio was reduced in iWAT of *Zfp423*-KO mice (Fig. 2H). Abundance of creatine kinase B (CKB), the major kinase isoenzyme in the

futile creatine cycle in thermogenic fat, was increased in iWAT of adipocyte *Zfp423*-KO mice during ad libitum HFD feeding (Fig. 2I) (14). Thus, deletion of *Zfp423* fuels adipocyte thermogenesis through increased uncoupled respiration, enhanced NE-stimulated respiration, increased glucose flux into glycolysis, and increased creatine cycling. Therefore, the transcriptional program regulated by *ZFP423* encompasses a wide range of downstream outputs that control UCPI-dependent and UCPI-independent thermogenic programs.

The increased abundance of CKB and futile creatine cycling in *Zfp423*-KO adipocytes led us to consider that diet-induced thermogenesis through creatine turnover may be a metabolic mechanism through which restricting feeding to the active phase improves health. To test this, we used mice with genetic reduction in adipocyte creatine synthesis through adipocyte-specific ablation of glycine amidinotransferase (GATM) (*Adiponectin-Cre;Gatm*^{flx/flx}, or *Gatm*-KO) (Fig. 3A) (15). As expected, control mice fed only during the light period gained more weight than control mice fed only during the dark period (Fig. 3B). By contrast, mice lacking GATM in adipocytes gained a similar amount of weight and showed similar adiposity as control mice fed only during the light

period, regardless of whether a HFD was provided during the light or dark period (Fig. 3, B and C). Cumulative food intake and activity rhythms did not differ among the groups (Fig. 3, D and E). Rhythms of oxygen consumption (when not adjusted for body weight) showed a similar trend independent of genotype (Fig. 3F). However, the slope of total energy expenditure versus body mass was greatest in control mice fed in the dark period compared with other groups (Fig. 3G). Total energy expenditure was equivalent in adipocyte *Gatm*-KO fed in the light or dark period when analyzed with ANCOVA using body mass as a covariate. This provides genetic evidence that adipocyte creatine cycling contributes to the metabolic benefits of TRF during the active (dark) period.

Deletion of *Zfp423* in adipocytes led to increased creatine cycling and protection from obesity during circadian mistimed feeding. Genetic disruption of adipocyte creatine cycling also reduced the metabolic benefits in response to TRF to the active period. Thus, creatine metabolism may be rhythmically regulated, with enhanced synthesis or cycling during the dark period when nocturnal mice eat. Indeed, the PCr/Cr ratio was decreased in adipose tissue during the active period (ZT14) compared with the inactive period (ZT2) in

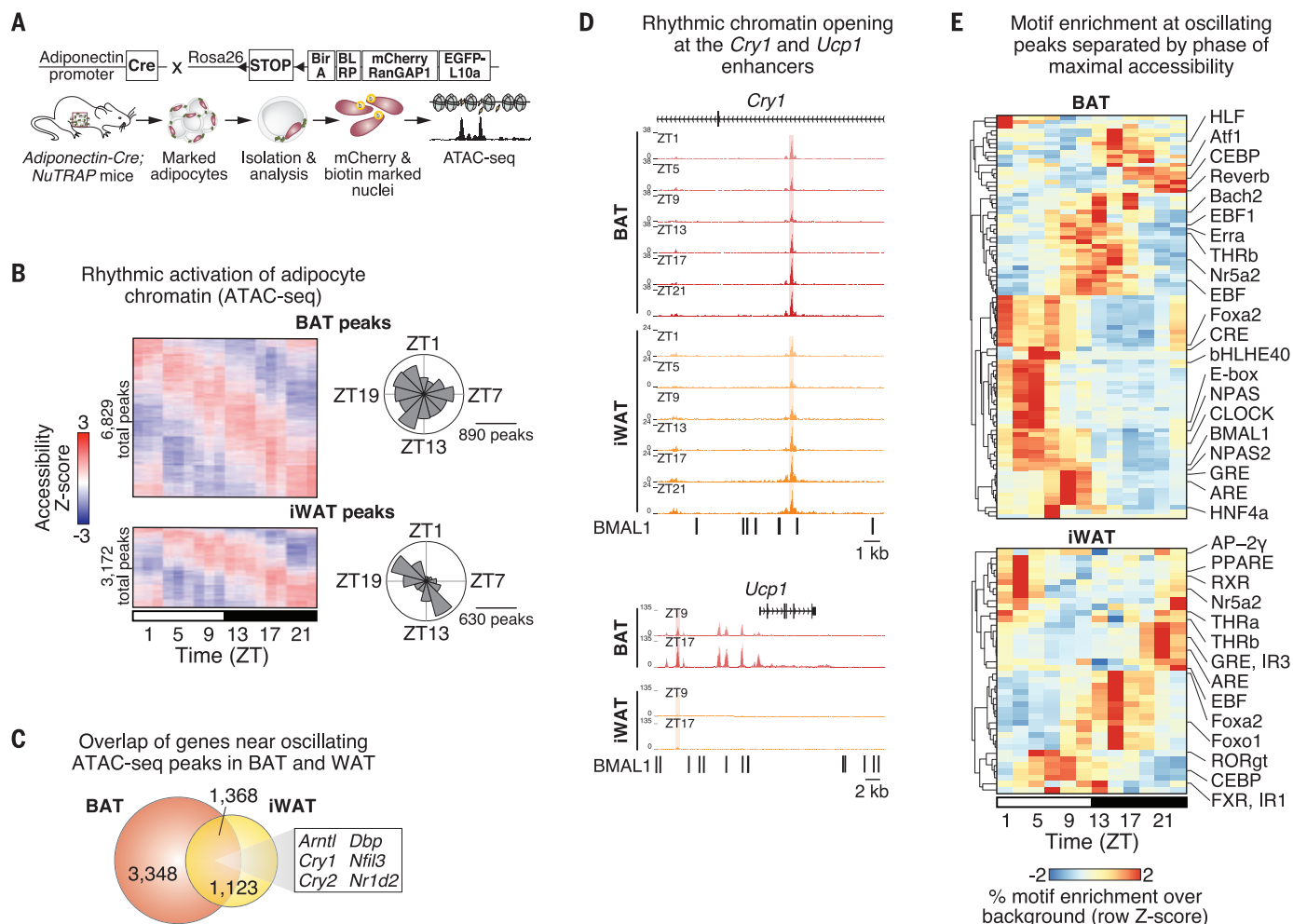


Fig. 4. Rhythmic chromatin profiling in adipocytes reveals distinct phases of accessibility in BAT and iWAT. (A) After Cre expression, *Adiponectin-Cre; NuTRAP^{lox/+}* mice express nuclear membrane labeled with mCherry and biotin and labeling of the translating mRNA polysome complex with enhanced green fluorescent protein (EGFP)-fused ribosomal protein L10a. Adipocyte nuclei from BAT and iWAT of male *Adiponectin-Cre; NuTRAP^{lox/+}* mice housed at thermoneutrality were isolated every 4 hours throughout the 24-hour day (ZT1, 5, 9, 13, 17, and 21) by fluorescence-activated cell sorting (FACS)

for ATAC-seq analysis. (B) Heatmaps showing rhythmic activation of adipocyte chromatin in BAT and WAT ($n = 3$ per time point) and radial histograms showing the phases of maximal accessibility for rhythmic peaks within each 2-hour window. (C) Overlap of genes near oscillating peaks in BAT and WAT. (D) Rhythmic opening of chromatin at *Cry1* and *Ucp1* enhancers, with tick marks below indicating the locations of known BMAL1 binding motifs. (E) Motif enrichment at oscillating peaks separated by phase of maximal accessibility in BAT and WAT throughout the day ($n = 3$ per time point).

mice fed chow ad libitum (Fig. 2H), indicative of enhanced creatine cycling in vivo during the active period when mice typically feed.

To further uncover adipocyte circadian chromatin architecture that underlies timing of metabolic outputs, we performed assay for transposase-accessible chromatin by sequencing (ATAC-seq) in fluorescently labeled adipocyte nuclei from WAT and BAT isolated every 4 hours throughout the 24-hour day by nuclear tagging and translating ribosome affinity purification (NuTRAP) with *Adiponectin-Cre; NuTRAP^{lox/+}* mice housed at thermoneutrality (Fig. 4A). We analyzed the subcutaneous iWAT depot and the interscapular BAT depot specifically to identify distinct rhythmic patterns of chromatin regulation in white or beige and brown adipocytes. We identified

83,322 nucleosome-free regions (“peaks”) in WAT and 112,985 peaks in BAT, with most of the accessible peaks located in intergenic and intronic enhancer regions (79.7% in iWAT and 82.7% in BAT) (fig. S4A). We removed peaks with low read depth to avoid false-positive detection of rhythmic chromatin opening. To detect genes that were rhythmic across the day, we performed Jonckheere-Terpstra-Kendall (JTK) cycle analysis using normalized and filtered read counts across 25,050 WAT and 42,572 BAT peaks and identified genome-wide oscillations in adipocyte chromatin accessibility. In BAT, we identified that 16.0% of ATAC-seq peaks (6829 total peaks) oscillated with a broad distribution throughout the day, and maximal openness occurring during the dark period (Fig. 4B and table S1). In iWAT, we

found that 12.7% of peaks (3172 peaks total) oscillated with a biphasic pattern of accessibility (Fig. 4B and table S2). In BAT and iWAT, adipocyte chromatin accessibility exhibited dynamic opening across the light-dark cycle in canonical circadian genes and *Ucp1* (Fig. 4, C and D, and fig. S4B). Principal components analysis (PCA) of normalized reads at rhythmic peaks highlighted the cyclical 24-hour patterns in chromatin opening in both BAT and iWAT genome-wide (fig. S4, C and D).

Motif enrichment analyses at oscillating peaks at a 2-hour resolution showed strong rhythmic chromatin opening in areas occupied by transcription factors, including peroxisome proliferator-activated receptor γ (PPAR γ), early B cell factor (EBF), estrogen-related receptor β (ESRR β), CCAAT enhancer-binding proteins

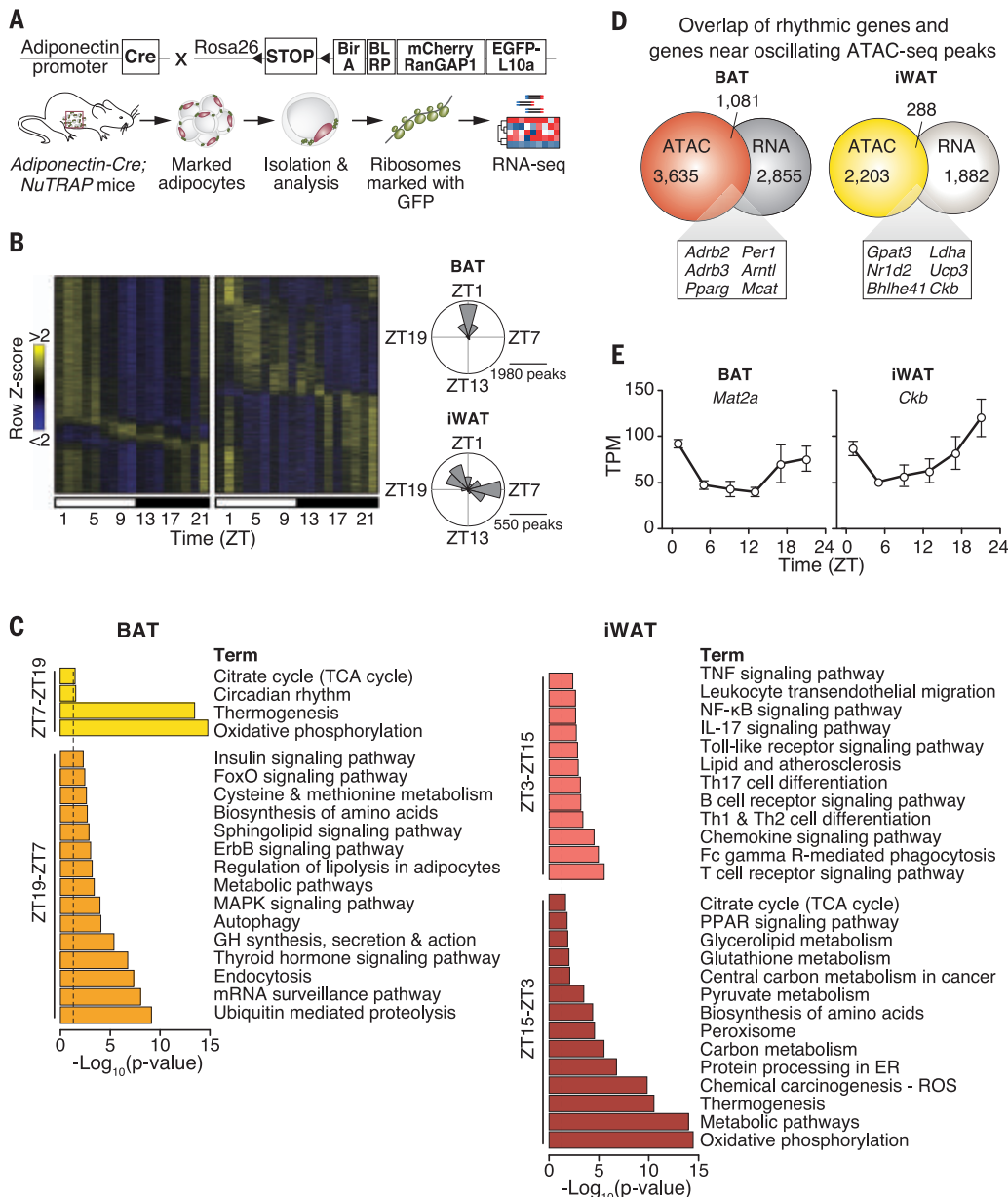


Fig. 5. Ribosomal RNA profiling reveals diurnal control of adipocyte metabolism. (A) Adipocyte ribosomal RNA for RNA-seq was isolated from BAT and iWAT harvested every 4 hours throughout the 24-hour day (ZT1, 5, 9, 13, 17, and 21) from male *Adiponectin-Cre; NuTRAP^{fllox/+}* mice housed at thermoneutrality. (B) Heatmaps showing rhythmic adipocyte RNA expression in BAT and iWAT ($n = 3$ per time point except $n = 2$ for BAT at ZT17) and radial histograms showing the number of genes whose oscillations peak within each 2-hour window in BAT and iWAT. (C) KEGG pathway analysis of oscillating genes in BAT from ZT7-19 and ZT19-7 and in WAT from ZT3-15 and ZT15-3. ER, endoplasmic reticulum; ErbB, epidermal growth factor receptor; FoxO, forkhead box O; GH, growth hormone; IL-17, interleukin-17; MAPK, mitogen-activated protein kinase; NF-κB, nuclear factor κB; Th17; T helper 17; TNF, tumor necrosis factor. (D) Overlap of rhythmic genes identified through RNA-seq and genes near oscillating ATAC-seq peaks. (E) Examples of rhythmic gene expression [shown in transcripts per million (TPM)] identified through RNA-seq in BAT and iWAT ($n = 3$ per time point everywhere except $n = 2$ for BAT at ZT17). Data are represented as mean \pm SEM.

(CEBP), glucocorticoid receptor (GR), and retinoic acid receptor (RAR)-related orphan receptor γ (ROR γ) that regulate bioenergetic, adipogenic, and inflammatory gene networks in both iWAT and BAT (Fig. 4E). We also identified known BMAL1 binding motifs at rhythmic accessible regions (± 1 kb) near genes that function in creatine metabolism such as *Ckb* ($p < 0.05$ in iWAT), the rate-limiting enzyme in creatine biosynthesis *Gatm* ($p < 0.05$ in BAT), and methionine adenosyltransferase 2A (*Mat2a*) ($p < 0.05$ in iWAT), which generates S-adenosylmethionine (SAM) for creatine synthesis (fig. S4E) (14, 15).

We investigated whether genome-wide changes in chromatin accessibility corresponded with time-of-day-dependent alterations in the adipocyte transcriptome by sequencing RNA

from mice maintained at thermoneutrality. We isolated adipocyte-specific translating RNA from BAT and iWAT of *Adiponectin-Cre; NuTRAP* mice for RNA sequencing (RNA-seq) (Fig. 5A). We found the expected enrichment of adipocyte- and depot-specific gene expression in BAT and iWAT (fig. S5). We identified 3936 oscillating transcripts (28.0% of genes) in BAT by JTK_cycle analysis at an adjusted $p < 0.05$ and observed that most of the rhythmic transcripts reach maximal abundance during a single phase of the circadian cycle ZT19-7, whereas a smaller number of genes are maximally expressed during the opposite phase (ZT7-19) (Fig. 5B and table S3). Kyoto Encyclopedia of Genes and Genomes (KEGG) pathway analysis revealed enrichment of genes associated with endocrine signaling (thyroid

hormone pathway and insulin signaling), metabolism pathways (regulation of lipolysis, sphingolipid signaling, and methionine metabolism), and cellular maintenance pathways (proteolysis and autophagy) during ZT19-7 (Fig. 5C). During the opposite phase of peak rhythmic RNA transcripts (ZT7-19), we identified KEGG pathways related to the TCA cycle, thermogenesis, oxidative phosphorylation, and circadian rhythm (Fig. 5C). In iWAT, we identified 2170 oscillating transcripts (17.3% of genes) through JTK_cycle analysis with an adjusted $p < 0.05$ and observed two phases of maximal amplitude in oscillating genes, similar to the two major phases in oscillating ATAC-seq peaks (Figs. 4B and 5B and table S4). During phase ZT3-15, we identified KEGG pathways mostly involved in inflammation [tumor necrosis factor (TNF),

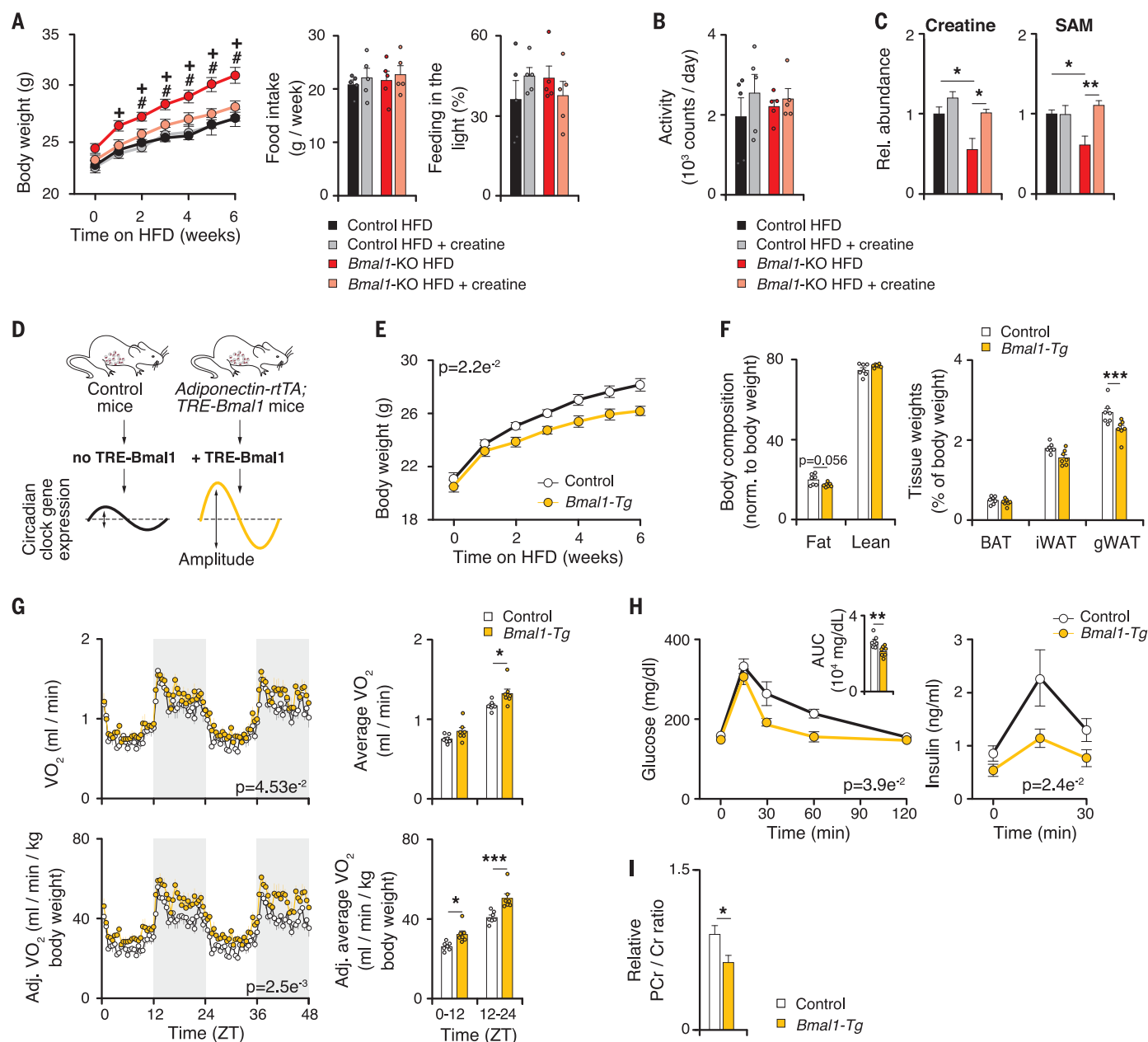


Fig. 6. The adipocyte clock regulates metabolic health through creatine metabolism. (A) Body weight of control (*Bmal1*^{flox/flox}) and *Bmal1*-KO (*Adiponectin-Cre;Bmal1*^{flox/flox}) male mice fed an ad libitum HFD supplemented with 2% creatine for 6 weeks at thermoneutrality ($n = 5$) with weekly food intake (middle) and percentage of food intake during the light period (right) from weeks 5 to 6 of the HFD. The # symbol denotes significance between *Bmal1*-KO HFD and *Bmal1*-KO HFD + creatine groups. The + symbol denotes significance between control HFD and *Bmal1*-KO HFD groups. (B and C) Average daily activity (B) detected by infrared sensors during weeks 5 and 6 of HFD feeding and relative metabolite abundance (C) in iWAT after 6 weeks of HFD ($n = 5$). (D) Experimental design showing that mice with doxycycline-inducible transgenic expression of the clock activator *Bmal1* in adipocytes have enhanced amplitude of core clock

expression. (E) Body weight of control (*Adiponectin-rtTA*) and *Bmal1*-Tg (*Adiponectin-rtTA;TRE-Bmal1*) mice during 6 weeks of ad libitum HFD feeding at thermoneutrality ($n = 7$). (F) Body composition and adipose tissue weights after 6 weeks of a HFD ($n = 7$). (G) VO_2 rhythms and average VO_2 levels nonadjusted (top) and adjusted for body weight (bottom) from weeks 5 to 6 of a HFD ($n = 7$). The p value shown is the ANOVA interaction effect. (H) Glucose tolerance test, AUC (inset), and insulin during the GTT at ZT2 at 6 weeks of a HFD ($n = 7$). The p value shown is the ANOVA interaction effect. (I) PCr/Cr ratio in iWAT after 6 weeks of a HFD ($n = 7$). Data are represented as mean \pm SEM. Statistical significance was calculated by two-way ANOVA for multiple comparisons [(A) to (C) and (E) to (H)] or unpaired Student's two-sided t test (I) (* $p < 0.05$, ** $p < 0.01$, and *** $p < 0.001$).

nuclear factor κ B (NF- κ B), and Toll-like receptor (TLR) signaling; leukocyte trans-endothelial migration; and T cell signaling], whereas during phase ZT15–3, we observed several pathways involved in metabolism [oxi-

dative phosphorylation, thermogenesis, pyruvate and carbon metabolism, reactive oxygen species (ROS), and the TCA cycle] (Fig. 5C).

Analysis of overlap of rhythmic genes identified through RNA-seq and genes near oscil-

lating ATAC-seq peaks revealed 1016 common genes in BAT and 285 common genes in iWAT (Fig. 5D and table S5). Several of these rhythmic genes in BAT are components of the core molecular clock (*Arntl*, *Per1*, *Per3*, *Nr1d1*,

Nr1d2), factors involved in adrenergic activation (*Adrb2*, *Adrb3*, *Creb1*), brown adipocyte transcription factors (*Ebf1*, *Ebf3*), and metabolic enzymes (*Ldha*, *Pcx*, *Pdk4*). In iWAT, we observed overlap of genes involved in circadian rhythms (*Dbp*, *Ncor2*, *Nr1d2*), inflammation (*Ccl5*, *Irf4*), and metabolism and oxidative stress (*Cs*, *Ldha*, *Sod1*, *Ucp3*). In addition, we identified significant overlap in genes involved in creatine metabolism between rhythmic analysis of ATAC-seq and RNA-seq, including *Mat2a* in BAT ($p < 0.01$) and *Ckb* in iWAT ($p < 0.01$) (Fig. 5E). Collectively, these findings reveal that rhythmicity of the adipocyte circadian clock and the creatine metabolic pathway throughout the day are regulated at the genomic and transcriptomic levels.

To analyze whether these changes in genomic architecture and transcription of genes involved in creatine metabolism are functional, we performed metabolomics in iWAT collected every 6 hours throughout the day from mice fed ad libitum and housed at thermoneutrality. Creatine abundance and the PCr/Cr ratio were rhythmic throughout the day, with the peak in creatine abundance occurring during the dark cycle (ZT13) and maximal creatine cycling (low PCr/Cr ratio) during the dark period (fig. S6A). CKB protein was most abundant at ZT13 (fig. S6B). We assessed whether TRF of a HFD affected circadian rhythmicity of creatine metabolism in WAT. Mice fed during the active (dark) period had a peak in creatine abundance in iWAT during ZT13 that was lacking in mice fed during the inactive (light) period. iWAT from mice fed during the inactive (light) period lacked the decline in the PCr/Cr ratio during the dark period, indicating reduced creatine cycling (fig. S6A). The timing of accumulation of CKB protein was similar in mice fed in the dark and light period (fig. S6B). Thus, creatine abundance and futile cycling are rhythmic in adipose tissue at thermoneutrality.

Our data suggest that the adipocyte clock in BAT and WAT may affect bioenergetic transcription factor activation or CLOCK-BMAL1-dependent activation of creatine metabolism. We analyzed gene expression and metabolite abundance in primary adipocytes that lack the core clock activator BMAL1 (*Bmal1*-KO). Such cells had decreased expression of genes that function in creatine metabolism, decreased abundance of creatine, and an increase in the PCr/Cr ratio (fig. S7, A to C). We observed similar results in vivo in iWAT from adipocyte-specific *Bmal1*-KO mice (fig. S7, D to G). We also saw significant decreases in the abundance of SAM, MAT2A, and CKB in iWAT of adipocyte-specific *Bmal1*-KO mice (fig. S7, F to H). Creatine synthesis from guanidinoacetate consumes more than 40% of all methyl groups (16); therefore, the reduced abundance of creatine in adipocytes that lack

BMAL1 might result, in part, from limited SAM synthesis.

To test whether BMAL1 directly regulates creatine enzymes at the genomic level, we performed chromatin immunoprecipitation-sequencing (ChIP-seq) of BMAL1 in WAT. We did not observe a BMAL1 genomic binding site for *Gatm* or *Ckb* in WAT (table S6). Therefore, these enzymes may be indirectly regulated by BMAL1 through other circadian clock genes or clock-controlled genes. However, we identified a BMAL1 binding site at the promoter of *Mat2a* (fig. S7I). Given that *Mat2a* expression was lower in adipocytes that lack BMAL1, it is possible that the decline in *Mat2a* and SAM may decrease creatine synthesis in *Bmal1*-KO adipocytes. Collectively, our genomic and metabolomic findings indicate that the adipocyte molecular clock generates rhythmic cycles of creatine synthesis and metabolism in alignment with the environmental light-dark cycle.

To evaluate whether clock-controlled rhythms in creatine metabolism underlie enhanced thermogenesis during TRF, we used mice that lack BMAL1 specifically in adipocytes (*Bmal1*-KO). These mice consume more food during the light period and gain more weight on a HFD fed ad libitum at room temperature than control mice (17). We housed adipocyte *Bmal1*-KO mice at thermoneutrality and provided a HFD evenly dispersed throughout the dark or light period. As expected, control mice gained more weight when fed during the inactive (light) period than did mice fed during the active (dark) period (fig. S8A). Adipocyte *Bmal1*-KO mice fed a HFD restricted to the light or dark period gained equal amounts of weight and had similar glucose tolerance as control mice fed during the inactive (light) period (fig. S8, A to C). These results reveal that the adipocyte clock is essential for metabolic benefits during TRF to the active (dark) period. *Bmal1*-KO adipocytes had decreased abundance of creatine and futile creatine cycling (fig. S7, F to H). To investigate whether increasing the abundance of creatine in mice that lack adipocyte BMAL1 could restore diet-induced thermogenesis, we fed control and *Bmal1*-KO mice a HFD supplemented with creatine. Creatine supplementation largely restored the weight gain, loss of glucose homeostasis, and amounts of iWAT creatine and SAM in adipocyte *Bmal1*-KO mice with no change in food intake or activity (Fig. 6, A to C, and fig. S8, C and D).

Consumption of a HFD dampens clock gene expression rhythms in a tissue-specific manner, particularly in adipose tissue (18). Decreased adipocyte clock function might thus drive metabolic defects in mice on a HFD through disruption of rhythmic creatine metabolism. To test this, we generated mice with inducible adipocyte-specific transgenic expression

of BMAL1 (*Bmal1*-Tg). Constitutive expression of the clock activator BMAL1 in adipocytes was sufficient to enhance clock rhythms by increasing the amplitude of expression of core clock genes (Fig. 6D and fig. S9A) (19). When adipocyte *Bmal1*-Tg mice were fed a HFD at thermoneutrality, they gained less weight than control mice and had significantly increased oxygen consumption (nonadjusted for body weight) during the dark period with similar feeding and activity rhythms (Fig. 6, E to G, and fig. S9, B and C). Total energy expenditure was not significantly different when analyzed with body weight as a covariate (ANCOVA). However, adjusting oxygen consumption (VO_2) by body mass revealed significantly increased oxygen consumption during both the light and dark period (Fig. 6G). Glucose tolerance was also improved in adipocyte *Bmal1*-Tg mice (Fig. 6H). Adipocyte *Bmal1*-Tg mice had increased creatine cycling and increased expression of *Ckb* and *Gatm* in iWAT (Fig. 6I and fig. S9D). Therefore, amplifying core clock rhythms in adipocytes is sufficient to enhance energy expenditure and reduce weight gain.

Discussion

Our results establish that misalignment of feeding time with intrinsic circadian cycles of adipocyte thermogenesis contributes to metabolic syndrome in the setting of overnutrition. Our analyses build upon advances in the identification of transcriptional regulators of adipose ontogeny that have established a major role for ZFP423 in suppressing thermogenic capacity (11, 20). We identify energy dissipation through the futile creatine cycle as an intrinsic thermogenic mechanism in adipocytes that lack ZFP423, an effect likely regulated through disinhibition of EBF2 (21).

Our analyses circumvented a common challenge in bioenergetic experiments because we housed mice at thermoneutrality, where adipose tissue energy cycles track with time rather than thermal stress. UCPI is under control of the core molecular clock (9), consistent with our finding that enhanced thermogenesis during alignment of feeding time with the active (dark) cycle requires an intact adipocyte molecular clock. Our observation that creatine supplementation counters the obesogenic effect of adipocyte clock ablation indicates that the etiology of weight gain caused by mistimed feeding rhythms results, at least in part, from impaired creatine-induced thermogenesis. Our analyses establish a primary role for the adipocyte clock in diet-induced thermogenesis because augmentation of adipocyte circadian function was sufficient to attenuate diet-induced obesity.

In settings in which humans experience rapid or frequent shifts in feeding schedules due to shiftwork, sleep loss, or exposure to blue light, misalignment between feeding and the

endogenous circadian phase of adipose thermogenesis may exacerbate metabolic disease. We propose that alignment of feeding with intrinsic thermogenic rhythms may underlie the healthful benefits of TRF.

REFERENCES AND NOTES

1. A. Kohsaka *et al.*, *Cell Metab.* **6**, 414–421 (2007).
2. F. W. Turek *et al.*, *Science* **308**, 1043–1045 (2005).
3. D. M. Arble, J. Bass, A. D. Laposky, M. H. Vitaterna, F. W. Turek, *Obesity* **17**, 2100–2102 (2009).
4. M. Hatori *et al.*, *Cell Metab.* **15**, 848–860 (2012).
5. S. Cienfuegos *et al.*, *Cell Metab.* **32**, 366–378.e3 (2020).
6. H. M. Feldmann, V. Golozubova, B. Cannon, J. Nedergaard, *Cell Metab.* **9**, 203–209 (2009).
7. A. I. Mina *et al.*, *Cell Metab.* **28**, 656–666.e1 (2018).
8. S. Hui *et al.*, *Nature* **551**, 115–118 (2017).
9. Z. Gerhart-Hines *et al.*, *Nature* **503**, 410–413 (2013).
10. M. Shao, R. K. Gupta, *Biochim. Biophys. Acta Mol. Cell Biol. Lipids* **1864**, 20–28 (2019).
11. M. Shao *et al.*, *Cell Metab.* **23**, 1167–1184 (2016).
12. E. T. Chouchani, L. Kazak, B. M. Spiegelman, *Cell Metab.* **29**, 27–37 (2019).
13. V. Panic *et al.*, *eLife* **9**, e25558 (2020).
14. J. F. Rahbani *et al.*, *Nature* **590**, 480–485 (2021).
15. L. Kazak *et al.*, *Cell Metab.* **26**, 660–671.e3 (2017).
16. J. T. Brosnan, R. P. da Silva, M. E. Brosnan, *Amino Acids* **40**, 1325–1331 (2011).
17. G. K. Paschos *et al.*, *Nat. Med.* **18**, 1768–1777 (2012).
18. H. K. Hong *et al.*, *Genes Dev.* **32**, 1367–1379 (2018).
19. E. L. McDearmon *et al.*, *Science* **314**, 1304–1308 (2006).
20. P. Seale *et al.*, *J. Clin. Invest.* **121**, 96–105 (2011).
21. M. Shao *et al.*, *Genes Dev.* **35**, 1461–1474 (2021).

ACKNOWLEDGMENTS

We thank all members of the Bass, Barish, Beutler, and Peek laboratories for helpful discussions. We also thank B. Spiegelman for providing the GATM-flox mice and J. Takahashi for providing the TRE-Bmal1 mice. We thank the Northwestern University Metabolomics Core, NUSeq Core, and Mouse Histology and Phenotyping Laboratory Core for excellent guidance and assistance with experiments performed in this study. **Funding:** Research support was provided by NIH National Institute of Diabetes and Digestive and Kidney Diseases (NIDDK) grants R01DK127800, R01DK113011, and R01DK090625 and National Institute on Aging (NIA) grants R01AG065988 and P01AG011412 (to J.B.); NIDDK grant F32DK122675 (to C.H.); NIDDK grant F30DK116481 (to B.J.W.); NIDDK grant F31DK130589 (to N.J.W.); NIDDK grant K99DK124682 (to J.C.); American Heart Association Career Development Award 19CDA34670007 (to M.S.); and NIDDK grants R01DK104789 and R01DK119163 (to R.K.G.). **Author contributions:** C.H. and J.B. conceived the study and wrote the manuscript. C.H., B.J.W., N.J.W., J.C., M.S., R.K.G., and J.B. designed experiments. C.H., B.J.W., N.J.W., A.K.T., Y.K., R.N., M.V.N., and P.G. performed experiments. C.H., B.J.W., N.J.W., and B.M. visualized and curated the data. C.H., K.M.R., and J.B. edited the manuscript. **Competing interests:** The authors declare that they have no competing financial interests. **Data and materials availability:** Data from this study are publicly available in the GEO repository (GSE181443). **License information:** Copyright © 2022 the authors, some rights reserved; exclusive licensee American Association for the Advancement of Science. No claim to original US government works. <https://www.science.org/about/science-licenses-journal-article-reuse>

SUPPLEMENTARY MATERIALS

science.org/doi/10.1126/science.abl8007
Materials and Methods
Figs. S1 to S9
Tables S1 to S7
References (22–31)
MDAR Reproducibility Checklist

Submitted 5 August 2021; resubmitted 15 February 2022
Accepted 23 August 2022
10.1126/science.abl8007

CYSTIC FIBROSIS

Molecular structures reveal synergistic rescue of $\Delta 508$ CFTR by Trikafta modulators

Karol Fiedorczuk¹ and Jue Chen^{1,2*}

The predominant mutation causing cystic fibrosis, a deletion of phenylalanine 508 ($\Delta 508$) in the cystic fibrosis transmembrane conductance regulator (CFTR), leads to severe defects in CFTR biogenesis and function. The advanced therapy Trikafta combines the folding corrector tezacaftor (VX-661), the channel potentiator ivacaftor (VX-770), and the dual-function modulator elxacaftor (VX-445). However, it is unclear how elxacaftor exerts its effects, in part because the structure of $\Delta 508$ CFTR is unknown. Here, we present cryo-electron microscopy structures of $\Delta 508$ CFTR in the absence and presence of CFTR modulators. When used alone, elxacaftor partially rectified interdomain assembly defects in $\Delta 508$ CFTR, but when combined with a type I corrector, did so fully. These data illustrate how the different modulators in Trikafta synergistically rescue $\Delta 508$ CFTR structure and function.

Cystic fibrosis (CF) is a common genetic disease (1) caused by mutations in the gene that encodes the cystic fibrosis transmembrane conductance regulator (CFTR) (2, 3). CFTR is widely expressed in epithelial cells, regulating salt and fluid homeostasis in a variety of tissues. The absence or dysfunction of CFTR causes health issues, including malnutrition, liver disease, recurrent bacterial infection, chronic inflammation, and respiratory failure (4).

CFTR belongs to the ATP-binding cassette (ABC) transporter family but functions as an ATP-gated anion channel (5–7). It contains an N-terminal interfacial structure called the lasso motif, two transmembrane domains (TMDs) that form an anion conduction pathway, two cytoplasmic nucleotide-binding domains (NBDs) that bind and hydrolyze ATP (8), and a unique regulatory (R) domain that must be phosphorylated to open the channel (9, 10). Although >300 mutations cause CF, ~90% of patients carry at least one copy of $\Delta 508$ CFTR in which a single phenylalanine at position 508 is deleted (11, 12). This $\Delta 508$ mutant exhibits a severe trafficking defect that results in intracellular retention and premature degradation of the channel (13). Furthermore, the few channels that reach the plasma membrane are unstable and functionally compromised (14–16).

The structure of wild-type (WT) CFTR shows that F508 resides on the surface of NBD1, where it makes extensive interactions with the cytosolic region of TM helix 11 and intracellular loop 4 (8, 17). These interactions are critical for both CFTR folding and coupling of ATP-dependent NBD dimerization to pore opening (18), suggesting that disruption of these interactions may underlie both trafficking and functional defects in $\Delta 508$ CFTR. In-

deed, a previous crystal structure of an isolated NBD1 containing $\Delta 508$ revealed a conformation nearly identical to WT NBD1 (19), supporting the hypothesis that $\Delta 508$ primarily affects interdomain assembly (8, 19–22). Other studies have shown that a lack of F508 causes thermodynamic instability of NBD1 and the entire CFTR protein (20, 23). Unfortunately, the intrinsic instability of $\Delta 508$ CFTR has hindered efforts to structurally characterize the mutant in the context of the entire CFTR protein.

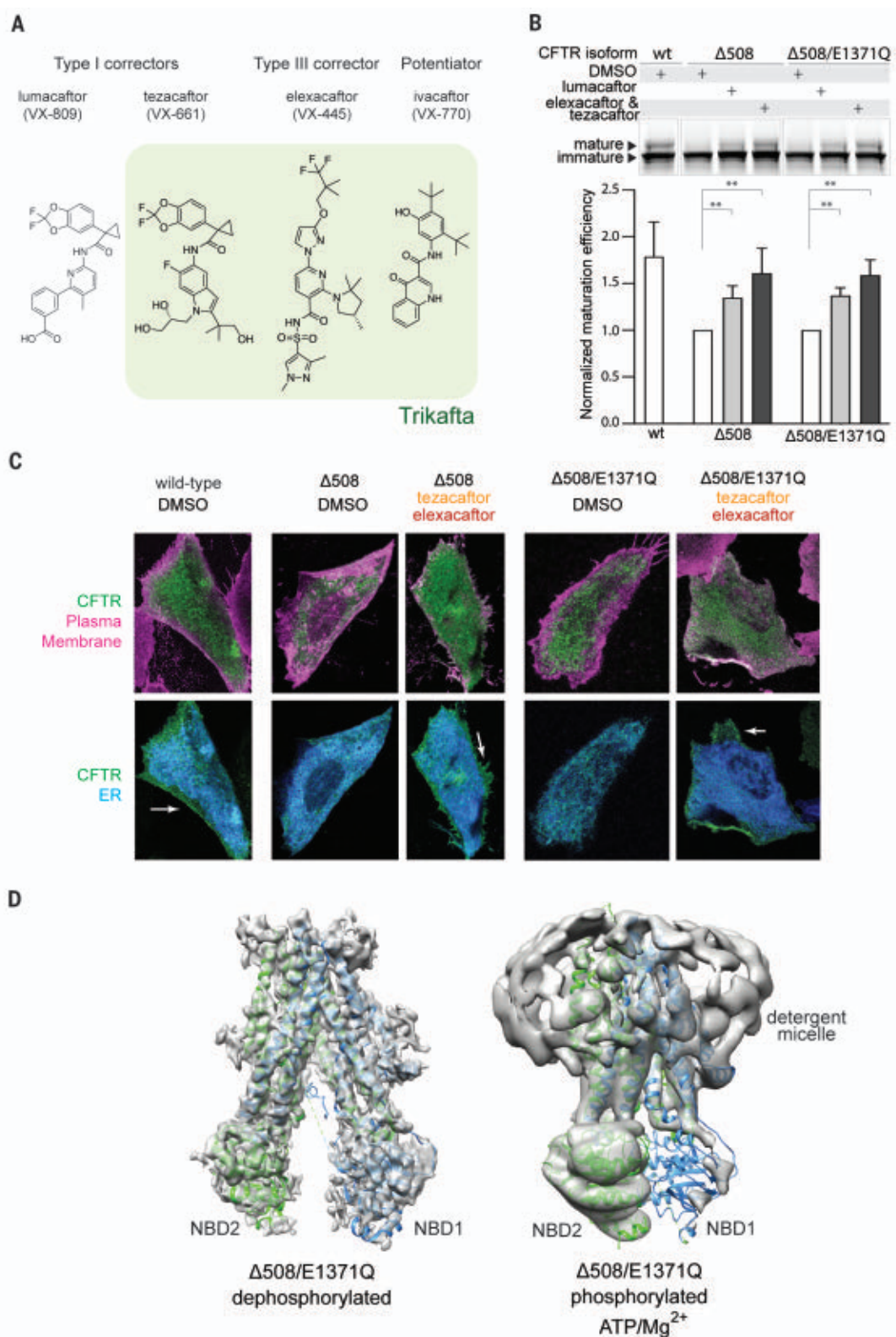
Despite these structural obstacles, recently developed CFTR modulators have transformed CF therapy from symptom management to disease correction. These modulators include potentiators that enhance the function of CFTR in the plasma membrane and correctors that increase the abundance of CFTR at the cell surface (24, 25). CFTR correctors are further categorized into three different classes on the basis of their functional redundancy (26, 27). Currently, there are four pharmacological molecules used in CF therapy, either singly or in combination. These include the potentiator ivacaftor (VX-770), the type I correctors lumacaftor (VX-809) and tezacaftor (VX-661), and the type III corrector elxacaftor (VX-445) (Fig. 1A). The most advanced therapy, Trikafta (branded as Kaftrio in Europe) is a combination of ivacaftor, tezacaftor, and elxacaftor. The molecular mechanisms of ivacaftor and type I correctors have been well studied (28, 29). Elxacaftor, however, was discovered only recently and little is known about its mode of action. It has been shown to have a dual function, improving CFTR folding as well as ion conductance (27, 30–33), but it is unknown whether it potentiates and corrects through the same binding site.

In this study, we determined cryo-electron microscopy (cryo-EM) structures of $\Delta 508$ CFTR and analyzed the molecular effects of lumacaftor, tezacaftor, and elxacaftor, revealing how elxacaftor might potentiate the activity of $\Delta 508$ and stabilize its structure. We also solved

¹Laboratory of Membrane Biology and Biophysics, The Rockefeller University, New York, NY 10065, USA. ²Howard Hughes Medical Institute, Chevy Chase, MD 20815, USA. *Corresponding author. Email: juechen@rockefeller.edu

Fig. 1. $\Delta 508$ CFTR exhibits defective NBD assembly.

(A) Four CFTR modulators currently used in the clinical setting. Green highlights the composition of the triple therapy (Trikafta in the United States and Kaftrio in Europe). **(B)** Maturation assay in human embryonic kidney 293F (HEK293F) cells. Top panel: SDS–polyacrylamide gel electrophoresis (SDS–PAGE) of cell lysates; mature and immature CFTR were visualized with a C-terminal green fluorescent protein (GFP) tag. Bottom panel: Quantification of $n = 3$ to 6 biological repeats. SDs are indicated by error bars. Concentrations were as follows: lumacaftor, 1 μM ; tezacaftor, 10 μM ; and elexacaftor, 0.5 μM in 0.1% dimethylsulfoxide (DMSO). Statistical significance was calculated using paired t test. $^{**}0.001 < P < 0.01$. **(C)** Confocal laser scanning microscopy analysis. Chinese hamster ovary (CHO) cells expressing CFTR variants were treated with DMSO (control) or 10 μM tezacaftor and 0.5 μM elexacaftor. ER (blue) was visualized by exciting mCherry-tagged tapasin. Plasma membrane (magenta) was visualized by exciting Alexa Fluor 647–conjugated wheat germ agglutinin stain. CFTR (green) was visualized by exciting enhanced GFP (eGFP)–tagged CFTR. **(D)** Structures of dephosphorylated and phosphorylated, ATP-bound $\Delta 508/\text{E1371Q}$ CFTR. Cryo-EM maps (gray) are superposed with structures of WT CFTR in the same conditions (dephosphorylated PDB, 7SVR; phosphorylated, ATP-bound PDB, 7SVD).



the structure of $\Delta 508$ CFTR in the presence of the three modulators comprising the triple therapy, providing a molecular description of how they synergistically rectify $\Delta 508$ CFTR to a functional state.

$\Delta 508$ CFTR exhibits defective NBD assembly

We sought to determine the molecular structure of $\Delta 508$ CFTR to investigate the mechanisms underlying its trafficking defect and gating deficiency. For WT CFTR (29, 34, 35),

substituting the catalytic residue E1371 with a glutamine was necessary to stabilize an ATP-bound, NBD-dimerized conformation for the cryo-EM study. To test whether E1371Q alters the folding of $\Delta 508$ CFTR both with

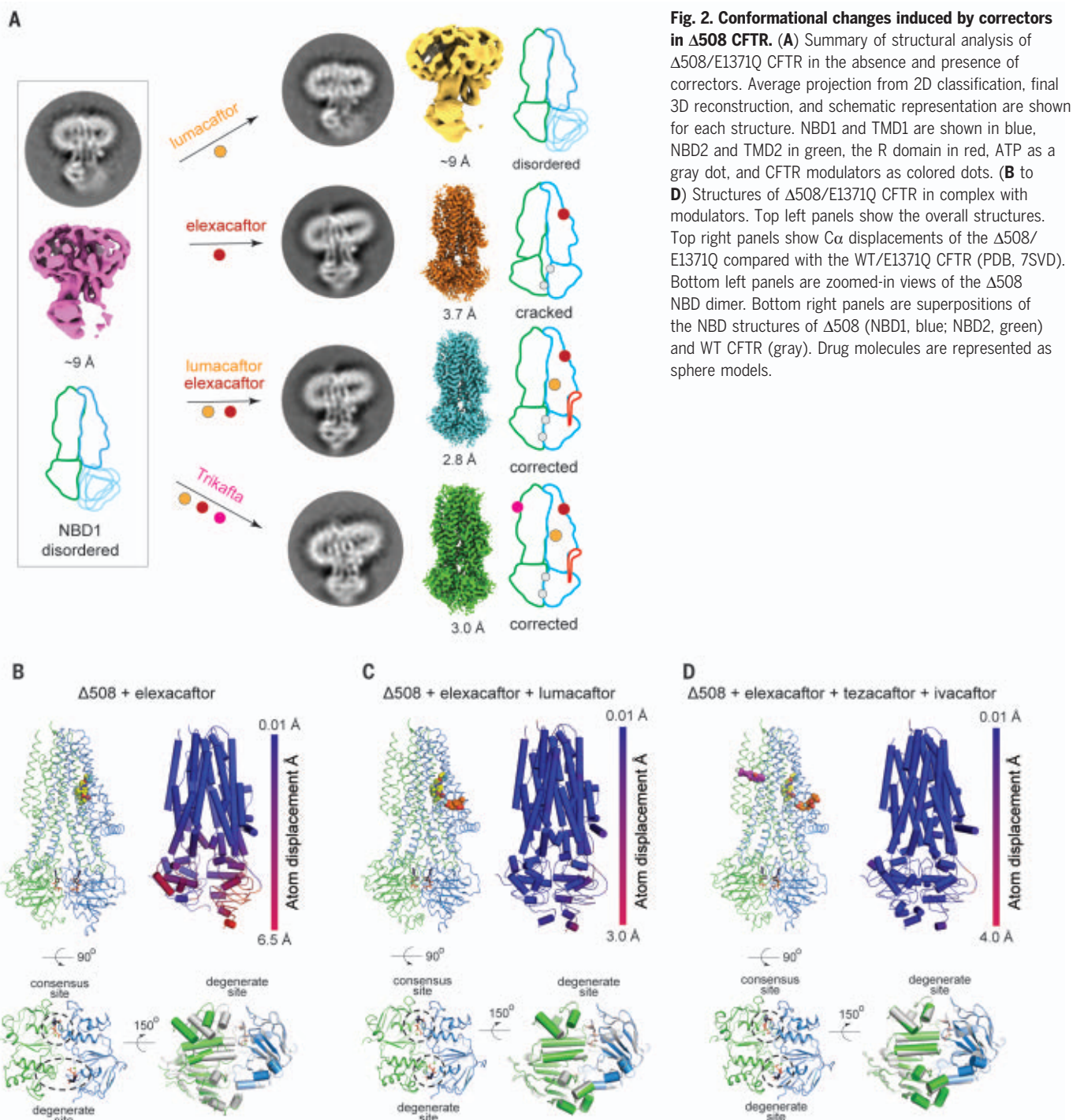


Fig. 2. Conformational changes induced by correctors in $\Delta 508$ CFTR. (A) Summary of structural analysis of $\Delta 508$ /E1371Q CFTR in the absence and presence of correctors. Average projection from 2D classification, final 3D reconstruction, and schematic representation are shown for each structure. NBD1 and TMD1 are shown in blue, NBD2 and TMD2 in green, the R domain in red, ATP as a gray dot, and CFTR modulators as colored dots. (B to D) Structures of $\Delta 508$ /E1371Q CFTR in complex with modulators. Top left panels show the overall structures. Top right panels show $C\alpha$ displacements of the $\Delta 508$ /E1371Q compared with the WT/E1371Q CFTR (PDB, 7SVD). Bottom left panels are zoomed-in views of the $\Delta 508$ NBD dimer. Bottom right panels are superpositions of the NBD structures of $\Delta 508$ (NBD1, blue; NBD2, green) and WT CFTR (gray). Drug molecules are represented as sphere models.

and without pharmacological correctors, we used a gel-shift assay to quantify the relative abundance of the fully glycosylated mature protein relative to the core-glycosylated immature form (36). In the absence of correctors, $\Delta 508$ and $\Delta 508$ /E1371Q CFTR were predominantly in their immature form (core-glycosylated, lower molecular weight). The addition of correctors increased the abundance of the mature forms (fully glycosylated, higher molecular weight) for both variants to a

similar extent (Fig. 1B). Confocal microscopy confirmed that $\Delta 508$ and $\Delta 508$ /E1371Q CFTR were retained in the endoplasmic reticulum (ER), and that correctors increased their presence at the plasma membrane (Fig. 1C and fig. S1). These data demonstrate that, similar to $\Delta 508$ CFTR, the double mutant $\Delta 508$ /E1371Q exhibits folding defects that can be reverted by correctors.

Next, we purified the ER-retained $\Delta 508$ /E1371Q CFTR without any pharmacological

correctors (fig. S2) and determined its structure in the absence and presence of phosphorylation and ATP (Fig. 1D). In both conditions, the flexibility of NBD1 became apparent in the initial two-dimensional (2D) classification steps of data processing (fig. S3). After extensive 3D classification, the structure of the dephosphorylated, ATP-free form was determined at ~ 6 -Å resolution (Fig. 1D and fig. S3), revealing an NBD-separated conformation similar to that of WT CFTR (8, 17).

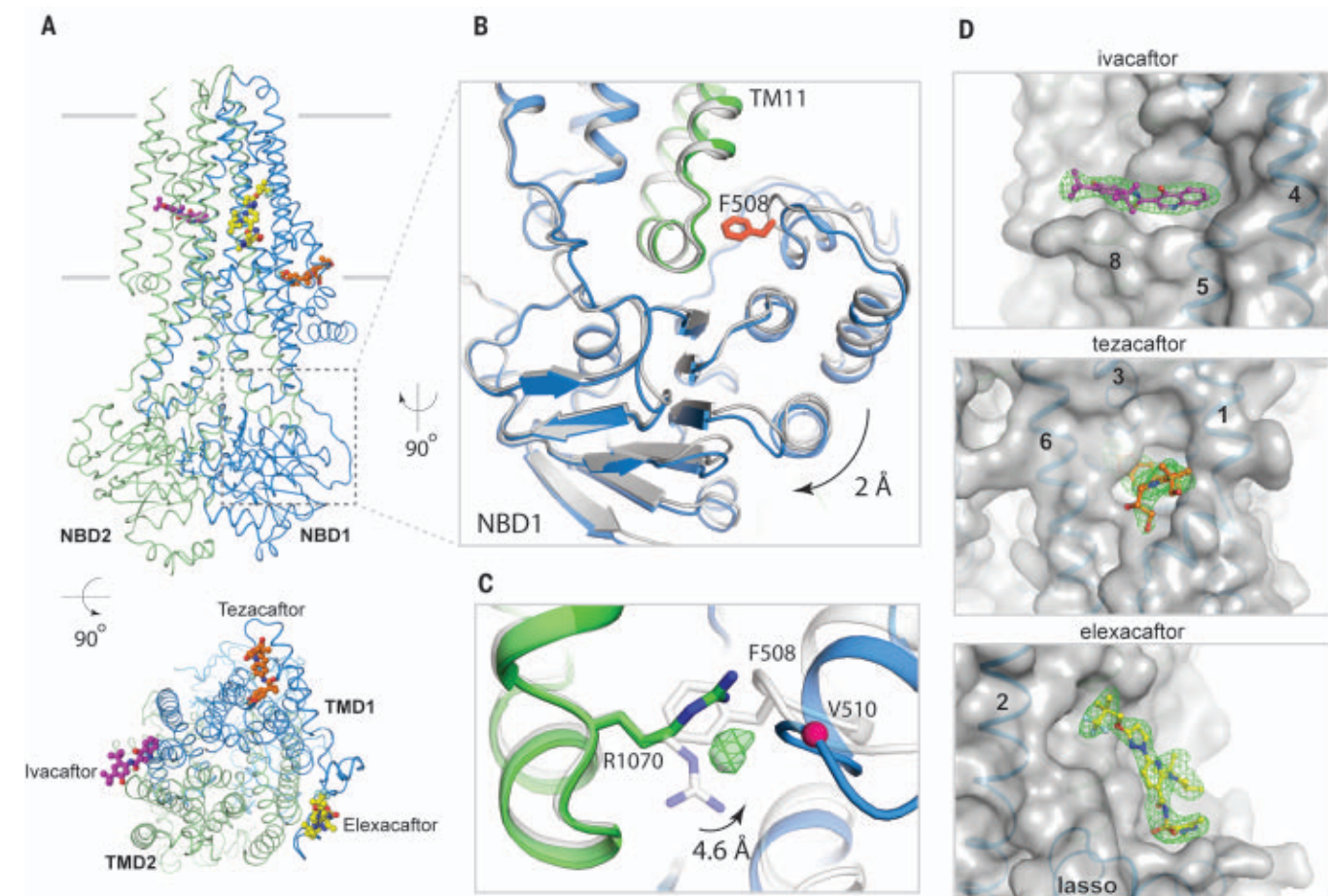


Fig. 3. Structure of Trikafta-corrected $\Delta 508$ CFTR. (A) Orthogonal views of $\Delta 508$ /E1371Q CFTR in complex with ivacaftor, elexacaftor, and tezacaftor. Shown is a $\Delta 508$ CFTR ribbon diagram with ball-and-stick models of drug molecules. Membrane location is indicated by two gray lines. (B) Zoomed-in view of F508 site. The $\Delta 508$ CFTR structure (blue/green) is superimposed

with the WT CFTR structure (gray). F508 is highlighted in red. (C) R1070 conformational change. Unassigned density is shown as a green mesh. (D) Zoomed-in views of drug-binding sites. Drug densities are shown as a green mesh, CFTR is shown as a transparent surface model, and the TM helices and lasso motif are labeled.

Densities corresponding to the TM helices and NBD2 revealed well-defined secondary structural features. The density for NBD1 was visible but amorphous, with a size and shape consistent with that of NBD1, indicating that $\Delta 508$ NBD1 is folded but flexibly attached to the TM helices. This structural observation supports the hypothesis that $\Delta 508$ disrupts interdomain assembly (8, 19–22). In contrast to WT CFTR, in which the structured R domain inserts into a cytosolic cleft (8, 17), little density corresponding to the R domain was visible in $\Delta 508$ CFTR. Because the R domain packs mainly along the surface of NBD1, it is possible that defects in NBD1 assembly also disrupt its correct positioning.

The lack of structural stability in $\Delta 508$ CFTR was even more pronounced in the phosphorylated, ATP-bound conformation. Previous structures of WT, phosphorylated, and ATP-bound CFTR carrying the same E1371Q mutation were determined to resolutions between 2.7 and 3.8 Å (29, 34, 35). However, the anal-

ogous cryo-EM analysis of $\Delta 508$ CFTR stalled at ~9-Å resolution because of the heterogeneous nature of the particles (Fig. 1D and fig. S2). The overall structure is consistent with an NBD-dimerized conformation, but a notable difference is the absence of visible density corresponding to NBD1 (Fig. 1D and fig. S3). On the basis of these data, we suggest that the R domain disengages upon phosphorylation as it does in the WT protein, permitting the TMDs to come into close contact. However, in the absence of F508, NBD1 is too flexible to support a stable NBD dimer. Because NBD dimerization is coupled to channel gating in CFTR (37), the inability of the NBDs to dimerize in $\Delta 508$ explains its impaired channel function (14–16, 38).

Correctors restore NBD dimerization in $\Delta 508$ CFTR

To investigate the conformational changes that CFTR correctors induce, we performed cryo-EM analyses of phosphorylated, ATP-

bound $\Delta 508$ /E1371Q CFTR in four pharmacological conditions: (i) lumacaftor, (ii) elexacaftor, (iii) a combination of these two correctors, and (iv) the triple Trikafta therapy of ivacaftor, tezacaftor, and elexacaftor (Fig. 2 and figs. S2 and S3). The $\Delta 508$ /E1371Q CFTR was expressed in the absence of correctors and solubilized from the ER membrane. Correctors were added during protein purification (fig. S2) to reveal their posttranslational effects on the structure of $\Delta 508$ CFTR without any confounding effects on folding kinetics and other cellular processes involved in $\Delta 508$ biogenesis.

The structure of $\Delta 508$ CFTR in the presence of lumacaftor was similar to that in its absence, indicating that posttranslational addition of lumacaftor alone is insufficient to correct the structural defects of $\Delta 508$ (Fig. 2A). This observation is consistent with the understanding that type I correctors bind to and stabilize TMD1 at an early stage of CFTR biogenesis, preventing its premature degradation and increasing the overall

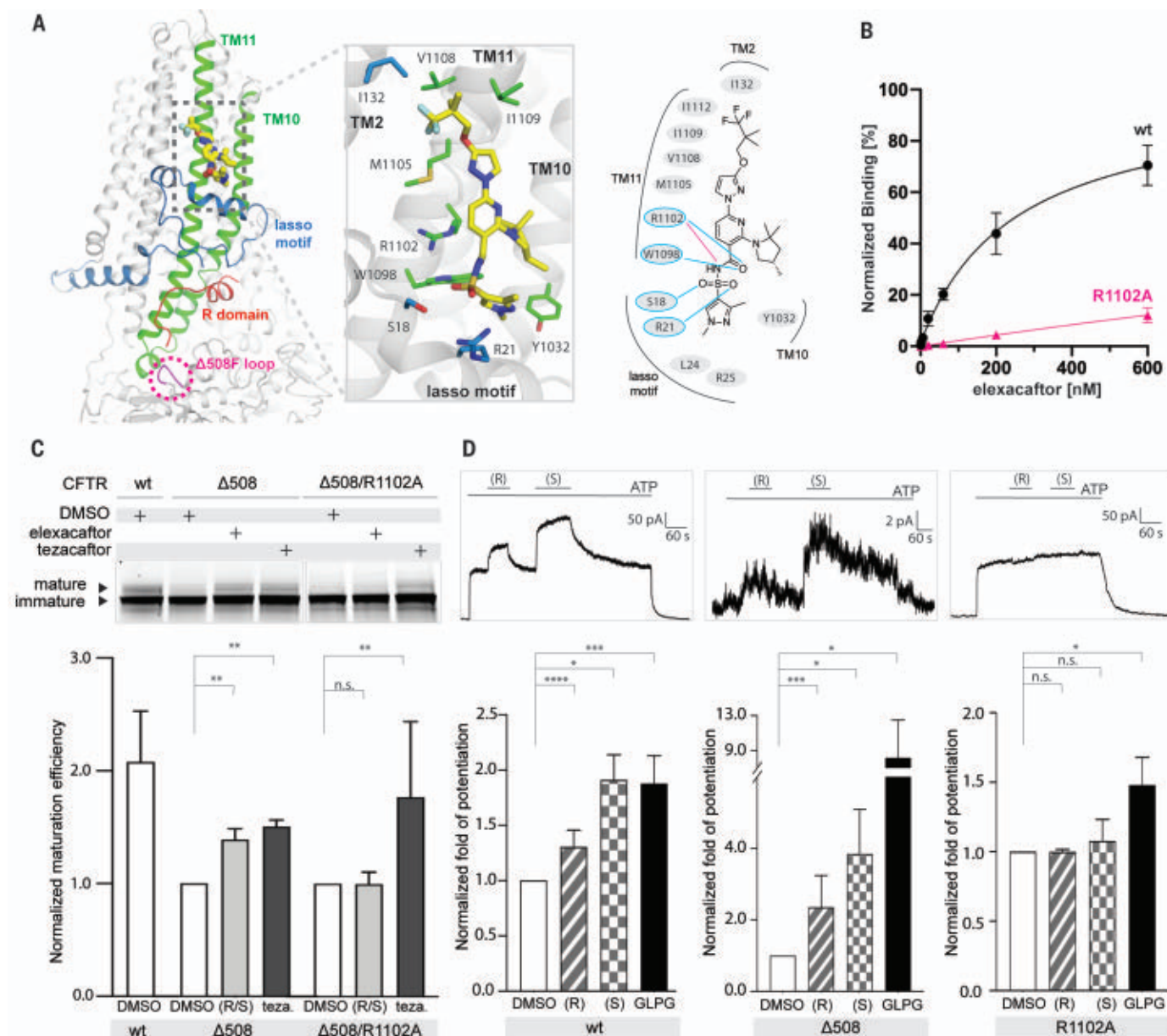


Fig. 4. Ellexacaptor binding site. (A) Molecular structure of ellexacaptor binding site. Left panel is a ribbon diagram. Middle panel is a zoomed-in view of the molecular interactions. Residues within 4.5 Å of ellexacaptor are shown as stick models. Right panel is a schematic of the molecular interactions. The salt bridge is shown as a magenta line, and hydrogen bonds are shown as blue lines. (B) Quantitative measurement of ellexacaptor binding. Data points represent mean and SD for $n = 6$ to 12 technical repeats ($n = 3$ to 4 biological repeats). The apparent dissociation constant (K_d) of ellexacaptor for WT CFTR is 244 ± 50 nM. (C) R1102A mutation diminishes correction by ellexacaptor. Top: SDS-PAGE of

cell lysates. Bottom: Quantification of $n = 3$ biological repeats. R/S, racemic mixture of ellexacaptor (0.5 μ M); Teza, tezacaftor (10 μ M). (D) Ellexacaptor potentiation. Top: Representative macroscopic current traces of fully phosphorylated WT and mutant CFTR in inside-out CHO cell membrane patches. Bottom: Quantification of $n = 3$ to 8 biological repeats. Concentrations used were as follows: ATP, 3 mM; ellexacaptor, 1 μ M; and GLPG1837, 10 μ M. Fold potentiation was normalized to currents with 3 mM ATP in the absence of potentiators. Statistical significance was calculated using paired t test. n.s., not significant; * $P < 0.05$; ** $P < 0.01$; *** $P < 0.001$; **** $P < 0.0001$.

probability of fully folded CFTR being formed (29, 39, 40).

By contrast, the type III corrector ellexacaptor stabilized NBD1, resulting in a cryo-EM reconstruction of 3.7-Å resolution with ordered NBDs (Fig. 2, A and B). The TMDs of ellexacaptor-bound Δ508 CFTR closely resemble those of WT/E1371Q CFTR in the phosphorylated, ATP-bound conformation (35), but the NBDs are

very different (Fig. 2B). Ellexacaptor-bound Δ508 has a “cracked-open” NBD dimer in which the catalysis-incompetent (degenerate) site is solvent accessible, and ATP makes contacts exclusively with the NBD1 face of the composite site (Fig. 2B).

The combination of ellexacaptor and lumacaftor had an effect that was greater than the sum of each corrector alone, fully restoring

Δ508 to an NBD-dimerized conformation with ATP fully occluded both the consensus and degenerate sites (Fig. 2, A and C). Moreover, this structure is essentially identical to that obtained in the presence of Trikafta (Fig. 2A), indicating that ivacaftor does not induce further conformational changes. This is consistent with ivacaftor being a potentiator, not a corrector. Both structures closely resemble

that of WT CFTR, having an overall root mean square deviation to the WT protein of 0.5 Å over 1090 C α positions (Fig. 2, C and D). We therefore designated both elexacaftor plus lumacaftor and Trikafta-bound Δ 508 CFTR structures as having a “corrected” conformation and selected Trikafta-bound Δ 508 for further analysis.

Pharmacologically corrected Δ 508 CFTR has a modified NBD1/TMD interface

The corrected Δ 508 structure in the presence of Trikafta differs from that of WT CFTR in the region of the F508 deletion site (Fig. 3, A to C). F508 is located in a loop on the surface of NBD1, projecting its aromatic side chain into a hydrophobic pocket at the end of TM helix 11 (Fig. 3B). Deletion of F508 shortens this loop, leaving a crevice at the NBD1/TMD interface. In addition, the helical subdomain of Δ 508 NBD1 (residues 500 to 564) is shifted away from the interface by \sim 2 Å (Fig. 3B). The crevice at the NBD1/TMD interface is partially filled by R1070, the side chain of which swings into contact with main chain atoms in NBD1 (Fig. 3C). We also observed a strong spherical density in the Δ 508 cavity area, which may be an ion or a water molecule.

Previous work has shown that the V510D mutation can stabilize Δ 508 CFTR, likely due to aspartic acid forming a salt bridge with R1070 (41). The structure of Δ 508 is compatible with a salt bridge between these residues and thus lends support to this hypothesis (fig. S4A). The structural differences at the NBD1/TMD interface also explain the opposing effects of the R1070W mutation in WT versus Δ 508 CFTR. In WT CFTR, substituting R1070 with tryptophan inhibits protein folding and leads to CF (20, 42, 43). This is because the large tryptophan side chain at position 1070 sterically clashes with F508 (fig. S4B). By contrast, the same substitution in the Δ 508 background partially restores CFTR folding (20, 22, 41, 43, 44), likely due to R1070W strengthening the NBD1/TMD interface by filling the space devoid of F508 and forming hydrophobic and hydrophilic contacts with Δ 508 NBD1 (fig. S4C).

Trikafta modulators bind to distinct sites on Δ 508 CFTR

In the cryo-EM reconstruction of Trikafta-bound Δ 508 CFTR, the densities for ivacaftor, tezacaftor, and elexacaftor were strong and unambiguous (Fig. 3). Viewed from the extracellular space perpendicular to the membrane, these compounds form a triangular belt encircling the TMDs (Fig. 3A). The potentiator ivacaftor (Fig. 3, purple molecule) binds to a cleft formed by TM helices 4, 5, and 8 approximately halfway through the lipid bilayer, coincident with the TM helix 8 hinge region involved in gating (28). The molecular

details of ivacaftor binding are identical to those in WT CFTR (28), indicating that ivacaftor potentiates both WT and Δ 508 CFTR through the same mechanism. Similarly, tezacaftor (Fig. 3, orange molecule) binds to Δ 508 by inserting into a hydrophobic pocket in TMD1 (Fig. 3D) in a manner identical to that in the WT protein (29). As previously discussed, such a penetrating cavity would cause substantial destabilization of the protein in the absence of tezacaftor (29). Furthermore, TM helices 1, 2, 3, and 6, which form the binding site, are predicted to be unstable in the membrane, so type I correctors would stabilize TMD1 both by filling the cavity and by structurally linking together the four unstable helices (29).

By contrast, the binding site for elexacaftor has not been observed previously. Densities corresponding to elexacaftor are very similar and well defined in the three elexacaftor-bound reconstructions (elexacaftor alone, elexacaftor plus lumacaftor, and Trikafta), enabling an accurate description of elexacaftor's binding pose and the chemistry of drug recognition (fig. S5A). Elexacaftor (Fig. 3, yellow molecule) binds to CFTR within the membrane, extending from the center of the lipid bilayer to the edge of the inner leaflet (Fig. 4A). The binding pocket is much shallower than that of type I correctors as if the drug molecule were patched onto the surface of CFTR. Elexacaftor interacts most extensively with TM helix 11 through electrostatic and van der Waals interactions. It also forms contacts with TM helices 2 and 10 and the lasso motif (Fig. 4A and fig. S5B).

Studies of ivacaftor binding to CFTR have shown that hydrogen bonds are critical for drug recognition because they stabilize polar groups in the low dielectric environment of the membrane (28). To determine whether this principle applies to elexacaftor binding, we substituted R1102 with an alanine to eliminate the formation of a hydrogen bond and a salt bridge (Fig. 4A) and then directly measured binding using a scintillation proximity assay (Fig. 4B). Specific binding of elexacaftor to WT CFTR increased as a function of drug concentration. Conversely, the interaction of elexacaftor with the R1102A mutant was barely detectable. We also evaluated the contribution of R1102 to the restoration of Δ 508 folding by elexacaftor using the gel-shift assay (Fig. 4C). The R1102A mutation abolished correction by elexacaftor, but not tezacaftor, which binds to a pocket distant from R1102. Finally, to determine whether R1102 also contributes to the potentiation activity of elexacaftor, we measured macroscopic current in inside-out membrane patches containing phosphorylated CFTR (Fig. 4D). We consistently observed stronger potentiation by the S enantiomer in both WT and Δ 508 CFTR, in agreement with the higher efficacy of the S enantiomer ob-

served in prior work (45). However, R1102A CFTR did not respond to either the R or the S enantiomer, indicating that both enantiomers bind to the site identified in the structures. A control potentiator, GLPG1837, increased macroscopic current in all CFTR variants (Fig. 4D). Together, these data suggest that elexacaftor achieves both correction and potentiation through the same binding site.

Discussion

The structures of Δ 508 CFTR reveal that the absence of F508 disrupts the ability of NBD1 to assemble with the TM helices, which leads to intracellular retention and degradation of the protein (14, 20, 46). Furthermore, the inability to form a stable NBD dimer after phosphorylation and ATP binding results in a dysfunctional channel, even if Δ 508 CFTR reaches the plasma membrane (14). Pharmacological correctors used in the clinical setting, even added during protein purification, can partially or fully restore the NBD-dimerized conformation. These correctors can improve the folding of WT CFTR and disease-causing mutations (47–51). Although it is theoretically possible that correctors salvage the different mutant and WT forms of CFTR by entirely different mechanisms, it is likely that their mechanism of action is the same in all cases. Indeed, lumacaftor binds to Δ 508 CFTR and WT CFTR at the same site and by interacting with the same residues. Likewise, ivacaftor interacts with WT and Δ 508 CFTR in an identical manner, indicating that its mechanism of potentiation is the same for both WT and mutant CFTR.

The dual-function modulator elexacaftor engages TM helices 10 and 11 and the lasso motif, all of which are important for CFTR folding and function. Mutations in the lasso motif can cause intracellular retention or abnormal gating, and some lead to CF (52–59). TM helices 10 and 11 are the “domain-swapped” helices of TMD2 that extend into the cytosol and interact with NBD1. This interface is important, not only for protein assembly, but also for transmitting conformational changes of the NBDs to the TMDs to control ion permeation. Although the details of how elexacaftor potentiates CFTR await incisive electrophysiology measurements, our structural observations indicate that elexacaftor stabilizes TM helices 10 and 11, thereby strengthening the TMD/NBD1 interface, which is particularly vulnerable to disease-causing mutations (60).

Recently, Braakman and colleagues demonstrated that CFTR folding occurs in a stepwise manner (60). It is likely that the type I corrector tezacaftor binds at an early stage of CFTR biogenesis to stabilize the N-terminal TMD1 (29), and the type III corrector elexacaftor binds at a later stage when TMDs assemble to form a protease-resistant form. Together, these

two correctors prevent premature degradation in the ER. Once CFTR reaches the plasma membrane, the presence of elxacaftor strengthens allosteric communication between ATP-bound NBD dimers and the channel gate, thereby increasing ion conductance. Channel activity is further enhanced by ivacaftor, which stabilizes the open configuration of the pore (28). In this manner, the three modulators in the triple therapy act synergistically to improve the folding and function of CFTR.

REFERENCES AND NOTES

- M. Shteinberg, I. J. Haq, D. Polineni, J. C. Davies, *Lancet* **397**, 2195–2211 (2021).
- B. Kerem et al., *Science* **245**, 1073–1080 (1989).
- J. R. Riordan et al., *Science* **245**, 1066–1073 (1989).
- D. B. Sanders, A. K. Fink, *Pediatr. Clin. North Am.* **63**, 567–584 (2016).
- M. P. Anderson et al., *Cell* **67**, 775–784 (1991).
- M. P. Anderson, D. P. Rich, R. J. Gregory, A. E. Smith, M. J. Welsh, *Science* **251**, 679–682 (1991).
- M. L. Drumm et al., *Cell* **62**, 1227–1233 (1990).
- Z. Zhang, J. Chen, *Cell* **167**, 1586–1597.e9 (2016).
- F. S. Seibert et al., *Biochim. Biophys. Acta* **1461**, 275–283 (1999).
- L. S. Ostedgaard, O. Baldursson, M. J. Welsh, *J. Biol. Chem.* **276**, 7689–7692 (2001).
- M. D. Amaral, C. M. Farinha, *Curr. Pharm. Des.* **19**, 3497–3508 (2013).
- J. R. Riordan, *Annu. Rev. Biochem.* **77**, 701–726 (2008).
- S. H. Cheng et al., *Cell* **63**, 827–834 (1990).
- W. Dalemans et al., *Nature* **354**, 526–528 (1991).
- G. L. Lukacs et al., *J. Biol. Chem.* **268**, 21592–21598 (1993).
- M. Sharma, M. Benharouga, W. Hu, G. L. Lukacs, *J. Biol. Chem.* **276**, 8942–8950 (2001).
- F. Liu, Z. Zhang, L. Csanády, D. C. Gadsby, J. Chen, *Cell* **169**, 85–95.e8 (2017).
- P. Vergani, S. W. Lockless, A. C. Nairn, D. C. Gadsby, *Nature* **433**, 876–880 (2005).
- H. A. Lewis et al., *J. Biol. Chem.* **280**, 1346–1353 (2005).
- W. M. Rabeh et al., *Cell* **148**, 150–163 (2012).
- K. Du, M. Sharma, G. L. Lukacs, *Nat. Struct. Mol. Biol.* **12**, 17–25 (2005).
- L. He et al., *FASEB J.* **24**, 3103–3112 (2010).
- L. He et al., *J. Mol. Biol.* **427**, 106–120 (2015).
- S. M. Rowe, A. S. Verkman, *Cold Spring Harb. Perspect. Med.* **3**, a009761 (2013).
- A. Zaher, J. ElSaghy, D. Elorsi, H. ElSaghy, A. Sanni, *Cureus* **13**, e16144 (2021).
- T. Okiyonedo et al., *Nat. Chem. Biol.* **9**, 444–454 (2013).
- G. Veit et al., *JCI Insight* **5**, e139983 (2020).
- F. Liu et al., *Science* **364**, 1184–1188 (2019).
- K. Fiedorczuk, J. Chen, *Cell* **185**, 158–168.e11 (2022).
- D. Keating et al., *N. Engl. J. Med.* **379**, 1612–1620 (2018).
- G. Veit, C. Vaccarin, G. L. Lukacs, *J. Cyst. Fibros.* **20**, 895–898 (2021).
- C. A. Shaughnessy, P. L. Zeitlin, P. E. Bratcher, *Sci. Rep.* **11**, 19810 (2021).
- O. Laselva et al., *Eur. Respir. J.* **57**, 2002774 (2021).
- Z. Zhang, F. Liu, J. Chen, *Cell* **170**, 483–491.e8 (2017).
- Z. Zhang, F. Liu, J. Chen, *Proc. Natl. Acad. Sci. U.S.A.* **115**, 12757–12762 (2018).
- X. B. Chang et al., *J. Cell Sci.* **121**, 2814–2823 (2008).
- L. Csanády, P. Vergani, D. C. Gadsby, *Physiol. Rev.* **99**, 707–738 (2019).
- K. Y. Jih, M. Li, T. C. Hwang, S. G. Bompadre, *J. Physiol.* **589**, 2719–2731 (2011).
- T. W. Loo, M. C. Bartlett, D. M. Clarke, *Biochem. Pharmacol.* **86**, 612–619 (2013).
- B. Kleizen et al., *J. Mol. Biol.* **433**, 166955 (2021).
- T. W. Loo, M. C. Bartlett, D. M. Clarke, *Biochemistry* **49**, 6352–6357 (2010).
- K. V. Krasnov, M. Tzetis, J. Cheng, W. B. Guggino, G. R. Cutting, *Hum. Mutat.* **29**, 1364–1372 (2008).
- J. L. Mendoza et al., *Cell* **148**, 164–174 (2012).
- P. H. Thibodeau et al., *J. Biol. Chem.* **285**, 35825–35835 (2010).
- V. Capurro et al., *Int. J. Mol. Sci.* **22**, 5262 (2021).
- H. Hoelen et al., *PLOS ONE* **5**, e15458 (2010).
- F. Van Goor et al., *Proc. Natl. Acad. Sci. U.S.A.* **108**, 18843–18848 (2011).
- G. L. Lukacs, A. S. Verkman, *Trends Mol. Med.* **18**, 81–91 (2012).
- S. Moniz et al., *ACS Chem. Biol.* **8**, 432–442 (2013).
- L. He et al., *FASEB J.* **27**, 536–545 (2013).
- H. Y. Ren et al., *Mol. Biol. Cell* **24**, 3016–3024 (2013).
- A. P. Naren, M. W. Quick, J. F. Collawn, D. J. Nelson, K. L. Kirk, *Proc. Natl. Acad. Sci. U.S.A.* **95**, 10972–10977 (1998).
- A. P. Naren et al., *Science* **286**, 544–548 (1999).
- L. S. Prince et al., *J. Biol. Chem.* **274**, 3602–3609 (1999).
- K. W. Peters, J. Qi, J. P. Johnson, S. C. Watkins, R. A. Frizzell, *Pflügers Arch.* **443**, S65–S69 (2001).
- G. G. Gené et al., *J. Cell Sci.* **117**, 1923–1935 (2004).
- A. Jurkuvenaite et al., *J. Biol. Chem.* **281**, 3329–3334 (2006).
- G. G. Gené et al., *Hum. Mutat.* **29**, 738–749 (2008).
- J. Fu, H. L. Ji, A. P. Naren, K. L. Kirk, *J. Physiol.* **536**, 459–470 (2001).
- J. Im et al., ABC-transporter CFTR folds with high fidelity through a modular, stepwise pathway. bioRxiv 500765 [Preprint] (2022); <https://doi.org/10.1101/2022.07.20.500765>.

ACKNOWLEDGMENTS

We thank M. Ebrahim, H. Ng, and J. Sotiris at Rockefeller's Evelyn Gruss Lipper Cryo-Electron Microscopy Resource Center for assistance in electron microscopy data collection; F. Glickman of the Rockefeller High Throughput and Spectroscopy Resource Center for help with the scintillation proximity assay experiments; P. Banerjee at the Frits and Rita Markus Bio-Imaging Resource Center at The Rockefeller University for assistance in confocal microscopy data collection; J. Levring from the Laboratory of

Membrane Biology and Biophysics for assistance in electrophysiology recordings; and D. Tallent for proofreading the manuscript.

Funding: This work was supported by the Howard Hughes Medical Institute (J.C.) and the Cystic Fibrosis Foundation Therapeutics (J.C. and K.F.). **Author contributions:** K.F. performed all of the experiments. K.F. and J.C. conceptualized the study, analyzed the data, and wrote the manuscript. **Competing interests:** The authors declare no competing interests. **Data and materials availability:** Protein models and cryo-EM maps are available at the RCSB Protein Data Bank (<https://www.rcsb.org/>) and the Electron Microscopy Data Bank (<https://www.ebi.ac.uk/emdb/>), respectively, under codes 8EJ1 and EMD-28172 (dephosphorylated Δ508/E1371Q), 8EIG and EMD-28155 (phosphorylated Δ508/E1371Q with ATP/Mg²⁺/elxacaftor), 8EIO and EMD-28160 (phosphorylated Δ508/E1371Q with ATP/Mg²⁺/elxacaftor/lumacaftor), and 8EIQ and EMD-28161 (phosphorylated Δ508/E1371Q with ATP/Mg²⁺/Trikafta). All other data and information are available in the main text or the supplementary materials. **License information:** Copyright © 2022 the authors, some rights reserved; exclusive licensee American Association for the Advancement of Science. No claim to original US government works. <https://www.science.org/about/science-licenses-journal-article-reuse>

SUPPLEMENTARY MATERIALS

science.org/doi/10.1126/science.ade2216

Materials and Methods

Figs. S1 to S5

Table S1

References (61–71)

MDAR Reproducibility Checklist

Submitted 1 August 2022; accepted 27 September 2022
10.1126/science.ade2216

REPORTS

EVOLUTIONARY BIOLOGY

An evolutionary trade-off between host immunity and metabolism drives fatty liver in male mice

Joni Nikkanen^{1,2}, Yew Ann Leong^{2,3}, William C. Krause¹, Denis Dermadi^{4,5}, J. Alan Maschek^{6,7}, Tyler Van Ry^{6,7}, James E. Cox^{6,7}, Ethan J. Weiss², Omer Gokcumen⁸, Ajay Chawla^{2,9,*}†, Holly A. Ingraham^{1,*}

Adaptations to infectious and dietary pressures shape mammalian physiology and disease risk. How such adaptations affect sex-biased diseases remains insufficiently studied. In this study, we show that sex-dependent hepatic gene programs confer a robust (~300%) survival advantage for male mice during lethal bacterial infection. The transcription factor B cell lymphoma 6 (BCL6), which masculinizes hepatic gene expression at puberty, is essential for this advantage. However, protection by BCL6 protein comes at a cost during conditions of dietary excess, which result in overt fatty liver and glucose intolerance in males. Deleting hepatic BCL6 reverses these phenotypes but markedly lowers male survival during infection, thus establishing a sex-dependent trade-off between host defense and metabolic systems. Our findings offer strong evidence that some current sex-biased diseases are rooted in ancient evolutionary trade-offs between immunity and metabolism.

Infections are one of the strongest evolutionary pressures shaping human physiology and disease. As such, the immune system and host defense responses are often prioritized at the expense of other physiological systems (1, 2). As a result, genetic variants that are associated with noninfectious diseases

may be maintained in the population if they simultaneously improve survival during infection. For example, variants in human *HBB* and *APOL1* increase the risk of sickle cell anemia and chronic kidney disease (3) but exert a strong protective effect against malaria and trypanosome infections, respectively. These

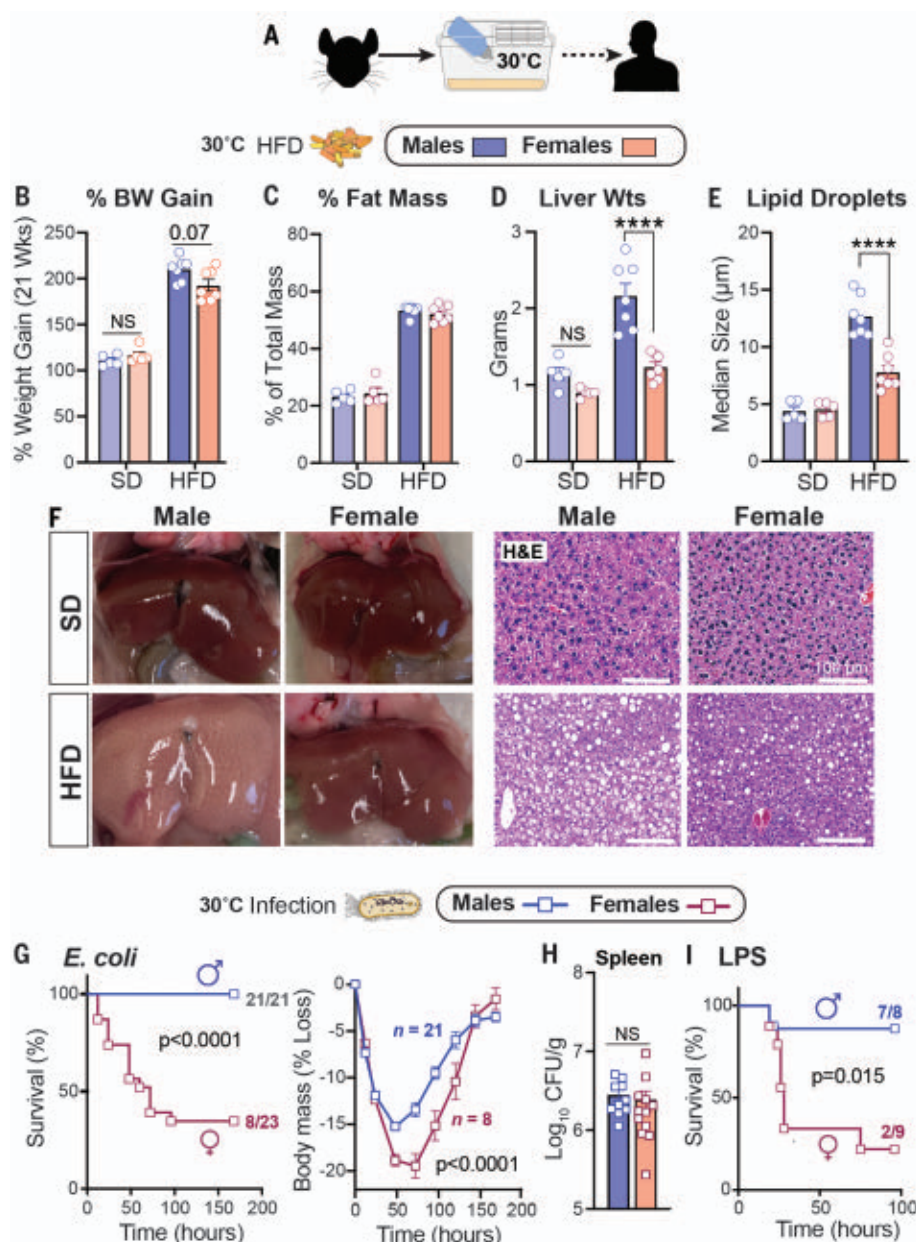


Fig. 1. HFD and infection elicit strong sex-dependent phenotypes in mice.

(A) Schematic of housing conditions. (B to F) Body weight gain (B), fat percentage (C), liver weights (Wts) (D), hepatic lipid droplet size (E), and whole livers with corresponding hematoxylin and eosin (H&E) staining (F) after 21 weeks of SD or HFD. (G) Survival curves and body weights of C57BL/6J mice that were infected with *E. coli* [1×10^8 colony-forming units (CFU)]. Weight curves were analyzed by two-way analysis of variance (ANOVA). (H) Bacterial CFUs of mice that were infected with *E. coli* (1×10^7 CFU). (I) Survival curves of mice treated with LPS (2 mg/kg). All mice were housed at 30°C. Data are presented as mean \pm SEM; NS, not significant; **** $p < 0.0001$. Scale bars, 100 μ m.

studies highlight the notion of an “evolutionary trade-off” whereby natural selection fails to optimize two traits simultaneously, which causes increased adaptation for one trait at the expense of another and ultimately may elevate disease risk.

Shifting environments also magnify the disease risk associated with trade-offs, resulting in so-called mismatch diseases (4). Thus, the

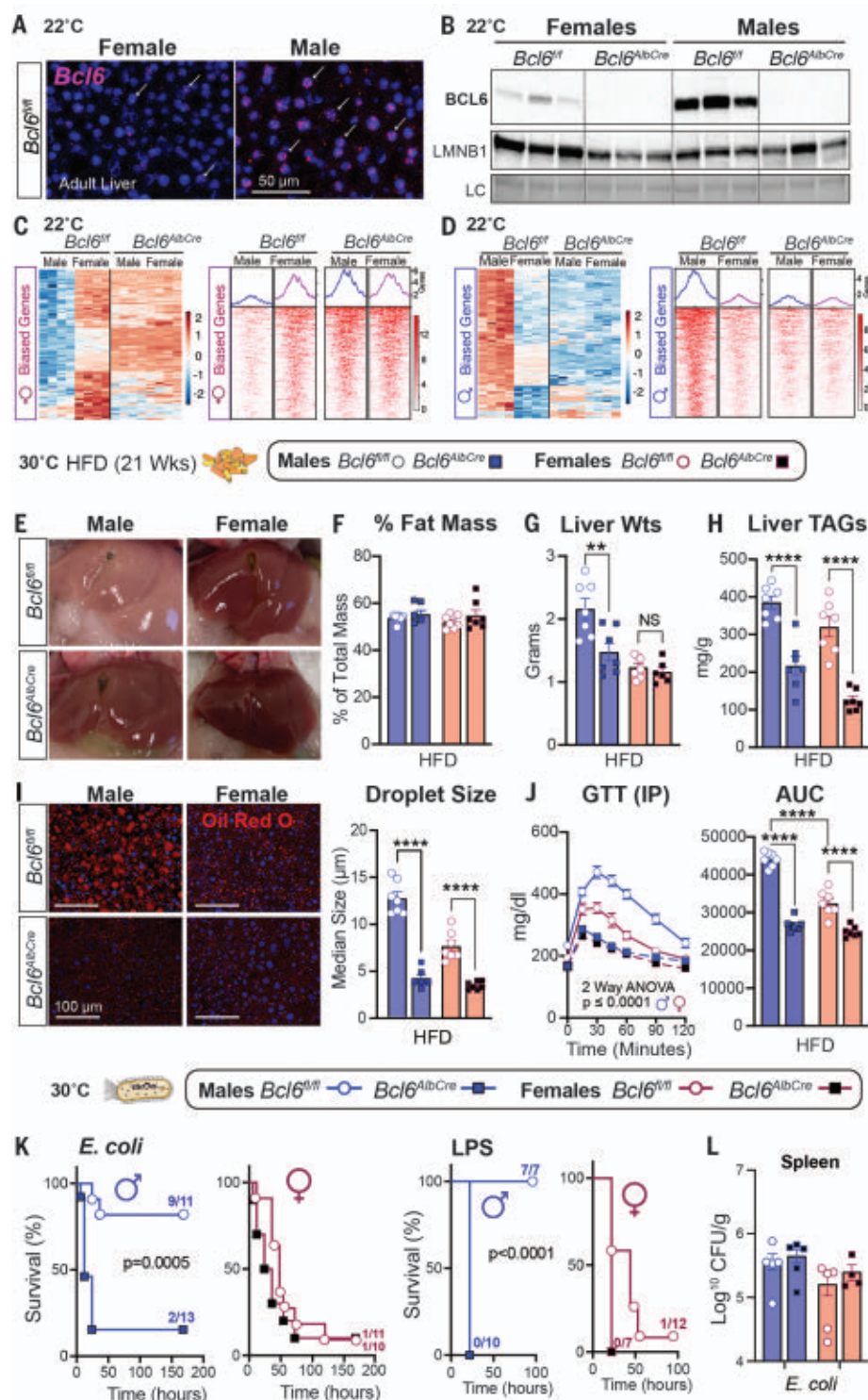
initial benefit of a trait becomes detrimental in a new environment. For example, a mismatch between our genetic legacy and the modern diet that is high in calories, fat, and refined sugars is proposed to account for the high prevalence of chronic metabolic diseases, such as type 2 diabetes (T2D), heart disease, and fatty liver (5). However, although the evolutionary mismatch theory can ex-

plain chronic diseases that affect immunity and metabolism, their marked sex bias in the human population is poorly understood. Notably, men carry a much higher disease burden for common metabolic disorders compared with premenopausal women (6–8). Similarly, some infectious diseases exhibit a strong sex bias with poorer outcomes observed in either males or females depending

¹Department of Cellular and Molecular Pharmacology, University of California San Francisco, San Francisco, CA 94143, USA. ²Cardiovascular Research Institute, University of California San Francisco, San Francisco, CA 94143, USA. ³Centre for Inflammatory Diseases, Department of Medicine, School of Clinical Sciences at Monash Health, Monash University, Melbourne, 3800, Australia. ⁴Institute of Immunity, Transplantation, and Infection, Stanford University School of Medicine, Stanford, CA 94305, USA. ⁵Biomedical Informatics Research, Department of Medicine, Stanford University School of Medicine, Stanford, CA 94305, USA. ⁶Department of Biochemistry, University of Utah, Salt Lake City, UT 84112, USA. ⁷Metabolomics Core Research Facility, University of Utah, Salt Lake City, UT 84112, USA. ⁸Department of Biological Sciences, University at Buffalo, Buffalo, NY 14260, USA. ⁹Departments of Physiology and Medicine, University of California San Francisco, San Francisco, CA 94143, USA.

*Corresponding author. Email: ajay.chawla@merck.com (A.C.); holly.ingraham@ucsf.edu (H.A.I.). †Present address: Cardiometabolic Disease, Merck Research Labs, 213 E. Grand Avenue, South San Francisco, CA 94080, USA.

Fig. 2. BCL6 maintains hepatic maleness and survival to infection but impairs metabolism. (A) In situ hybridization for *Bcl6* (magenta, white arrows) in livers of mice at 22°C. Scale bar, 50 μ m. (B) Immunoblot for BCL6 and LMNB1 in liver nuclear extracts of 8-week-old *Bcl6*^{f/f} and *Bcl6*^{AlbCre} mice at 22°C. (C and D) Heatmaps for top hepatic 100 (C) female- and (D) male-biased genes (filtered by fold change) with corresponding female- or male-biased H3K27ac peaks (adjusted *p* value for both <0.05) in mice that were housed at 22°C. Scale bars, Z-scores. (E to H) Livers (E), fat percentage (F), liver weights (G), and liver TAGs (H) from mice that were fed a HFD at 30°C. (I) Hepatic Oil Red O staining (ORO) and quantification of lipid droplet (red) size from mice that were fed a HFD for 21 weeks at 30°C. Nuclei stained with 4',6-diamidino-2-phenylindole (DAPI) (blue). Scale bars, 100 μ m. (J) Glucose concentrations and area under the curve (AUC) after an intraperitoneal (IP) glucose tolerance test (GTT) in mice that were fed a HFD for 8 weeks at 30°C. (K and L) Survival curves of mice that were fed a SD and infected with *E. coli* (1×10^8 CFU) or treated with LPS (1.75 mg/kg) at 30°C (K) and spleen bacterial counts at 30°C (L). Data for control *Bcl6*^{f/f} mice in (F), (G), and (I) are regraphed from Fig. 1, C to E (HFD). Data are presented as mean \pm SEM. LC, loading control (total protein). ***p* < 0.01; *****p* < 0.0001.



on the pathogen (9). Together, inherent sex differences in physiological systems dictate disease progression in males and females. In this study, we examined the relationship between biological sex during a dietary excess challenge and infection in mice.

Prior studies found that mice housed at thermoneutral temperature (30°C) are sus-

ceptible to the metabolic consequences of chronic dietary excess (10, 11) and infection (12). We therefore used thermoneutral conditions to examine the potential trade-offs between metabolism and host defense mechanisms in C57BL/6J males and females (Fig. 1A). Despite an equivalent increase in body weight and fat mass when fed a high-fat diet (HFD)

(Fig. 1, B and C), only male mice developed severe fatty liver and overt macrosteatosis (Fig. 1, D to F, and fig. S1A). Using thermoneutral conditions, we then examined how sex affects host survival during infection with a sublethal dose of *Escherichia coli* (strain O111:B4) in mice that were fed standard chow. Males were far less susceptible to infection

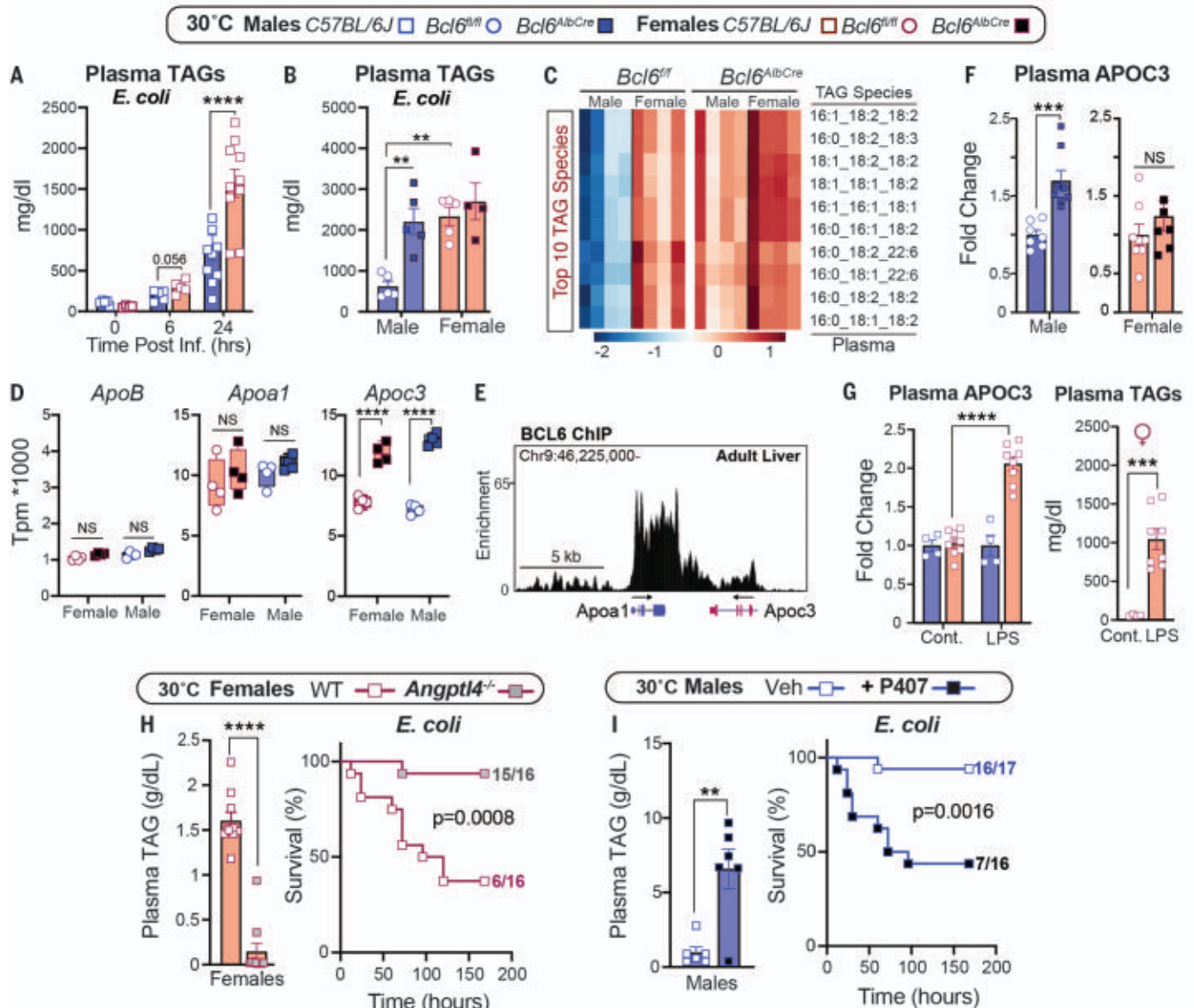


Fig. 3. Sex-dependent hyperlipidemia is linked to host defense responses.

(A and B) Plasma TAGs of (A) wild-type mice over time and (B) $Bcl6^{fl/fl}$ and $Bcl6^{AlbCre}$ mice that were infected with *E. coli* (1×10^7 CFU) at 30°C. (C) Top 10 most abundant TAG species measured by lipidomics in infected $Bcl6^{fl/fl}$ and $Bcl6^{AlbCre}$ mice. Scale bar, Z-scores. (D) Transcript abundances of hepatic *ApoB*, *Apoa1*, and *Apoc3* in $Bcl6^{fl/fl}$ and $Bcl6^{AlbCre}$ mice (RNA-seq) at 30°C. TPM, transcripts per million. (E) Genomic binding of BCL6 in *Apoc3/Apoa1* locus in the

male liver (ChIP-seq) at 22°C. (F) Plasma APOC3 in $Bcl6^{fl/fl}$ and $Bcl6^{AlbCre}$ mice that were housed at 30°C. (G) Plasma APOC3 and TAGs in control and LPS-treated (0.5 mg/kg) C57BL/6J female mice at 30°C. Cont., control. (H) Plasma TAGs (1×10^7 CFU) and survival curves (1×10^8 CFU) of female mice that were infected with *E. coli* at 30°C. (I) Plasma TAGs (1×10^7 CFU) and survival curves (1×10^8 CFU) of male mice that were infected with *E. coli* at 30°C. Data are presented as mean \pm SEM. ** $p < 0.01$; *** $p < 0.001$; **** $p < 0.0001$.

and showed a markedly higher survival rate and body mass preservation at thermoneutrality than females (Fig. 1G and fig. S1, B and C). Spleen bacterial counts were equivalent in both sexes (Fig. 1H), suggesting that males limit their immunopathology and that pathogen clearance fails to account for the sex differences in survival. Greater survival in males was also observed after activation of host immunity by the endotoxin lipopolysaccharide

(LPS) (Fig. 1I). Collectively, our results expose a stark relationship, specifically in males, between hepatic fat accumulation after dietary excess and host survival after bacterial infection.

In searching prior literature for a sex-dependent hepatic factor that might mediate these divergent outcomes between the sexes, the transcriptional repressor B cell lymphoma 6 protein (BCL6) emerged as a

top candidate given its role in hepatic lipid handling (13, 14) and its enrichment in the male liver as previously shown (15, 16). We found that BCL6 is male biased at both 22°C and 30°C, with *Bcl6* transcripts and protein highly expressed in male hepatocytes and livers (Fig. 2, A and B, and fig. S2A). Conditional deletion of *Bcl6* in the liver ($Bcl6^{AlbCre}$) (Fig. 2B) feminizes the adult male liver and eliminates its male-biased gene signature

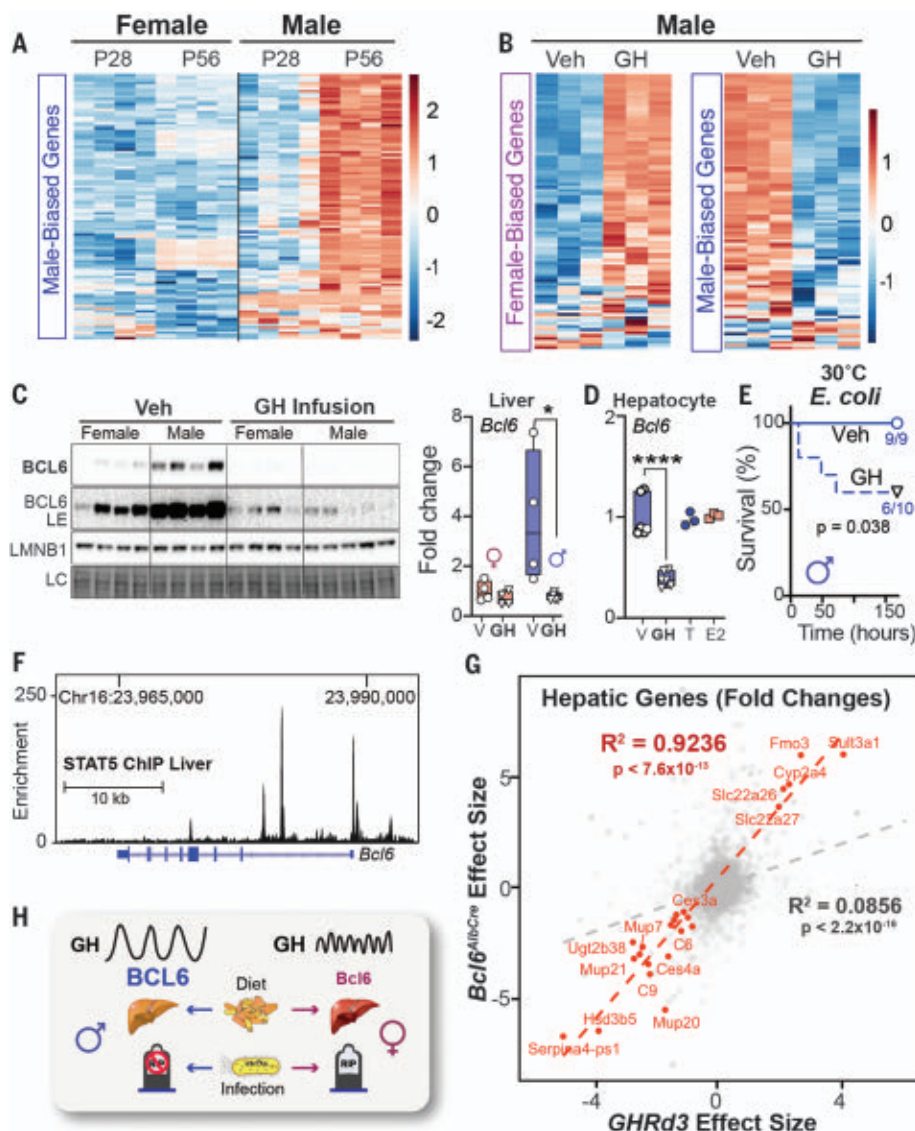


Fig. 4. Sex-dependent GH signaling controls BCL6 expression and survival to infection. (A and B) Heatmaps of top 100 (A) male-biased genes and (B) female-/male-biased genes at postnatal day 28 (P28) and P56 or in male mice after GH treatment at 22°C. Scale bars, Z-scores. (C) Immunoblotting and reverse transcription–quantitative polymerase chain reaction (RT-QPCR) for hepatic BCL6 protein and transcript in adult mice infused with vehicle (Veh) or recombinant mouse GH for 15 days at 22°C. (D) *Bcl6* mRNA expression in primary mouse hepatocytes treated with vehicle (V), T, estradiol benzoate (E2) ($n = 3$), or GH ($n = 6$). (E) Survival curves of male mice infused with Veh or GH for 13 days and then infected with *E. coli* (1×10^8 CFU) at 30°C. (F) STAT5 binding to *Bcl6* locus in the male liver (ChIP-seq) at 22°C. Chr, chromosome. (G) Effect size correlation of all (gray) or differentially expressed (red) transcripts in livers of *Bcl6*^{AlbCre} and *Ghrd3* male mice. (H) Schematic of the GH–BCL6 axis in regulating sex-dependent endpoints when challenged by diet or infection. LE, long exposure. Data are presented as mean \pm SEM; $*p < 0.05$, $****p < 0.0001$.

(Fig. 2, C and D; data S1; and fig. S2, B to D). Profiling active enhancers and promoters for acetylated histone 3 lysine 27 (H3K27ac) by chromatin immunoprecipitation sequencing (ChIP-seq) also revealed an essential role of BCL6 in maintaining sex-dependent hepatic chromatin acetylation and male-biased

H3K27ac peaks (Fig. 2, C and D, and fig. S2, E and F).

Having established the masculinizing role of BCL6 in hepatic gene signatures, we assessed whether BCL6 is essential for maintaining the distinct sex-specific outcomes of HFD and infection. Indeed, deleting hepatic *Bcl6* abol-

ished all morphological hallmarks of fatty liver in males without changing their total fat mass or percent body weight gain (Fig. 2, E and F, and fig. S3, A and B). Liver weights, hepatic triglycerides (TAGs), lipid accumulation, and droplet size were all reduced in *Bcl6*^{AlbCre} male mice (Fig. 2, G to I), which is consistent with a prior study that found that BCL6 blocks the breakdown of fat by lowering fatty acid oxidation (14). Hepatic TAGs also fell in *Bcl6*^{AlbCre} mice that were fed a standard diet (SD) (fig. S3C). Eliminating the low amounts of BCL6 present in female livers also attenuated hepatic TAGs, but more subtly (Fig. 2, G to I). The loss of hepatic BCL6 markedly improved glucose homeostasis in mutant male cohorts that were fed either a HFD or a SD and abolished any notable sex differences in this metabolic parameter (Fig. 2J and fig. S3D). In stark contrast to the improved metabolic state in *Bcl6*^{AlbCre} males, their survival dropped precipitously after *E. coli* infection or LPS treatment, plummeting to the levels exhibited by control females (Fig. 2K and fig. S3E). Pathogen clearance in the spleen was unaffected in *Bcl6*^{AlbCre} mice (Fig. 2L). Thus, high hepatic BCL6 in males is essential for optimizing host survival during infection but drives fatty liver and glucose intolerance during dietary excess, suggesting a strong association between hepatic lipid handling and host defense responses.

Low survival in females that were fed a SD at 30°C is closely correlated with extremely high plasma TAGs, a condition that is observed in septic humans (17) and rats (18). Infection-induced hyperlipidemia is only observed at thermoneutrality (Fig. 3A and fig. S4A). Likewise, compromised survival in infected *Bcl6*^{AlbCre} males was linked with a substantial rise in the concentrations of circulating TAG species, similar to those of infected control females (Fig. 3, B and C, and fig. S4B). Increased plasma TAGs in infected *Bcl6*^{AlbCre} mutant male mice prompted us to investigate whether genes that are crucial in the packaging and clearance of very low-density lipoproteins (VLDLs) and their TAG cargo are regulated by BCL6. Of the three candidate genes examined, hepatic *Apoc3*, whose gene product inhibits TAG clearance, increased sharply in *Bcl6*^{AlbCre} mice, whereas *ApoB* and *ApoA1* were unchanged (Fig. 3D and fig. S4C). Reanalysis of the hepatic BCL6 ChIP-seq dataset by Waxman's group (16) revealed that BCL6 binds directly to the *Apoc3* locus to dampen its expression (Fig. 3E). Thus, as predicted, increased plasma APOC3 occurs after eliminating high hepatic BCL6 in uninfected males. This relationship is not as clear-cut in *Bcl6*^{AlbCre} females, who fail to exhibit high APOC3 levels despite an increase in *Apoc3* transcripts. These results suggest that posttranscriptional factors are at play during the packaging of

female hepatic APOC3 into lipoproteins (Fig. 3F). Nevertheless, wild-type females that are treated with LPS exhibit a notable increase in both circulating APOC3 and TAGs (Fig. 3G), which is consistent with the essential role of *APOC3* in maintaining plasma TAGs (19). Our findings support the postulate by Scholl and colleagues (18) that decreased clearance of plasma TAGs by lipoprotein lipase (LPL) contributes to sepsis-induced hyperlipidemia.

To determine whether high plasma TAGs contribute directly to poor survival in females, we used ANGPTL4 knockout (KO) mice (20) that clear out TAGs because of increased LPL activity (Fig. 3H). Normalizing TAGs in infected *Angptl4*^{-/-} females restored both survival and body weights (Fig. 3H and fig. S4D). *Angptl4*^{-/-} males also showed a drop in TAGs and remained resistant to infection (Fig. S4, E and F). Conversely, increasing plasma TAGs by using poloxamer 407 (P407), a synthetic inhibitor of LPL, worsened the survival of males after infection (Fig. 3I). Our results establish that the marked sex differences in infection outcomes are tightly linked with the amounts of circulating TAGs.

We next investigated what factors enable BCL6 to control the hepatic gene programs in male mice. The appearance of male-biased genes coincides with puberty, which becomes apparent at 8 weeks of age (Fig. 4A and fig. S5A). Surgical castration (GDX) of prepubescent males enhanced female-biased gene expression in the liver (fig. S5B), led to a steep drop in survival that was accompanied by elevated plasma TAGs after *E. coli* infection (fig. S5, C and D), and diminished hepatic BCL6 levels, which were partially restored by a testosterone (T) treatment (fig. S5E). Pulsatile secretion of growth hormone (GH) from the anterior pituitary is distinctive in males and consists of peaks with prolonged extended dips; this pattern is required for male-biased hepatic gene expression in mice (16, 21). Indeed, after reanalyzing datasets from (22), focusing on our set of 200 sex-biased genes, we confirmed that continuous infusion of GH feminizes male livers (Fig. 4B and fig. S5F). We also found that GH treatment strongly represses hepatic BCL6 protein and transcripts (Fig. 4C). Although saturating levels of GH in primary hepatocytes also suppressed *Bcl6*, T and estradiol (E) had no effect in this setting, which implies that the T-induced rescue of BCL6 expression in vivo must be indirect (Fig. 4D and fig. S5E). Expectedly, disrupting normal GH pulsatility by continuous GH infusion reduced hepatic BCL6 and diminished host survival in males (Fig. 4E). As shown by Waxman's group, the major effector of hepatic GH signaling, STAT5, binds to the *Bcl6* locus (16), which provides a

direct molecular link between GH and BCL6 levels (Fig. 4F).

To extend these findings, we leveraged a mouse model that carries the common human variant of growth hormone receptor (*GHRd3*, deletion of exon 3) that mimics increased GH signaling and confers a marked protective effect in humans (~4-fold) against developing T2D (23). This variant feminizes livers in male mice and is thought to impart an evolutionary advantage during periods of food scarcity in humans (24). The significant ($R^2 = 0.92$, $p < 7.6 \times 10^{-13}$) overlap in hepatic gene changes detected in *Ghrd3* and *Bcl6*^{AlbCre} mutant males (Fig. 4G and fig. S5G) suggests that this common *GHR* variant attenuates hepatic BCL6 function. In contrast to the notable hepatic gene changes with the onset of puberty or after castration, we failed to find any significant changes in our sex-biased gene signatures in estrogen receptor alpha (*Esr1*) liver KO mice after reanalyzing datasets by Maggi and colleagues (25) (fig. S5H). The ability of the *GHRd3* variant to stave off nutritional stress (24), coupled with our study, might suggest that the GH–BCL6 signaling axis creates a trade-off for females that diminishes survival during infection while enhancing survival in the fasted state. This notion is partially supported by the fact that survival rates for women outpace men during famine (26).

In male mice, the hepatic GH–BCL6 axis is essential for mounting protective defenses against infection while promoting substantial hepatic fat accumulation and glucose intolerance during caloric excess (Fig. 4H). Although sex differences in this pathway remain to be documented in humans, it has been noted that patients with hypopituitarism and low GH develop fatty liver, which improves after GH therapy (27). On the basis of the conserved features of metabolic programs across mammals, we speculate that the current prevalence of fatty liver in males might stem from older host defense mechanisms that coevolved from increased exposure to pathogens due to aggressive behaviors required for mating and social status (28). Our study leads us to propose that adaptations to infectious and dietary pressures sculpt sexually dimorphic pathways, contributing to modern sex-biased diseases.

REFERENCES AND NOTES

1. A. Wang, H. H. Luan, R. Medzhitov, *Science* **363**, eaar3932 (2019).
2. S. C. Stearns, R. Medzhitov, *Evolutionary Medicine* (Sinauer, 2016).
3. M. L. Benton *et al.*, *Nat. Rev. Genet.* **22**, 269–283 (2021).
4. A. Di Rienzo, R. R. Hudson, *Trends Genet.* **21**, 596–601 (2005).
5. M. B. Manus, *Evol. Med. Public Health* **2018**, 190–191 (2018).
6. A. Lonardo *et al.*, *Hepatology* **70**, 1457–1469 (2019).
7. L. Mosca, E. Barrett-Connor, N. Kass Wenger, *Circulation* **124**, 2145–2154 (2011).

8. B. Tramunt *et al.*, *Diabetologia* **63**, 453–461 (2020).
9. S. L. Klein, K. L. Flanagan, *Nat. Rev. Immunol.* **16**, 626–638 (2016).
10. A. W. Fischer, B. Cannon, J. Nedergaard, *Mol. Metab.* **26**, 1–3 (2019).
11. D. A. Giles *et al.*, *Nat. Med.* **23**, 829–838 (2017).
12. K. Ganesan *et al.*, *Cell* **177**, 399–413.e12 (2019).
13. D. A. Salisbury *et al.*, *Nat. Metab.* **3**, 940–953 (2021).
14. M. A. Sommars *et al.*, *eLife* **8**, e43922 (2019).
15. R. D. Meyer, E. V. Laz, T. Su, D. J. Waxman, *Mol. Endocrinol.* **23**, 1914–1926 (2009).
16. Y. Zhang, E. V. Laz, D. J. Waxman, *Mol. Cell. Biol.* **32**, 880–896 (2012).
17. J. I. Gallin, D. Kaye, W. M. O'Leary, *N. Engl. J. Med.* **281**, 1081–1086 (1969).
18. R. A. Scholl, C. H. Lang, G. J. Bagby, *J. Surg. Res.* **37**, 394–401 (1984).
19. N. Maeda *et al.*, *J. Biol. Chem.* **269**, 23610–23616 (1994).
20. S. Kersten, *Curr. Opin. Lipidol.* **30**, 205–211 (2019).
21. J. N. MacLeod, N. A. Pampori, B. H. Shapiro, *J. Endocrinol.* **131**, 395–399 (1991).
22. D. Lau-Corona, A. Suvorov, D. J. Waxman, *Mol. Cell. Biol.* **37**, e00301-17 (2017).
23. R. J. Strawbridge *et al.*, *Growth Horm. IGF Res.* **17**, 392–398 (2007).
24. M. Saitou *et al.*, *Sci. Adv.* **7**, eabi4476 (2021).
25. S. Della Torre *et al.*, *Cell Metab.* **28**, 256–267.e5 (2018).
26. V. Zarull *et al.*, *Proc. Natl. Acad. Sci. U.S.A.* **115**, E832–E840 (2018).
27. S. J. Kang *et al.*, *Endocr. Pract.* **27**, 1149–1155 (2021).
28. S. L. Klein, *Behav. Processes* **51**, 149–166 (2000).

ACKNOWLEDGMENTS

We thank members of the Chawla and Ingraham labs for comments on the manuscript and X. Cui and J. Argiris for assistance with mouse husbandry. We also thank A. Capra and E. Goldberg for intellectual discussions. In addition, we thank S. Koliwad for providing *Angptl4*^{-/-} mice and J. Hellman for the *E. coli* strain that was used in experiments. **Funding:** The authors' work was supported by grants from NIH (AG062331, DK121657, and GCRLE Senior Scholar Award to H.A.I.), NIH (DK094641 and DK101064 to A.C.), EMBO (ALTF 1185-2017 to J.N.), HFSP (LT000446/2018-L to J.N.), UCSF PBBR (7000/7002124 to J.N.), NIH (DK129763 to J.N.), and NIMRC (GNT1142229 to Y.A.L.). Mass spectrometry equipment was obtained through NIH Shared Instrumentation Grant 1S100D016232-01 (J.E.C.), 1S100D018210-01A1 (J.E.C.), and 1S100D021505-01 (J.E.C.). **Author contributions:** J.N., Y.A.L., W.C.K., E.J.W., A.C. and H.A.I. conceived and designed the experiments, interpreted the results, and wrote the paper. J.N., Y.A.L., and W.C.K. performed the experiments. D.D. assisted with the analysis of RNA sequencing (RNA-seq) and ChIP-seq datasets, and J.A.M., T.V.R., and J.E.C. performed lipidomics on plasma and liver samples. O.G. performed the analysis comparing *Bcl6*^{AlbCre} and *Ghrd3* liver transcriptomes and provided conceptual input. **Competing interests:** The authors declare that they have no competing interests. **Data and materials availability:** The RNA-seq and ChIP-seq datasets generated and analyzed during the study are available in the Gene Expression Omnibus (GEO) repository (ncbi.nlm.nih.gov/geo/) under the SuperSeries accession number GSE138396. **License information:** Copyright © 2022 the authors, some rights reserved; exclusive licensee American Association for the Advancement of Science. No claim to original US government works. <https://www.science.org/about/science-licenses-journal-article-reuse>

SUPPLEMENTARY MATERIALS

science.org/doi/10.1126/science.abn9886
Materials and Methods
Figs. S1 to S5
References (29–37)
MDAR Reproducibility Checklist
Data S1 to S6

Submitted 12 January 2022; resubmitted 27 June 2022
Accepted 29 August 2022
[10.1126/science.abn9886](https://doi.org/10.1126/science.abn9886)

OPTICS

Miniaturized spectrometers with a tunable van der Waals junction

Hoon Hahn Yoon^{1,2*}, Henry A. Fernandez^{1,2}, Fedor Nigmatulin^{1,2}, Weiwei Cai³, Zongyin Yang⁴, Hanxiao Cui⁵, Faisal Ahmed¹, Xiaoli Cui^{1,2}, Md Gius Uddin^{1,2}, Ethan D. Minot⁶, Harri Lipsanen¹, Kwanyo Kim⁷, Pertti Hakonen², Tawfique Hasan⁸, Zhipei Sun^{1,2*}

Miniaturized computational spectrometers, which can obtain incident spectra using a combination of device spectral responses and reconstruction algorithms, are essential for on-chip and implantable applications. Highly sensitive spectral measurement using a single detector allows the footprints of such spectrometers to be scaled down while achieving spectral resolution approaching that of benchtop systems. We report a high-performance computational spectrometer based on a single van der Waals junction with an electrically tunable transport-mediated spectral response. We achieve high peak wavelength accuracy (~ 0.36 nanometers), high spectral resolution (~ 3 nanometers), broad operation bandwidth (from ~ 405 to 845 nanometers), and proof-of-concept spectral imaging. Our approach provides a route toward ultraminiaturization and offers unprecedented performance in accuracy, resolution, and operation bandwidth for single-detector computational spectrometers.

Spectrometers are indispensable for various applications, including industrial inspection, chemical and biological characterization, and image sensing and analysis (1, 2). Their miniaturization with high spectral resolution and wide operation bandwidth is highly desirable to meet the emerging and future demands in portable and on-chip applications (1). However, conventional spectroscopy systems typically rely on bulky dispersive optical components (e.g., gratings) and detector or filter arrays, which impose strict restrictions on ultraminiaturization (2).

Common spectrometer miniaturization approaches therefore replace the functions of these dispersive optical elements through various schemes (fig. S1), including photonic crystals (3), metasurfaces (4), and compact interferometers (5). Recently, a profound technological leap has seen the emergence of miniaturized computational spectrometers, which leverage the power of mathematical algorithms for spectrum reconstruction (1). Examples of such approaches include quantum dot filter arrays on top of charge-coupled device sensors (6), bandgap engineered multiple nanowires (7), a single nanowire with bandgap gradation (8), Stark effect in black

phosphorus (9), in situ perovskite modulation (10), and a single superconducting nanowire with tunable quantum efficiency (11). However, the performance and usability of these computational spectrometers remain limited: Spectral resolution and operation bandwidth are typically restricted by the number of integrated detectors (6–8), bandgap modulation limits (9, 10), and cryogenic operational requirements (11).

Photodetection with two-dimensional (2D) layered materials is advantageous owing to their strong light-matter interaction, atomically sharp interface, and electrically tunable

photoresponse (12–14). However, insufficient band structure modulation makes it challenging to achieve high-resolution broadband spectral sensing using a single 2D material. On the other hand, 2D material-based van der Waals (vdW) junctions offer highly tunable functionalities beyond the constituent materials (15–17) and could overcome these limitations. Specifically, we suggest that wavelength-dependent photodetection with vdW junctions recently exploited for optoelectronic logic computing (18, 19) and color sensing (20, 21) could also be key to high-resolution computational spectral sensing.

Here, we demonstrate a high-performance ultraminiaturized computational spectrometer using a single vdW junction with an electrically tunable transport-mediated spectral response. Our device, with its footprint defined by the junction size ($\sim 22 \mu\text{m}$ by $8 \mu\text{m}$) shows unprecedented performance for a single-detector computational spectrometer, with the ability to resolve peak monochromatic wavelengths with ~ 0.36 nm accuracy, reconstruct broadband spectra with ~ 3 nm resolution, and acquire spectral images by spectral scanning. Our single-junction spectrometer concept can be extended to other tunable junctions to achieve high spectral resolution and broad operation bandwidth with its ultracompact size, representing the ultimate miniaturization strategy without sacrificing spectrometer performance.

The performance of computational spectrometers relies on the variability of their wavelength-dependent photoresponsivity (1, 6–11). The single-detector miniaturized spectrometers reported thus far are limited by

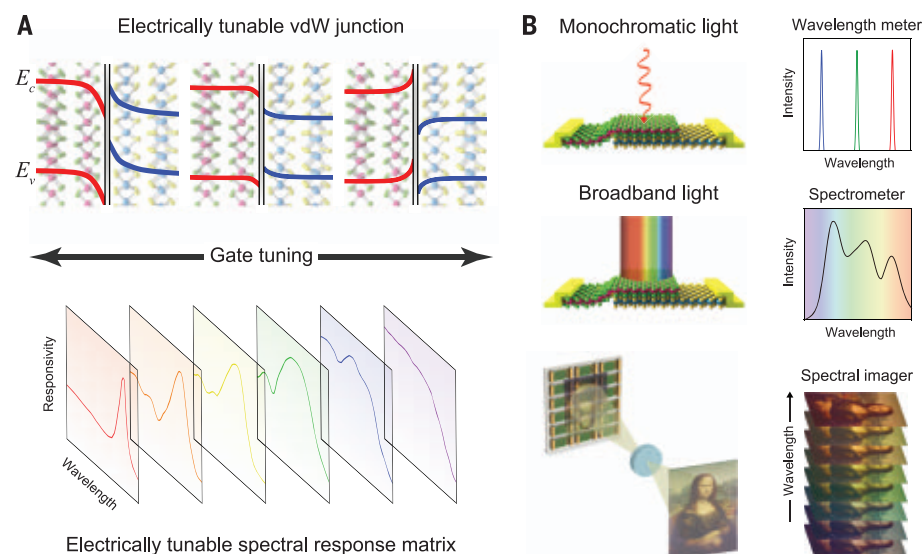


Fig. 1. Ultraminiaturized spectrometer concept with a single vdW junction. (A) A typical gate-tunable band alignment at the vdW junction interface (top) with its distinct gate-tunable spectral response matrix (bottom). E_c (E_v) represents the conduction (valence) band edge. (B) Schematic of various application examples using a single-junction spectrometer: wavelength meter to distinguish peak wavelengths of monochromatic light (top), spectrometer to resolve broadband spectra (middle), and spectral imager to analyze spectral information of images (bottom).

¹Department of Electronics and Nanoengineering, Aalto University, Espoo 02150, Finland. ²QTF Centre of Excellence, Department of Applied Physics, Aalto University, Aalto 00076, Finland. ³Key Lab of Education Ministry for Power Machinery and Engineering, School of Mechanical Engineering, Shanghai Jiao Tong University, Shanghai 200240, China. ⁴College of Information Science and Electronic Engineering and State Key Laboratory of Modern Optical Instrumentation, Zhejiang University, Hangzhou 310027, China. ⁵School of Aeronautics and Astronautics, Sichuan University, Chengdu 610065, China. ⁶Department of Physics, Oregon State University, Corvallis, OR 97331, USA. ⁷Department of Physics, Yonsei University, Seoul 03722, Republic of Korea. ⁸Cambridge Graphene Centre, University of Cambridge, Cambridge CB3 0FA, UK.

*Corresponding author. Email: hoonhahn.yoon@aalto.fi (H.H.Y.); zhipei.sun@aalto.fi (Z.S.)

their performance (9, 10) and usability (9, 11) owing to the limited band structure modulation and, consequently, the spectral response. In contrast, electrical tuning of the interfacial band alignment of a vdW junction (Fig. 1A, top panel) enables controllable and distinctive interlayer transport (15–17). Such electrically controllable interlayer transport allows for a tunable spectral response (Fig. 1A, bottom panel) with high sensitivity and variability over a wide spectral range (12–14), suggesting that a single vdW junction spectrometer could achieve substantially higher performance than previously reported spectrometers (supplementary text section ST1 and table S1). We combine an electrically tunable single vdW junction with a computational reconstruction algorithm for various applications (Fig. 1B). To experimentally realize our spectrometer concept, the following three steps are required (fig. S2): (i) measuring the gate-tunable spectral responses with multiple known incident spectra (i.e., the learning process), (ii) measuring the gate-tunable photocurrent of the unknown incident light to be analyzed (i.e., the testing process), and (iii) computing the spectral information of the unknown incident light on the basis of the results obtained in the learning and testing processes using the reconstruction algorithm (i.e., the reconstructing process).

The distinct and varied photoresponse of a vdW junction, tuned at different gate voltages and incident light wavelengths, is critical to our spectrometer (1). We choose a MoS₂/WSe₂ heterojunction (Fig. 2A) as an example, because of its distinct spectral response due to the gate-tunable photovoltaic effect from the visible to the near-infrared (22–28). The MoS₂/WSe₂ heterojunction is encapsulated by top and bottom hexagonal boron nitride (h-BN) layers for insulation and passivation, respectively (materials and methods section MM1). A monolayer graphene film below the stack is used as a local gate electrode for effective gate tuning. Each stacking layer was characterized by Raman spectroscopy and atomic force microscopy (fig. S3) to confirm the quality of the vdW heterostructure.

The transfer curves (drain-source current, I_{DS} , as a function of the gate-source voltage, V_{GS}) of the MoS₂ or WSe₂ channels and their heterojunction are measured at drain-source voltage $V_{DS} = 3$ V in dark conditions (Fig. 2B). The individual MoS₂ (WSe₂) channel exhibits n-type (p-type) characteristics owing to the donor (acceptor) impurities in MoS₂ (WSe₂). Thus, a depletion region and built-in electric field are expected at their vdW interface (22–28). The MoS₂/WSe₂ heterojunction is characterized by positive V_{DS} applied to the WSe₂ side, corresponding to the forward biasing of the diode. The sign change of transconductance, $\frac{dI_{DS}}{dV_{GS}}$, occurs at $V_{GS} = -5$ V, matching the hole current from WSe₂ with the electron current

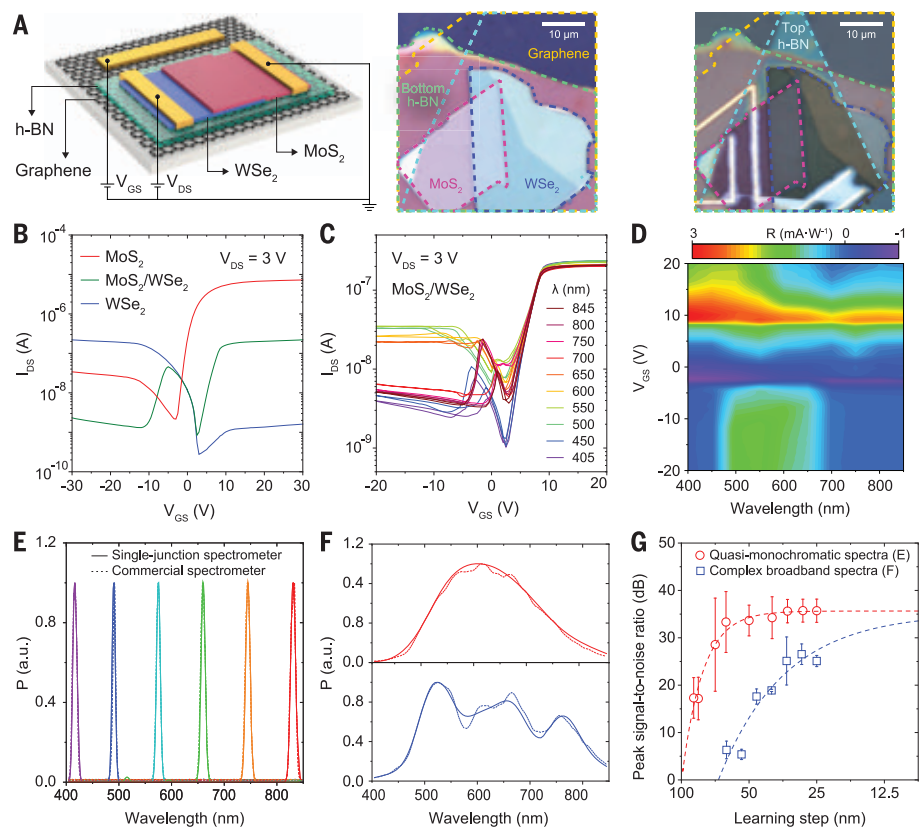


Fig. 2. Single-junction spectrometer demonstration. (A) Schematic of our MoS₂/WSe₂ heterojunction spectrometer (left) and its optical images on the h-BN and graphene layers before (middle) and after (right) depositing electrodes and stacking the top h-BN passivation layer. The top h-BN layer was omitted from the images in this panel for better visibility. (B and C) Transfer curves of the MoS₂ and WSe₂ channels and their heterojunction with the graphene gate without (B) and with (C) light illumination at different wavelengths with a fixed power of ~ 20 μ W. (D) Color contour plot of the spectral response matrix. (E and F) Quasi-monochromatic [(E); bandwidth: ~ 10 nm] and two different broadband (F) spectra reconstructed with our spectrometer (solid curve) and measured using a commercial spectrometer (dashed curve). a.u., arbitrary units. (G) Peak signal-to-noise ratio between reconstructed and reference spectra as a function of learning step.

from MoS₂. This “anti-ambipolar” behavior and other transport properties (figs. S4 to S7) are typical of MoS₂/WSe₂ heterojunctions (22–28), providing clearly distinguishable V_{GS} dependence.

The transfer curves of the MoS₂/WSe₂ heterojunction measured under multiple known incident lights with a bandwidth of ~ 10 nm indicate a strong wavelength dependence (Fig. 2C). The photoresponsivity, $R = \frac{I_{ph}}{P}$, measured at different V_{GS} and incident light wavelengths is used to encode the spectral response matrix, where the photocurrent is defined as $I_{ph} = I_{light} - I_{dark}$, with I_{light} and I_{dark} representing I_{DS} with and without light illumination at $V_{DS} = 3$ V, respectively, and with P representing the incident light power (fig. S8). The gate-tunable spectral response of the MoS₂/WSe₂ heterojunction with high sensitivity over a wide spectral range is due to the wavelength-dependent absorption (29) of MoS₂ and WSe₂ as well as the controllable charge carrier transport (22–28) through the MoS₂/WSe₂ interface, unlike the

individual MoS₂ and WSe₂ materials. The spectral response matrix (Fig. 2D) inherits a rich structure from the dynamics of photo-excited charge carriers generated across the tunable MoS₂/WSe₂ heterojunction (22–29), confirming fast and stable spectral detection with giant gate tunability in our MoS₂/WSe₂ heterojunction (figs. S9 to S13).

After encoding this spectral response matrix (Fig. 2D) for the learning process, our single-junction spectrometer is ready to measure unknown incident light spectra, following the workflow diagram (fig. S2). Briefly, we measure the gate-tunable photocurrent of the unknown incident light and then compute its constrained least-squares solution to reconstruct the spectrum using an adaptive Tikhonov regularization method by minimizing the residual norm with a regularization factor (1, 8). Details of the optical setup, electrical and optoelectrical measurements, and computational reconstruction are provided in fig. S14 and materials and methods sections MM2 to MM4.

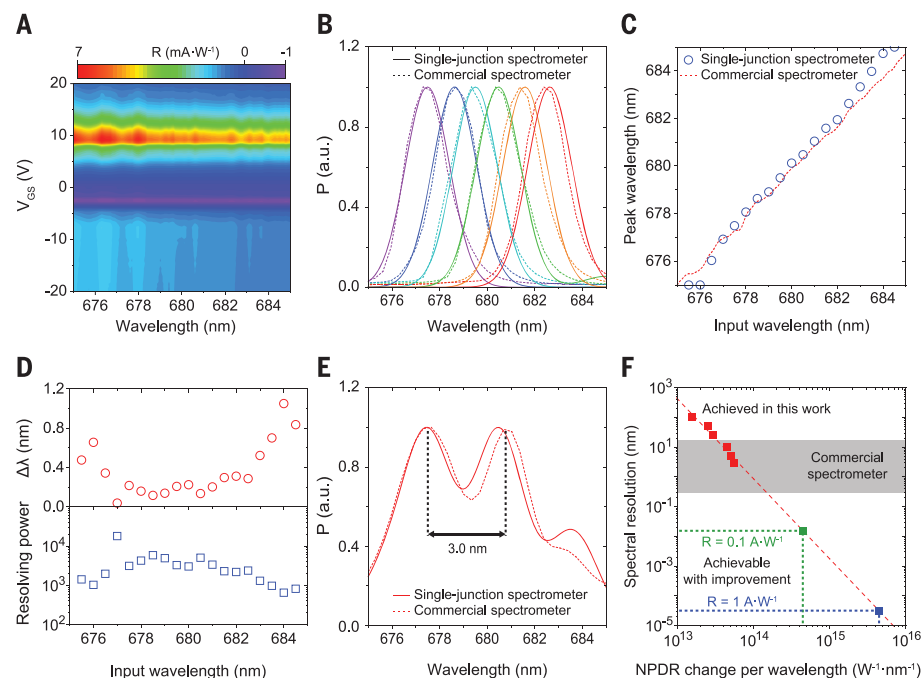


Fig. 3. High-performance wavelength resolving power and spectral resolution. (A) Color contour plot of the high-density spectral response matrix with a learning step of ~ 0.1 nm. (B) Monochromatic (bandwidth: ~ 2 nm) spectra reconstructed with our spectrometer (solid curve) and measured using a commercial spectrometer (dashed curve). (C) Peak wavelengths of the reconstructed and measured spectra as a function of input wavelength. (D) Peak wavelength difference between reconstructed and reference spectra (top) and wavelength resolving power of our single-junction spectrometer (bottom). (E) Complex spectra reconstructed (solid curve) and measured (dashed curve). (F) Future prospect of our single-junction spectrometer aiming for ultrahigh resolution.

The quasi-monochromatic and complex broadband spectra reconstructed with our single-junction spectrometer agree well with the reference spectra measured using a commercial spectrometer, demonstrating the viability of the single-junction spectrometer concept (Fig. 2, E and F). Although the demonstrated bandwidth (from ~ 405 to 845 nm) is limited because of the availability of the light wavelengths in our laboratory, the MoS₂/WSe₂ heterojunction exhibits photoresponse from ~ 400 to 2400 nm (25). Indeed, the vdW junctions are known to exhibit photodetection capability for incident light whose wavelength corresponds to about half of (or even much smaller than) the bandgap of each material (15–17, 25). Therefore, in principle, the single-junction spectrometer is not limited by the material bandgap and feasibly offers an operation bandwidth broader than that of our demonstration. Our single-junction spectrometer using the interlayer transport-mediated photoresponse is fundamentally different from the previously demonstrated spectrometer concepts, such as bandgap engineering and grading (7–10). Detailed comparisons of our work and the current state-of-the-art miniaturized spectrometers [including black phosphorus-based spectrometers with the Stark effect (9)] are given in supplementary text section ST2 and table S1.

To evaluate deviations between the reconstructed and reference spectra, the peak signal-to-noise ratio (PSNR) has previously been used to analyze the mean squared error (supplementary text section ST3). The maximum PSNR estimated from the extrapolation is ~ 35.7 and 33.6 dB for the quasi-monochromatic and complex broadband spectra, respectively (Fig. 2G). A reasonable learning step (i.e., a step in wavelength for encoding the spectral response matrix) can be chosen on the basis of the saturated PSNR. Therefore, a high-speed learning process is achievable with a large learning step and slightly reduced accuracy (11).

The wavelength-resolving power is an important measure of spectrometers in practical applications (1, 2). To demonstrate high spectral resolution capability with our single-junction ultraminiaturized spectrometer, we construct a high-density spectral response matrix through an ultrasmall learning step of ~ 0.1 nm using monochromatic light of wavelengths from ~ 675 to 685 nm for the learning process (Fig. 3A). Our single-junction spectrometer encoded by the high-density spectral response matrix can resolve monochromatic light with high accuracy (Fig. 3, B and C). The average peak wavelength difference ($\Delta\lambda$) between reconstructed and reference spectra is $\sim 0.36 \pm 0.06$ nm, with a minimum of ~ 0.04 nm (Fig. 3D). This is comparable to the learning

step of ~ 0.1 nm. The average wavelength resolving power, $R_\lambda = \frac{\lambda}{\Delta\lambda}$ at a given input wavelength λ , is ~ 3470 (Fig. 3D).

Furthermore, we measure complex incident spectra to study the spectral resolution. Two peaks at ~ 679 nm, separated by ~ 3 nm, are successfully distinguished (Fig. 3E). Our spectrometer can also resolve broadband spectra and identify their peak wavelengths with high resolution (~ 0.9 nm, demonstrated in fig. S15). This indicates that our spectrometer has a spectral resolution comparable to or better than that of current state-of-the-art miniaturized spectrometers (3–11), with a footprint ($\sim 22 \mu\text{m}$ by $8 \mu\text{m}$) comparable to or smaller than most. This footprint is several orders of magnitude smaller than that of commercial miniaturized spectrometers (30) and recently demonstrated spectrometers using metasurfaces (4), quantum dots (6), or a single-dot perovskite (10) (see table S1 for a detailed comparison). We note that the demonstrated accuracy (~ 0.36 nm) and resolution (~ 3 nm), which are limited by the smallest incident wavelength step available in our laboratory, can be further improved by minimizing the learning step during the learning process. We suggest that such a learning process—similar to the calibration process in traditional spectrometers—is practical for various applications.

Many strategies can be considered for improving the resolution, accuracy, and speed of our single-junction spectrometer (1). These include: (i) increasing the dataset size to create higher-density spectral response matrix by minimizing the learning step (7–11), (ii) designing junctions with higher response and larger wavelength or gate dependence (15–17), and (iii) optimizing the reconstruction algorithm [e.g., suppressing the perturbation with more advanced regularization (1, 8) or increasing the accuracy with convolutional processing (20, 21)]. Ideally, decreasing the learning step is a straightforward approach to forming a denser spectral response matrix for more accurate spectral reconstruction. However, there is a trade-off: Signal difference, measured at small learning steps, comparable to the measurement noise could result in errors during reconstruction.

To illustrate the future development possibilities of single-junction spectrometers, we consider the normalized photocurrent-to-dark current ratio (NPDR) change per wavelength step of two resolved peaks (supplementary text section ST4). The extrapolated line in Fig. 3F indicates the potential of our approach with improved photoresponsivity for higher resolution than the commercial miniaturized spectrometers (30). The achievable resolution is highlighted on the basis of recently reported photoresponse (~ 0.1 to $1 \text{ A}\cdot\text{W}^{-1}$ at 532 nm) of MoS₂/WSe₂ heterojunctions (25). The resolution and bandwidth can be further improved by engineering junctions with different combinations of various

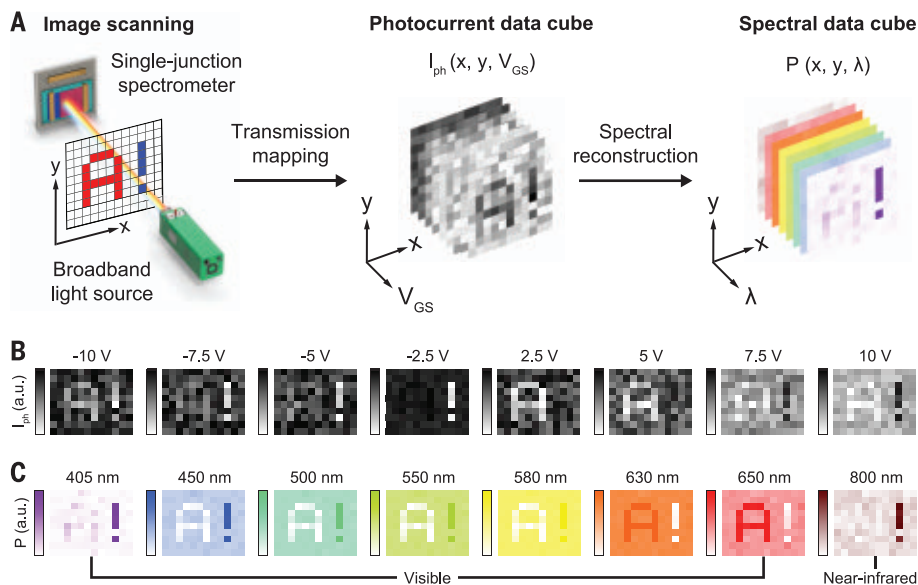


Fig. 4. Proof-of-concept demonstration of spectral imaging. (A) Configuration of spectral imaging using our single-junction spectrometer with a spatial scanning method. A broadband light source filtered with a color image is incident to our spectrometer for spectral imaging. (B) Photocurrent mapping data scanned at different V_{GS} . (C) Spectral images reconstructed at different wavelengths, covering the visible to near-infrared ranges. Higher intensity at each wavelength indicates that more broadband light is transmitted through the color image. The pixel intensity in (B) and (C) is normalized with each maximum intensity.

2D materials or integrating waveguides (15–17). Additional strategies for improving performance are provided in supplementary text section ST5. With the potential to substantially improve performance, our single-junction spectrometer can not only be adapted to other tunable junction architectures but also integrated with CMOS (complementary metal-oxide semiconductor)-compatible platforms.

Our single-junction spectrometer can benefit from the recently developed large-scale 2D material synthesis to construct an array for future spectral imaging. We demonstrate proof-of-concept spectral imaging of a color filter consisting of red, blue, and transparent areas with spatial scanning using our spectrometer (Fig. 4A). At each mapping position, the measured photocurrent data at different V_{GS} are recorded in the spatial response data cube for spectral reconstruction. A series of photocurrent mapping data scanned at different V_{GS} is displayed (Fig. 4B) and converted to a series of spectral data reconstructed at different wavelengths (Fig. 4C). The spectral images indicate that the red and blue filters absorb more incident broadband light from ~405 to 580 nm, and from ~600 to 700 nm, respectively. As a result, the spectra of the red uppercase letter “A” (from ~450 to 700 nm) and the blue exclamation mark “!” (from ~405 to 845 nm) are distinguishable from that of the background. Note that a strong light signal at near 800 nm for the exclamation mark can be fully detected, highlighting the advantages of spectral imaging over conventional RGB color im-

aging (see fig. S16 for the spectra reconstructed with different color filters). In our demonstration, the image resolution is defined by the mapping step. However, our concept has great potential for large-scale spectral imaging by future array devices, offering high spatial resolution with the junction at the micrometer or nanometer scale.

In our spectrometer, no photodetector array, filter array, or other bulky dispersive components are required to achieve high resolution, subnanometer accuracy, and broad operation bandwidth. The compact footprint of our single-junction spectrometers may provide scalability and compatibility with the current photonic integrated circuits and CMOS-compatible processes for direct integration into modern smartphones, lab-on-a-chip systems, and other customized devices ranging from bio-implants to drones and satellites.

Note added in proof: During the proofreading stage, we became aware of a recent work (31) using a $\text{ReS}_2/\text{Au}/\text{WSe}_2$ heterostructure, but with limited resolution and operation.

REFERENCES AND NOTES

1. Z. Yang, T. Albrow-Owen, W. Cai, T. Hasan, *Science* **371**, eaeb0722 (2021).
2. R. F. Wollfenbuttel, *IEEE Trans. Instrum. Meas.* **53**, 197–202 (2004).
3. Z. Wang et al., *Nat. Commun.* **10**, 1020 (2019).
4. A. Tittl et al., *Science* **360**, 1105–1109 (2018).
5. D. M. Kita et al., *Nat. Commun.* **9**, 4405 (2018).
6. J. Bao, M. G. Bawendi, *Nature* **523**, 67–70 (2015).
7. J. Meng, J. J. Cadusch, K. B. Crozier, *Nano Lett.* **20**, 320–328 (2020).
8. Z. Yang et al., *Science* **365**, 1017–1020 (2019).
9. S. Yuan, D. Naveh, K. Watanabe, T. Taniguchi, F. Xia, *Nat. Photonics* **15**, 601–607 (2021).

10. L. Guo et al., *Adv. Mater.* **34**, e2200221 (2022).
11. L. Kong et al., *Nano Lett.* **21**, 9625–9632 (2021).
12. F. Xia, T. Mueller, Y. M. Lin, A. Valdes-Garcia, P. Avouris, *Nat. Nanotechnol.* **4**, 839–843 (2009).
13. M. Buscema et al., *Chem. Soc. Rev.* **44**, 3691–3718 (2015).
14. F. H. Koppens et al., *Nat. Nanotechnol.* **9**, 780–793 (2014).
15. A. K. Geim, I. V. Grigorieva, *Nature* **499**, 419–425 (2013).
16. M. M. Furchi, A. Pospischil, F. Libisch, J. Burgdörfer, T. Mueller, *Nano Lett.* **14**, 4785–4791 (2014).
17. N. Ubrig et al., *Nat. Mater.* **19**, 299–304 (2020).
18. S. Wang et al., *ACS Nano* **16**, 4528–4535 (2022).
19. Y. Sun, Y. Ding, D. Xie, *Adv. Funct. Mater.* **31**, 2105625 (2021).
20. S. Lee, R. Peng, C. Wu, M. Li, *Nat. Commun.* **13**, 1485 (2022).
21. L. Pi et al., *Nat. Electron.* **5**, 248–254 (2022).
22. C.-H. Lee et al., *Nat. Nanotechnol.* **9**, 676–681 (2014).
23. T. Roy et al., *ACS Nano* **9**, 2071–2079 (2015).
24. A. Nourbakhsh, A. Zubair, M. S. Dresselhaus, T. Palacios, *Nano Lett.* **16**, 1359–1366 (2016).
25. M. Long et al., *Nano Lett.* **16**, 2254–2259 (2016).
26. Y. Son et al., *Nano Lett.* **16**, 3571–3577 (2016).
27. M.-H. Doan et al., *ACS Nano* **11**, 3832–3840 (2017).
28. X. Sun et al., *ACS Nano* **15**, 16314–16321 (2021).
29. H. S. Ra et al., *Adv. Mater.* **34**, e2107468 (2022).
30. Hamamatsu, Mini-spectrometers product lineup; <https://www.hamamatsu.com/eu/en/product/optical-sensors/spectrometers/mini-spectrometer.html>.
31. W. Deng et al., *Nat. Commun.* **13**, 4627 (2022).
32. H. H. Yoon, W. Cai, F. Nigmatulin, Spectral reconstruction based on tunable vdW junction spectrometers, version 1.1, Zenodo (2022); <https://doi.org/10.5281/zenodo.7152385>.

ACKNOWLEDGMENTS

We acknowledge the provision of facilities and technical support from the Otaniemi research infrastructure (OtaNano-Micronova Nanofabrication Centre and OtaNano-Nanomicroscopy Centre). We thank A. Liapis, M. Du, Y. Dai, S.-T. Akkanen, J. Camilo Arias, and X. Bai for valuable discussions and M. Turunen, D. Li, Y. Zhang, V. Pelgrin, and S. Das for access to the optical instruments and components.

Funding: This work was supported by the Academy of Finland (grants 314810, 333982, 336144, 336813, 336818, and 348920), Academy of Finland Flagship Programme (grant 320167, PREIN), the EU H2020-MSCA-RISE-872049 (IPN-Bio), EPSRC (grant EP/T014601/1), ERC (grant 834742), and National Natural Science Foundation of China (grants 51976122 and 52061135108). P.H. was supported by the Jane and Aatos Erkkö foundation and the Technology Industries of Finland centennial foundation (Future Makers 2021).

Author contributions: Z.S. conceived of the ideas during discussions with H.H.Y. and F.A. H.H.Y. designed the experiments and carried out the characterizations and measurements. H.H.Y., H.A.F., F.N., and M.G.U. fabricated the van der Waals heterostructures and spectrometer devices. H.A.F. provided the home-built optical system and prepared the optical instruments and components. F.A. and X.C. helped with the electrical and optoelectrical measurements. H.H.Y., F.N., W.C., Z.Y., and H.C. developed the reconstruction code. W.C., Z.Y., H.C., and T.H. shared the processing strategies. H.H.Y., H.A.F., F.N., F.A., and Z.S. analyzed the data. W.C., E.D.M., P.H., K.K., H.L., and T.H. commented on the experimental results and helped with the data analysis. H.A.F. and X.C. helped with the graphic design. H.H.Y. wrote the manuscript, and Z.S. supervised the research. All authors participated in the scientific discussion extensively and contributed to the writing of the manuscript. **Competing interests:** The authors declare that they have no competing interests. **Data and materials availability:** All data needed to evaluate the conclusions in the paper are present in the main text or the supplementary materials. Code used for spectral reconstruction based on tunable vdW junction spectrometers is available at <https://github.com/fonj/Reconstruction> and archived at Zenodo (32). **License information:** Copyright © 2022 the authors; some rights reserved; exclusive licensee American Association for the Advancement of Science. No claim to original US government works. <https://www.science.org/about/science-licenses-journal-article-reuse>

SUPPLEMENTARY MATERIALS

science.org/doi/10.1126/science.add8544

Materials and Methods

Supplementary Text

Figs. S1 to S16

Table S1

References (33–67)

Submitted 8 July 2022; accepted 25 August 2022
10.1126/science.add8544

WILDLIFE DISEASE

Disease outbreaks select for mate choice and coat color in wolves

Sarah Cubaynes^{1*}, Ellen E. Brandell², Daniel R. Stahler³, Douglas W. Smith³, Emily S. Almberg⁴, Susanne Schindler⁵, Robert K. Wayne⁶, Andrew P. Dobson^{7,8}, Bridgett M. vonHoldt⁷, Daniel R. MacNulty⁹, Paul C. Cross¹⁰, Peter J. Hudson², Tim Coulson¹¹

We know much about pathogen evolution and the emergence of new disease strains, but less about host resistance and how it is signaled to other individuals and subsequently maintained. The cline in frequency of black-coated wolves (*Canis lupus*) across North America is hypothesized to result from a relationship with canine distemper virus (CDV) outbreaks. We tested this hypothesis using cross-sectional data from wolf populations across North America that vary in the prevalence of CDV and the allele that makes coats black, longitudinal data from Yellowstone National Park, and modeling. We found that the frequency of CDV outbreaks generates fluctuating selection that results in heterozygote advantage that in turn affects the frequency of the black allele, optimal mating behavior, and black wolf cline across the continent.

Variation in animal color is frequently used to assess the quality of potential mates and their fit to environmental conditions (1). In many species, color covaries with aspects of the environment such as latitude, weather, and the presence of specific parasites, food resources, and predators. An individual's color can signal its condition or immunological status (2). Honest signals need coloration to be correlated with fitness-associated traits, and under these conditions, this may select for particular mate choice strategies because individuals choose partners that maximize the expected fitness of their offspring (3). When the environment varies spatially, generating a cline in selection pressures, this could lead to landscape-level variation in coloration (4) and spatial variation in strategies of mate choice behavior (5).

Although rare at high latitudes, black wolves increase in frequency along a southwest cline toward forested areas in North America (6), with the highest frequencies at each latitude observed along the Rocky Mountains (Fig. 1A). The absence of geographical barriers that prevent gene flow, coupled with molecular signals of selection, points to regional variation

in coat color being due to a cline in selection pressures (7).

Coat color in wolves (*Canis lupus*) is determined by genotype at the *K* locus gene *CBD103* (8). The ancestral wild-type *k* allele allows a normal *Agouti* and *Mc1r* gene interaction, resulting in gray coat color, whereas a three-nucleotide deletion in the *K* locus gene causes the protein to prevent *Agouti* function, leading to dominant inheritance of a black coat (9). After a single introgression event into a North American wolf population in the past 7250 years, the black allele has undergone a selective sweep, revealing one of the most rapid spreads of an adaptive variant known in vertebrates (10). The homozygote *KK* and the heterozygote *Kk* have indistinguishable black pelage but very different fitnesses (11). Therefore, coat color phenotype is not itself under direct selection, but the black allele must have a function that affects fitness directly or through pleiotropic effects, conferring a strong selective advantage in certain environments (7, 12). Because the *K* locus encodes for a β -defensin protein that plays a direct role in innate and adaptive immunity in mammals (13), we postulate that it is involved in immunity to respiratory infections such as the morbillivirus that causes canine distemper virus (CDV), a pathogen of carnivores (14) that can cause substantial mortality among immunologically naive individuals, particularly juveniles (15).

The ability to fight disease can generate a fitness cost in the absence of these threats (16, 17). We investigated whether the environment-dependent fitness benefits of certain genotypes could explain the North American cline in wolf coat color frequency. CDV infects most carnivores, and the frequency of outbreaks varies depending on the composition of the carnivore communities (18). To test the prediction that coat color varies with CDV occurrence, we

analyzed 12 wolf populations to determine whether the probability of a wolf being black was predicted by the presence of CDV antibodies (19).

Wolves seropositive for CDV are more likely to be black, especially at older ages (Fig. 1B). We constructed a model to assess the individual- and population-level effects of CDV on the probability of a wolf being black (19). We predicted the probability of being seropositive for CDV while standardizing for age and confounding factors (fig. S2). The population effect is the positive correlation between the population-level disease exposure and whether an individual is black or gray (Fig. 1C). The individual effect captures whether a previously CDV-exposed individual is more likely to be black, perhaps because it is more likely to survive the infection and be sampled later. We found that if an individual was seropositive for CDV, then its probability of being black increased from 25 to 32% ($P = 0.03$) (fig. S4). These results are consistent with our hypothesis that CDV exposure is positively associated with coat color frequency and provide extensive comparative support.

Next, we report an analysis of the Yellowstone wolf population using individual life history and coat color data collected since their reintroduction in 1995–1997 (19). The population consists of ~55% gray wolves (genotype *kk*) and 45% black wolves (genotypes *Kk* and *KK*), with only 5% of these being homozygotes (Fig. 2). Previous research has revealed that female gray wolves have 25% higher annual reproductive success in all years compared with black females, and that CDV outbreaks generate a 50% reduction in female reproductive success independently of coat color (20). However, because so few genotyped black homozygote individuals have reproduced in Yellowstone ($n = 5$), there is insufficient statistical power to determine whether there is any difference in reproductive performance between black genotypes. A survival advantage of black heterozygotes over the other two genotypes across all years has previously been reported (17), but we do not know whether coat color and CDV infection interact to influence survival, and therefore the relative fitness, of the three genotypes.

We used longitudinal data to explore how annual age-specific survival rates varied between 1998 and 2020 among homozygote black, heterozygote black, and homozygote gray wolves with individual exposure to CDV during five CDV outbreaks (19). We developed a mark-recapture model that included transitions among susceptible, exposed, and immune states. We also included information on permanent dispersal and non-natural and known natural deaths while simultaneously modeling recapture rates. Pack identity and year were included as random effects.

¹CEFE, University of Montpellier, CNRS, EPHE-PSL University, IRD, 34090 Montpellier, France. ²Center for Infectious Disease Dynamics, Department of Biology, Pennsylvania State University, State College, PA 16802, USA. ³Yellowstone Center for Resources, Yellowstone National Park, WY 82190, USA. ⁴Wildlife Division, Montana Fish Wildlife & Park, Bozeman, MT 59718, USA. ⁵School of Biological Sciences, University of Bristol, Bristol BS8 1QU, UK. ⁶Department of Ecology and Evolutionary Biology, University of California, Los Angeles, Los Angeles, CA 90095, USA. ⁷Department of Ecology and Evolutionary Biology, Princeton University, Princeton, NJ 08544, USA. ⁸Santa Fe Institute, Santa Fe, NM 87501, USA. ⁹Department of Wildland Resources and Ecology Center, Utah State University, Logan, UT 84322, USA. ¹⁰US Geological Survey, Northern Rocky Mountain Science Center, Bozeman, MT 59715, USA. ¹¹Department of Biology, University of Oxford, Oxford OX1 3SZ, UK.

*Corresponding author. Email: sarah.cubaynes@cefe.cnrs.fr

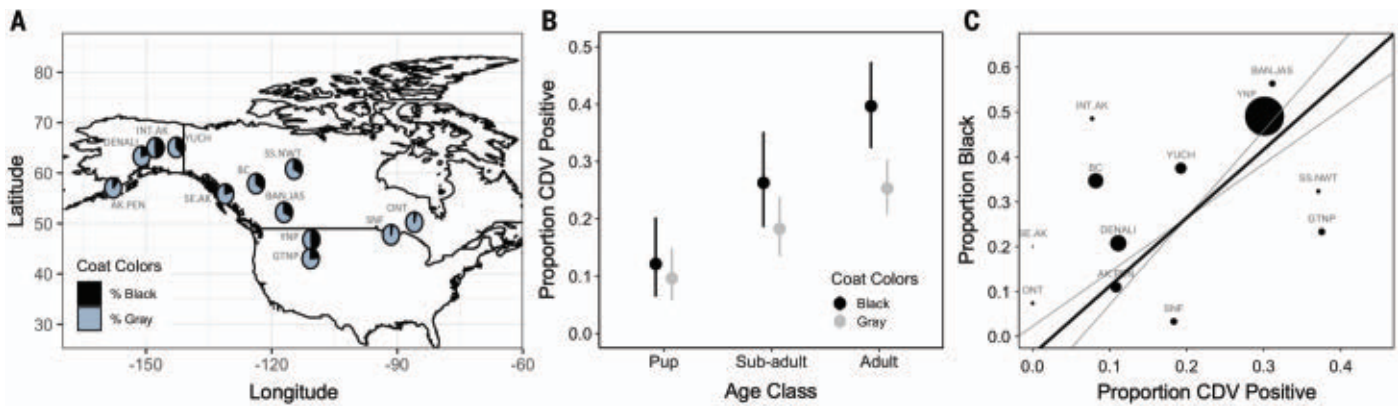
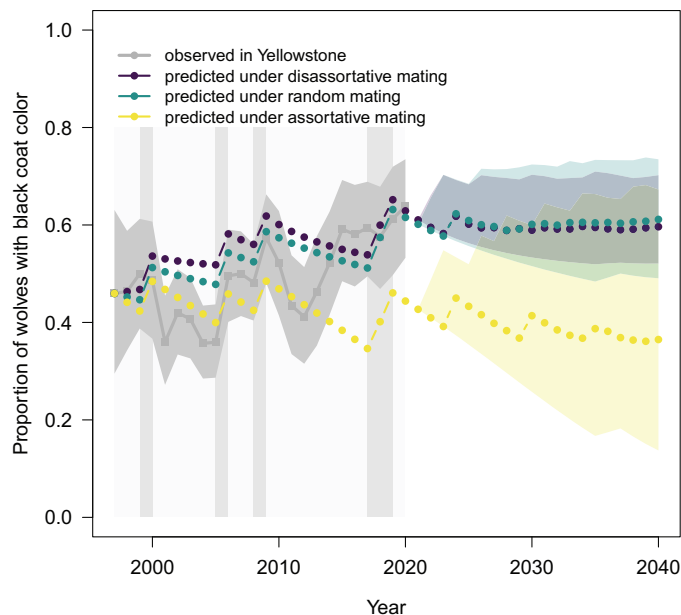


Fig. 1. Occurrence of CDV and coat color in wolves across North America. (A) Proportion of each coat color phenotype. Wolf sampling locations included Alaska Peninsula (AK.PEN), Denali National Park (DENALI), interior Alaska (INT.AK), Yukon Charley Rivers National Preserve (YUCH), southeastern Alaska (SE.AK), British Columbia (BC), South Slave Northwest Territories (SS.NWT), Banff and Jasper National Parks (BAN.JAS), Yellowstone National Park (YNP), Grand Teton National Park (GTNP), Ontario (ONT), and Superior National Forest (SNF). YNP and

GTNP are offset for visual purposes ($n = 1274$) (19). (B) Proportion of pup, subadult, and adult wolves seropositive for CDV among $N = 1134$ with known age and sex from the wolf populations sampled in (A). Also shown are 95% confidence intervals (95% CIs). (C) Relationship between CDV prevalence and proportion of wolves with black coat color. The thick black line is a restricted major axis regression weighted by sample size, and gray lines show the 95% bounds of the regression estimate. Circles are scaled to sample size ($N = 1166$).

Fig. 2. Observations and predictions of the frequency of black wolves in Yellowstone National Park. Dark gray lines are point estimates. Shaded area represents 95% CIs. Vertical gray lines represent past CDV outbreaks. Up to 2020, colored lines and dots represent a single model projection accounting for past CDV outbreaks for random (green), disassortative (purple), and assortative (yellow) mating. After 2020, the colored shaded areas represent 95% CIs estimated from 500 model runs assuming the same frequency of CDV outbreaks (annual probability of 0.2).



Mirroring the results of our broad-scale surveys, our analyses revealed that black heterozygote wolves have higher survival compared with gray wolves, but only in CDV-infected individuals (Fig. 3). Because inheritance at the *K* locus is Mendelian, if the survival advantage to the heterozygote exposed to CDV compensates for the reduced fertility of black females, then it may be advantageous to mate with a partner of the opposite color to maximize the likelihood of producing heterozygote offspring when epizootics are frequent. We thus hypothesize

that fluctuating, frequency-dependent selection due to CDV outbreak frequency can alter the relative fitness of the genotypes, resulting in a fitness advantage to heterozygotes when disease is frequent enough and selecting for the disassortative mating strategy observed in Yellowstone (21).

We constructed a stochastic, demographic, two-sex model of the dynamics of the three genotypes (19). We used a mating function that allowed us to alter the mating preference from random through disassortative to assortative and evaluate which mate choice strategy was optimal under various disease outbreak frequencies.

tative and evaluate which mate choice strategy was optimal under various disease outbreak frequencies.

When the model was parameterized with initial starting conditions equal to the observed coat color frequencies at reintroduction into Yellowstone and observed CDV outbreaks, the simulations captured the observed dynamics of coat color frequency adequately when we assumed random or disassortative mating (Fig. 2). The model did not perform well with assortative mating, consistent with the excess of black-gray pairs reported in Yellowstone (21). Therefore, despite its simplicity, our model captures the dynamics of wolf coat color genotypes in Yellowstone.

Our model predicted that the frequency of black wolves depends upon the frequency of CDV outbreaks and mate choice strategy (Fig. 4A). Under all mate choice strategies, the frequency of black wolves increased with the frequency of CDV outbreaks. The rate of increase was steepest when wolves mated assortatively and shallowest when they mated disassortatively. In Yellowstone, wolves mate disassortatively, but is this adaptive?

Disease-induced mortality selects for the evolution of mate choice, but the evolutionarily stable strategy (ESS) changes on either side of a threshold in disease frequency (19). Below an outbreak frequency of 0.1 (≈ 1 outbreak every 10 years), an assortative mating strategy is the ESS (Fig. 4B), whereas above it, a disassortative mating strategy has greater fitness. Random mating is never the ESS. The black allele is always eliminated in the absence of CDV when the ESS is assortative mating, whereas disassortative mating results in a stable polymorphism.

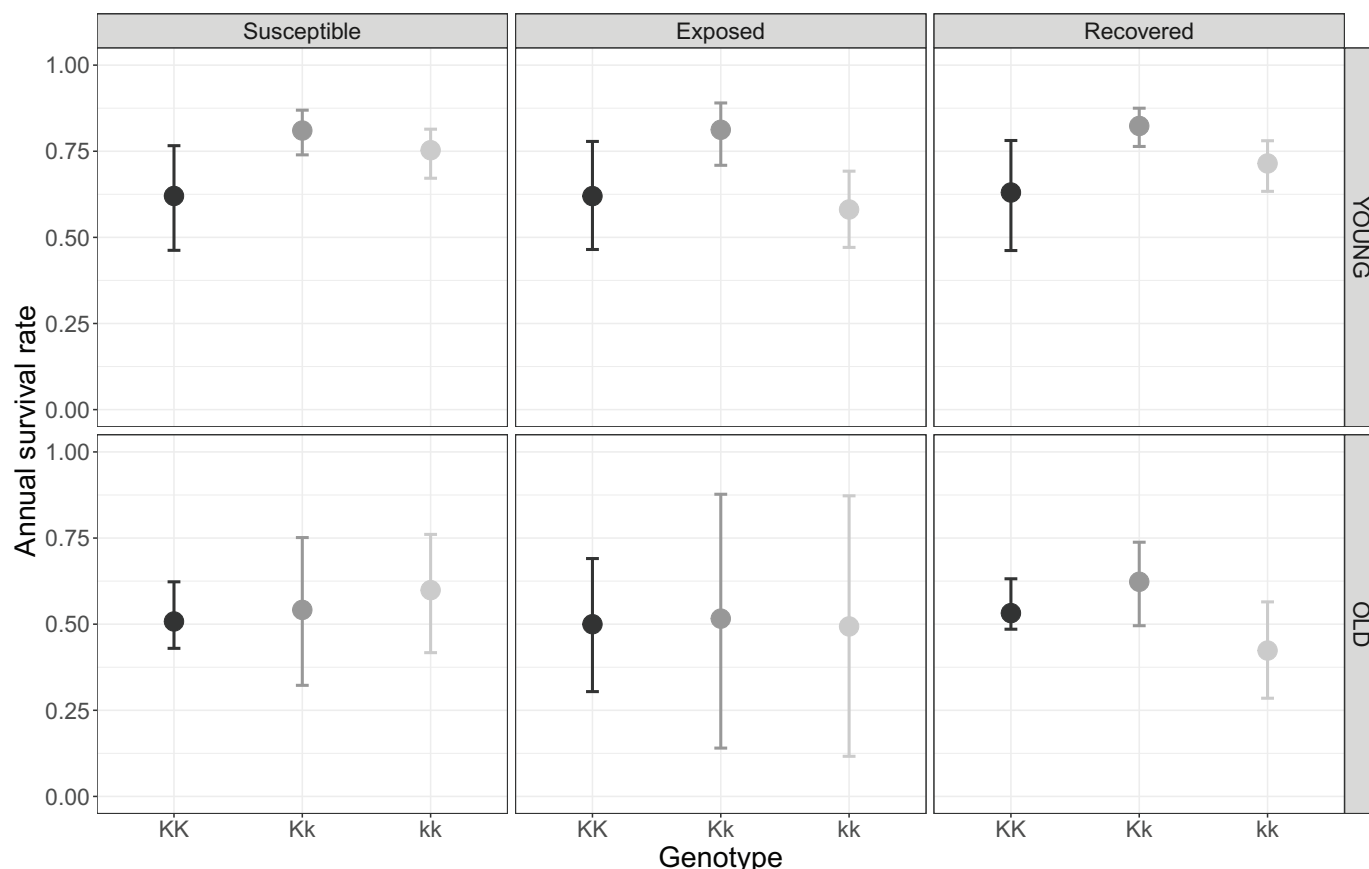


Fig. 3. Survival analysis results. Effects of age (top, young; bottom, old), disease status (columns), and *K* locus genotype (KK for homozygote black, Kk for heterozygote black, and kk for homozygote gray) on survival rates. Medians with 80% credible intervals are displayed.

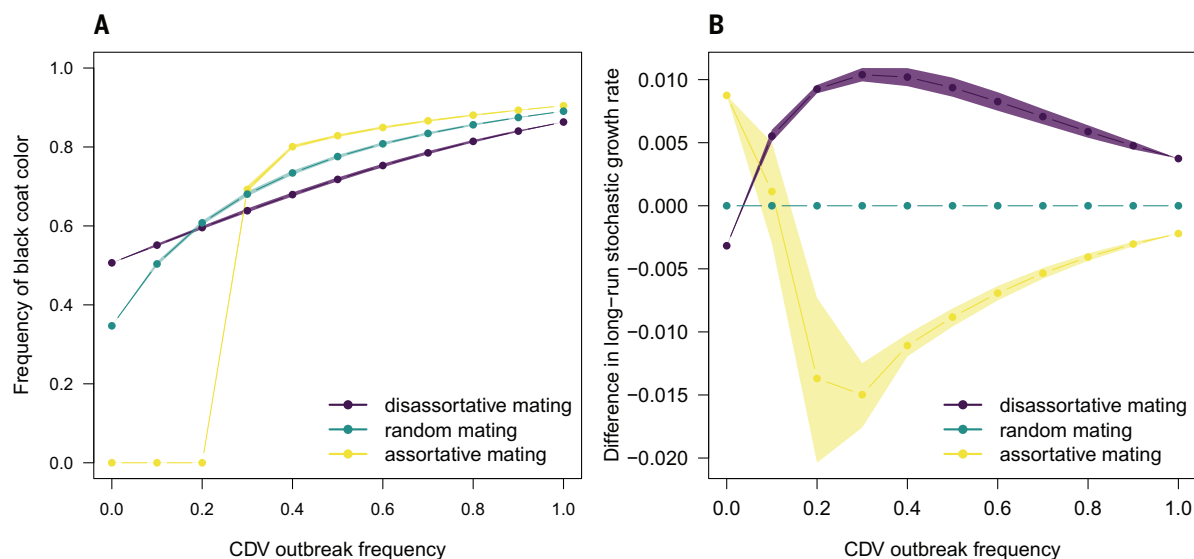


Fig. 4. Model predictions as CDV outbreak frequency varies. (A) Effect of CDV outbreak frequency and mating system on the frequency of black wolves. (B) Difference in strategy fitness relative to random mating (green) for assortative (yellow) and disassortative (purple) mating strategies as a function of CDV outbreak frequency. Lines represent point estimates, and shaded polygons represent 95% CIs from 500 simulations.

Our modeling results are consistent with our hypothesis that the frequency of disease outbreaks is responsible for the observed cline in coat color seen across North America, and they also explain why Yellowstone wolves mate

disassortatively. We would expect an assortative mating strategy when CDV outbreaks occur less than once every decade. Although our results are consistent with observations, recent laboratory experiments challenging wolf cell cultures

with a range of pathogens have so far failed to discern genotype-specific responses to CDV (22). Although elegant, that work cannot answer the question that we have addressed because it fails to capture susceptibility to infection

and the complexity of immune responses expected within free-living individuals (22). In addition, genetic findings have reported positive selection on coat color genes, major histocompatibility complex (MHC) genes, and immunity genes along a gradient of temperature and humidity (7), a finding that is consistent with our conclusions.

Our results are unlikely to be specific to wolves. In many insects, amphibians, reptiles, birds, and nonhuman mammals, disease resistance is associated with coloration (1, 2, 12, 23), a trait that can act as a signal for pathogen resistance in mate choice (2, 3). Recent findings have identified associations between disease-resistance MHC genes and coloration in mammals (10, 24), amphibians (25), reptiles (26), and birds (27), possibly through pleiotropic effects or the action of “supergenes” (1, 28). For example, in some bird species, carotenoid-dependent coloration (23) can drive mate choice through associations with disease-resistant MHC genes that influence the sensory functions of odor, vision, and hearing (24).

When coloration is genetically determined and disease resistance is heritable and associated with coloration, a preference for a mate of a specific color will enhance fitness by maximizing the chances of producing resistant offspring in environments with frequent and virulent enough pathogens. When the environment varies spatiotemporally, alternative mating strategies could explain the maintenance of color polymorphism (5) through negative-frequency-dependent selection, as shown here for wolves. Incidental color byproducts of immune response genes may consequently be widespread drivers of the mating behaviors observed across a diverse array of animal species. It is possible that we have significantly underestimated the role of pathogens in generating the diversify of morphological and behavioral traits observed in nature (25, 29).

CDV requires a high population density to persist, and because wolves live at low densities, CDV cannot be endemic within a population (18). Instead, it requires a broad community of carnivores to persist and intermittent spillover transmission back to wolves. The reservoir community, species, or population is not well understood for CDV in North America, but we show that CDV prevalence is positively associated with human density (fig. S4) (19). CDV probably evolved from human measles epidemics that decimated indigenous South American populations when the virus spilled over into the abundant dog population and evolved into CDV before being found in North America in the 1760s (30). Wolves have genes for black coat color because they reproduced with the dogs of First Nations People, and this introgression happened between 1598

and 7248 years ago (10). It is therefore likely that other pathogens or mechanisms have contributed to the rapid spread of the black allele.

None of our analyses, on its own, provides conclusive support for the hypothesis that the frequency of black wolves across North America is determined by the frequency of CDV outbreaks, but each separate, complementary line of evidence provides support. These results are important because, first, they reveal how the frequency of disease outbreaks imposes selection on immune function, generating heterozygote advantage only under certain environments, similar to what is seen with sickle cell disease in humans. In the absence of CDV in the environment, the dominant *K* allele in wolves is expected to be lost because an assortative mating strategy would be selected, with the frequency of CDV outbreaks determining the frequency of the derived *k* allele. We provide support that variation in CDV outbreak frequency has generated the cline in wolf coat color observed across North America. An incidental byproduct of genetic variation at the *K* locus is coat color variation, a marked phenotypic pattern that has long puzzled researchers. The second line of evidence is that sexual selection has operated on this incidental cue to sculpt wolf behavior, with Yellowstone wolves mating disassortatively to maximize their fitness. This shows not only how the effects of a pathogen influence selection for resistance, but also how this is signaled between hosts and thus the mate choice behavior mechanism that results in host diversity. Finally, the results of our study show the true value of coupling geographically restricted, intensive, long-term, individual-based studies of wild populations with continent-wide, cross-sectional samples from multiple populations. We were able to link statistical results across these disparate forms of data using evolutionarily explicit population modeling. In doing so, we learned that the maintenance of genetic, morphological, and behavioral variation both within and between populations of a charismatic carnivore is the result of environmentally determined, fluctuating, frequency-dependent selection.

REFERENCES AND NOTES

1. A. Orteu, C. D. Jiggins, *Nat. Rev. Genet.* **21**, 461–475 (2020).
2. J. Côté et al., *Proc. Biol. Sci.* **285**, 20180285 (2018).
3. M. Milinski, T. Bakker, *Nature* **344**, 330–333 (1990).
4. S. Antoniazza, R. Burri, L. Fumagalli, J. Goudet, A. Roulin, *Evolution* **64**, 1944–1954 (2010).
5. M. R. Robinson, G. S. van Doorn, L. Gustafsson, A. Qvarnström, *Ecol. Lett.* **15**, 611–618 (2012).
6. P. S. Gipson et al., *Wildl. Soc. Bull.* **30**, 821–830 (2002).
7. R. M. Schweizer et al., *Mol. Ecol.* **25**, 380–402 (2016).
8. T. M. Anderson et al., *Science* **323**, 1339–1343 (2009).
9. S. I. Candille et al., *Science* **318**, 1418–1423 (2007).
10. R. M. Schweizer et al., *Mol. Biol. Evol.* **35**, 1190–1209 (2018).
11. T. Coulson et al., *Science* **334**, 1275–1278 (2011).
12. A.-L. Ducrest, L. Keller, A. Roulin, *Trends Ecol. Evol.* **23**, 502–510 (2008).

13. D. Yang et al., *Science* **286**, 525–528 (1999).
14. S. L. Deem, L. H. Spelman, R. A. Yates, R. J. Montali, *J. Zoo Wildl. Med.* **31**, 441–451 (2000).
15. E. S. Almberg, L. D. Mech, D. W. Smith, J. W. Sheldon, R. L. Crabtree, *PLOS ONE* **4**, e7042 (2009).
16. M. Aidoo et al., *Lancet* **359**, 1311–1312 (2002).
17. M. Fu, B. Waldman, *Immunogenetics* **69**, 529–536 (2017).
18. E. S. Almberg, P. C. Cross, D. W. Smith, *Ecol. Appl.* **20**, 2058–2074 (2010).
19. Materials and methods are available as supplementary materials.
20. D. R. Stahler, D. R. MacNulty, R. K. Wayne, B. vonHoldt, D. W. Smith, *J. Anim. Ecol.* **82**, 222–234 (2013).
21. P. W. Hedrick, D. W. Smith, D. R. Stahler, *Evolution* **70**, 757–766 (2016).
22. R. A. Johnston et al., *J. Hered.* **112**, 458–468 (2021).
23. M. J. P. Simons, A. A. Cohen, S. Verhulst, *PLOS ONE* **7**, e43088 (2012).
24. P. S. C. Santos, M. Mezger, M. Kolar, F.-U. Michler, S. Sommer, *Proc. Biol. Sci.* **285**, 20182426 (2018).
25. A. L. Trujillo, E. A. Hoffman, C. G. Becker, A. E. Savage, *Heredity* **126**, 640–655 (2021).
26. J. D. Hacking, D. Stuart-Fox, S. S. Godfrey, M. G. Gardner, *Ecol. Evol.* **8**, 9920–9933 (2018).
27. H.-Y. Liu, K. He, Y.-F. Ge, Q.-H. Wan, S.-G. Fang, *Animals (Basel)* **11**, 276 (2021).
28. P. Jay et al., *Philos. Trans. R. Soc. Lond. B Biol. Sci.* **377**, 20210193 (2022).
29. M. E. F. LaCava et al., *R. Soc. Open Sci.* **8**, 210802 (2021).
30. E. W. Uhl et al., *Int. J. Paleopathol.* **24**, 266–278 (2019).
31. Data for: S. Cubaynes et al., Disease outbreaks select for mate choice and coat color in wolves, Dryad (2022); <https://doi.org/10.5061/dryad.fqz612jw1>.
32. Code for: S. Cubaynes et al., Disease outbreaks select for mate choice and coat color in wolves, Zenodo (2022); <https://doi.org/10.5281/zenodo.7057987>.

ACKNOWLEDGMENTS

We thank Yellowstone Forever, V. Gates, and B. and V. Grahams for funding. W. Wang, L. Parsons, A. DeCandia, and C. Lawrence for assistance with developing the *K* locus amplicon-sequencing assay and genotyping pipeline and V. Gervasi and R. Villoutreix for comments on a previous version of the manuscript. S.C. is supported by a grant from the Agence Nationale de la Recherche (ANR-18-CE02-0011, MathKinD). T.C. and S.C. were supported by the Natural Environment Research Council. D.R.M., R.K.W., D.R.S., T.C., and D.W.S. were supported by the National Science Foundation (DEB-1021397 to R.K.W. and DEB-1245373 to D.W.S., D.R.S., T.C., and D.R.M.). E.E.B. and P.J.H. were supported by a Verne William Professorship that supported aspects of this work.

Author contributions: D.W.S. and D.R.S. oversee the Yellowstone Wolf Project and, along with D.R.M. and E.E.B., conducted or oversaw all data collection and developed the ideas with S.C., T.C., E.S.A., E.E.B., P.C., P.H., A.P.D., and R.K.W. B.V. conducted genotyping. E.S.A., P.C., and E.E.B. collected and analyzed the serological data and provided expertise on disease dynamics along with A.P.D. and P.H. S.C., E.E.B., and P.C. conducted the statistical analyses and modeling with expertise from T.C. and S.S. T.C. and S.C. wrote the paper with input from all authors. Any use of trade, product, or firm names is for descriptive purposes only and does not imply endorsement by the US Government.

Competing interests: The authors declare no competing interests.

Data and materials availability: Data and code used in this paper can be downloaded from Dryad (31) and Zenodo (32), respectively. **License information:** Copyright © 2022 the authors, some rights reserved; exclusive licensee American Association for the Advancement of Science. No claim to original US government works. <https://www.science.org/about/science-licenses-journal-article-reuse>

Submitted 7 April 2021; resubmitted 9 May 2022
Accepted 27 September 2022
10.1126/science.abi8745

EVOLUTION

Deep cis-regulatory homology of the butterfly wing pattern ground plan

Anyi Mazo-Vargas^{1,2*}, Anna M. Langmüller³, Alexis Wilder², Karin R. L. van der Burg¹, James J. Lewis^{1,4}, Philipp W. Messer³, Linlin Zhang^{1,5}, Arnaud Martin², Robert D. Reed^{1,*}

Butterfly wing patterns derive from a deeply conserved developmental ground plan yet are diverse and evolve rapidly. It is poorly understood how gene regulatory architectures can accommodate both deep homology and adaptive change. To address this, we characterized the cis-regulatory evolution of the color pattern gene *WntA* in nymphalid butterflies. Comparative assay for transposase-accessible chromatin using sequencing (ATAC-seq) and in vivo deletions spanning 46 cis-regulatory elements across five species revealed deep homology of ground plan-determining sequences, except in monarch butterflies. Furthermore, noncoding deletions displayed both positive and negative regulatory effects that were often broad in nature. Our results provide little support for models predicting rapid enhancer turnover and suggest that deeply ancestral, multifunctional noncoding elements can underlie rapidly evolving trait systems.

Trait evolution frequently occurs through sequence divergence in noncoding regions of the genome that control gene expression (1). Few case studies, however, have characterized the history of regulatory systems that underlie rapidly evolving traits (2). In this work, we performed comparative chromatin analyses and regulatory knockouts of the butterfly wing pattern gene *WntA* to investigate how trait homology is reflected in regulatory sequences of a highly diverse, continually adapting character system. *WntA* encodes a signaling ligand that induces major color pattern elements of the butterfly wing pattern ground plan (3–6), and *WntA* noncoding variation underlies color pattern adaptation in multiple unrelated butterfly species (4, 7). Thus, allelic variation at the *WntA* locus underlies pattern variation at microevolutionary scales yet also explains macroevolutionary aspects of pattern divergence.

To characterize the cis-regulatory architecture of the *WntA* [i.e., identities and locations of regulating cis-regulatory elements (CREs)], we first used Hi-C to infer the topologically associating domain (TAD) of the *WntA* locus in developing wings. Inside individual TADs, CREs and genes preferentially interact with each other (8). In imaginal discs of *Junonia coenia*, when *WntA* is expressed (5), we identified a TAD that spans *WntA* and its two intergenic regions (Fig. 1, A and B). The strongest CRE-to-promoter interactions occurred just

upstream of the *WntA* promoter and across its lengthy first intron. These data, coupled with sequence association studies (7, 9), led us to focus our functional screens for *WntA* CREs on these regions.

We performed the assay for transposase-accessible chromatin using sequencing (ATAC-seq) to profile chromatin accessibility in heads, forewings, and hindwings from the last larval instar of five nymphalids (Fig. 1C and fig. S1). By comparing head and wing profiles, we identified regions showing wing-specific activity. We next asked to what extent individual wing-specific CREs are conserved or are lineage specific. By overlapping the most conserved sequences (Fig. 1C) with the differentially accessible chromatin regions, we observed that 69 to 88% of wing-specific CREs in the *WntA* TAD were in areas with strong sequence conservation between the nymphaline, satyrine, and heliconiine subfamilies. The exception was the monarch butterfly, *Danaus plexippus*, for which 70.6% of the ATAC-seq peaks were in danaine-specific regions (fig. S2). Whereas the nymphaline and heliconiine datasets highlighted both orthologous and novel CREs, most wing-specific CREs were conserved within and between these nymphalid subfamilies. By contrast, the sister group to the rest of the nymphalids, the Danainae clade showed a largely lineage-specific repertoire of CREs (figs. S1 and S2), consistent with the divergent mode of *WntA* expression previously reported in monarchs (6).

We functionally assessed regions containing candidate *WntA* CREs using a CRISPR-Cas9 shotgun mosaic deletion approach (10), where we injected multiple single-guide RNAs (sgRNAs) tiled across open chromatin regions (Fig. 2A, fig. S3, and tables S1 and S2). This approach results in pattern mutant clones derived from a spectrum of deletions of different lengths and positions around candidate CREs. To identify regions that potentially play a role in establishing the nymphalid ground plan, we

targeted wing-specific CREs conserved between *J. coenia* and *Vanessa cardui*—two species with ancestral-like *WntA*-induced color patterns (5, 6). We observed that most of our deletions generated mutant clones affecting similar or overlapping wing color pattern elements (fig. S3 and data S1) (11) and also affected basal, central, and distal pattern elements across both wings (Fig. 2B and fig. S3). This high prevalence of overlapping phenotypic effects is consistent with the Hi-C data, which reveal physical interactions across multiple CREs and the *WntA* promoter (Fig. 1A) and support a model where color patterns are determined by a spatially distributed array of physically interacting noncoding sequences.

This conserved *WntA* regulatory architecture prompted us to investigate the role of recently evolved sequences in pattern formation. To test this, we deleted a region centered on CRE 24, which appears to be specific to *V. cardui*. CRE 24 is not found in congenics *Vanessa tameamea* or *Vanessa atalanta* (which diverged ~10 to 15 million years ago) (12) (fig. S4) or any other currently sequenced butterfly. Deletion of this region caused the reduction and/or loss of basal, central, and marginal pattern elements (figs. S1 and S5), thus demonstrating how even recently evolved noncoding sequences can be integrated into cis-regulatory networks.

Color pattern homologies of *Heliconius* butterflies are a long-standing question (13, 14). *WntA* specifies melanic patches in this genus that may be derived from the nymphalid ground plan (3, 6). We thus investigated to what degree ancestral versus *Heliconius*-specific CREs determine these patterns. ATAC-seq and comparative sequence analysis showed a large number of *WntA* CREs with deep sequence conservation between heliconiines and nymphalines (Fig. 1C and fig. S1), including CREs required for ground plan patterning in *J. coenia* and *V. cardui*. We generated deletions centered on five of these deeply conserved CREs in *Heliconius himera* (figs. S3C and S4). Notably, deletions spanning all five CREs, including on opposite ends of the first intron, had similar broad effects on melanic *Heliconius* wing patterns (Fig. 2D) (11). Deletions spanning two additional heliconiine-specific CREs revealed similar, overlapping phenotypes (11). We conclude that *Heliconius WntA* shares a conserved cis-regulatory architecture with nymphaline butterflies and that the highly derived mimicry-related color patterns of *Heliconius* appear to share deep regulatory homology with the nymphalid ground plan.

It has been speculated that the color patterns of basal heliconiines, which typically show fragmented black, brown, and silver spots, may represent an intermediate state bridging the ancestral ground plan with the *Heliconius* pattern archetype (13, 14). We tested this in the

¹Department of Ecology and Evolutionary Biology, Cornell University, Ithaca, NY, USA. ²Department of Biological Sciences, The George Washington University, Washington, DC, USA. ³Department of Computational Biology, Cornell University, Ithaca, NY, USA. ⁴Baker Institute for Animal Health, College of Veterinary Medicine, Cornell University, Ithaca, NY, USA. ⁵CAS and Shandong Province Key Laboratory of Experimental Marine Biology, Center for Ocean Mega-Science, Institute of Oceanology, Chinese Academy of Sciences, Qingdao, China.

*Corresponding author. Email: anyimv@gwu.edu (A.M.-V.); robertreed@cornell.edu (R.D.R.)

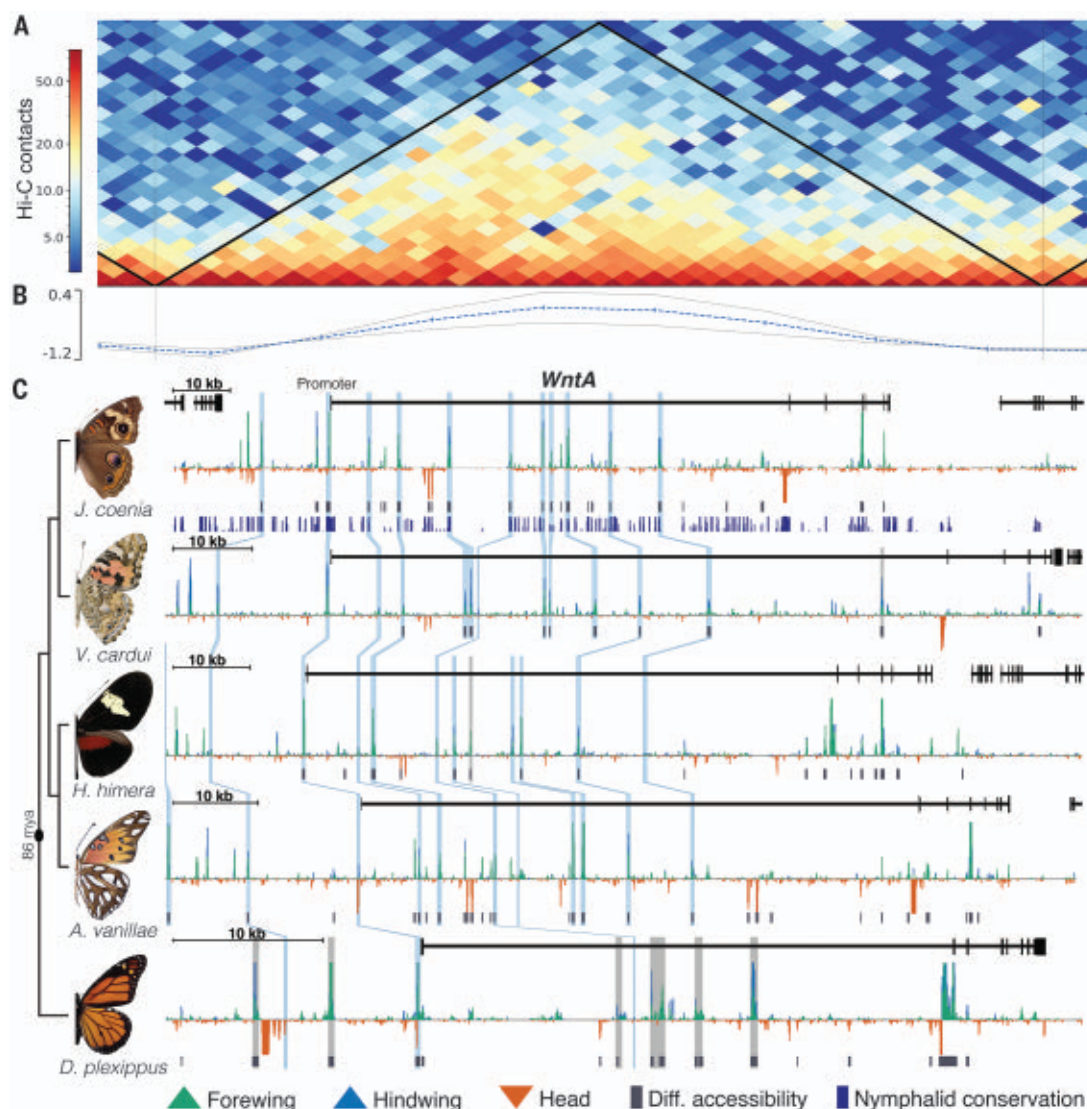


Fig. 1. Deeply conserved chromatin landscape of the *WntA* regulatory region.

(A) Hi-C reveals abundant chromatin interactions across the upstream and first-intron regions of *WntA*. Color intensity corresponds to the contact frequency per bin. (B) TAD separation score. Black lines in (A) depict TAD boundaries as predicted by the TAD separation score. (C) Chromatin accessibility tracks (ATAC-seq) for each species sampled in this study, with phylogenetic relationships shown. Orthologous CREs assessed in this study are in blue shadows connecting different species, whereas lineage-specific elements are shown in gray; see figs. S1 and S4 for details. mya, million years ago; Diff., differential.

basal heliconiine *Agraulis vanillae* by producing deletions spanning the same regulatory regions tested in *H. himera* (Fig. 2D) and several additional heliconiine-specific CRE regions (fig. S4). Again, we found similar results—deletions of regulatory sequences across very different regions of the first intron had overlapping effects distributed across all *WntA*-induced color patterns (data S1) (11). This supports models that heliconiine color patterns evolved through simplification of the nymphalid ground plan and suggests that this process occurred partly through the tinkering of an ancestral cis-regulatory apparatus.

We next examined *D. plexippus*, the monarch butterfly—an exemplar of the nymphalid subfamily Danainae—to investigate how deeply the cis-regulatory architecture described above is conserved in nymphalids. In monarchs, *WntA* shows distinctive vein-associated expression patterns, and *WntA* knockouts cause the loss of these patterns (6). These patterns are highly

derived and challenging to homologize with the nymphalid ground plan (6). Overall, the noncoding region of the monarch *WntA* locus shares relatively little sequence similarity with those of other nymphalids and shows a reduced number of ATAC-seq peaks (Fig. 1C), most of which are in danaine-specific genomic sequences (figs. S2 and S4). Although there are a few orthologous CREs, including the *WntA* promoter, most show no identifiable sequence similarity with other nymphalids, which suggests that they are independently derived or that their sequences are so divergent that orthology is difficult to ascertain (15, 16). To test the wing patterning function of monarch CREs, we generated mosaic deletions centered on six danaine-specific CREs and one ancestrally conserved CRE. Again, we found that even distantly spaced regions had similar effects on *WntA*-induced color patterns (Fig. 2E and data S1). Thus, although many nymphalid wing patterns appear to derive from a deeply conserved

regulatory architecture, there are also cases where divergent regulatory sequences underlie lineage-specific patterns.

Previous work has shown that *WntA* knockouts result in a highly specific loss of *WntA*-expressing color patterns (3, 6). Our deletions that phenocopy *WntA* coding knockouts (Fig. 2) validate the enhancer-like function of these noncoding regions. However, we were surprised to observe expansions of *WntA*-expressing color patterns in several mosaic deletion experiments (data S1) (11). These expansions are phenocopied by heparin injections, which enhance *WntA* signaling during color pattern formation (5, 6, 17). Because deletion-induced color pattern expansion accurately replicates *WntA* gain-of-function effects, we speculate that some regulatory deletions had a positive impact on *WntA* transcription. These dual gain- and loss-of-function effects are well illustrated in *A. vanillae*, in which *WntA* is expressed in a subset of silver and black spots (Fig. 3A). When

heparin is injected, the *Wnt4*-expressing silver spots expand, whereas *Wnt4*-negative spots melanize or disappear. *Wnt4* coding knock-outs present the opposite results—*Wnt4*-expressing silver spots disappear, whereas

Wnt4-negative spots extend (6). Both expansion and reduction effects were observed in many deletion clones (Fig. 3B) across all species (fig. S6 and data S1). Our results show that *Wnt4* regulatory sequences encode both pos-

itive and negative regulatory instructions for color pattern formation.

The color pattern expansion and contraction phenotypes described above are present in mosaic individuals that bear deletion alleles

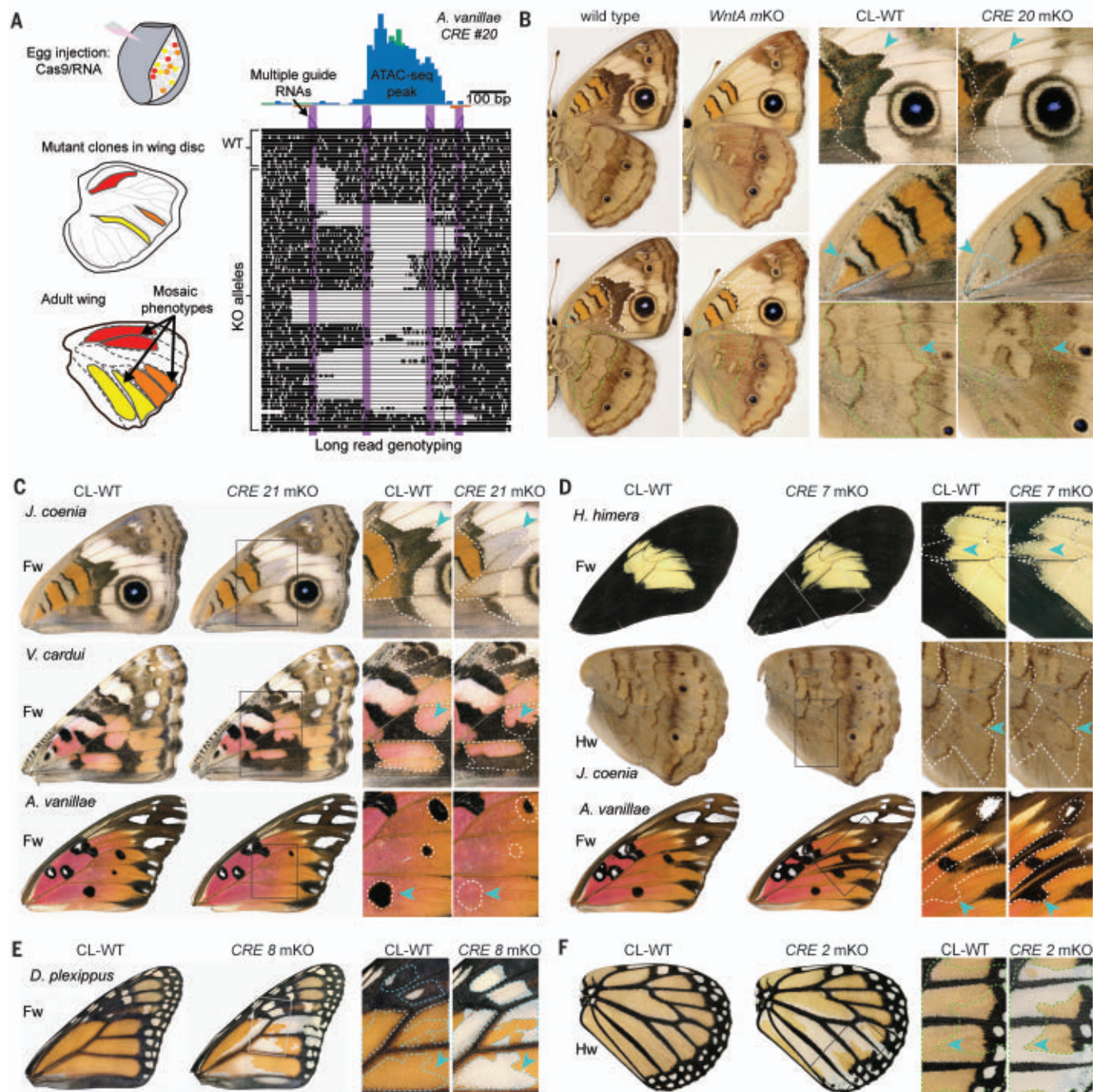


Fig. 2. In vivo mosaic deletions of *WntA* CREs reveal evolutionarily conserved wing pattern development functions. (A) Shotgun deletion generates butterflies that are mosaic for different deletion lengths. bp, base pair; WT, wild type. (B) A *J. coenia* *WntA* null mutant shows loss of *WntA*-expressing color pattern elements (left). This effect is phenocopied by the *CRE 20* mosaic knockout (mKO). (C) *CRE 21* ortholog mKOs across nymphaline (*J. coenia* and *V. cardui*) and heliconiine (*A. vanillae*) species illustrate deep evolutionary conservation of wing pattern ground plan CREs. (D) *CRE 7* ortholog mKOs

across nymphaline (*V. cardui*) and heliconiine (*H. himera* and *A. vanillae*) species suggest that the highly divergent *Heliconius* wing patterns share a deep regulatory architecture with the nymphalid ground plan. (E and F) *D. plexippus* lineage-specific wing pattern CREs illustrated by *CRE 8* (E) and *CRE 2* (F) mKOs. CL-WT refers to contralateral wings with mostly or completely wild-type color patterns from the same individuals as the pictured mKO phenotypes. Cyan arrowheads point to asymmetric color patterns. Fw, forewing; Hw, hindwing.

of different lengths (Fig. 2A). The mosaic nature of the shotgun mutations, however, limits our ability to make precise mechanistic conclusions about the functions encoded within individual CREs. Therefore, to link specific color pattern effects to specific mutant

alleles, we in-crossed *V. cardui* G_0 crispants to generate F_1 's and then in-crossed further to get F_2 germline mutants bearing deletions in *CRE 23* (Fig. 3, E and F, and fig. S7). We confirmed heterozygous and compound inheritance of deletions within this single CRE (fig. S7), which

caused different color pattern changes exemplified by specific gain-of-function effects in dorsal and ventral melanic subelements on the forewings (Fig. 3, E and F). This allelic series shows that small changes in a single CRE are enough to cause localized phenotypic

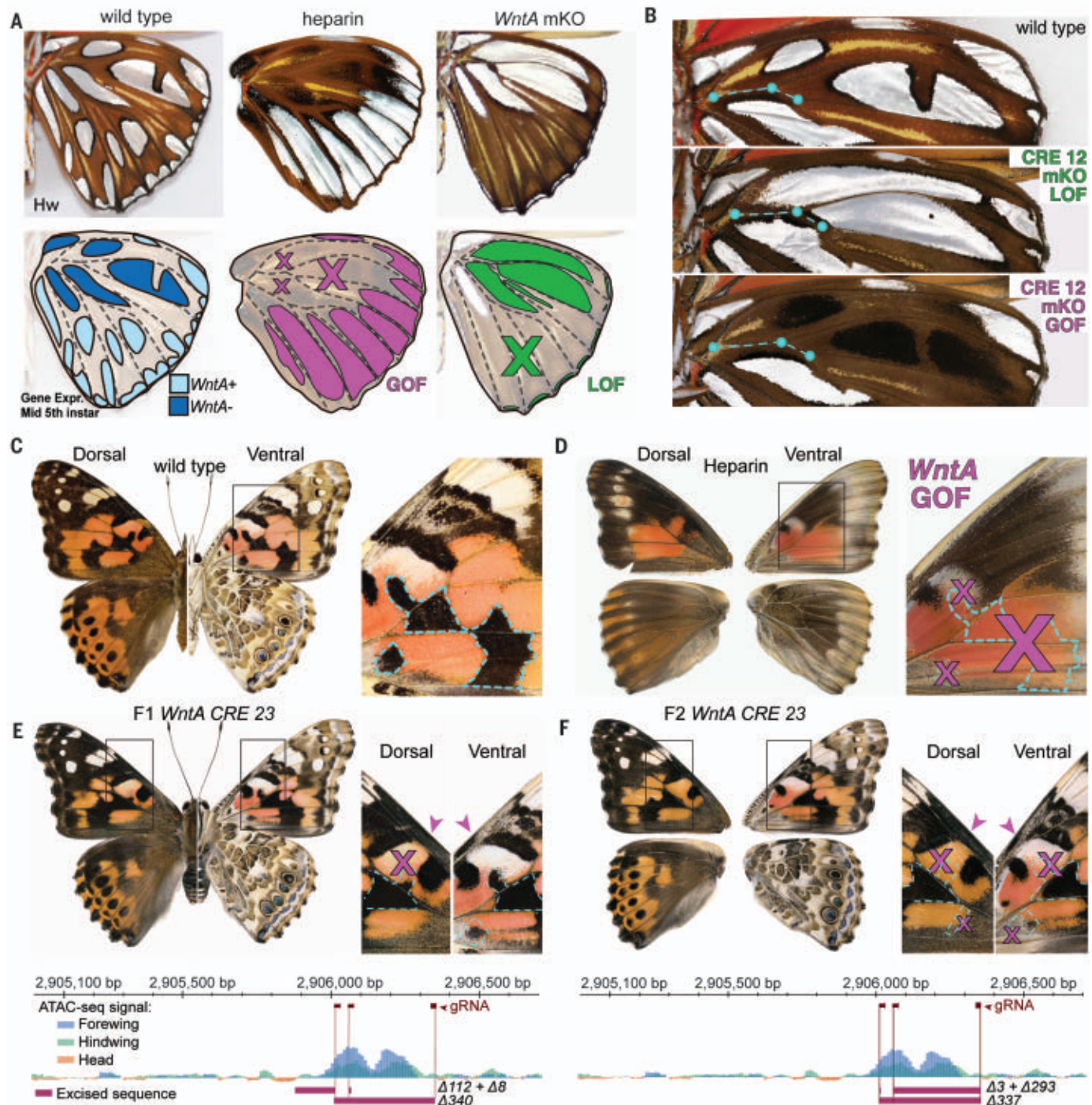


Fig. 3. Positive and negative regulatory activity is a characteristic of color pattern regulation. (A) Heparin injections [gain-of-function (GOF), magenta] and *WntA* knockouts [loss-of-function (LOF), green] in *A. vanillae* highlight the effects of experimental manipulations of the *WntA* signaling axis. Expr., expression. (B) Mosaic shotgun deletions of *WntA* CRE 12 in *A. vanillae* variably result in expansion and contraction of the anterior hindwing silver spots, consistent with a *WntA* LOF and GOF, respectively.

(C) Wild-type *V. cardui* butterfly with closeup of ventral middle forewing region. (D) Heparin injections in *V. cardui* illustrate the *WntA* GOF phenotype. (E and F) F_1 (E) and F_2 (F) *WntA* CRE 23 deletion in *V. cardui*. Each individual represents a different combination of deletion alleles (fig. S7). Cyan dots and dashed annotations show wing landmarks. The "X" marks indicate an absence of pattern with respect to the wild-type phenotype. Arrowheads point to the extension of melanic pigmentation. gRNA, guide RNA.

changes (Fig. 3E) and illustrates the role of negative, silencer-like regulatory directives during patterning.

In testing the wing patterning functions of many orthologous and lineage-specific regulatory regions across five different butterfly species, we made several discoveries that reshape our understanding of the regulatory architecture of morphological evolution. First, in contrast to traditional models, most noncoding deletions that we studied acted globally across forewings and hindwings, often without restriction to any specific *WntA*-expressing color pattern elements. These broad effects suggest an unexpected regulatory fragility to wing patterning. Similar sensitivity to perturbation was also observed for the *Heliconius* color pattern gene *optix* (10) and may indicate that these loci require the assembly of clusters of CREs into transcriptional hubs to mediate gene expression, consistent with emerging superenhancer models (18–20). Second, many deeply conserved wing pattern CREs are shared between nymphalid butterflies. These conserved elements control homologous ground plan components as well as divergent color patterns in species that evolved derived modes of *WntA* expression. We propose that this deep conservation reflects an ancestral regulatory homology that underlies the nymphalid ground plan. Third, noncoding regions have the capacity to both promote and suppress *WntA* color patterns. Overall, the combination of deep conservation and dense functionality of *WntA* regulatory sequences suggests a mode of evolution marked less by the gain and loss of pattern-specific enhancers and more by nuanced modification of an array of deeply ancestral, multifunctional ground plan sequences.

REFERENCES AND NOTES

1. M. Rebeiz, M. Tsiantis, *Curr. Opin. Genet. Dev.* **45**, 115–123 (2017).
2. A. Monteiro, M. D. Gupta, *Curr. Top. Dev. Biol.* **119**, 205–226 (2016).
3. C. Concha et al., *Curr. Biol.* **29**, 3996–4009.e4 (2019).
4. A. Martin et al., *Proc. Natl. Acad. Sci. U.S.A.* **109**, 12632–12637 (2012).
5. A. Martin, R. D. Reed, *Dev. Biol.* **395**, 367–378 (2014).
6. A. Mazo-Vargas et al., *Proc. Natl. Acad. Sci. U.S.A.* **114**, 10701–10706 (2017).
7. J. R. Gallant et al., *Nat. Commun.* **5**, 4817–4827 (2014).
8. J. R. Dixon et al., *Nature* **485**, 376–380 (2012).
9. S. M. Van Belleghem et al., *Nat. Ecol. Evol.* **1**, 0052 (2017).
10. J. J. Lewis et al., *Proc. Natl. Acad. Sci. U.S.A.* **116**, 24174–24183 (2019).
11. A. Mazo-Vargas, R. D. Reed, Deep cis-regulatory homology of the butterfly wing pattern groundplan, dataset, Dryad (2022); <https://doi.org/10.5061/dryad.8cz8w9gpr>.
12. J. Zhang, Q. Cong, J. Shen, P. A. Opler, N. V. Grishin, bioRxiv 829887 [Preprint] (2019).
13. H. F. Nijhout, *The Development and Evolution of Butterfly Wing Patterns* (Smithsonian Institution Press, 1991).
14. H. F. Nijhout, G. A. Wray, *Biol. J. Linn. Soc. Lond.* **33**, 345–365 (1988).
15. M. Kazemian et al., *Genome Biol. Evol.* **6**, 2301–2320 (2014).
16. L. Minnoye et al., *Genome Res.* **30**, 1815–1834 (2020).
17. A. Sourakov, L. T. Shirai, *Trop. Lepid. Res.* **30**, 4–19 (2020).

18. F. Grosveld, J. van Staalduinen, R. Stadhouders, *Annu. Rev. Genomics Hum. Genet.* **22**, 127–146 (2021).
19. E. Z. Kvon, R. Waymack, M. Gad, Z. Wunderlich, *Nat. Rev. Genet.* **22**, 324–336 (2021).
20. A. Tsai, M. R. Alves, J. Crocker, *eLife* **8**, e45325 (2019).

ACKNOWLEDGMENTS

We thank J. Sanders for experimental and analysis input in addition to building a laboratory in the basement of his house and bringing laboratory equipment that allowed us to perform Nanopore genotyping at the beginning of the COVID-19 pandemic. We thank A. Picard Hastings and A. Agrawal for sharing monarch stocks; J. Hanly, S. Van Belleghem, and R. Papa for comments and experimental input; C. Peng, J. Kwan, B. Brack, R. Geltman, and C. Robertson for assistance rearing caterpillars; L. Livraghi and the personnel from genomics core facilities at Cornell University, Duke University, and the University of Maryland–Baltimore for DNA sequencing; and A. Fungtammasan at DNANexus for preassembling PacBio genomes. **Funding:** This study was supported by National Science Foundation grant DGE-1650441 (to A.M.-V.; Graduate Research Fellowship Program); National Science Foundation grants IOS-1656514, IOS-1753559, and IOS-2128164 (to R.D.R.); and National Science Foundation grant IOS-1656553 (to A.M.). **Authors contributions:** Conceptualization: A.M.-V. and R.D.R. Investigation: A.M.-V. Experiments: A.M.-V. and A.W. Writing – original draft: A.M.-V. and R.D.R. Writing – review & editing: A.M.-V. and R.D.R. Simulation analysis: A.M.L. and

P.W.M. Resources: K.R.L.v.d.B., L.Z., J.J.L., A.M., and R.D.R.

Competing interests: The authors declare no competing interests. **Data and materials availability:** Sequence data from ATAC-seq and Hi-C sequencing that support the findings of this study have been deposited in the National Center for Biotechnology Information BioProject PRJNA695303 under BioSamples accession nos. SAMN17611226 to SAMN17611270 and SRX8598136. Additionally, all butterfly wings showing mutations were scanned and deposited in a Dryad repository (11). **License information:** Copyright © 2022 the authors, some rights reserved; exclusive licensee American Association for the Advancement of Science. No claim to original US government works. <https://www.science.org/about/science-licenses-journal-article-reuse>

SUPPLEMENTARY MATERIALS

science.org/doi/10.1126/science.abi9407
Materials and Methods
Figs. S1 to S11
Tables S1 to S7
References (21–47)
MDAR Reproducibility Checklist
Data S1 and S2

Submitted 17 April 2021; accepted 7 September 2022
10.1126/science.abi9407

MEMBRANES

Highly flexible and superhydrophobic MOF nanosheet membrane for ultrafast alcohol-water separation

Li-Hao Xu[†], Shen-Hui Li[†], Heng Mao, Yan Li, Ao-Shuai Zhang, Sen Wang, Wei-Min Liu, Jing Lv, Tao Wang, Wei-Wei Cai, Le Sang, Wen-Wen Xie, Chan Pei, Zheng-Zheng Li, Ying-Nan Feng*, Zhi-Ping Zhao*

High-performance pervaporation membranes have potential in industrial separation applications, but overcoming the permeability-selectivity trade-off is a challenge. We report a strategy to create highly flexible metal-organic framework nanosheet (MOF-NS) membranes with a faveolate structure on polymer substrates for alcohol-water separation. The controlled growth followed by a surface-coating method effectively produced flexible and defect-free superhydrophobic MOF-NS membranes. The reversible deformation of the flexible MOF-NS and the vertical interlamellar pathways were captured with electron microscopy. Molecular simulations confirmed the structure and revealed transport mechanism. The ultrafast transport channels in MOF-NS exhibited an ultrahigh flux and a separation factor of 8.9 in the pervaporation of 5 weight % ethanol-water at 40°C, which can be used for biofuel recovery. MOF-NS and polydimethylsiloxane synergistically contribute to the separation performance.

As an energy-efficient separation technology, membrane-based separation processes have attracted attention because of the demand to reduce carbon emissions and pollution (1–3). Recovery of biofuels, such as alcohols, from fermentation broths is essential to improve production yield (4). Hydrophobic polymeric membranes are widely applied in pervaporation for bioethanol recovery (5, 6). However, the separation performances of polymer-based pervaporation membranes are generally limited by relatively

low permeability or selectivity and the trade-off between permeability and selectivity, which restrict their application (7). Developing a strategy to fabricate high-performance pervaporation membranes helps reduce energy consumption and improve efficiency for industrial biofuel production.

Metal-organic frameworks (MOFs) are widely studied because of their specific absorption affinities, high designability, and diversified pore structures and sizes (8–10). High-porosity MOFs have been embedded in polymeric matrix to prepare mixed-matrix membranes (MMMs); for example, we used pearl necklace-like MOFs with continuous molecular pathways generated by successive MOF nanoparticles in MMMs (11). However, transport pathways in MMMs were

School of Chemistry and Chemical Engineering, Beijing Institute of Technology, Beijing 102488, P.R. China.
*Corresponding author. Email: fengyn@bit.edu.cn (Y.-N.F.); zhaozp@bit.edu.cn (Z.-P.Z.) [†]These authors contributed equally to this work.

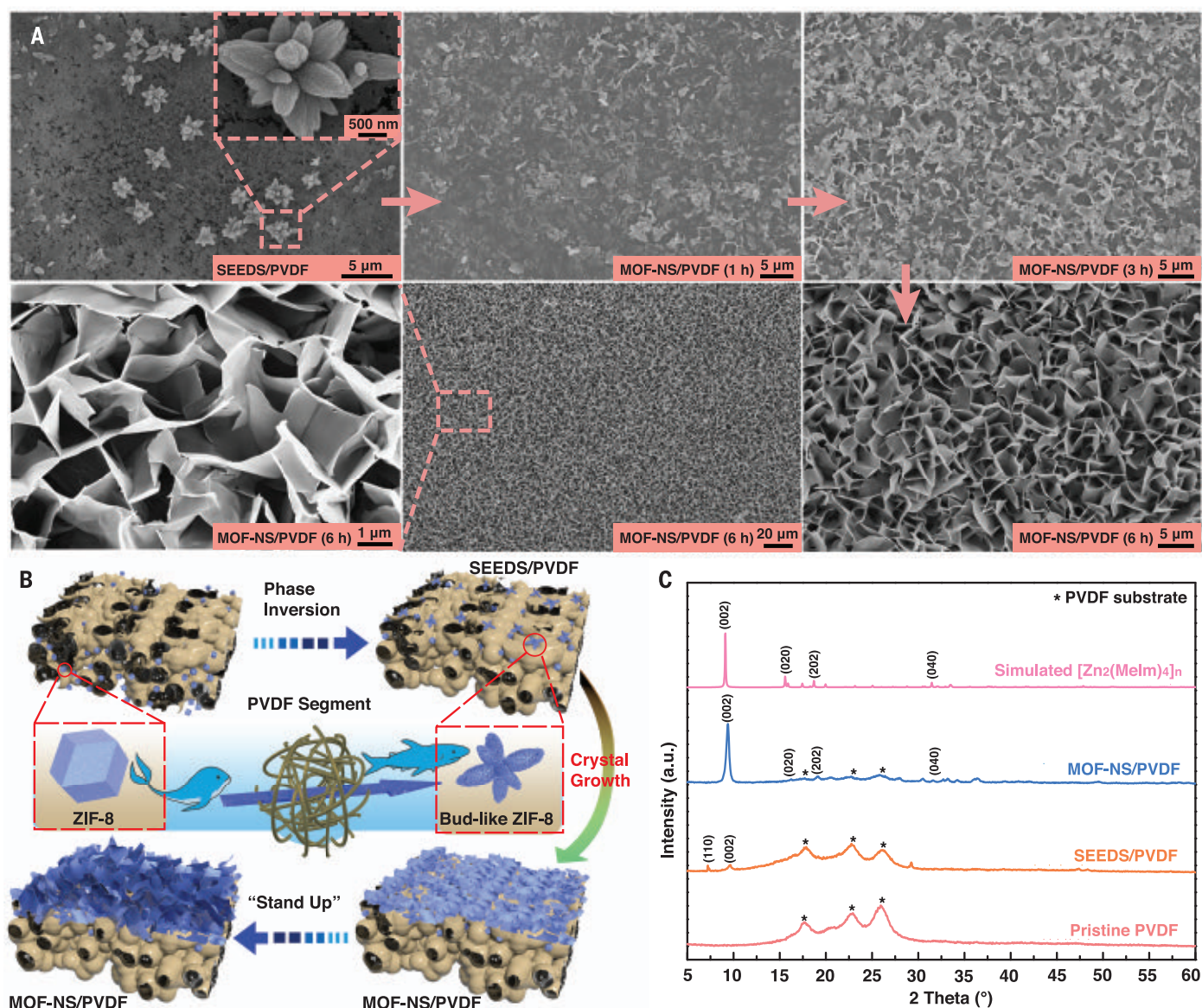


Fig. 1. Preparation protocols and structures of the MOF-NS/PVDF membrane. (A) Surface morphologies of the membranes (evolution of surface morphology during the growth process from SEEDS/PVDF substrate to MOF-NS/PVDF). (B) Schematic of the membrane fabrication process for SEEDS/PVDF and MOF-NS/PVDF. (C) XRD patterns of the pristine PVDF, SEEDS/PVDF, MOF-NS/PVDF, and simulated $[Zn_2(Melm)_4]_n$ membranes.

still dominated by the polymer matrix. Besides MMMs, applications of substrate-supported heteroepitaxial MOF membranes in liquid separation are limited (12, 13). Ineffective control over crystal growth and defects caused unsatisfactory separation performances (12). Inorganic discs and metal mesh are the most reported substrates for MOF membranes, but they can hardly be scaled up. Polymeric substrates with good processability are preferred for mass production (14). Moreover, oriented two-dimensional MOF nanosheet (MOF-NS) membranes usually show promising separation performances compared with that of three-dimensional MOF membranes (15). However, controlled growth of MOF nanosheets on

polymeric substrates is challenging owing to the conflation between rigid MOFs and flexible substrates.

We report a strategy to fabricate MOF-NS membranes with excellent flexibility and permselective properties. The MOF-NS membranes possess a faveolate structure, which provides large specific surface area with high roughness and fast molecular transport channels. After facile polydimethylsiloxane (PDMS) coating, the resultant defect-free superhydrophobic membranes demonstrate ultrafast pervaporation performances in alcohol-water separation.

Polyvinylidene fluoride (PVDF) is a commonly used inert substrate material for pervapo-

ration membranes. In this work, we prepared a PVDF substrate with purposely embedded ZIF-8 seeds to enable subsequent MOF-NS growth on a membrane surface (ZIF, zeolitic imidazolate framework). The seeded PVDF membrane (SEEDS/PVDF) was prepared with PVDF solution containing ZIF-8 seeds by means of immersion precipitation. ZIF-8 seeds are enriched on the surface of SEEDS/PVDF (Fig. 1A and fig. S1). Unlike the reported bud-shaped ZIF-8 (16), a shape transformation of ZIF-8 from rhombic dodecahedron (fig. S2) to a bud-like shape (Fig. 1A) occurred, which may be the result of the strong shear force exerted to ZIF-8 during the membrane formation process (Fig. 1B) (17). X-ray diffraction (XRD)

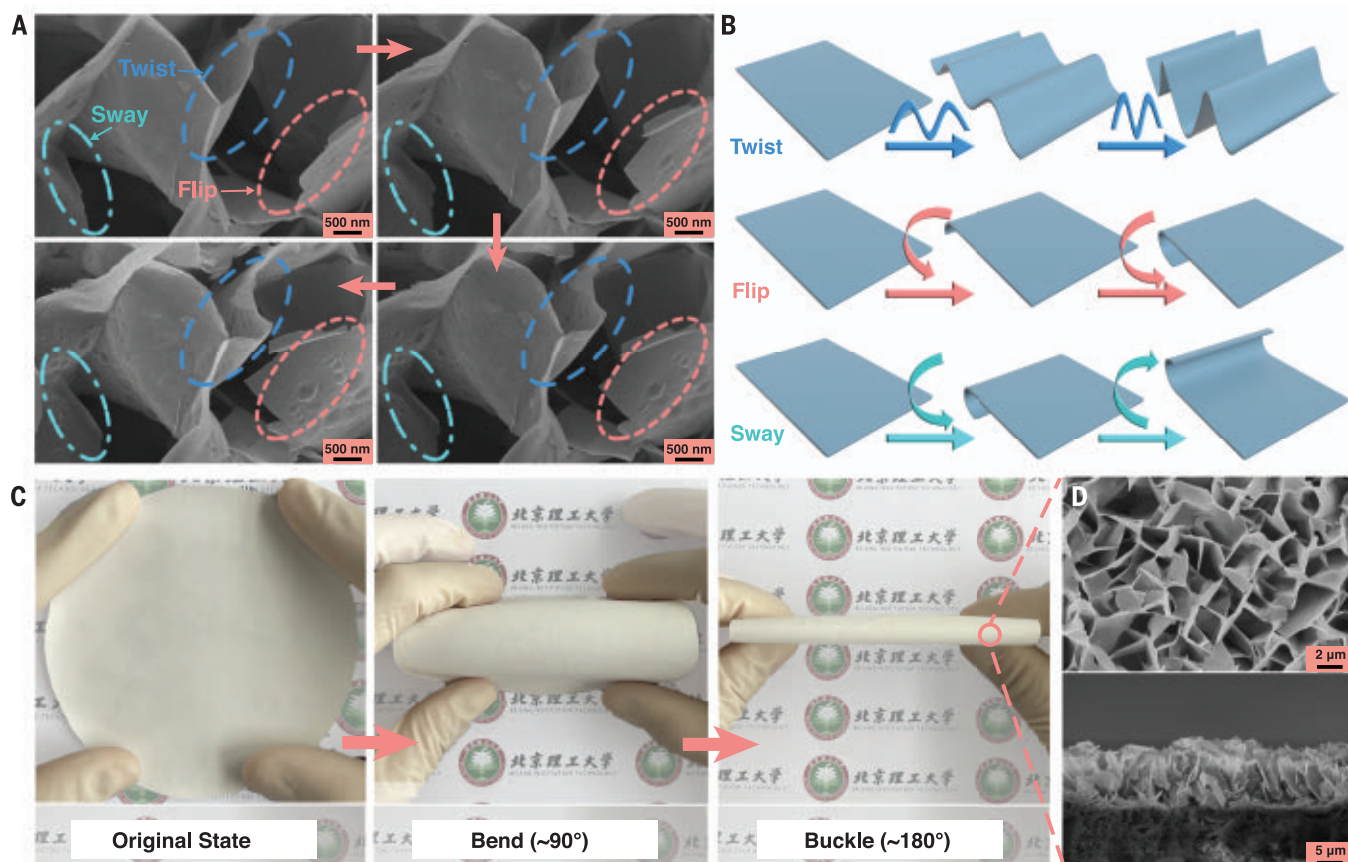
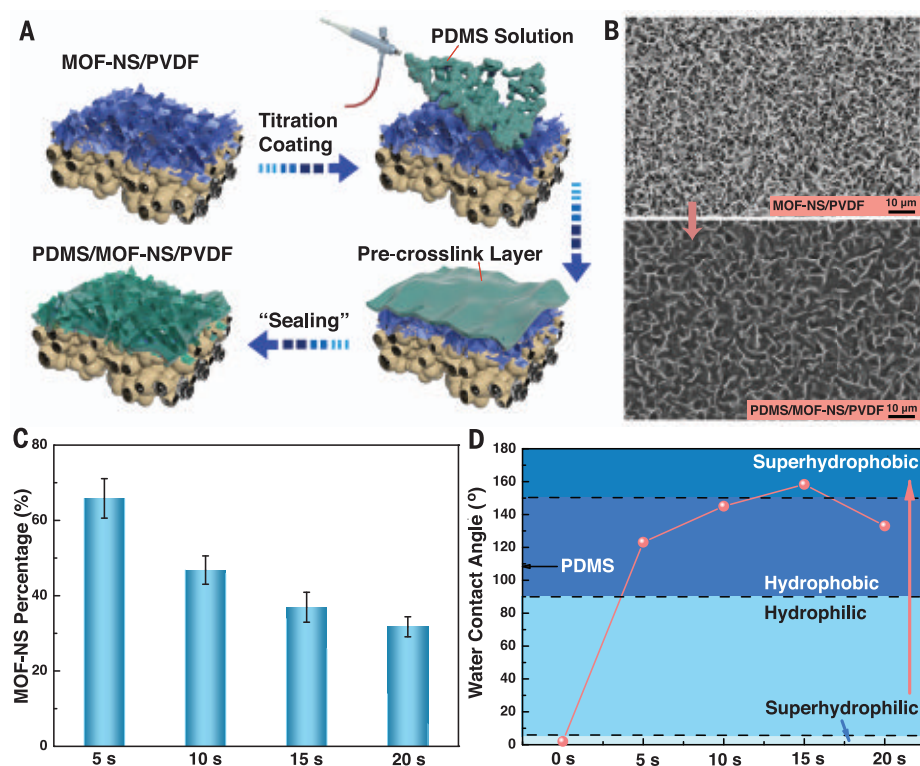


Fig. 2. Highly flexible structure of MOF-NS/PVDF membrane. (A) SEM images of morphology variations of MOF-NS/PVDF under electron beam bombardment. (B) Illustration of the reversible deformations. (C) Bending resistance test of MOF-NS/PVDF. (D) Surface and cross-section morphologies of MOF-NS/PVDF after bending resistance test.

Fig. 3. Titration coating protocols, structures, and surface characteristics of the PDMS-modified MOF-NS/PVDF membrane. (A) Schematic of titration coating. (B) Surface morphologies of MOF-NS/PVDF and PDMS/MOF-NS/PVDF-15s. (C) MOF-NS percentage in the composite layer with different titration coating time. (D) Surface hydrophilicity and hydrophobicity of MOF-NS/PVDF and PDMS/MOF-NS/PVDF membranes with different titration coating time.



showed that a new diffraction peak ($\sim 9.4^\circ$) appeared in the curve of SEEDS/PVDF (Fig. 1C) that corresponds to the peak at 10.5° of ZIF-8 seeds (fig. S3). Moreover, the main peak of ZIF-8 seeds at 7.5° (corresponding to the [011] plane) was retained in SEEDS/PVDF, whereas a red

shift from 7.5° to 7.2° indicates the lattice distortion of ZIF-8 during membrane formation.

The well-distributed bud-like MOF seeds on the SEED/PVDF surface offer heterogeneous nucleation sites for MOF growth. A layer of oriented nanosheets completely covered the

SEED/PVDF substrate (Fig. 1A and fig. S4). The presence of ZIF-8 seeds provides the basis for MOF-NS growth and regulates the growth direction. In comparison, only a few polycrystalline ZIF-8 nanoparticles adhere to the unseeded PVDF substrate (fig. S5). A continuous

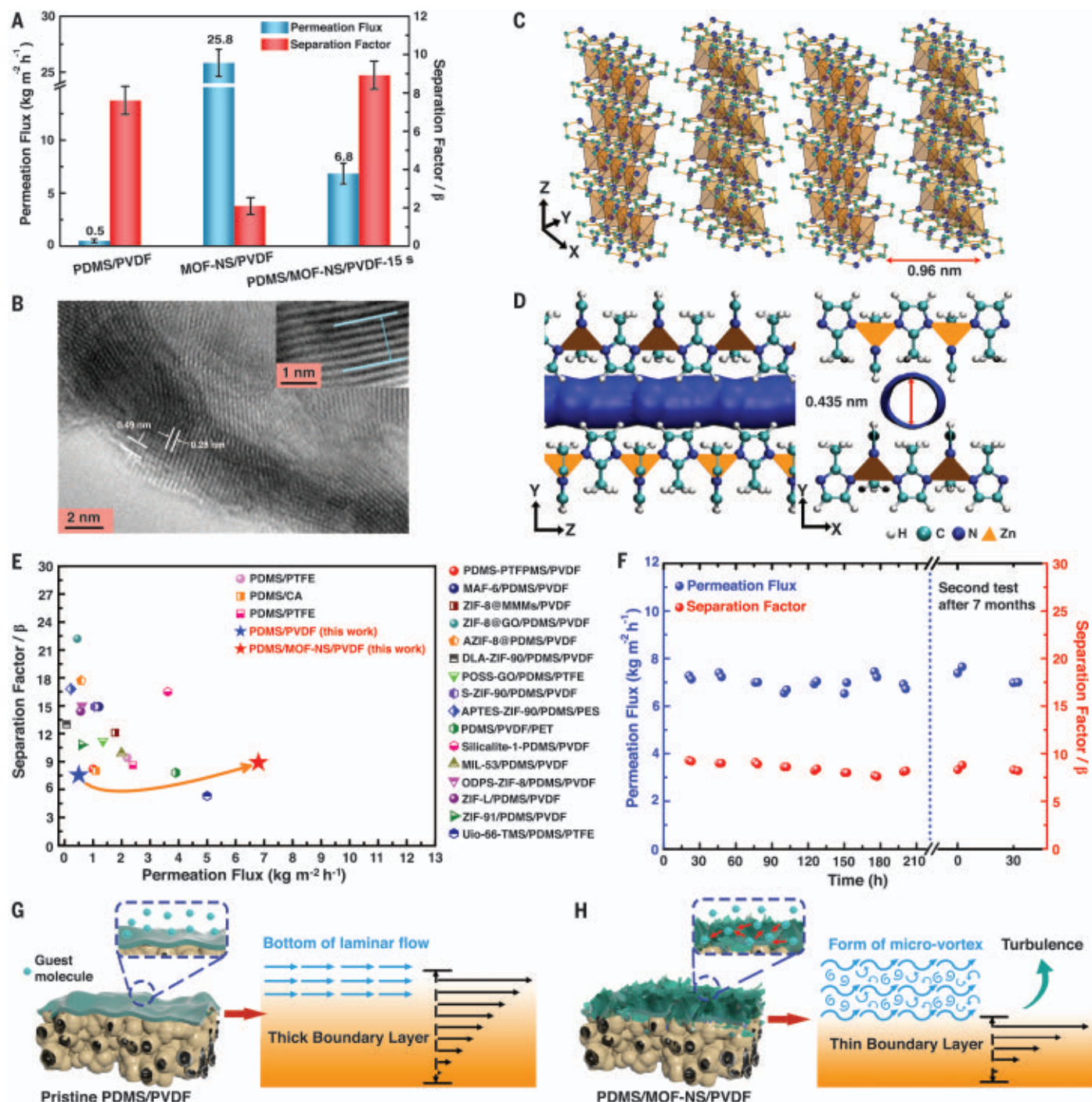


Fig. 4. Pervaporation performances and simulated transport channels of the membranes and the morphology effect on flow behavior of feed. (A) Pervaporation performance for separating 5 wt % ethanol-water solutions at 40°C . (B) HR-TEM images of MOF-NS nanosheets. (Inset) The diffraction from [040] planes within a several-layered nanosheet. (C) Lamellar structure and interlayer channels of MOF-NS. (D) One-dimensional channel and pore diameter of $\text{Zn}_2(\text{Melm})_4$. (E) Separation performance of PDMS/MOF-NS/PVDF-15s (red solid star) compared with other state-of-the-art membranes. (F) Long-term separation performance of PDMS/MOF-NS/PVDF-15s. (G and H) Flow field around the membrane surface for (G) pristine PDMS/PVDF and (H) PDMS/MOF-NS/PVDF.

and uniform MOF-NS/PVDF membrane with a faveolate structure was established after 6 hours. The crystals grew along the direction of the seeds and formed a continuous layer in the horizontal direction initially. When the crystal grew in the in-plane orientation, the growth resistance would be inescapably intensified as the growth time increases, resulting in the growth orientation gradually changing to the low-resistance vertical direction, which agrees with the Van der Drift competitive growth theory (18, 19). The thickness of MOF-NS/PVDF membranes increased stepwise (fig. S6).

The sharp epitaxy of the MOF-NS and the cavities created by the vertically grown nanosheets lead to a highly rough membrane surface [surface roughness (R_a) = 275 ± 16 nm] (fig. S7). The XRD peak that occurred in SEEDS/PVDF at about 9.4° is presented in MOF-NS/PVDF (Fig. 1C), implying evolution of the MOF-NS from the ZIF-8 seeds. In contrast to the XRD pattern of ZIF-8 seeds (fig. S3), the MOF-NS/PVDF membrane almost shows only the [002] plane with a layer spacing of 9.6 \AA , indicating a parallel orientation along the c axis perpendicular to the PVDF substrate. The high-resolution transmission electron microscopy (HR-TEM) images (fig. S8) display the laminated structure of MOF-NS and its higher surface crystallinity than that of ZIF-8 (fig. S8, C and D). The lattice fringes with interplanar spacings of 0.28 and 0.49 nm are attributed to the [040] and [202] planes of MOF-NS. The interlayer spacing of ~ 1.0 nm agrees well with the XRD result (fig. S9). The pore characteristics (figs. S10 and S11) demonstrate decreased surface area and pore volume of MOF-NS than those of ZIF-8 seeds, which is generally observed in the morphological changes of MOFs from three-dimensional to two-dimensional (20).

Density functional theory (DFT) calculations show that the crystal structure consists of a $[\text{Zn}_2(\text{MeIm})_4]_n$ grid-like plane and interlamellar spacing (fig. S12). The XRD of simulated $[\text{Zn}_2(\text{MeIm})_4]_n$ corroborates the measured data (Fig. 1C). The Zn-OH bonding (figs. S13 and S14) can form competitive coordination effects between hydroxyl and imidazole groups. Furthermore, the hydrogen bonding interactions between hydroxyl groups and N-H of imidazole in MOF-NS facilitate the formation of lamellar structures and lead to the faveolate structure (21).

The MOF-NS/PVDF membrane possesses excellent flexibility. Reversible deformations of the MOF-NS layer were captured with scanning electron microscopy (SEM) (Fig. 2A and movie S1). The vertically grown direction with the soft configuration enables the nanosheets to deform when exposed to the high-power electron beam. We observed three types of deformation: flip, twist, and sway (Fig. 2B).

The nanosheets were intactly anchored to the substrate by the preembedded ZIF-8 seeds during the deformation process. This phenomenon does not exist in the bulk-type pure MOF membranes or the MMMs. Moreover, regardless of bending or buckling (Fig. 2C), no morphological change was observed on the surface or cross-section (Fig. 2D), proving the overall flexibility of the membrane.

The performance of pervaporation membranes is mainly influenced by two factors: the differences in solubility of guest molecules into membrane surface and the diffusion rate of guest molecules in membrane matrix. We used a convenient titration coating to seal molecular-scale defects on the MOF-NS/PVDF and construct a dual-functional membrane with superhydrophobicity and internal fast molecular diffusion pathways (Fig. 3A). PDMS is a hydrophobic material that preferentially dissolves alcohols over water molecules. PDMS/MOF-NS/PVDF membranes were produced by tuning PDMS-coating conditions (figs. S15 to S17).

Rough surface morphology of the MOF-NS/PVDF membrane remains when the titration coating duration does not exceed 15 s (Fig. 3B and figs. S18 and S19). The membrane surface is evenly covered by PDMS, whereas the shape of nanosheets is still visible. As the coated PDMS increases with titration time, the MOF-NS percentage in the composite layer decreases (Fig. 3C). This strategy of first growing MOFs on PVDF substrate followed by PDMS coating could achieve uniformly distributed and highly loaded fillers in the polymer.

The high roughness of MOF-NS/PVDF causes a nearly zero water contact angle (Fig. 3D and movie S2). The contact angle reaches 158.3° with 15-s titration coating (PDMS/MOF-NS/PVDF-15s), demonstrating superhydrophobicity (fig. S20 and movie S3), which is much greater than that of the PDMS/PVDF membrane (108.0°). This composite membrane has a higher affinity toward ethanol than water (fig. S21), which is preferred in organophilic pervaporation. A prolonged coating time leads to PDMS completely covering the MOF-NS, debasing the structural advantages.

Compared with pristine PDMS/PVDF (flux, $0.5 \text{ kg}\cdot\text{m}^{-2}\cdot\text{hour}^{-1}$; separation factor, 7.6), MOF-NS/PVDF exhibits an ultrahigh flux ($25.8 \text{ kg}\cdot\text{m}^{-2}\cdot\text{hour}^{-1}$) but a low separation factor (2.1) because of the molecular-scale defects (Fig. 4A). The MOF-NS with high surface crystallinity are composed of a $[\text{Zn}_2(\text{MeIm})_4]_n$ grid-like plane and vertical interlamellar spacing of 9.6 \AA (Fig. 4, B and C). The pore diameter of MOF-NS interlamination calculated from DFT is about 4.2 to 4.4 \AA (Fig. 4D and fig. S22), which leads to confined mass transfer of ethanol (dynamic diameter, 4.4 \AA). The flexible aperture of imidazole could increase the window size (22), and the flopping motion of ligands allows ethanol molecules to diffuse

effectively (movie S4). The vertically oriented flow channels (Fig. 4C) align with the flow direction of guest molecules, reducing the transportation resistance. The sealed PDMS/MOF-NS/PVDF-15s exhibits a total flux of $6.8 \text{ kg}\cdot\text{m}^{-2}\cdot\text{hour}^{-1}$, which is 12.6 times higher than that of pristine PDMS/PVDF and a slight increase in the separation factor (8.9) (Fig. 4A and fig. S23). It exhibits notably improved flux in comparison with other state-of-the-art polymeric substrate-supported membranes (Fig. 4E and table S1).

The performance tests (Fig. 4F and fig. S24) demonstrate membrane's structural stability and durability. PDMS prevents excessive scour of the feed on MOF-NS. The constructed structure of PDMS/MOF-NS/PVDF is beneficial to pervaporation performance in two ways: (i) The rough surface increases the turbulence of the feed (Fig. 4H), reducing the mass transfer resistance within the boundary layer as well as increasing driving force of molecular transport by mitigating the concentration and temperature polarization phenomena; additionally, the nanostructured superhydrophobic surface could also improve fouling resistance for fermentation broth pervaporation (23). (ii) The rough surface also increases the effective contact area for permeation.

To better analyze the transport mechanism, we tested the membranes for *n*-butanol-water separation (fig. S25). Because of the preferential absorption and swelling of PDMS for butanol over ethanol, the flux of PDMS/PVDF in *n*-butanol-water separation ($1.0 \text{ kg}\cdot\text{m}^{-2}\cdot\text{hour}^{-1}$) is twice the flux in ethanol-water separation ($0.5 \text{ kg}\cdot\text{m}^{-2}\cdot\text{hour}^{-1}$) (11). Meanwhile, the PDMS/MOF-NS/PVDF membrane shows a *n*-butanol-water flux of $9.4 \text{ kg}\cdot\text{m}^{-2}\cdot\text{hour}^{-1}$, which is about 40% higher than the ethanol-water flux ($6.8 \text{ kg}\cdot\text{m}^{-2}\cdot\text{hour}^{-1}$). Because the dynamic diameter of butanol molecules (5.1 \AA) is larger than the calculated pore diameter of MOF-NS's interlamination, butanol molecules would encounter high diffusion resistance when passing through the MOF-NS layer. By contrast, ethanol (4.4 \AA) and water (2.7 \AA) molecules could diffuse through the interlamellar channels more easily. The sieving effect of the MOF-NS layer for butanol leads to the smaller flux increment of PDMS/MOF-NS/PVDF-15s (40%) than that of PDMS/PVDF (100%) and to the decrease of separation factor (26.5 to 12.1).

We used molecular dynamics simulations to reveal the molecular transport mechanism when separating the alcohol-water mixtures with MOF-NS and PDMS/MOF-NS (figs. S26 to S29 and tables S2 to S6). The higher ethanol concentration around the surface of MOF-NS (25.4 mol %) than the bulk feed (2 mol %) indicates that the MOF-NS could preferentially adsorb ethanol from feed owing to the organophilicity of dimethylimidazole (fig. S27), which

enhances the separation of alcohol and water molecules. Ethanol molecules can establish a dynamic equilibrium more quickly in MOF-NS than can butanol molecules—continuous molecular transport channels (fig. S27 and movies S4 and S5). Because of the large dynamic diameter, butanol molecules are subjected to greater resistance as they pass through the MOF-NS (fig. S27, first 5 ns of density distribution). The free-energy barrier required for molecular diffusion is butanol > ethanol > water (fig. S28), which leads to the higher residence time of butanol (9.56 ns) in MOF-NS than ethanol (5.04 ns) and water (0.28 ns) (fig. S29). This corroborates the sieving effect of the MOF-NS layer to butanol molecules. Although water molecules diffuse faster in the initial transport pathways, the presence of organic molecules would inhibit the continuous diffusion of water in MOF-NS, especially for butanol-water. “Molecule queuing” was distinctly observed in the MOF-NS system (fig. S29), which was not found in the PDMS/MOF-NS system. Alcohol or water molecules can avoid the water-alcohol coupling effect (24) because of the screening effect by PDMS when passing through the MOF-NS. The simulation results confirm the synergistic contribution of PDMS and MOF-NS to the superior pervaporation performance.

REFERENCES AND NOTES

1. K. A. Thompson *et al.*, *Science* **369**, 310–315 (2020).
2. B. Van der Bruggen, *Nat. Rev. Chem.* **5**, 217–218 (2021).
3. S. Karan, Z. Jiang, A. G. Livingston, *Science* **348**, 1347–1351 (2015).
4. Y. Liao *et al.*, *Science* **367**, 1385–1390 (2020).
5. N. Petzetakis *et al.*, *Nat. Commun.* **6**, 7529 (2015).
6. J. Baeyens *et al.*, *Pror. Energy Combust. Sci.* **47**, 60–88 (2015).
7. X. Chen *et al.*, *Adv. Mater.* **32**, e2002320 (2020).
8. H. Furukawa, K. E. Cordova, M. O’Keeffe, O. M. Yaghi, *Science* **341**, 1230444 (2013).
9. Z. Jiang *et al.*, *Nature* **586**, 549–554 (2020).
10. H. Furukawa *et al.*, *Science* **329**, 424–428 (2010).
11. L.-H. Xu *et al.*, *J. Mater. Chem. C* **9**, 11853–11862 (2021).
12. X. Li *et al.*, *Chem. Soc. Rev.* **46**, 7124–7144 (2017).
13. M. S. Denny Jr., J. C. Moreton, L. Benz, S. M. Cohen, *Nat. Rev. Mater.* **1**, 16078 (2016).
14. Y. Zhao *et al.*, *J. Am. Chem. Soc.* **142**, 20915–20919 (2020).
15. Y. Peng *et al.*, *Science* **346**, 1356–1359 (2014).
16. J. B. James, Y. S. Lin, *J. Phys. Chem. C* **120**, 14015–14026 (2016).
17. X. Wang *et al.*, *Nat. Commun.* **8**, 14460 (2017).
18. Y.-S. Li *et al.*, *Adv. Mater.* **22**, 3322–3326 (2010).
19. Y. Sun *et al.*, *Angew. Chem. Int. Ed.* **57**, 16088–16093 (2018).
20. H. Fu, Z. Wang, X. Wang, P. Wang, C.-C. Wang, *CrystEngComm* **20**, 1473–1477 (2018).
21. H. Zhang, M. Zhao, Y. Yang, Y. S. Lin, *Microporous Mesoporous Mater.* **288**, 109568 (2019).
22. D. Fairen-Jimenez *et al.*, *J. Am. Chem. Soc.* **133**, 8900–8902 (2011).
23. F. S. Kameliani, T. Mohammadi, F. Naeimpoor, M. Sillanpää, *ACS Appl. Mater. Interfaces* **12**, 56587–56603 (2020).
24. S. Liu *et al.*, *AIChE J.* **67**, aic17170 (2021).

ACKNOWLEDGMENTS

The authors are grateful to the Analysis and Testing Center at Beijing Institute of Technology, Beijing, China, for research support.

Funding: This work was supported by the Natural Science Foundation of China (21736001), National Key Research and Development Program of China (2021YFC2101203), and Beijing Institute of Technology Research Fund Program for Young Scholars.

Author contributions: Conceptualization: L.-H.X. and Z.-P.Z. Methodology: L.-H.X. and S.-H.L. Investigation: L.-H.X., Y.L., J.L., W.-W.X., C.P., and Z.-Z.L. Visualization: L.-H.X., H.M., Y.L., A.-S.Z., S.W., and W.-M.L. Project administration: Z.-P.Z., T.W., Y.-N.F., W.-W.C., and L.S. Supervision: Z.-P.Z. Writing – original

draft: L.-H.X. and S.-H.L. Writing – review and editing: L.-H.X., S.-H.L., H.M., Y.-N.F., and Z.-P.Z. **Competing interests:** Z.-P.Z., L.-H.X., Y.-N.F., and H.M. are inventors on a Chinese patent application (202111014312.4) submitted by the Beijing Institute of Technology. **Data and materials availability:** All data are available in the manuscript or the supplementary materials. **License information:** Copyright © 2022 the authors, some rights reserved; exclusive licensee American Association for the Advancement of Science. No claim to original US government works. <https://www.science.org/about/science-licenses-journal-article-reuse>

SUPPLEMENTARY MATERIALS

science.org/doi/10.1126/science.abo5680
Materials and Methods
Figs. S1 to S29
Tables S1 to S6
References (25–69)
Movies S1 to S5

Submitted 11 February 2022; accepted 24 August 2022
10.1126/science.abo5680

MARINE CONSERVATION

Spillover benefits from the world’s largest fully protected MPA

Sarah Medoff¹, John Lynham^{2*}, Jennifer Raynor³

Previous research has cast doubt on the potential for marine protected areas (MPAs) to provide refuge and fishery spillover benefits for migratory species as most MPAs are small relative to the geographic range of these species. We test for evidence of spillover benefits accruing from the world’s largest fully protected MPA, Papahānaumokuākea Marine National Monument. Using species-specific data collected by independent fishery observers, we examine changes in catch rates for individual vessels near to and far from the MPA before and after its expansion in 2016. We find evidence of spillover benefits for yellowfin (*Thunnus albacares*) and bigeye tuna (*Thunnus obesus*).

A number of governments around the world (including the USA) have committed to protecting 30% of their ocean territory by the year 2030 (1). Although the definition of protection varies across (and sometimes within) countries, achieving this goal will require the creation of new marine protected areas (MPAs): spatial zones in the ocean where activities such as fishing or mining are strictly controlled or prohibited (2). Part of the debate surrounding MPA impacts is the degree to which the cost of lost fishing grounds may be offset by the recovery and subsequent spillover of fish populations beyond the boundaries of an MPA (3). We define a spillover benefit as the recovery of a previously fished species within a protected area combined with some movement of the recovered population beyond the boundaries of the protected area, resulting in a higher catch rate of the species near the protected area than what would have been observed if the protected area had not been created.

There are several reasons why spillover benefits have been hard to detect. First, ocean ecosystems are complex and dynamic (4, 5). Many factors that affect the abundance and location of fish species are changing concur-

rently with the creation of MPAs (6). Second, marine protected areas lead to changes in human behavior that may exaggerate or mask spillover effects, as most analyses rely on data derived from human activities (7). Third, most marine protected areas are relatively new and more time may be needed for populations to recover to the point that a spillover benefit is generated. For example, over 95% of the area contained in MPAs in the USA received protection only within the last 20 years (8). Finally, spillover benefits may not be detected simply because they are not occurring (9).

The aim of this study is to identify whether spillover benefits have accrued from the world’s largest fully protected MPA, the Papahānaumokuākea Marine National Monument (PMNM) surrounding the northwest Hawaiian islands. We use the term “fully protected” to describe an MPA that prohibits extractive or other destructive activities, in line with *The MPA Guide* (2). The northwest Hawaiian islands have long been recognized for their conservation value. In 1909, a small area was designated as a refuge for seabird nesting colonies. In 2006, US President George W. Bush expanded this area, making it the largest MPA in US waters (at 360,000 km²), and renamed it Papahānaumokuākea Marine National Monument (10). On 26 August 2016, President Barack Obama further expanded the reserve’s boundaries, thereby establishing the largest, contiguous reserve within a single national jurisdiction in the world (at 1,510,000 km²; see Fig. 1A). Our analysis focuses on the 2016 expansion.

¹Cooperative Institute for Marine and Atmospheric Research, School of Ocean and Earth Science and Technology, University of Hawai‘i at Mānoa, Honolulu, HI, USA.

²Department of Economics and UHERO, University of Hawai‘i at Mānoa, Honolulu, HI, USA. ³Department of Forest and Wildlife Ecology, University of Wisconsin-Madison, Madison, WI, USA.

*Corresponding author. Email: lynham@hawaii.edu

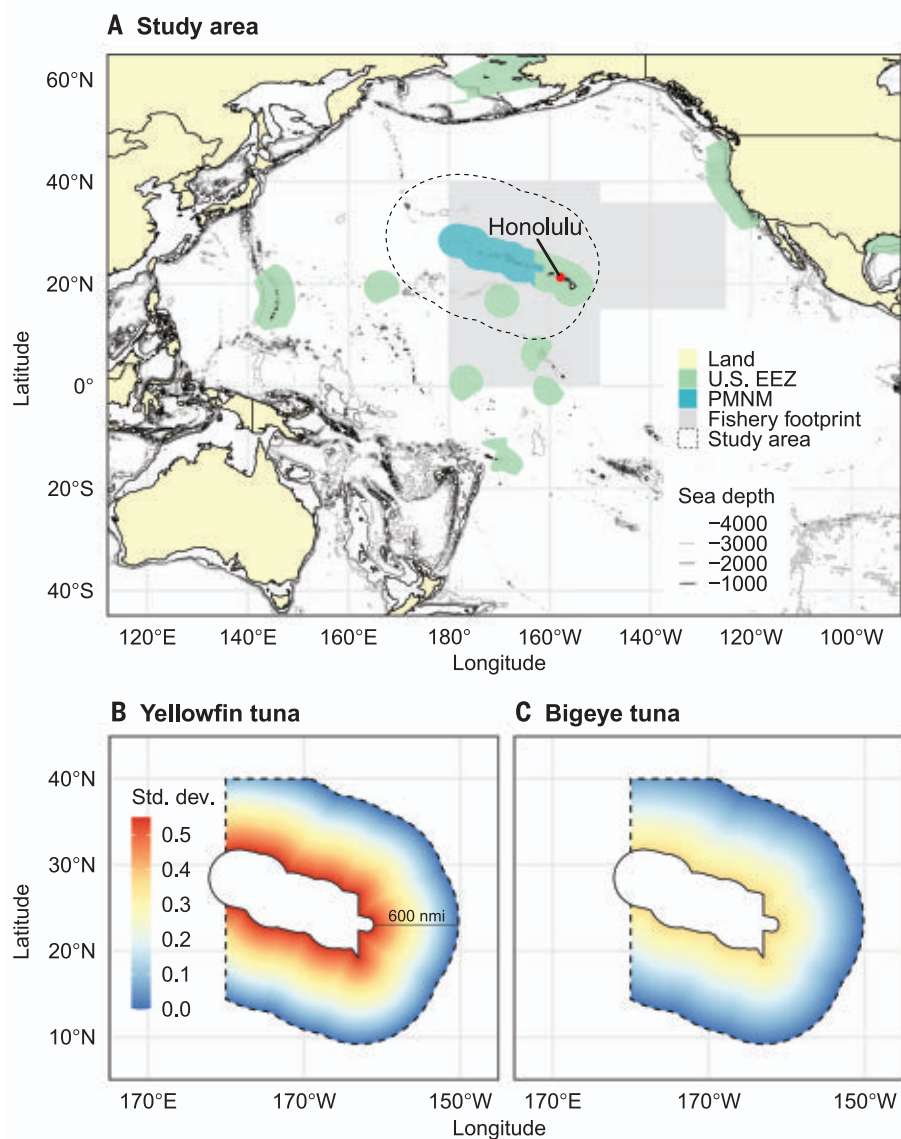


Fig. 1. Increase in standardized CPUE over 1-nmi increments from the PMNM border. (A) Map of PMNM surrounding the northwest Hawaiian islands. The exclusive economic zone (EEZ) is an area of coastal water and seabed within 200 nmi of a country's coastline, to which the country claims exclusive rights for fishing, drilling, and other economic activities. PMNM is part of the U.S. EEZ. Fishery footprint refers to the full spatial extent of Hawai'i-based deep-set longline fishing activity during the study period (2010 to 2019). The study area comprises a 600-nmi buffer around the PMNM. (B and C) Difference between pre- and post-expansion standardized CPUE within the study area; units are the number of standard deviations above the mean value of pre-expansion standardized CPUE and the spatial extent is the part of the study area within the fishery footprint.

Our approach follows the “gold standard” proposed by (11) for testing for the presence of a spillover benefit from an MPA: “did a particular vessel deploying a particular type and quantity of gear catch more in an area near the reserve after formation of the reserve than it would have caught had the reserve never been established?” (p. 154). This approach specifically accounts for changes in fishing effort across space which may create the false impression that spillover benefits are occurring—

an increase in total catch [or even catch per unit effort (CPUE)] near the boundary of an MPA could be caused by greater fishing intensity or more efficient vessels fishing there, and not necessarily by an increase in fish abundance. The gold standard approach holds fishing effort and fishing efficiency as fixed. This approach also controls for time-invariant spatial heterogeneity that may cause differences in catch rates across space (such as the presence of seamounts).

Testing for the presence of a spillover benefit requires spatiotemporal data on catch by species, fishing locations, vessel characteristics, and gear configurations. Our primary data source is the National Marine Fisheries Service Pacific Islands Region Observer Program, which collects detailed information on catch and fishing effort for the Hawaii-based, limited-entry, longline fishery (12). We focus on the deep-set segment of the longline fleet, which primarily targets bigeye (*Thunnus obesus*) and yellowfin (*Thunnus albacares*) tuna and accounts for the vast majority (97 to 99%) of US longline fishing activity in this region (13). Bigeye and yellowfin tuna have life expectancies of around 7 years and reach reproductive maturity at age 2 or 3 (14, 15) but recent evidence from the Eastern Pacific suggests that yellowfin tuna are maturing earlier and at smaller sizes (16). The Hawaii-based longline fishery accounts for most fishing activity within 300 nautical miles (nmi) of the MPA, according to data provided by Global Fishing Watch (17) (table S1). Because the PMNM expansion took place in 2016, we restricted our main analysis to observations since 2010.

In accordance with (11), we tested for spillover benefits based on distance from the PMNM border. We defined regions that are “near” to versus “far” from the border. We defined a near region as one that extends $(0, x]$ nmi from the monument border and a far region that extends $(x, 2x]$ nmi from the monument border. We set x to be 100, 200, and 300 because these radii have a convenient interpretation. The MPA extends exactly 200 nmi from land, so these buffers translate to 0.25, 0.5, and 0.75 times the “diameter” of the monument. The amount of historical fishing effort in each of these zones (and inside the MPA prior to closure) is summarized in table S2 and fig. S1.

We start by examining spatial and then temporal trends in CPUE near to and far from the MPA boundary, with CPUE defined as fish per 1000 hooks. To examine spatial patterns, we first calculated how CPUE changes as a function of distance from the monument boundary; we did this separately for the pre- and post-expansion time periods. We then calculated the difference between pre- and post-expansion CPUE as a function of distance from the monument, after accounting for any overall change in CPUE post expansion (12). The results are shown in Fig. 1, B and C. The color scale represents the number of standard deviations away from the mean value of pre-expansion CPUE for each species. The results are suggestive of a spillover benefit for bigeye tuna and yellowfin tuna, with a stronger effect for the latter as CPUE for yellowfin increases by ~0.55 standard deviations as a vessel moves 600 nmi closer to the monument boundary.

Next, we examine temporal patterns in CPUE for the 100-, 200-, and 300-nmi region radius

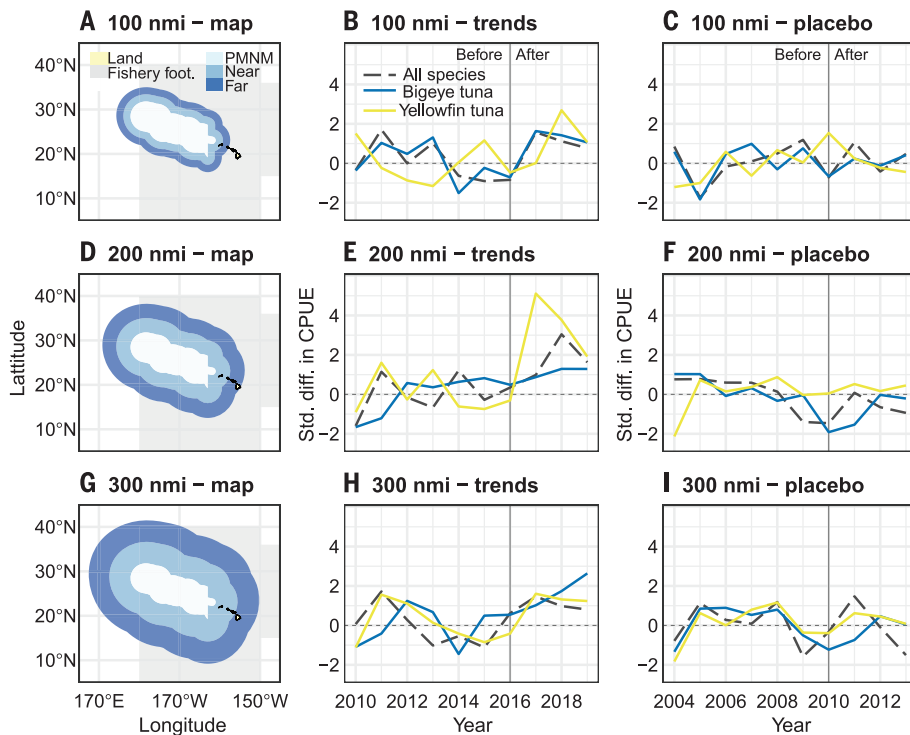


Fig. 2. Standardized difference in CPUE between regions near to and far from the PMNM. The near region extends $(0, x]$ nmi from the monument border and the far region extends $(x, 2x]$ nmi from the monument border, with x equal to 100, 200, and 300 in rows 1, 2, and 3, respectively. Fishery footprint (fishery foot) refers to the full spatial extent of the Hawai'i-based deep-set longline fishery during the study period (2010 to 2019). (A, D, and G) Maps for each radius. (B, E, and H) Standardized differences between pre- and post-expansion CPUE over time. (C, F, and I) Standardized differences in CPUE before and after a monument expansion time placebo date (2010). For (B) and (C), (E) and (F), and (H) and (I), negative values indicate that CPUE was higher in the far area whereas positive values indicate CPUE was higher in the near area.

specifications (Fig. 2, A, D, and G). For each year in the sample, we calculated the difference between CPUE for the near and far regions for each species (and for all fish species combined). We then standardized each time series based on its pre-expansion moments (subtract the pre-expansion mean and divide by the pre-expansion standard deviation of the difference in CPUE). The results are shown in the second column of Fig. 2, B, E, and H. The vertical axis for each graph represents the number of standard deviations away from the pre-expansion mean difference in CPUE. If the difference in CPUE between the near and far regions remains the same following expansion of the monument (i.e., there is no suggestive evidence of a spillover benefit), then each time series would fluctuate around zero. By contrast, if catch rates increase in the near region more than in the far region (i.e., there is suggestive evidence of a spillover benefit) then each time series will rise above zero. For each species grouping we observe suggestive evidence of a spillover benefit—CPUE is increasing in the near region relative to the far region following monument expansion. The spillover benefit appears strongest for yellowfin tuna,

especially for the 100- and 200-nmi region radii. Differences in catch rates for bigeye tuna become more apparent with the 300-nmi radius. For example, by 2019 the difference in CPUE for bigeye tuna between the near and far regions was more than 2 standard deviations larger than the pre-expansion mean difference.

To quantify the effects of the monument expansion on CPUE more precisely and to control for other confounding factors and possible selection bias, we developed a species-specific difference-in-differences linear regression model. We tested the null hypothesis that there was no spillover benefit using the approach proposed by (11). We used three model specifications, each imposing additional layers of control variables. The first model is a basic difference-in-differences setup (baseline). The second model adds month-year and vessel fixed effects (time-vessel fixed effects). The final and most restrictive model adds controls related to gear configurations, which can affect catch rates (gear controls). The outcome variable for each model is catch per 1000 hooks for each species or species group, standardized by its pre-expansion mean and stan-

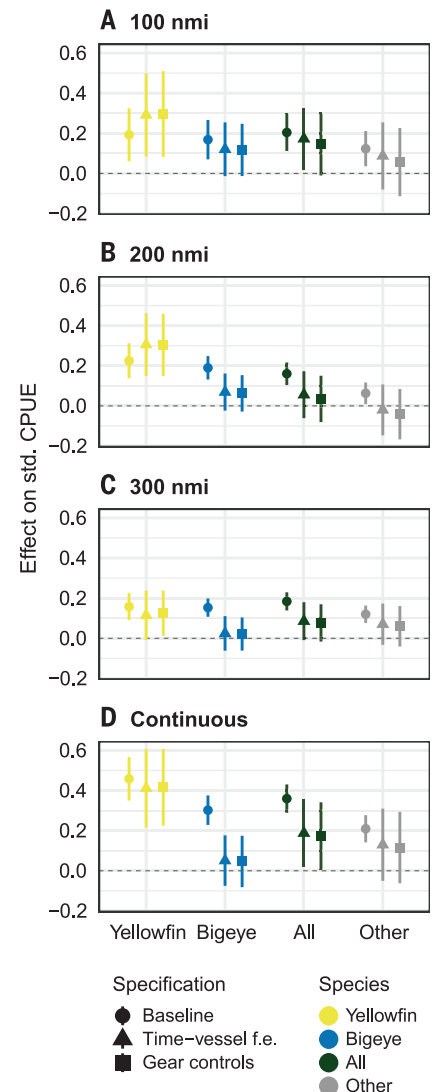


Fig. 3. Coefficient estimates for the effect of the monument expansion on CPUE. (A to C) Results for the 100 nmi, 200 nmi, and 300 nmi specifications, respectively. (D) Results for the continuous distance specification. Results are scaled such that the estimated coefficient represents the effect of moving 500 nmi closer to the boundary of the monument. Symbols indicate point estimates and lines indicate 95% confidence intervals constructed using White heteroskedasticity-robust standard errors.

dard deviation. This allows for easy comparisons across species and species groups. The estimated difference-in-differences coefficients represent the change in CPUE as a result of the monument expansion, measured in standard deviations above or below the mean value of pre-expansion CPUE. Results are summarized in graphical form in Fig. 3 and in tables S3 to S5. We also show the mean and standard deviation for baseline pre-expansion CPUE, as well as the results using raw CPUE (number of

fish caught per 1000 hooks) for the time-vessel fixed effects (preferred) model in table S6.

Across specifications and species, we consistently estimate positive spillover benefits from the monument expansion on CPUE. Focusing on the time-vessel fixed effects (preferred) model (table S4) and the 100-nmi near region, the monument expansion leads to an increase of 0.12 standard deviations in CPUE ($P < 0.1$) for bigeye tuna, 0.291 for yellowfin tuna ($P < 0.01$), and 0.173 for all species ($P < 0.05$). This is equivalent to an increase of 0.5 bigeye tuna per 1000 hooks (with a pre-expansion mean of 4.3 fish per 1000 hooks), 0.6 yellowfin per 1000 hooks (with a pre-expansion mean of 1 fish per 1000 hooks), and 1.9 fish of any species per 1000 hooks (with a mean value of 23.6 fish pre expansion). See table S6 for the same calculations for the 200- and 300-nmi specifications.

To deal with the possibility that the chosen region-radii specifications (100, 200, and 300 nmi) could be biasing our analysis in favor of finding a positive spillover effect, we also use a continuous distance measure instead of a binary near or far indicator as our treatment variable. By interacting the continuous distance variable with a dummy variable for the post-expansion period (and multiplying by -1), we estimate the change in CPUE of moving closer to the current monument boundary following monument expansion. We estimate this model with the same sets of covariates used in the region-radii specifications above. Results are summarized in graphical form in Fig. 3D (for a movement of 500 nmi) and in tables S3 to S5 (for a movement of 1000 nmi). Across the three specifications, as a fishing vessel moves closer to the monument border (following the expansion of the monument in 2016) CPUE increases for both bigeye tuna and yellowfin tuna. For example, for the baseline specification for yellowfin tuna, moving 1000 nmi closer to the monument results in a 0.92-standard deviation increase in CPUE. For bigeye tuna, the coefficient estimate is only statistically significant for the baseline specification (0.6 standard deviations); the estimate is always statistically significant for yellowfin tuna ($P < 0.01$). The implications of the baseline coefficient estimates are visualized in Fig. 1, B and C.

To test the robustness of our findings, we explored whether the data source affects the results. In addition to the data collected by National Marine Fisheries Service observers, CPUE in this region can also be derived from captains' logbooks. We reconstruct the region-radii and continuous distance specifications explained above for the time-vessel fixed effects (preferred) model using logbook data (tables S7 and S8). The results using logbook data are consistent with the previous results except that we now see stronger evidence of a spillover benefit for bigeye tuna [it is

statistically significant ($P < 0.05$) in all specifications]. A common robustness check in analyses of the type presented here is to apply the same methodology in a setting or subset of the data where the expectation is that no effect will be detected—in other words, a placebo test. We conducted a series of temporal placebo tests (12), altering the start date of the MPA expansion to be in 2010 instead of 2016 (column 3 of Fig. 2, C, F, and I). These placebo tests failed to detect a statistically significant spillover benefit for bigeye or yellowfin tuna (table S9). Finally, to encourage easy replication, refinement, and criticism of our results, we demonstrate that the general pattern of our findings can be replicated using a non-confidential but aggregated version of the logbook data (fig. S2).

If a large MPA was providing protection to a number of migratory fish species and subsequently providing a spillover benefit beyond its boundaries, one would expect to observe an increase in CPUE near the MPA relative to any changes in CPUE far from the MPA (17). Further, confirmation should be sought that this increase is being observed for the same vessel (or, at the very least, vessels of similar technical efficiency) and not simply because vessels are reallocating their fishing effort across space (6) or altering fishing intensity across space. The increase in CPUE should be most pronounced for species that have experienced heavy fishing pressure (18–20). The spillover effect should be stronger for species that are less migratory, exhibit stronger site fidelity, and have been documented to spawn in or near the MPA (21–25). Finally, the increase should not be immediate but rather should have built up over time (7). We observe all of these signals in the data.

REFERENCES AND NOTES

1. E. Dinerstein et al., *Sci. Adv.* **5**, eaaw2869 (2019).
2. K. Grorud-Colvert et al., *Science* **373**, eabf0861 (2021).
3. S. D. Gaines, C. White, M. H. Carr, S. R. Palumbi, *Proc. Natl. Acad. Sci. U.S.A.* **107**, 18286–18293 (2010).
4. *El Niño Southern Oscillation in a Changing Climate*, M. J. McPhaden, A. Santoso, W. Cai, Eds. (Wiley, 2020), pp. 429–451.
5. C. Heinze et al., *Proceedings of the National Academy of Sciences* **118** (2021).
6. P. J. Ferraro, J. N. Sanchirico, M. D. Smith, *Proc. Natl. Acad. Sci. U.S.A.* **116**, 5311–5318 (2019).
7. R. Hilborn, *Science* **295**, 1233–1235 (2002).
8. R. Richards, "Measuring conservation progress in North America" (Technical report, Center for American Progress, 2018).
9. D. Ovando et al., *Conserv. Biol.* (2021).
10. K. Kikiloi et al., *Coast. Manage.* **45**, 436–451 (2017).
11. M. D. Smith, J. Zhang, F. C. Coleman, *Can. J. Fish. Aquat. Sci.* **63**, 153–164 (2006).
12. See supplementary materials.
13. "Annual Stock Assessment and Fishery Evaluation Report Pacific Island Pelagic Fishery Ecosystem Plan 2020" (Technical report, Western Pacific Regional Fishery Management Council, 2021).
14. NOAA, Pacific Bigeye Tuna (NOAA Fisheries, 2022); <https://www.fisheries.noaa.gov/species/pacific-bigeye-tuna>.
15. NOAA, Pacific Yellowfin Tuna (NOAA Fisheries, 2022); <https://www.fisheries.noaa.gov/species/pacific-yellowfin-tuna>.
16. K. M. Schaefer, D. W. Fuller, *Fish. Res.* **248**, 106225 (2022).
17. D. A. Kroodsma et al., *Science* **359**, 904–908 (2018).

18. R. Hilborn et al., *Ocean Coast. Manage.* **47**, 197–205 (2004).
19. C. D. Buxton, K. Hartmann, R. Kearney, C. Gardner, *PLOS ONE* **9**, e107032 (2014).
20. S. E. Lester et al., *Mar. Ecol. Prog. Ser.* **384**, 33–46 (2009).
21. J. N. Sanchirico, J. E. Wilen, *J. Environ. Econ. Manage.* **42**, 257–276 (2001).
22. C. H. Lam, C. Tam, D. R. Kobayashi, M. E. Lutcevage, *Front. Mar. Sci.* **7**, 138 (2020).
23. R. D. Wells, J. R. Rooker, D. G. Itano, *Mar. Ecol. Prog. Ser.* **461**, 187–196 (2012).
24. D. G. Itano, K. N. Holland, *Aquat. Living Resour.* **13**, 213–223 (2000).
25. J. R. Rooker, R. David Wells, D. G. Itano, S. R. Thorrold, J. M. Lee, *Fish. Oceanogr.* **25**, 277–291 (2016).
26. S. Medoff, J. Lynham, J. Raynor, Spillover Benefits from the World's Largest Fully Protected MPA, Zenodo (2022); <https://doi.org/10.5281/zenodo.7150720>.

ACKNOWLEDGMENTS

We thank the Pacific Islands Fisheries Science Center for data access. S.M. was funded by Cooperative Agreement NA16NMF4320058 between the Joint Institute for Marine and Atmospheric Research and the National Oceanic and Atmospheric Administration (NOAA). The scientific results and conclusions, as well as any views or opinions expressed herein, are those of the authors and do not necessarily reflect the views of NOAA or the Department of Commerce. We sincerely thank D. Lerner and D. Luther (both at University of Hawai'i at Mānoa) for their assistance and support. We also thank D. Kroodsma (Global Fishing Watch) for assisting in the analysis of non-US-flagged fishing activity. J.L. acknowledges the National Science Foundation, specifically grant DISES 2108566, for supporting his work on this project during the summer of 2022. **Funding:** This work was supported by the following: NOAA Cooperative Agreement NA16NMF4320058 (to S.M.); National Science Foundation DISES 2108566 (to J.L.). **Author contributions:** Conceptualization: J.L. Data Curation: J.L. and S.M. Formal analysis: J.L., S.M., and J.R. Investigation: J.L., S.M., and J.R. Methodology: J.L., S.M., and J.R. Project administration: J.L. Software: S.M. and J.R. Supervision: J.L. and J.R. Validation: J.L., S.M., and J.R. Visualization: J.R. Writing – original draft: S.M. Writing – review and editing: J.L., S.M., and J.R. **Competing interests:** S.M. and J.R. declare no competing interests. Within the last 3 years, J.L. has received consulting fees from the Conservation Strategy Fund (CSF) for a research project evaluating the economic impact of the Papahānaumokuākea Marine National Monument. That work was completed in 2019 and published in early 2020: <https://doi.org/10.1038/s41467-020-14588-3>. CSF did not play any role in the present contribution. **Data and materials availability:** All of the code used to produce the figures and statistical analysis in this paper are available at Zenodo (26). The observer and logbook data used in this paper are subject to confidentiality of information requirements under the Magnuson-Stevens Fishery Conservation and Management Act (Magnuson-Stevens Act or MSA) and are not immediately available to the public except in summary aggregate form. Information on requesting access to these data (including details on who to contact) can be found at <https://www.fisheries.noaa.gov/inport/item/9027> (observer data) and <https://www.fisheries.noaa.gov/inport/item/2721> (logbook data). The nonconfidential Western and Central Pacific Fisheries Commission (WCPFC) version of the logbook data is posted on the Zenodo depository referenced above and is also available here: <https://www.wcpfc.int/wcpfc-public-domain-aggregated-catcheffort-data-download-page>. The database provided to us by Global Fishing Watch is available to the general public here: <https://globalfishingwatch.org/>. We have also posted a copy of the database used in the Zenodo depository referenced above. **License information:** Copyright © 2022 the authors, some rights reserved; exclusive licensee American Association for the Advancement of Science. No claim to original US government works. <https://www.sciencemag.org/about/science-licenses-journal-article-reuse>

SUPPLEMENTARY MATERIALS

science.org/doi/10.1126/science.abn0098
Materials and Methods
Supplementary Text
Figs. S1 to S2
Tables S1 to S9
References (27, 28)

Submitted 29 October 2021; accepted 21 September 2022
10.1126/science.abn0098

CELL BIOLOGY

MTCH2 is a mitochondrial outer membrane protein insertase

Alina Guna^{1†}, Taylor A. Stevens^{2†}, Alison J. Inglis^{2†}, Joseph M. Replogle^{1,3,4,5}, Theodore K. Esantsi^{1,5}, Gayathri Muthukumar^{1,6}, Kelly C. L. Shaffer², Maxine L. Wang^{1,2,6}, Angela N. Pogson^{1,5}, Jeff J. Jones², Brett Lomenick^{2†}, Tsui-Fen Chou², Jonathan S. Weissman^{1,5,6,7*}, Rebecca M. Voorhees^{2*}

In the mitochondrial outer membrane, α -helical transmembrane proteins play critical roles in cytoplasmic-mitochondrial communication. Using genome-wide CRISPR screens, we identified mitochondrial carrier homolog 2 (MTCH2), and its paralog MTCH1, and showed that it is required for insertion of biophysically diverse tail-anchored (TA), signal-anchored, and multipass proteins, but not outer membrane β -barrel proteins. Purified MTCH2 was sufficient to mediate insertion into reconstituted proteoliposomes. Functional and mutational studies suggested that MTCH2 has evolved from a solute carrier transporter. MTCH2 uses membrane-embedded hydrophilic residues to function as a gatekeeper for the outer membrane, controlling mislocalization of TAs into the endoplasmic reticulum and modulating the sensitivity of leukemia cells to apoptosis. Our identification of MTCH2 as an insertase provides a mechanistic explanation for the diverse phenotypes and disease states associated with MTCH2 dysfunction.

Mitochondria are organelles of endosymbiotic origin that have evolved to play a central role in eukaryotic cell metabolism and signaling (1). Mitochondrial function and their ability to communicate with the cytosol depend on proteins embedded in the outer mitochondrial membrane. As a result, dysregulation of outer membrane protein function is associated with aging and the pathogenesis of a variety of human diseases including Alzheimer's, Parkinson's, and many cancers (2–4). In mammals, the insertion of α -helical proteins into the outer membrane, a function that would not have been required in the ancestral endosymbiont, remains poorly understood (5). In yeast and trypanosomes the mitochondrial import protein 1 (Mim1) and pATOM36, respectively, have been implicated in this process (6, 7), but no clear homologs exist in mammalian mitochondria. One important class of α -helical outer membrane proteins is tail-anchored proteins (TAs), which are characterized by a single C-terminal transmembrane domain (TMD) and mediate diverse

functions, including apoptosis, innate immunity, and mitochondrial turnover and dynamics. Therefore, we set out to systematically identify and characterize the factors required for mitochondrial TA biogenesis in human cells.

Using an in vitro competition assay, we first showed that TA insertion does not strictly require the TOM complex, the major outer membrane translocase (Fig. 1A and figs. S1 and S2) (8). Therefore, to enable CRISPR-based screens (9), we adapted and validated (Fig. 1B and fig. S3) a split green fluorescent protein (GFP) reporter (10) to measure insertion of the model TA, OMP25, into mitochondria. Among hits that increased mitochondrial integration of OMP25 were the endoplasmic reticulum (ER) membrane protein complex (EMC) and the ubiquilin (UBQLN) chaperone family (Fig. 1C and fig. S4A). These results are consistent with the EMC serving as the major insertase for mislocalized mitochondrial TAs into the ER (fig. S4) (11), and the UBQLNs' role in degrading mislocalized mitochondrial TAs (12), leading to their accumulation in the cytosol (fig. S5).

Conversely, depletion of the outer membrane resident mitochondrial carrier homolog 2 (MTCH2) resulted in the most pronounced loss of OMP25 integration (Fig. 1D and fig. S6A). MTCH2 is a member of the solute carrier 25 (SLC25) family, integral membrane proteins best known for their role in transporting metabolites into the mitochondrial matrix, but its localization and sequence suggest that its function has potentially diverged, and it has no known substrates or transporter activity (13). Further, loss of MTCH2 is associated with a variety of pleiotropic phenotypes, including defects in mitochondrial fusion, lipid homeostasis, and apoptosis (14–16). However, the

underlying biochemical activity of MTCH2 is not known.

Because of the diverse phenotypes attributed to MTCH2, we excluded the possibility that dysregulation of lipogenesis (fig. S6, B and C) (14), the outer membrane, or general mitochondrial protein biogenesis (Fig. 1E) could explain the observed biogenesis defect on OMP25. We next sought to determine whether MTCH2 could be playing a more general role in the biogenesis of other mitochondrial outer membrane proteins. Using a quantitative proteomics strategy, we compared the steady-state levels of endogenous proteins in mitochondria isolated from wild-type or MTCH2-depleted cells (Fig. 2A, fig. S7A, and tables S2 and S3). We identified several outer membrane α -helical TA, signal-anchored (SA), and multipass proteins that were reproducibly decreased upon loss of MTCH2 (Fig. 2B). Because MTCH2 levels do not appreciably alter the mRNA levels for these proteins (fig. S7C) (17), we concluded that the effects of MTCH2 on the mitochondrial outer membrane proteome must be occurring post-transcriptionally. To determine whether MTCH2 exerts these effects specifically on biogenesis of nascent substrates, we tested a panel of mitochondrial proteins using our fluorescent reporter strategy (Fig. 1B). Consistent with the proteomics, MTCH2 affected the biogenesis of a functionally and biophysically diverse set of TA (18), SA, and multipass proteins (Fig. 2, C and D, and fig. S8).

On the basis of these experiments, we reasoned that MTCH2 may have evolved the ability to insert α -helical proteins into the outer membrane. To test this hypothesis, we focused on TA proteins, because they are the largest class of α -helical outer membrane proteins and adopt a uniform topology. Using an in vitro insertion assay with purified mitochondria (Fig. 3A and figs. S1C and S9), we found that loss of MTCH2 affected the insertion of several mitochondrial TA proteins but not unrelated intermembrane- or matrix-targeted controls (Fig. 3, B and C, and figs. S10 and S11). Further, using site-specific cross-linking (Fig. 3D and table S4) (19), we demonstrated that MTCH2 physically associated with nascent substrates during their insertion (Fig. 3E and fig. S12).

To determine whether MTCH2 is sufficient for TA insertion, we purified MTCH2 (Fig. 3F) and optimized conditions for its reconstitution into liposomes (fig. S13). Using a panel of α -helical substrates, we showed that purified MTCH2 specifically stimulated insertion of MTCH2-dependent, but not MTCH2-independent, TA and SA proteins (Fig. 3G and fig. S14). To reconcile these results with earlier observations that trypsin-treated mitochondria remain competent for TA insertion, we found that, in contrast to several subunits of the TOM complex, MTCH2 is largely trypsin resistant

¹Whitehead Institute for Biomedical Research, Massachusetts Institute of Technology, Cambridge, MA 02142, USA. ²Division of Biology and Biological Engineering, California Institute of Technology, 1200 East California Avenue, Pasadena, CA 91125, USA. ³Medical Scientist Training Program, University of California, San Francisco, San Francisco, CA 94158, USA. ⁴Tetrad Graduate Program, University of California, San Francisco, San Francisco, CA 94158, USA. ⁵Howard Hughes Medical Institute, Massachusetts Institute of Technology, Cambridge, MA 02142, USA. ⁶Department of Biology, Massachusetts Institute of Technology, Cambridge, MA 02142, USA. ⁷David H. Koch Institute for Integrative Cancer Research, Massachusetts Institute of Technology, Cambridge, MA 02142, USA.

*Corresponding author. Email: weissman@wi.mit.edu (J.S.W.); voorhees@caltech.edu (R.M.V.)

†These authors contributed equally to this work. ‡Present address: Oncovalent Therapeutics 1290 Rancho Conejo Boulevard, Ste 101-F, Thousand Oaks, CA 91320, USA.

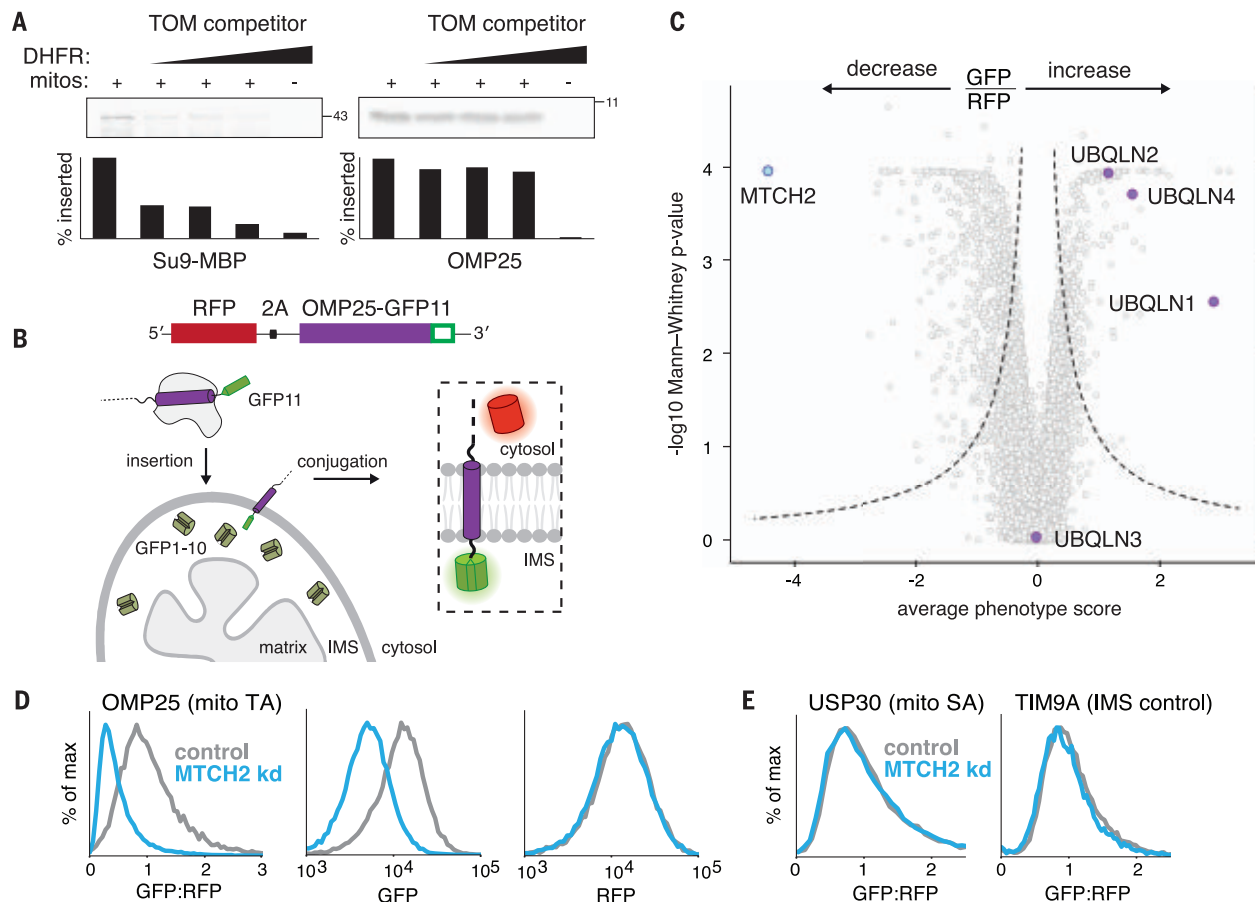


Fig. 1. Systematic characterization of human mitochondrial TA biogenesis.

(A) An ³⁵S-methionine labeled TOM substrate (made from a fusion of the canonical TOM-targeting sequence Su9 and the globular protein MBP, maltose binding protein) or OMP25 (a mitochondrial TA protein) were translated in rabbit reticulocyte lysate and released from the ribosome using puromycin. Competition assays were performed by incubation with purified mitochondria (fig. S1) in the presence of increasing concentrations of a recombinant TOM competitor (Su9-DHFR dihydrofolate reductase). Mitochondrial insertion was assessed by protease protection and analyzed by SDS-polyacrylamide gel electrophoresis (PAGE) and autoradiography. See also fig. S2. (B) Schematic of the split GFP reporter system used to specifically query integration of substrates into the outer mitochondrial membrane. A mitochondrial membrane protein fused to GFP11 is expressed in a cell that constitutively expresses GFP1-10 in the intermembrane space (IMS) along with a translation normalization marker (red fluorescent

protein, RFP) Successful integration into the outer membrane results in complementation and GFP fluorescence. (C) Volcano plot of GFP:RFP stabilization phenotype for the three strongest single guide RNAs (sgRNAs) versus Mann-Whitney *p* values from two independent replicates of a genome-wide CRISPR interference (CRISPRi) screen using OMP25-GFP11. Individual genes are displayed in gray, and specific factors that increase or decrease OMP25 mitochondrial integration are highlighted and labeled. (D) Integration into mitochondria of the OMP25-GFP11 reporter described in (B) was assessed in K562 cells that express a nontargeting (control) or MTCH2 knockdown sgRNA. GFP fluorescence relative to the normalization marker RFP was determined by flow cytometry and displayed as a histogram. Individual channels are also shown. (E) Biogenesis of GFP11-USP30, an outer membrane-resident signal-anchored protein, and TIM9A-GFP11, an IMS-localized protein, were assessed as in (D).

(Fig. 3H). Cumulatively, the requirement for MTCH2 in vivo and in vitro for TA insertion, together with its reconstituted insertase activity and physical association with substrates, rigorously establish MTCH2 as an insertase for α -helical mitochondrial outer membrane proteins.

Bioinformatic analysis reveals that in addition to MTCH2, other examples of SLC25 family members lacking canonical sequence motifs are found in both mitochondria and peroxisomes (Fig. 4A and figs. S15 and S16). Indeed, depletion of the close paralog MTCH1 (20), which is also localized to the mitochondrial outer membrane, had an additive effect

to loss of MTCH2 on biogenesis of many mitochondrial TAs (Fig. 4B and fig. S17). This result is consistent with our genome-wide screen (fig. S17C) and the synthetic lethal relationship between MTCH1 and 2 (27). We therefore propose that MTCH1 and 2 are the founding members of a distinctive class of membrane protein insertases that exploit the SLC25 transporter fold (fig. S18).

In contrast to other solute carrier family members, in which the transmembrane helices close to form a pore that allows charged species to cross the membrane, the AlphaFold2 (22) predicted model of MTCH2 contains a prominent groove that is accessible to the membrane and

lined with charged and polar residues (Fig. 4C and fig. S19). By introducing mutations at positions that altered the electrostatic potential of its intramembrane surfaces, we identified mutants that both diminish and enhance biogenesis of MTCH2-dependent, but not MTCH2-independent substrates (Fig. 4C and figs. S19 and S20). We therefore concluded that MTCH2's role in TA insertion relies on a hydrophilic surface within the bilayer.

Given MTCH2's central role in mitochondrial TA biogenesis, we asked whether it may broadly affect cellular proteostasis. We found that indeed, depletion of MTCH2 leads to an increase in ER insertion of mitochondrial TAs,

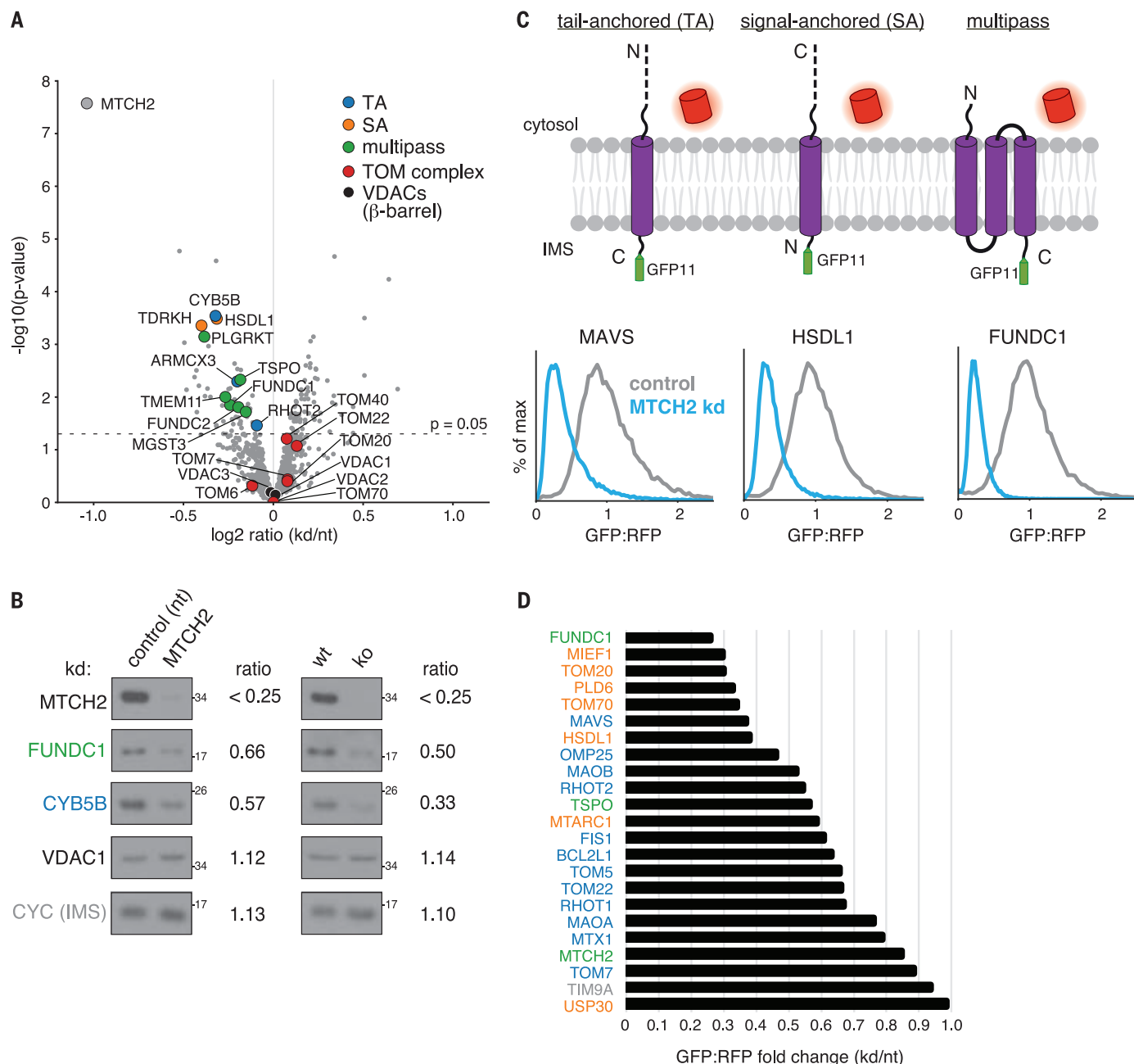


Fig. 2. MTCH2 is required for mitochondrial outer membrane protein biogenesis. (A) Label-free mass spectrometry analysis of purified mitochondria isolated from K562 cells using a Percoll gradient (fig. S1B) that express a MTCH2-targeting sgRNA (kd, knockdown) compared to a nontargeting (nt) control. Displayed are proteins that across four biological replicates were statistically altered in MTCH2-depleted versus nontargeting guide-expressing cells colored according to the indicated key (signal anchored, SA). (B) Immunoblotting of endogenous proteins in mitochondria isolated from MTCH2 depleted (kd) and control cells [generated as in (A); left], and wild-type (wt) and MTCH2 knockout (ko) cells (right). Substrates are colored by topology based on the key

shown in (A). Quantification of fold change in depleted versus control cells is displayed as determined using a dilution series for each antibody. (C) Flow cytometry analysis of integration of outer membrane protein reporters using the split GFP system described in Fig. 1B. GFP fluorescence relative to an RFP expression control is displayed as histograms in MTCH2 knockdown versus nontargeting K562 CRISPRi cells. Displayed are representative examples of a TA, signal anchored (SA), and multipass membrane protein that have a MTCH2-dependent biogenesis defect. (D) Summary of dependence on MTCH2 for the indicated outer membrane substrates determined using the fluorescent reporter system shown in (C) and colored by topology based on the key in (A).

whereas MTCH2 overexpression leads to a commensurate decrease in their mistargeting to the ER (Fig. 4D and figs. S21 and S22). This effect was enhanced by further depleting ATP13A1 (19), an ER dislocase for mislocalized

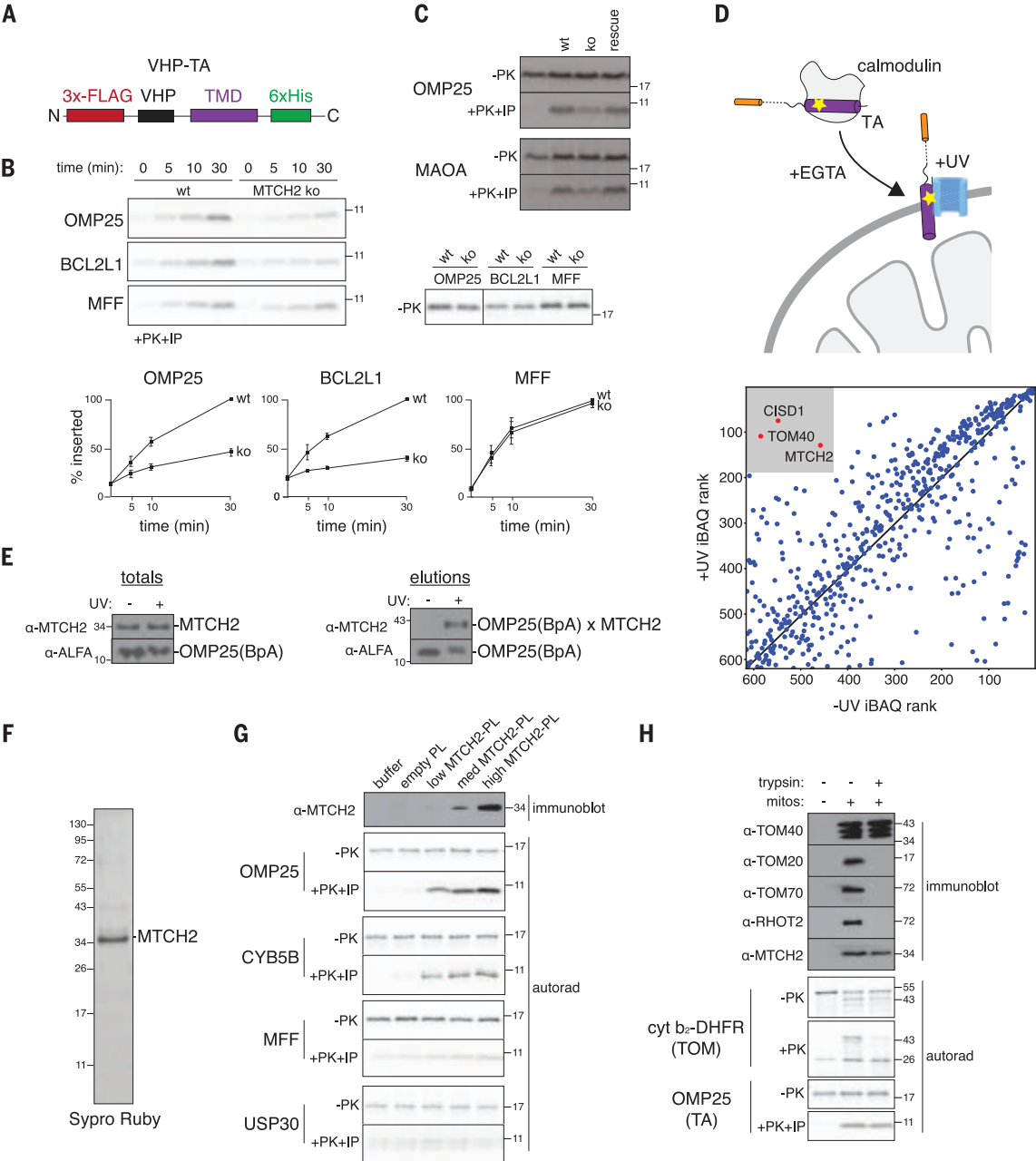
mitochondrial TAs (fig. S21C). These data suggest that MTCH2 is a central “gatekeeper” for the mitochondrial outer membrane: MTCH2 levels and activity dictate the cytosolic reservoir of mitochondrial TAs, which then can be

rerouted to the ER if unable to successfully integrate into mitochondria (Fig. 4D).

Lastly, considering that insertion of several MTCH2-dependent TAs play a central role in apoptosis, we reasoned that MTCH2 activity

Fig. 3. MTCH2 inserts diverse mitochondrial TAs into the outer membrane. (A) Schematic of the fusion between an inert N-terminal globular protein (VHP) and the TMDs of a panel of mitochondrial TAs (see also fig. S9) generated to probe TMD-dependent insertion by MTCH2.

(B) The indicated ³⁵S-methionine-labeled TA proteins were analyzed for in vitro insertion over time into mitochondria isolated from wild type (wt) or MTCH2 knockout (ko) K562 cells. Displayed are the samples before addition of protease (-PK; top right) and the protease-protected fragment that has been affinity purified via a 6xHIS tag on the C terminus of each substrate (+PK+IP; top left), ensuring insertion in the correct topology. (Bottom) Quantification of three biological replicates are plotted with error bars indicating one standard deviation at each time point. (C) As in (B), comparing insertion of the indicated TA proteins into wild type, MTCH2 ko, and MTCH2 ko + MTCH2 rescue mitochondria. (D) (Top) Schematic showing the photocrosslinking strategy. OMP25 containing the photoactivatable amino acid BpA within its TMD was expressed and purified from *Escherichia coli* as a complex with calmodulin. OMP25^{BpA} was released from calmodulin by addition of EGTA in the presence of mitochondria purified from K562 cells using a Percoll gradient (fig. S1B). Cross-linking was activated by ultraviolet (UV) irradiation, and the resulting cross-linked species were affinity purified via the Alfa-tag on the N terminus of OMP25^{BpA} for identification by mass spectrometry. (Bottom) All proteins identified by mass spectrometry were ranked by iBAQ abundance, and those specifically enriched in the UV compared to the -UV control are highlighted. Though TOM40 and CISD1 were identified, they were not notable hits in our screen (fig. S12), and TOM40 was not required for biogenesis both in vitro (Fig. 1A) and in cells (fig. S12B). (E) As in (D), with the resulting elution analyzed by immunoblotting to assess levels of cross-linked OMP25^{BpA}-MTCH2. (F) MTCH2 was



expressed and purified from human cells and analyzed by SDS-PAGE and Sypro-Ruby staining. (G) After reconstitution (see fig. S13 for optimization of conditions), the recovered proteoliposomes were analyzed by immunoblotting for incorporation of MTCH2. Using a protease protection assay, the indicated MTCH2-dependent (OMP25, CYB5B) and MTCH2-independent (MFF, USP30) ³⁵S-methionine-labeled substrates synthesized in rabbit reticulocyte lysate were tested for insertion into liposomes reconstituted with increasing amounts of purified MTCH2 compared to an empty control. The resulting protease protected fragments were immunoprecipitated and then imaged by autoradiography (autorad). (H) Mitochondria from wt K562 cells were treated with trypsin, and their ability to insert TOM (Su9-DHFR) or TA substrates (OMP25) was assayed by protease protection as in (A). The indicated outer membrane proteins were confirmed to be degraded in a trypsin-dependent manner by immunoblot, whereas MTCH2 remained largely intact.

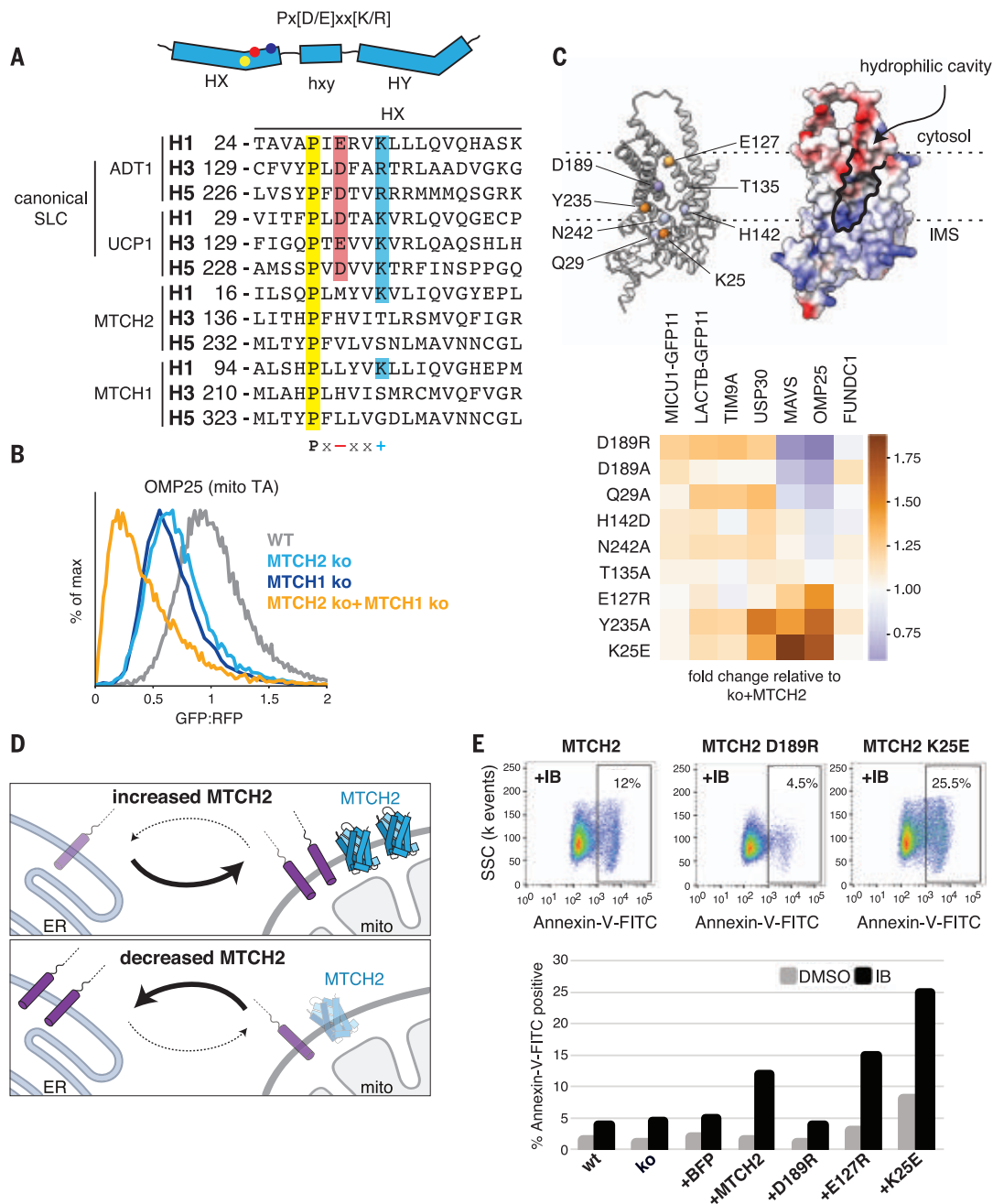


Fig. 4. MTCH2 is a master regulator of outer membrane function. (A) (Top) SLC25 transporters are composed of three sets of two TMDs (six total). The location of the characteristic Px[D/E]xx[K/R] motif within a single SLC25 repeat is indicated. (Bottom) Sequence alignment of helices 1, 3, and 5 (with starting residues indicated) from two canonical inner membrane SLC25 transporters (ADT1, UCP1) and two diverged outer membrane SLC25 transporters (MTCH1, MTCH2), with residues from the Px[D/E]xx[K/R] motif highlighted, where x is any amino acid. (B) Flow cytometry analysis of OMP25-GFP11 integration into the outer membrane using the reporter assay described in Fig. 1B. MTCH1 was depleted by transient knockout in either wild-type (wt) or MTCH2 knockout (ko) cell lines. (C) (Top) AlphaFold2-predicted model of MTCH2 highlighting conserved polar and charged residues within the bilayer colored based on their effects on OMP25 shown below. (Bottom) Using the reporter strategy shown in Fig. 1B, we tested the indicated MTCH2 mutants, which alter the electrostatic potential of its TMDs, for their effect on the indicated reporters (fig. S20). Depicted is a heat map summarizing the stimulation of each mutant relative to wild-type MTCH2 on

biogenesis of MTCH2-independent (MICU1, LACTB1, TIM9A, USP30) and MTCH2-dependent (MAVS, OMP25, FUNDC1) substrates. (D) Cell lines expressing GFP10 in the ER lumen were used to monitor mislocalization to the ER of mitochondrial TAs fused to a C-terminal GFP11. Table summarizing the analysis when either MTCH2 is depleted or overexpressed (data in figs. S20A, S21, and S22). (E) K562 cells expressing varying levels of MTCH2 or inactive (D189R) or hyperactive MTCH2 mutants (E127R or K25E; Fig. 4C) were treated with the chemotherapeutic imatinib mesylate (IB; 1 μ M) or carrier (dimethyl sulfoxide, DMSO) for 72 hours. Apoptosis was assessed by staining with Annexin-V-fluorescein isothiocyanate (FITC) and analyzed by flow cytometry. Shown are representative dot plots displaying the fraction of apoptotic cells upon imatinib (IB) treatment expressing wt MTCH2 compared to an inactive (D189R) or hyperactive mutant (K25E) (top) as well as a summary table for all MTCH2 constructs in IB- versus carrier-treated control. Single-letter abbreviations for the amino acid residues are as follows: A, Ala; C, Cys; D, Asp; E, Glu; F, Phe; G, Gly; H, His; I, Ile; K, Lys; L, Leu; M, Met; N, Asn; P, Pro; Q, Gln; R, Arg; S, Ser; T, Thr; V, Val; W, Trp; and Y, Tyr.

may affect cellular sensitivity to apoptotic stimuli. To test this, we overexpressed MTCH2 in human K562 cells, which are derived from a myelogenous leukemia cell line known to up-regulate the anti-apoptotic TA, BCL2L1 (23). We treated cells with imatinib, a leukemia treatment that targets the BCR-ABL oncogene, and measured apoptosis. We found that, whereas knockout of MTCH2 did not appreciably alter apoptosis propensity in this system, overexpression of wild-type MTCH2 markedly sensitized K562 cells to imatinib treatment (Fig. 4E). Critically, by expressing a series of MTCH2 mutants, we found that this sensitization depends on MTCH2's insertase activity.

We have demonstrated that MTCH2 is a defining member of a family of membrane protein insertases that are necessary and sufficient for insertion of TAs into human mitochondria. MTCH2's insertase activity relies on a hydrophilic groove within the bilayer, an apparent example of convergent evolution of many membrane protein translocases, including the EMC (24–26), Hrd1 (27), and YidC (28). A substantial number of mitochondrial TAs are enriched in basic residues immediately C terminal to their TMDs (29) and may be particularly reliant on charged surfaces along their route into the membrane. MTCH2's role also appears to extend to the integration of a broader class of α -helical proteins into the outer membrane, including SA and multipass proteins. Homologs of MTCH2 are present in metazoan peroxisomes, and its orthologs are found throughout holozoa, suggesting that the MTCH2 family has co-opted the SLC25 transporter fold to function in diverse biological membranes. The transition from a solute carrier, which mediates transport of small molecules across the membrane, to an insertase appears to have been enabled by the evolution of a membrane-accessible hydrophilic groove absent from MTCH2's SLC25 ancestors.

Previously, loss of MTCH2 has been reported to lead to a diverse range of phenotypes, including dysregulation of mitophagy, mitochondrial fragmentation (14), recruitment of tBID (16), and altered lipid homeostasis (15), and was also identified in a recent genome-wide association study for Alzheimer's disease (30–32). The identification of MTCH2 as a key gatekeeper for α -helical outer membrane proteins now provides a molecular explanation for its pleiotropic phenotypes, many of which can be directly ascribed to defects in biogenesis of MTCH2 substrates.

REFERENCES AND NOTES

1. J. R. Friedman, J. Nunnari, *Nature* **505**, 335–343 (2014).
2. W. Wang, F. Zhao, X. Ma, G. Perry, X. Zhu, *Mol. Neurodegener.* **15**, 30 (2020).
3. A. Bose, M. F. Beal, *J. Neurochem.* **139** (Suppl 1), 216–231 (2016).
4. S. Vyas, E. Zaganjor, M. C. Haigis, *Cell* **166**, 555–566 (2016).
5. N. Wiedemann, N. Pfanner, *Annu. Rev. Biochem.* **86**, 685–714 (2017).
6. K. N. Doan et al., *Cell Rep.* **31**, 107567 (2020).
7. D. G. Vitali et al., *eLife* **7**, e34488 (2018).
8. K. Setoguchi, H. Otera, K. Mihara, *EMBO J.* **25**, 5635–5647 (2006).
9. L. A. Gilbert et al., *Cell* **159**, 647–661 (2014).
10. M. Le Vasseur et al., *eLife* **10**, e67624 (2021).
11. R. Coukos et al., *eLife* **10**, e69142 (2021).
12. E. Itakura et al., *Mol. Cell* **63**, 21–33 (2016).
13. J. J. Ruprecht, E. R. S. Kunji, *Trends Biochem. Sci.* **45**, 244–258 (2020).
14. K. Labbé et al., *J. Cell Biol.* **220**, e202103122 (2021).
15. V. Rottiers et al., *Obesity (Silver Spring)* **25**, 616–625 (2017).
16. Y. Zaltsman et al., *Nat. Cell Biol.* **12**, 553–562 (2010).
17. J. M. Replogle et al., *Cell* **185**, 2559–2575.e28 (2022).
18. M. Y. Fry, S. M. Saladi, A. Cunha, W. M. Clemons Jr., *Traffic* **22**, 306–318 (2021).
19. M. J. McKenna et al., *Science* **369**, eabc5809 (2020).
20. F. Palmieri, *Mol. Aspects Med.* **34**, 465–484 (2013).
21. X. Shi et al., *Nat. Commun.* **13**, 2483 (2022).
22. J. Jumper et al., *Nature* **596**, 583–589 (2021).
23. A. Benito, D. Grillot, G. Nuñez, J. L. Fernández-Luna, *Am. J. Pathol.* **146**, 481–490 (1995).
24. T. Pleiner et al., *Science* **369**, 433–436 (2020).
25. L. E. Miller-Vedam et al., *eLife* **9**, e62611 (2020).
26. L. Bai, Q. You, X. Feng, A. Kovach, H. Li, *Nature* **584**, 475–478 (2020).
27. X. Wu et al., *Science* **368**, eaaz2449 (2020).
28. K. Kumazaki et al., *Nature* **509**, 516–520 (2014).
29. M. Rao et al., *eLife* **5**, e21301 (2016).

30. C. M. Karch, L. A. Ezerskiy, S. Bertelsen, A. M. Goate; Alzheimer's Disease Genetics Consortium (ADGC), *PLOS ONE* **11**, e0148717 (2016).
31. M. Allen et al., *Neurol. Genet.* **1**, e15 (2015).
32. V. Escott-Price et al., *PLOS ONE* **9**, e94661 (2014).

ACKNOWLEDGMENTS

We thank J. Nunnari and M. Le Vasseur for sharing the mitochondrial split GFP system. We thank T. Pleiner for technical assistance and Z. Levine for careful reading and input on the manuscript. We thank the Whitehead Institute Flow Cytometry Core and K. Daniels for access to FACS machines; the Whitehead Institute Genome Technology Core for support with sequencing of screen libraries; the Caltech Flow cytometry facility; and T. Y. Wang and for support for mass spectrometry. **Funding:** Research reported in this publication was supported by Howard Hughes Medical Institute (J.S.W.), Human Frontier Science Program 2019L/LT000858 (A.G.), the Heritage Medical Research Institute (R.M.V.), the Larry L. Hillblom Foundation (A.J.I.), and NIH F31-NS115380 (J.M.R.). **Author contributions:** A.G., J.S.W., and R.M.V. conceived the study. A.G., T.A.S., A.J.I., J.M.R., J.S.W., and R.M.V. were responsible for the design, analysis, and interpretation of experiments. A.G., T.A.S., and A.J.I. performed most of the experiments in the study with help from J.M.R., T.K.E., G.M., B.L., K.C.S., M.L.W., and A.N.P. T.C., B.L., and J.J.J. advised the design, sample processing, and analysis for all mass spectrometry experiments. A.G. and R.M.V. drafted the manuscript with input from all authors. **Competing interests:** J.M.R. consults for Maze Therapeutics and is a consultant for and equity holder in Waypoint Bio. J.S.W. declares outside interest in 5 AM Venture, Amgen, Chroma Medicine, KSQ Therapeutics, Maze Therapeutics, Tenaya Therapeutics, Tessera Therapeutics, and Third Rock Ventures. R.M.V. is a consultant and equity holder in Gate Bioscience.

Data and materials availability: All data needed to evaluate the conclusions in this paper are present in the paper or the supplementary materials. **License information:** Copyright © 2022 the authors, some rights reserved; exclusive licensee American Association for the Advancement of Science. No claim to original US government works. <https://www.science.org/about/science-licenses-journal-article-reuse>

SUPPLEMENTARY MATERIALS

science.org/doi/10.1126/science.add1856

Materials and Methods

Figs. S1 to S22

Tables S1 to S4


References (33–72)

MDAR Reproducibility Checklist


Submitted 26 May 2022; resubmitted 5 September 2022

Accepted 28 September 2022

10.1126/science.add1856



myIDP:
A career plan customized
for you, by you.




There's only one


Science




Features in myIDP include:



- Exercises to help you examine your skills, interests, and values.
- A list of 20 scientific career paths with a prediction of which ones best fit your skills and interests.




Visit the website and start planning today!
myIDP.sciencecareers.org

Science Careers In partnership with: 



ASSOCIATE DEPARTMENT HEAD & ASSOCIATE OR FULL PROFESSOR
Department of Immunobiology
College of Medicine, University of Arizona Health Sciences

The University of Arizona College of Medicine-Tucson (COM-T) is seeking an outstanding scientist who works in any area of immunology and microbiology to serve as **Associate Department Head (ADH) of the Department of Immunobiology**. The Department hosts a group of well-funded investigators with research interests in basic immunology, microbiology, and host-pathogen interactions. The ADH will serve a key role in the administration of the Department including functioning as a liaison between Department faculty, students, staff, and COM-T administration. A successful ADH candidate will engage in leadership and innovation in support of the research, teaching, and service missions of the Department, including, but not limited to, faculty promotion, tenure and evaluation reviews; trainee progress assessment; curricular and educational issues; and hiring. In addition, the ADH must be prepared and willing to step in for the Department Head in any facet of DH function.

Diversity, equity, and inclusion are the core values of the Department of Immunobiology, COM-T and UArizona. and candidates of all backgrounds are welcome and invited to apply. The successful candidate will join the UA Department of Immunobiology (primary) at the rank of **Associate** or **Full Professor**. If appropriate, the successful candidate will also join one or more of the UA Centers or institutes. Tenure can be awarded if applicable.

Competitive candidates are expected to have a track record of national or international prominence, active research programs, scholarly productivity and demonstrated ability to secure independent, peer-reviewed funding such as an NIH R01. Competitive candidates will also have a history of successfully working with a diverse group of students, trainees, and colleagues.

Modern, functional shared resources in clinical trials, biostatistics, bioinformatics, mouse models, and tissue acquisition and analysis, flow cytometry, mass spectrometry, structural biology and functional genomics are available to all University scientists.

Applicants must have a PhD and/or MD degree at a current rank of Associate (minimum 3 years in the rank) or Full Professor. Salary and start-up funds are attractive and commensurate with qualifications and experience.

The University of Arizona has been recognized on Forbes list of America's Best Employers in the United States and has been awarded the Work-Life Seal of Distinction by World@Work! For more information about working at the University of Arizona and relocations services, please go to talent.arizona.edu.

For full details and qualifications, and to complete an on-line application, see req9637 at talent.arizona.edu.

Outstanding UA Benefits! The University of Arizona is an Equal Opportunity Employer Minorities/Women/Vets/Disabled.



CAREER PLANNING

Science Careers helps you advance your career. Learn how !

- Register for a free online account on ScienceCareers.org.
- Search hundreds of job postings and find your perfect job.
- Sign up to receive e-mail alerts about job postings that match your criteria.
- Upload your resume into our database and connect with employers.
- Watch one of our many webinars on different career topics such as job searching, networking, and more.

Visit ScienceCareers.org
today — all resources are free



FROM THE JOURNAL SCIENCE 



SCIENCECAREERS.ORG




FACULTY POSITION IN APPLICATION OF DIGITAL HEALTH TO THE TREATMENT OF SUBSTANCE USE DISORDERS AND/OR RELATED FIELDS

The Department of Biomedical Data Science at the Geisel School of Medicine at Dartmouth (Geisel) seeks an outstanding individual to join our faculty within the Center for Technology and Behavioral Health (CTBH), an interdisciplinary research group whose mission is to inform the optimal development, scientific evaluation, and sustainable implementation of digital therapeutics for behavioral health. Candidates who currently hold the rank of **Associate** or **Full Professor** are preferred.

The successful candidate will be leading a vigorous research program on the application of digital health to the treatment of substance use disorders and/or related fields. This individual should be particularly experienced in leading clinical effectiveness trials and/or implementation science studies and should have a strong track record of extramural funding and leadership in research on substance use disorders.

Applicants must have earned a PhD and/or MD (or equivalent), have formal advanced training in the fields described above, and should have a successful track record of peer-reviewed publications, and a history of extramural funding. Expectations for teaching and mentoring are a critical part of this role, and individuals will be provided with such opportunities through membership in relevant PhD graduate programs.

The Geisel School of Medicine at Dartmouth College is located in the picturesque Upper Connecticut River Valley on the NH and VT border; a vibrant, academic and professional community offering excellent schools, lively arts, and an unmatched quality of life in a beautiful setting.

Dartmouth College is an equal opportunity/affirmative action employer with a strong commitment to diversity and inclusion. We prohibit discrimination on the basis of race, color, religion, sex, age, national origin, sexual orientation, gender identity or expression, disability, veteran status, marital status, or any other legally protected status. Applications by members of all underrepresented groups are encouraged.

Using Interfolio (<http://apply.interfolio.com/107745>), applicants should submit a cover letter (addressed to Chair of the Search Committee, Alan Budney, PhD), a curriculum vitae, and a 2-3 page description of their research interests and future research plans and arrange for submission of 3 letters of recommendation. Review of applications will continue until the position is filled.


CHANGE YOUR JOB AND YOU JUST MIGHT CHANGE THE WORLD.



Find your next job at [ScienceCareers.org](https://www.sciencecareers.org)

The relevance of science is at an all-time high these days. For anyone who's looking to get ahead in—or just plain get into—science, there's no better, more trusted resource or authority on the subject than *Science Careers*. Here you'll find opportunities and savvy advice across all disciplines and levels. There's no shortage of global problems today that science can't solve. Be part of the solution.

ScienceCareers

FROM THE JOURNAL SCIENCE  AAAS

Where Science Gets Social.

AAAS.ORG/COMMUNITY



AAAS' Member Community is a one-stop destination for scientists and STEM enthusiasts alike. It's "Where Science Gets Social": a community where facts matter, ideas are big and there's always a reason to come hang out, share, discuss and explore.

Member
COMMUNITY
AAAS

AMERICAN ASSOCIATION FOR THE ADVANCEMENT OF SCIENCE

U.S. POSTAL SERVICE

Statement required by the Act of 12 August 1970, Section 3685, Title 39, United States Code, showing the ownership, management, and circulation of:

1-9. *Science*, Publication No. 0036-8075, is published weekly on Friday, except the last week in December, at 1200 New York Avenue, N.W., Washington, DC 20005. Date of filing: 29 September 2022. This is also the address of the publisher, the editor, and the managing editor, who are, respectively, Bill Moran, Holden Thorp, and Valda Vinson.

10. The owner is the American Association for the Advancement of Science, 1200 New York Avenue, N.W., Washington, DC 20005. Stockholders: None.

11. Known bondholders, mortgages, and other security holders owning or holding 1 percent or more of total amount of bonds, mortgages, or other securities: None.

12. The purpose, function, and nonprofit status of this organization and the exempt status for federal income tax purposes have not changed during the preceding 12 months.

13-15. The average number of copies of each issue during the preceding 12 months is (A) Total number of copies printed: 45,795; (B) Paid circulation: 41,624; (1) Paid/Requested outside-county mail subscriptions stated on form 3541: 36,823; (2) Paid/Requested in-county subscriptions stated on form 3541: 0; (3) Sales through dealers and carriers, street vendors, counter sales: 4,796. (4) Other classes mailed through USPS: 5; (C) Total paid circulation: 41,624; (D) Free distribution: samples, complimentary, and other free copies: 3,278; (1) Outside-county as stated on form 3541: 2,952; (2) In-county as stated on form 3541: 0; (3) Other classes mailed through the USPS: 0; (4) Free distribution outside of mail carrier or other means: 326; (E) Total free distribution: 3,278; (F) Total distribution: 44,902; (G) Copies not distributed: 893; (H) Total: 45,795; (I) Percent paid and/or Requested Circulation: 92.7%.

Actual number of copies of single issue (9/23/2022) published nearest to filing date are (A) Total number of copies printed: 44,039; (B) Paid circulation: 39,856; (1) Paid/Requested outside-county mail subscriptions stated on form 3541: 35,260; (2) Paid/Requested in-county subscriptions stated on form 3541: 0; (3) Sales through dealers and carriers, street vendors, counter sales: 4,591; (4) Other classes mailed through USPS: 5; (C) Total paid circulation: 39,856; (D) Free distribution: Samples, complimentary, and other free copies: 3,328; (1) Outside-county as stated on form 3541: 3,037; (2) In-county as stated on form 3541: 0; (3) Other classes mailed through the USPS: 0; (4) Free distribution outside of mail: Carrier or other means: 291; (E) Total free distribution: 3,328; (F) Total distribution: 43,184; (G) Copies not distributed: 855; (H) Total: 44,039; (I) Percent paid and/or Requested Circulation: 92.29%.

I certify that the statements made above are correct and complete. (signed) Bill Moran, Publisher.

Search more jobs online

Access hundreds
of job postings on
[ScienceCareers.org](https://www.sciencecareers.org).

**Expand your
search today.**



By Daphne S. Ling

Lost in a sea of faces

A few months ago, I logged into a Zoom talk to discover that every little box was labeled “Jane.” The organizer had accidentally sent out the host link, which somehow gave us all the same name. Most of the other 78 attendees found this amusing. A professor even quipped, “Hey, this must be what Daphne sees every day. It’s so cool!” But it really isn’t cool. I have congenital prosopagnosia—face blindness, as it is colloquially known. I can see faces, but the individual details, such as the distance between the eyes or the shape of the nose, are fuzzy. As a result, recognizing faces—something so instant and unconscious for most—is a major challenge.

Over the years I developed coping mechanisms, such as offering equal-opportunity smiles to all—or, when that was too exhausting, resorting to equal-opportunity snubs. To distinguish people, I relied on extrafacial cues—the flamboyant Fluevog heels one person wears, the way another’s head bobs when they walk, the scent of cigarettes, the tap-tap-tap of cycling shoe cleats, a habitual lunch spot on a bench. There were many cringe-inducing faux pas as I pursued my neuroscience career, like when I asked the wrong professor how his sick husband was doing. But overall, I was managing.

Then, the pandemic hit. As interactions moved online, suddenly everyone became a stranger. For my peace of mind, I needed to get to the bottom of why I see the world so differently from most people. Through a combination of luck and privilege, I connected with a specialist who gave me an official diagnosis. Even though I had already essentially diagnosed myself, it was a relief to have a professional put a formal name to it.

I also developed new coping mechanisms. In Zoom meetings, I find myself lost amid a sea of faces, which makes it very difficult to follow the discussion—especially when the other participants’ labels include “iPad,” “KP,” and “Batman Loves Cinderella” (true story). I’ve learned to wear something conspicuous on my head, like a ribbon, so at least there will be one face I can quickly identify (mine!) when I’m overwhelmed. And if I’m going to an in-person meeting or event where I’m expected to know people, I send out an email explaining that if I snub them, it won’t be intentional. I have found that people are less likely to be insulted when they know beforehand.

But in some cases, there’s little I can do. Networking at conferences, for example, isn’t easy when you come off as aloof because you’re wondering whether you’ve talked to that



“As interactions moved online, suddenly everyone became a stranger.”

person before. At a recent small conference, a faculty member I know found me to say hello, and I wanted to make sure I reciprocated when I saw her next. I thought I could recognize her by her hairstyle, but I ended up saying hello to four different women—none of whom were her. I’m still unsure whether our paths crossed again. But I’ve learned to beat myself up less about experiences like these.

Still, it can be incredibly alienating to constantly feel I need to educate people and explain myself; sometimes I feel like something out of a science-fiction plot. A recent Zoom presentation really hammered this home. Titled “You Don’t Belong Here,” it was intended to show how some environments can

be exclusionary and what can be done to address that. But as the panelists alternated between acting out scenes and commenting on them, referring to their alter egos in the third person, I was flummoxed. I left feeling exactly as the title said: “You don’t belong here.”

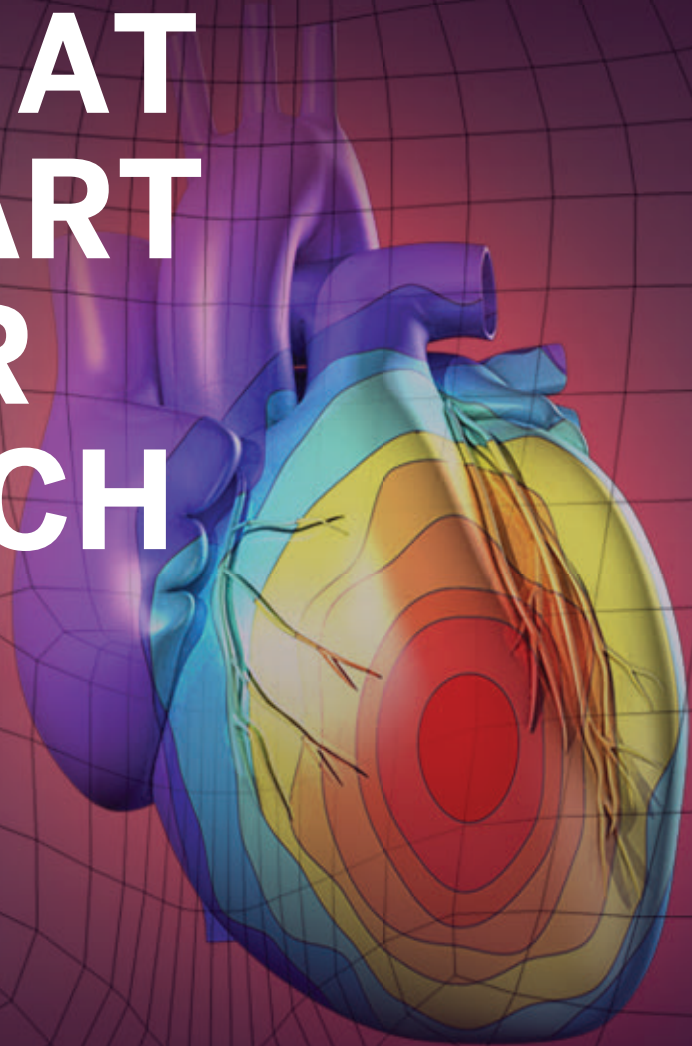
It would have been a great help if the presenters had explained at the outset that they were going to alternate between alter egos. I recognize that my condition is relatively rare, and it didn’t occur to them that such a simple step would make such a big difference for someone. But academics with disabilities exist, and we need our colleagues to think broadly and creatively about accessibility and inclusion. For starters, in-person events are better for me, whereas others benefit from virtual options, so let’s keep pushing for hybrid models to allow participation in the form that works best for each individual. Let’s create an environment where we all feel like we belong. ■

Daphne S. Ling is a Ph.D. student at the University of British Columbia, Vancouver. Send your career story to SciCareerEditor@aaas.org.


science.org/journal/stm

PUT HUMAN HEALTH AT THE HEART OF YOUR RESEARCH

Submit your research:
cts.ScienceMag.org



Science
Translational
Medicine
 AAAS

 Twitter: @ScienceTM

 Facebook: @ScienceTranslationalMedicine

UT Southwestern Medical Center Salutes Drs. Michael Brown and Joseph Goldstein

1972



2022



Celebrating 50 years of collaboration, discovery, and the science behind lifesaving statins.

UT Southwestern Medical Center is proud to honor Drs. Michael Brown and Joseph Goldstein as they celebrate 50 years of their collaborative research at UT Southwestern.

The duo launched their joint laboratory at UTSW in 1972 and were awarded the 1985 Nobel Prize in Physiology or Medicine for discovering the LDL (“bad cholesterol”) receptor and its role in hypercholesterolemia. That discovery revealed the mechanism by which the blood LDL-cholesterol level is controlled and laid the foundation for the pharmaceutical development of lifesaving statin drugs for heart health, which today are used by more than 200 million people around the globe.

The Brown and Goldstein Nobel Prize was the first of six Nobels received by UT Southwestern faculty members in the past 40 years.

Brown and Goldstein’s collaboration has been one of science’s most successful partnerships over the past five decades – and it endures to this day. The two jointly have trained 175 young scientists and continue to work daily in their lab, sharing their work ethic and intellect with succeeding generations of scientists.

The Brown and Goldstein story is one of exceptional creativity, unwavering diligence, dogged persistence, unrelenting focus, and a remarkable partnership.

“Joe and Mike’s brilliant science seems to me to be vaguely magical, and, even in science, without enchantment there is nothing. Their science is an act of creation, and through their creativity they have constructed biological edifices that have profoundly enhanced our world.”

– **Richard Axel, M.D.** | Nobel Laureate, 2004 | Co-Director of the Zuckerman Institute and University Professor | Columbia University

“Mike and Joe are a duo whose discoveries have eased the burden of human disease while illuminating the processes that make life possible. They are truly biomedical superheroes.”

– **David Baltimore, Ph.D.** | Nobel Laureate, 1975 | President Emeritus and Judge Shirley Hufstедler Professor of Biology | California Institute of Technology

UT Southwestern
Medical Center